NORTHWESTERN UNIVERSITY

Fundamental Electron Transfer Dynamics in Donor-Acceptor Compounds: One-, Two-, and Four- Pathway Systems

A DISSERTATION

SUBMITTED TO THE GRADUATE SCHOOL
IN PARTIAL FULFILLMENT OF THE REQUIREMENTS

for the degree

DOCTOR OF PHILOSOPHY

Field of Chemistry

By

Jeremy Fisher

EVANSTON, ILLINIOS

August 2023

Abstract

Fundamental Electron Transfer Dynamics in Donor-Acceptor Compounds: One-, Two-, and Four- Pathway Systems

Jeremy Fisher

This thesis document is comprised of three research projects. The first investigates the active vibrational modes involved in twisted intramolecular charge transfer in a Julolidine-BODIPY dyad using two-dimensional electronic spectroscopy along with DFT calculations. We identified two types of vibrations, compression and torsional motion, as playing an important role in this intramolecular charge transfer. The second project examines a four-pathway donor-acceptor compound, an extended perylene core connected to four naphthalene diimide units, in solution and in a single crystal using transient absorption and transient absorption microscopy spectroscopies. By comparing this multi-pathway system to its single-pathway analogue in solution, we concluded that the four acceptor units do not interact with one another in solution where the ensemble of molecules is dispersed throughout the solution. In a single crystal, however, the extremely long-lived charge separated state lifetime suggests charge migration across electron acceptor units. The third project studies a Zn-porphyrin dimer with two porphyrin units connected to a triptycene bridge that locks them into a co-facial geometry, with a single benzoquinone electron acceptor. There is significant evidence of porphyrin-porphyrin interaction in this dimer system and with the fast charge separation rate, we hope to see evidence of coherent multi-pathway electron transfer at cryogenic temperatures in a glassy matrix in the two-dimensional electronic spectroscopy data.

Acknowledgements

I came to Northwestern to pursue my PhD in chemistry for one simple reason: my love of chemistry. Though I was lucky to have many phenomenal professors in my undergraduate education, I am particularly grateful to Professor Austin Scharff who taught me organic chemistry, Professor Xander Barnes who taught me thermodynamics, and, of course, Professor Jonathan Barnes who took me into his lab for my last two years at WashU. With so many inspiring educators cultivating my scientifically curious mind, I entered my PhD program with an open mind, realizing that no matter where I looked, I was likely to find something incredible.

As I began considering which lab to join here, however, it quickly became clear that the Wasielewski group was the one for me. Professor Michael Wasielewski gave me the opportunity to immerse myself in physical organic chemistry while still being allowed to get my hands dirty in the synthesis lab. I was given the opportunity to study the exact material I was interested in—the details of light's interaction with chemical matter—in a world-class lab surrounded by incredible scientific minds and people. For giving me this opportunity and for seeing it through with me, I would like to thank Professor Michael Wasielewski.

Upon joining the group, it did not take long to find my place up in B-lab. With Dr. Michele Myong as my mentor, I felt comfortable and confident, even in such an unfamiliar space. Michele was always so kind and helpful; I am very lucky to have had her as my mentor. In addition to Michele, my original B-lab crew helped me tremendously in getting started here. Dr. Joseph Christensen, Prof. Jacob Olshansky, and Dr. Adam Coleman, thank you all for all the help along the way. And, of course, for introducing me to rock climbing! I am lucky to still be friends with all these people, and I will miss Joe dearly as I leave Chicago. Climbing with him

and going to his condo for dinner and hangouts with the kids has enriched my time here greatly. So, thank you Dr. Joe! In addition to all these great B-lab mentors, Dr. Jon Schultz was such an important mentor for me during my earlier years here. Jon would chat with me for hours on end as I tried to demystify all the secrets of quantum coherence and entanglement. Jon is such a strong force of positivity and encouragement; I am so lucky to have had him as a mentor and friend.

This brings me to my lab neighbor for the last five years: Jillian Bradley. Jillian and I have been through it all together, thick and thin. I am not always the easiest person to work next to. I have been very cranky on many occasions in B-lab, but Jillian's calm and positive energy has always been there to keep me grounded. In addition to Jillian, Emmaline, who also joined the group our year, has been such an important presence for me. In times of great turmoil, Emmaline has been there to listen and comfort. I'm not much of a hugger, but even I know Emmaline gives a mean hug. Thank you for everything.

As the years rolled by, I suddenly found myself as one of the older students in the lab and the spaces I knew were now filled with different people. After all my mentors had left, I felt a bit aimless for some time. That is until Dr. Yunfan Qiu (Dr. Q) came and joined B-lab. When Frank joined our space, I was in a very tough spot with my research. Frank has been by my side through the darkest times in the lab and has always been there to keep me calm and focused. I am so grateful for all I've learned from Frank and cherish our friendship dearly.

Along with this change in personnel was the continued onboarding of new students each year. The Waz group got four wonderful students who joined the year after me: Oscar, James, Paige, and Malik. Oscar has a kindness to him that shines straight through his big smile. He will be a force of good we are lucky to have on our side. James is a true sweetheart. Always mild-tempered and level-headed, James makes for a great friend. Though we went through something of a rough patch, I remain extremely grateful for all the help he gave me and for the good memories we shared. I still remember when this cohort first came to campus for orientation, my friends and I would watch a huge crowd of the first years following along after little old Paige Brown, who always wore a huge smile at the head of the pack. Paige is a natural born leader and is surely destined to do great things. She is always looking to take care of her friends, a truly selfless giver. Malik carries himself with an aura people just can't seem to get enough of. Quietly confident yet bashful, Malik is always looking to help others in the lab, whether through brainstorming ideas, training on an instrument, taking measurements, or helping vent. Malik is an invaluable member of the lab and has a very promising career ahead of him. I look forward to seeing what all these wonderful people accomplish.

The Waz group continued to attract great groups of people and I found myself with a new office mate, Hannah Eckvahl. Hannah has been a great person to chill in the office with. She's always good to bounce ideas off of or just goof around with. After having the office all to myself over covid, I was not too excited to have to share it, but I'm glad to have been able to share it with her in the end. Thanks for always keeping it real.

Over my five years here, there have been some great program coordinators to help us all including Amanda Mahoney, Melanie Sandberg, and now Corey Drennon. These three were always so helpful and generous with their time. They really helped in making the group a more welcoming and warm place.

There is one more person I am extremely grateful for in the Waz group and that is Professor Ryan Young. Ryan is always juggling a thousand things from family to malfunctioning equipment and lab drama, yet he is miraculously always able to make time for everyone. With so much uncertainty and stress in going through this program, Ryan has always been a tremendous source of comfort and encouragement. He has taught me so much about the world of physical chemistry (especially the physical side), but also about life in general and about growing up. I've matured a lot through the lessons I've learned from Ryan and feel so grateful to have had him by my side from the start.

Now moving beyond the lab, I have always considered myself very blessed to be surrounded by great friends. I have made so many great friends here and while I am grateful for all of them, there are three in particular that I would like to acknowledge. Those three would be Dillon Edwards, Tyler Jaynes, and Dr. Ian Peczak. The four of us became good friends early on and I'm not sure what any of us would have done without the others. Putting up with me as a roommate cannot be easy so I applaud you in surviving and thank you for your patience. Thank you for your friendship and for all the good times. Most of all, thank you for showing me the beautiful world of snowboarding out in the west coast. Tahoe Forever!

Finally, my family. Words escape me as I try to write. For now, I will keep it simple. I love you all endlessly and hold you in my heart always. Thank you.

I dedicate this work and all my accomplishments to my older brother, Sammy.

I hope to make us both proud one day.

Table of Contents

List of Figures

List of Schemes

List of Equations

List of Tables

Chapter 1: Two-Dimensional Electronic Spectroscopy Reveals Vibrational Modes Coupled to Charge Transfer in a Julolidine-BODIPY Dyad

Jeremy M. Fisher,† James P. O'Connor,† Paige J. Brown, Taeyeon Kim, Emmaline R. Lorenzo,
Ryan M. Young,* and Michael R. Wasielewski*
Department of Chemistry and Institute for Sustainability and Energy at Northwestern (ISEN),
Northwestern University, Evanston, IL 60208-3113

1.1 Abstract

Understanding charge transfer (CT) dynamics in molecular donor-acceptor dyads can provide insight into developing efficient donor-acceptor molecules for capturing solar energy. Here, we characterize the excited-state evolution of a julolidine-BODIPY (**Jul-BD**) donor-acceptor system with an emissive CT state using time-resolved fluorescence, femtosecond transient absorption, and two-dimensional electronic spectroscopies. Comparison of these results with those from phenyl-BODIPY (**Ph-BD**) allows us to identify the dynamics at play during CT state formation and its subsequent conversion to either a fully charge-separated (CS) or triplet state. Photoexcitation of **Jul-BD** in tetrahydrofuran results in formation of an initial emissive CT state that relaxes before fully charge separating. In contrast, **Jul-BD** in toluene exhibits similar CT state dynamics, albeit at slower timescales, before decaying to a terminal triplet species. Quantum beat analysis at early times in both solvents shows several vibronic modes, which are corroborated using density functional theory (DFT) calculations. For **Ph-BD**, a single 220 cm^{-1} compression mode about the single bond linking the phenyl to BODIPY modulates their orbital overlap. Three active vibronic modes, 147 cm^{-1}, 174 cm^{-1}, and 214 cm^{-1}, are found in **Jul-BD** regardless of the dielectric constant of the medium. These motions correspond to compression and torsional motions along the single bond joining **Jul** to **BD** and is responsible for the evolution of the spontaneous and stimulated

emission features in the time-resolved spectroscopic data, which is further supported by time-dependent DFT calculations of the steady-state absorption spectrum of the **Jul-BD** as a function of increasing donor-acceptor dihedral core angle. These findings show how torsional and compression motions can play a pivotal role in intramolecular charge transfer between a donor and acceptor linked by a single bond.

1.2 Introduction

Organic photovoltaics harness solar energy by generating free charge carriers following photoexcitation. Once a photon is absorbed, optimizing the charge separation (CS) efficiency is essential for realizing energy conversion applications.[1-3] It has been shown that prior to complete charge separation across the D-A interface, the photogenerated exciton can rapidly form a bound, electron-hole pair at the interface.[4-10] This bound pair is referred to as a charge-transfer (CT) state, or CT exciton, before evolving via full CS into free charge carriers.

The exact mechanism of exciton dissociation is a topic of considerable interest, as conversion of the CT state to the CS state often limits solar energy harvesting efficiencies. To this end, model organic molecular D-A systems have proven useful in understanding the more basic aspects of the CT conversion phenomenon. Studies have focused on tuning donor and acceptor energetics, D-A distances, the nature of covalent bridges linking D and A, and the relative D-A geometry throughout the electron transfer process.[11-30]

These studies have served to better define the nature of CT states and the role they play in promoting CS.[30-36] The evolution of CT to CS states involves increased ionicity over time until full electron-hole dissociation results in CS. Indeed, a recent study has demonstrated this distinction by exploring a two-step charge separation process, wherein a D-A dyad was initially photoexcited to form a bright exciton, which then produces a state with partial CT character before forming the final CS state.[33]

In model compounds, D and A are often linked by a single covalent bond, such that photoexcitation of the system results in torsional motion about that bond as charge transfer occurs.[33, 37-46] Indeed, many examples of twisted intramolecular charge transfer (TICT) states have been studied.[33, 38, 46-54] In these cases, when the photoexcited D-A system relaxes from its local exciton (LE) state, charge transfer is favored when the two π systems have large dihedral angles relative to one another, while conversely, maintaining planarity between the D and A π systems favors relaxation of the LE state, often via radiative decay by fluorescence.[38, 42] TICT states have proven useful in developing optimized organic light emitting diodes (OLEDs),[55-57] high efficiency OPVs,[58-61] finely tuned aggregation-induced emission luminogens (AIEgens),[41, 62] and techniques for sensing chemical species,[63-70] microenvironmental viscosity,[56, 71, 72] and environmental polarity.[48] For example, Sunahara and coworkers[48] took advantage of this architecture to develop a library of BODIPY-containing compounds exhibiting different degrees of TICT state formation to be utilized for solvent polarity sensing. Thus, fundamental studies into the nature of the structural changes that accompanies the CT and CS dynamics are important to further optimize the performance of these materials.

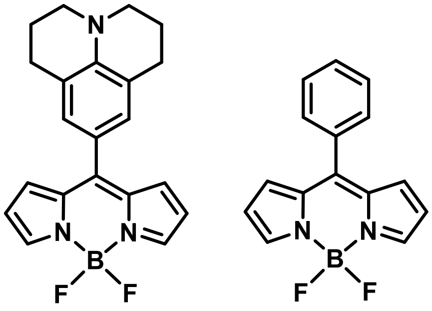

Jul-BD **Ph-BD**

Scheme 1.1 Structures of Jul-BD and Ph-BD.

In this work, we examine a D-A system containing a BODIPY chromophore as an electron acceptor covalently linked directly to a julolidine electron donor, **Jul-BD** (Scheme 1). BODIPY is an easily tunable chromophore that has well-understood photophysics, making it a desirable components for focusing on the CT dynamics.[73-76] The structure of julolidine restricts the conformation of the nitrogen lone pair to optimize its conjugation with its benzene π system. This results in **Jul-BD** having a strong CT absorption band that is relatively well-separated from its higher energy locally excited (LE) absorption band.[77] These distinct LE and CT absorptions allow their selective excitation to assist analysis of the subsequent excited state dynamics.

We utilized both time-resolved fluorescence (TRF) and transient absorption (TA) spectroscopies to initially determine the dynamics and kinetics of the system. Upon photoexcitation of **Jul-BD**, a multi-step charge separation process was revealed wherein an initial bright CT state relaxes before proceeding to form the fully CS species in tetrahydrofuran (THF), or the BODIPY triplet state in toluene. To assess the BODIPY contribution to the photophysics of **Jul-BD**, a control molecule was synthesized in which julolidine is replaced by a phenyl group, **Ph-BD** (Scheme1.1). Two-dimensional electronic spectroscopy (2DES) was then employed to explore the nature of the reaction coordinate along which these dynamics occur. Our broadband pump pulses preferentially excite large portions of the LE absorptions in **Jul-BD** and **Ph-BD** as well as the CT absorption in **Jul-BD** enabling the observation of how the states interact and to determine the overall excitation energy dependence in these systems. In addition, the vibrational modes that are coupled to the time dependent CT and CS processes were identified using 2DES. These vibronic interactions manifest as quantum beats, which have been used previously to elucidate both CT and singlet fission photophysics.[61, 78-82] Finally, density functional theory (DFT) calculations were used to build a microscopic picture of the excited-state dynamics, giving further context to the trends observed in the TRF, TA, and 2DES data. Using these methods the molecular vibrational modes that direct the dynamics were identified as contracting and torsional motions about the D-A single-bond linkage. These results demonstrate the importance of D-A geometry and the role these Raman-active vibrational modes can play in CT dynamics.

1.3 Methods

1.3.1 Synthesis. The two BODIPY derivatives studied in this paper were prepared following literature procedures (Scheme S1.1).[77] Further details can be found in the Supporting Information (SI).

1.3.2 Steady-State Optical Spectroscopy. UV-visible-NIR steady-state absorption spectra were measured at room temperature using a Shimadzu UV-1800 spectrometer. NIR emission was measured using a HORIBA Nanolog fluorimeter.

1.3.3 Electrochemistry. Electrochemical measurements were performed on a CH Instrument 750E electrochemical workstation. Measurements were made using a 1.0 mm diameter glassy carbon working electrode, a platinum wire auxiliary electrode, and a silver wire pseudo-reference electrode in 0.1 M solutions of n-butylammonium hexafluorophosphate ($TBAPF_6$) in acetonitrile purged with argon. Ferrocene was used as an internal standard.

1.3.4 Time-Resolved Fluorescence Spectroscopy. Picosecond time-resolved fluorescence data were collected using a commercial direct-diode-pumped 100 kHz amplifier (Spirit 1040-HE, Spectra-Physics), producing a fundamental beam of 1040 nm (350 fs, 12 W) which was attenuated and used to pump a non-collinear optical parametric amplifier (Spirit-NOPA, Spectra-Physics) capable of delivering tunable, high-repetition-rate pulses with pulse durations as short as sub-20 fs. The samples were excited with 570 nm, ~1 nJ laser pulses. Fluorescence was detected using a Hamamatsu C4780 Streakscope as previously described.[45] Samples were prepared in 2-mm pathlength quartz cuvettes. All data were acquired in single-photon-counting mode using the Hamamatsu HPD-TA software. The temporal resolution, given by the instrument response function (IRF), was approximately 3% of the sweep window, with the shortest time resolution being ~30 ps. Since the lifetime of the fastest of the species was within the IRF of the 1 ns time window, when performing global fitting analysis of the data in the 10 ns window, the decay time of the fastest species was fixed to 30 ps, well within the IRF of the 10 ns window (~300 ps).

1.3.5 Transient Absorption Spectroscopy. Femtosecond transient absorption (TA) experiments were performed on an apparatus that has been described previously.[82] Tunable excitation pulses were generated by using a commercial colinear optical parametric amplifier (TOPAS-Prime, Light-Conversion, LLC). The polarization was spatially randomized to eliminate the effects of polarization-dependent dynamics. Spectra were collected using commercial spectrometers (customized Helios/Eos, Ultrafast Systems, LLC). The total instrument response function was ~300 fs. Transient spectra were averaged for at least 3 s per delay point. Prepared samples had an absorbance of 0.2-0.7 at the excitation wavelength and were irradiated in 2-mm pathlength quartz cuvettes with 0.4-0.8 μJ/pulse focused to ~0.2 mm diameter spot.

1.3.6 Two-Dimensional Electronic Spectroscopy. 2DES experiments were conducted using an apparatus described earlier.[83] Pump pulses were generated using a noncollinear optical parametric amplifier (Spirit NOPA-3H, Spectra-Physics). Pump pulses with two distinct spectral profiles were used, one with a 480-545 nm bandwidth and one with a 500-640 nm bandwidth. Both NOPA pump beams were tuned to co-excite both the LE and CT absorption bands, but the shorter wavelength pulse is biased towards the LE absorption transition, while the longer wavelength pulse is biased towards the CT band.

1.3.7 Density Functional Theory Computations. Density functional theory (DFT) calculations using Q-Chem 5.1 were performed on Jul-BD at the level of ωB97X-D/6-31G* and on Ph-BD at the level of B3LYP/6-31G*. Constrained DFT (CDFT) was utilized for calculations involving compounds with CT character and compounds with specified geometric constraints. Absorption spectra were calculated using time-dependent DFT (TDDFT).

1.4 Results and Discussion

1.4.1 System Energetics

Steady-State Optical Spectroscopy. The UV-visible absorption spectra of **Ph-BD** and **Jul-BD** in THF and toluene as well as the 2DES pulse spectra are shown in Figure 1.1a. **Ph-BD** has a sharp absorptive feature attributed to the lowest singlet band (LE state, $S_1 \leftarrow S_0$) at λ_{max} = 500 nm and 505 nm in THF and toluene, respectively, with a shoulder (0-1 vibronic band). **Jul-BD** has a sharp absorptive feature attributed to the LE state at λ_{max} = 488 nm and 493 nm, as well as a broad absorptive feature attributed to the CT transition at λ_{max} = 564 nm and 556 nm in THF and toluene, respectively. The broadening and blue shifting of the LE band in **Jul-BD** compared to the LE band in **Ph-BD** implies that the **Jul-BD** LE state is mixed with the CT state. Additionally, the donor-acceptor coupling is larger in polar solvents, as the energy separation between the LE and CT bands is larger in THF than toluene by 452 cm^{-1}. The molar extinction coefficients for both compounds in both solvents can be found in the SI. To determine the relative contributions of the LE and CT bands upon selective excitation we fit a pair of Gaussian functions to the **Jul-BD** absorption spectra (Figure S1.9). Sole LE-like excitation was measured to be <465 or <472 nm and sole CT excitation is >557 or >560 nm in THF or toluene, respectively. See the Supporting Information for details.

Steady-state emission spectra were measured for both **Ph-BD** and **Jul-BD** in THF and toluene (Figure 1.11b), additional data can be found in the SI). **Ph-BD** shows a sharp emission band at 540 nm with a small Stokes shift. In contrast, the broad emission from **Jul-BD** ranges from 600-850 nm and has a 3,450 cm^{-1} Stokes shift, which strongly suggests this emission originates from a CT state. No steady-state emission was observed for **Jul-BD** in THF. The quantum yields of emission

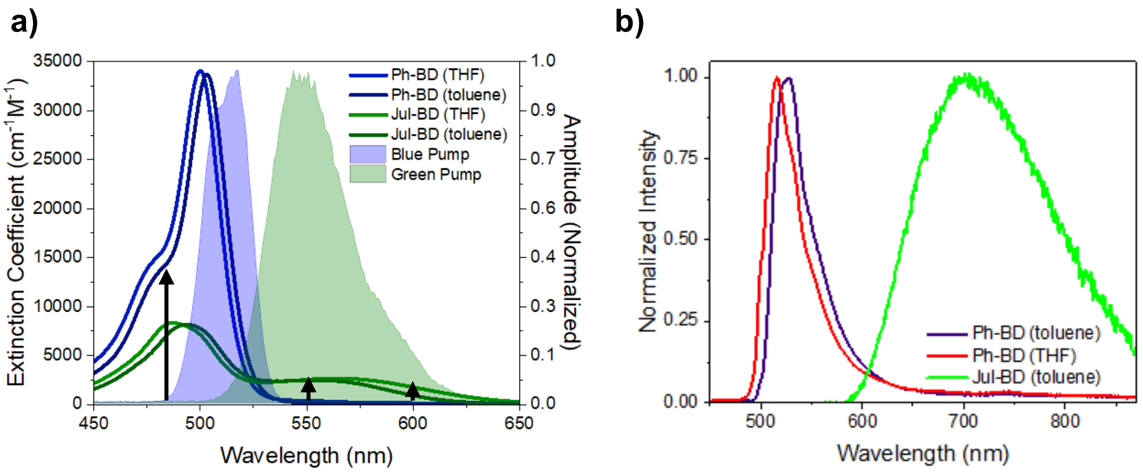

Figure 1.1 (a) UV-Vis absorption spectra of Ph-BD and Jul-BD in THF and toluene normalized to their respective molar extinction coefficients along with black arrows to indicate where photoexcitation was used in TA/TRF experiments and 2DES pump spectra for blue and green pulses to show the overlap of each with the BODIPY systems. (b) Fluorescence spectra of Ph-BD in toluene and THF and Jul-BD in toluene.

(Φ_f) were 2% for **Ph-BD** and 1% for **Jul-BD** in in toluene. In DCM, the value of Φ_f for **Ph-BD** was unaffected (2%), while emission for **Jul-BD** became undetectable ($\Phi_f < 0.5\%$).

We used these steady-state optical measurements to calculate the approximate energy levels for the LE state of **Ph-BD** from the crossing point of its normalized absorption and emission spectra (Figure S1.10). The data yield $E_{LE} = 2.44$ eV and 2.42 eV in THF and toluene, respectively. These data are also used as an estimate of the LE state energy of **Jul-BD**, as LE fluorescence is not observed from **Jul-BD**. The CT state energy of **Jul-BD** was calculated using time-resolved fluorescence spectra as described below.

The absorption spectrum of chemically oxidized **Jul-BD** in toluene was measured to be able to assign **Jul**$^{\bullet+}$ in the transient optical experiments (Figure S1.11). The spectrum has an absorption maximum at 520 nm and lacks the CT band present in neutral **Jul-BD**. The **BD**$^{\bullet-}$ anion has been reported previously to exhibit an absorption peak at 615 nm.[84]

Electrochemistry. Differential pulse voltammetry (DPV) measurements on **Jul-BD** reveal a reduction potential of -1.1 eV vs SCE and an oxidation potential of 0.6 eV vs. SCE in acetonitrile (Figure S1.12). We used these redox potentials to calculate the CS state energy of **Jul-BD** in THF and toluene. The Weller equation[85] was applied to these data to correct for the different dielectric constants between acetonitrile, the solvent in which the electrochemical potentials were measured, and THF and toluene, the solvents in which the transient optical experiments were performed (see the SI). This gives the energy of the fully charge-separated state as 1.97 eV and 1.72 eV in toluene and THF, respectively.

1.4.2 Excited-State Dynamics

Time-Resolved Fluorescence Spectroscopy. The time evolution of the emission spectra was investigated using TRF spectroscopy at room temperature in toluene following photoexcitation at 450 nm and 570 nm for **Ph-BD** and **Jul-BD**, respectively (Figure 1.2 and S1.13-S1.15). **Ph-BD** displays a strong emission at 522 nm that decays with a time constant of $\tau = 409 \pm 55$ ps. This emission spectrum is consistent with the steady-state spectrum as discussed above. **Jul-BD**, on the other hand, exhibits two distinct emission bands. The first band occurs at 550-750 nm with a maximum at about 630 nm. The second emission band strongly resembles the emissive feature observed in steady-state fluorescence measurements with a broad spectrum from 600-800 nm with a maximum at 690 nm. This first emission band decays to second weaker emission state in $\tau_1 < 30$ ps, while the second emission band decays in $\tau_2 = 1.15 \pm 0.03$ ns.

Transient Absorption Spectroscopy. Upon photoexcitation near 500 nm, the transient absorption spectrum of **Ph-BD** (Figures S1.16-S1.17) shows a ground-state bleach (GSB) at 5 nm with a stimulated emission (SE) shoulder at ~550 nm, consistent with the steady-state measurements. **Ph-**

^{1*}**BD** then undergoes a structural relaxation in $\tau_1 = 10.9 \pm 0.3$ ps and $\tau_1 = 13.8 \pm 0.3$ ps in THF and toluene, respectively before decaying to ground state in $\tau_2 = 237.9 \pm 0.4$ ps and 408.2 ± 0.3 ps in THF and toluene, respectively (see SI). No triplet states or other long-lived species are observed.

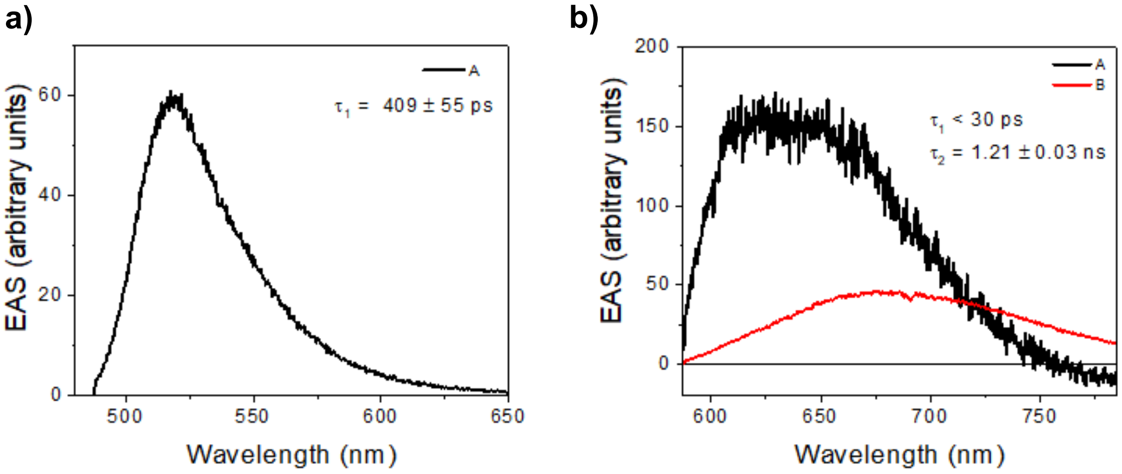

Figure 1.2 Evolution-associated spectra extracted from TRF data collected on (a) **Ph-BD** and (b) **Jul-BD** using excitation pumps of $\lambda_{ex} = 450$ nm and 570 nm, respectively, in toluene.

The excited-state dynamics of **Jul-BD** were investigated using three different excitation wavelengths (475/490 nm, 560/560 nm, and 615/590 nm for THF/toluene), to predominately excite into the LE-like state, the CT band at the edge of the LE absorption, and into the CT band far from any LE absorption, respectively. The TA data and the evolution-associated spectra (EAS) extracted from the data acquired with 560 nm excitation in both solvents are shown in Figure 3; additional TA data and fitting details are given Figures S1.18-S1.23.

In both solvents and across all three pump wavelengths, we see the rapid formation of an initial state consisting of four excited-state absorptions (ESA) at 350 nm, 415 nm, 510 nm, and 615 nm. The latter two features are assigned to **Jul**$^{\bullet+}$ (Figure S1.11) and **BD**$^{\bullet-}$, respectively.[84] There are also

GSB features at 490 nm and 570 nm, corresponding to the LE and CT absorption bands respectively, and overlap with the **Jul**$^{\bullet+}$ ESA. In addition, we observe a broad SE band from 600-800 nm, which closely matches the emission spectrum of the short-lived initial species observed in the TRF data in toluene.

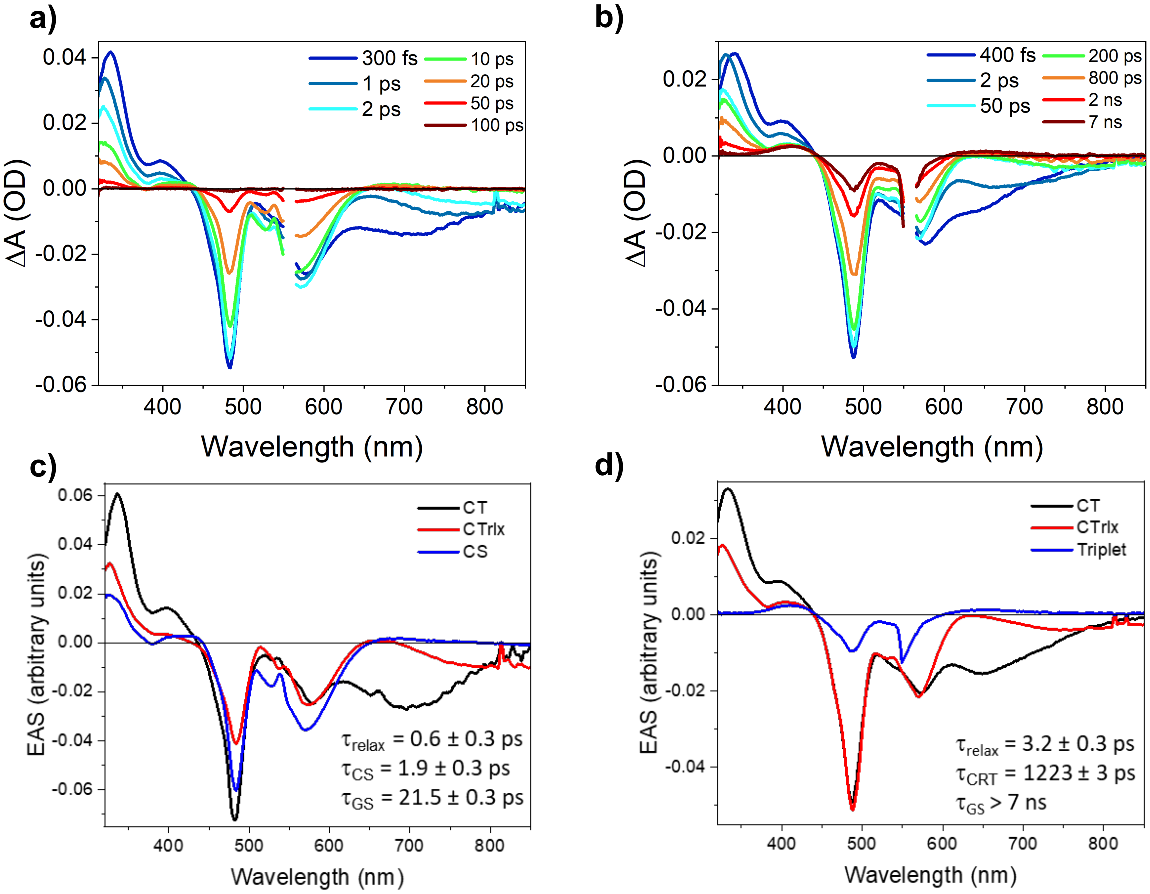

Figure 1.3 TA data of **Jul-BD** in (a) THF and (b) toluene acquired with λ_{ex} = 560 nm. Evolution-associated spectra of **Jul-BD** from TA in (c) THF and (d) toluene.

Following this, we observed the formation of another species having the same ESA features as the CT state, which exhibits a slightly redder SE spanning 650-800 nm, implying the CT state system has undergone relaxation to a lower energy state, CT$_{\text{rlx}}$, along with some population loss.

The changes in this emissive feature both in intensity and wavelength are consistent with the evolution observed in the TRF measurements in toluene. The time constant for the CT → CT_{rlx} transition extracted from the TA is τ_{rlx} = 0.6 ± 0.3 ps in THF and 3.2 ± 0.3 ps in toluene, respectively.

Following CT → CT_{rlx} relaxation, CT_{rlx} decays into one of two distinct terminal states before returning to the ground state, depending on the solvent. In THF, **Jul-BD** fully charge separates to form the CS state with a time constant of τ_{CS} = 1.9 ± 0.3 ps, displaying the same ESA and GSB features observed in the CT states, albeit with broadened and slightly red-shifted **BD**$^{\bullet-}$ ESA and no SE. On the other hand, the decay of the CT state in toluene occurs in τ_{CRT} = 1223 ± 3 ps to form the triplet state (**Jul-**^{3*}**BD**).[86] This time constant is consistent with TRF data and the CT state decay results in the loss of ESA at 350 nm, a major reduction in the CT state bleach, and the absence of SE. These results are consistent with the estimated **Jul-BD** CS state energies of 1.97 eV in toluene and 1.72 eV in THF. The relatively low-energy CS state in THF does not have sufficient energy to charge recombine to form **Jul-**^{3*}**BD** because its triplet energy is 1.9 eV according to our DFT calculations (see SI for details). In contrast, **Jul-BD** system does not undergo CS in toluene and has sufficient energy to form **Jul-**^{3*}**BD** from the CT state.

With our more complete understanding of these system dynamics, we can now estimate the energy difference between the CT and CT_{rlx} states for **Jul-BD.** For CT, we used the crossing point of the CT emission spectrum from the toluene TRF data and the **Jul-BD** absorption spectrum normalized to the CT band, which occurs at 607 nm, yielding a CT state energy of 2.04 eV (Figure S1.10c). This method is not an accurate approximation for the CT_{rlx} state, as it relies on negligible nuclear reorganization. Instead, we use the energy gap (ΔE) between the two emission spectra obtained from the TRF measurements, approximately 0.18 eV, to estimate the $\mathrm{CT_{rlx}}$ energy using the following equation: $E_{\mathrm{CTrlx}} = E_{\mathrm{CT}} - \Delta E/2$. This gives a relaxed CT state energy of 1.95 eV in toluene, which is similar to that in THF due to the similarity of the SE features. The Jablonski diagram in Figure 1.4 outlines the system energetics.

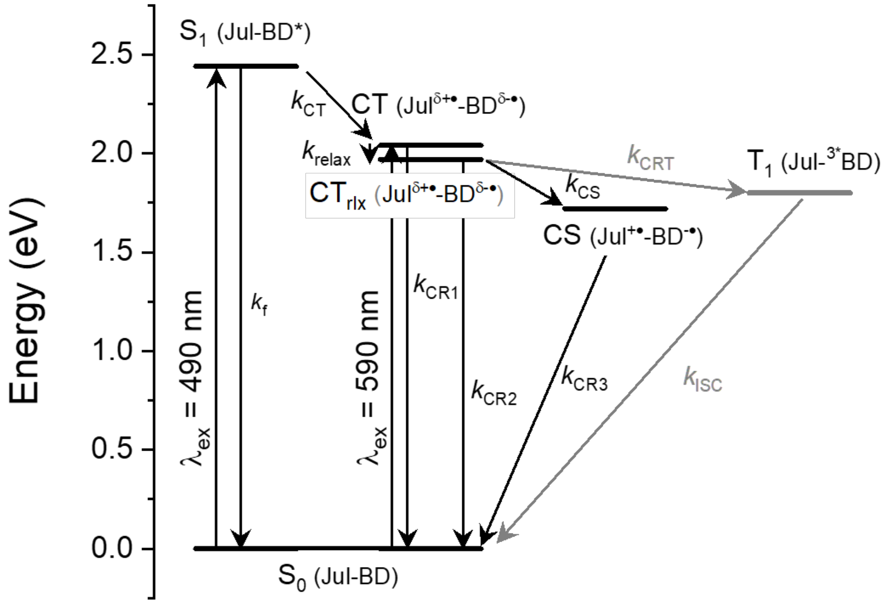

Figure 1.4. Jablonski diagram of **Jul-BD** where rates k = 1/t. The reaction pathway is the same regardless of dielectric medium until the CT state, whereupon in THF **Jul-BD** undergoes CS while in toluene it undergoes CRT. Gray indicates states and transitions accessible only in toluene.

1.4.3 Analysis of the CT Dynamics

Two-Dimensional Electronic Spectroscopy. 2DES experiments were performed to further probe the CT state evolution in **Jul-BD**. Two distinct pump pulses were used for this analysis, one blue (480-545 nm) and one green (500-640 nm), as shown in Figure 1.1a. The blue pump can co-excite both the LE-like and CT absorption bands but is biased towards the LE-like band. Meanwhile, the green pump is biased more towards the CT band. Representative spectra for **Ph-BD** and **Jul-BD** with the blue pump and **Jul-BD** with the green pump in THF can be seen in Figure 1.5; data in toluene can be seen Figure S1.25. No signal above the noise floor was seen in **Ph-BD** when excited with the green pump.

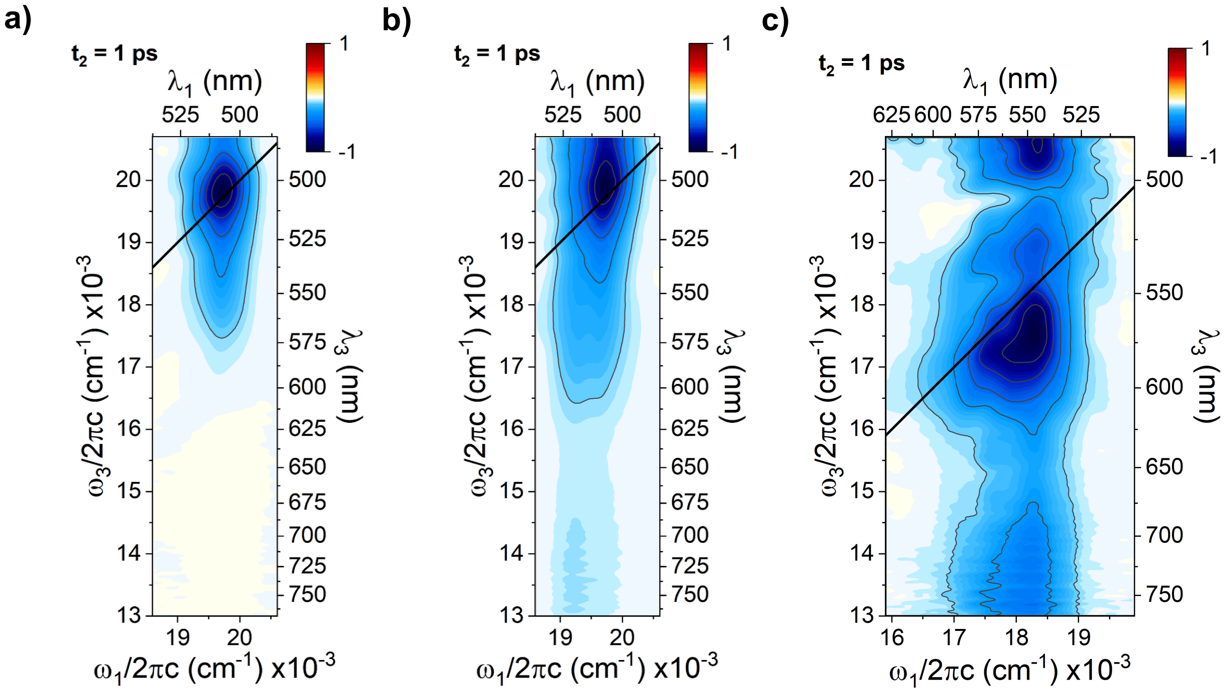

Figure 1.5 Representative 2DES spectra of (a) **Ph-BD** excited with the blue pump, and **Jul-BD** excited with the (b) blue pump and (c) green pump, all in THF at a 1 ps waiting time.

The data show that the red emissive features of **Jul-BD** from λ_3 = 600 to 800 nm exhibit a strong pump dependence. Interestingly, these SE features seem to be best accessed when exciting at the equivalent co-excitation point of the LE and CT bands at λ_1 = 523 nm, as they are more favorably formed with lower energy excitation while the LE-like features are stronger upon higher energy excitation. This is likely due to additional relaxation pathways from the LE state in competition with CT formation when the molecule is excited at shorter wavelengths. It is also evident in the 2DES data that the minimum of the CT emissive feature red shifts over early (0.1-1.5 ps) waiting times, starting from λ_3 = 600 nm, and finishing around λ_3 = 800 nm. In contrast,

Ph-BD exhibits a single GSB centered at λ_3 = 510 nm and around the peak of the pump intensity, along with a weak ESA feature around at λ_3 = 675 nm. These results are consistent with the trends observed in the TA and TRF data.

Fast Fourier transform (FFT) analysis on the data for both compounds was used to extract relevant Raman active modes and the strength of their signals in different portions of the spectrum, namely, the LE GSB, CT GSB, ESA, and SE regions. The resulting power spectra are shown in Figure S1.26 and show a total of three active Raman modes for **Jul-BD** at 147 cm^{-1}, 174 cm^{-1}, and 214 cm^{-1}. The 174 cm^{-1} mode only appears when the system is photoexcited using the blue pump and is localized in the LE GSB region, indicating it is involved with the LE dynamics. The 147 cm^{-1} and 214 cm^{-1} modes, on the other hand, appear in both the blue and green pump data most strongly in the SE region and do not appear in the LE GSB region. Furthermore, the 147 cm^{-1} mode is stronger in toluene than in THF, while the 214 cm^{-1} mode does not show much solvent-dependence. For **Ph-BD**, a single active Raman mode was observed at 220 cm^{-1} in both toluene and THF.

Next, to gain further insight into the early time dynamics of **Ph-BD** and **Jul-BD**, a quantum beating analysis was performed on both systems in both pump regimes for the Raman-active modes determined from the power spectra (Figure 1.6). All modes observed in THF also appear in the toluene data as well (Figures S1.26 and S1.27). Because the modes were seen in both solvents, we infer that similar early time coherences and vibronic couplings occur regardless of the dielectric medium. For **Ph-BD**, the single 220 cm^{-1} mode was found centered about the singlet GSB at λ_3 = ~510 nm with cross peaks on either side and slight signal trailing down through the higher energy pump SE region of the spectrum up to λ_3 = ~600 nm (Figure 1.7a). These data indicate this mode corresponds to **Ph-BD** LE state formation and relaxation.

As predicted, the beatmaps for **Jul-BD** upon photoexcitation with the blue pump show that 174 cm^{-1} mode only exhibits intensity in the LE GSB region (Figures S1.28a-b), bearing a close resemblance to the 220 cm^{-1} beatmap in **Ph-BD**. The 147 and 214 cm^{-1} vibrational modes also have strong features centered around the LE bleach in their beatmaps but contain features in the CT SE region as well at λ_3 = 600-725 nm (Figures 1.6b-c and S1.27b-c). In toluene these SE beating features have relatively equal intensity for both modes, while in THF they are more prominently

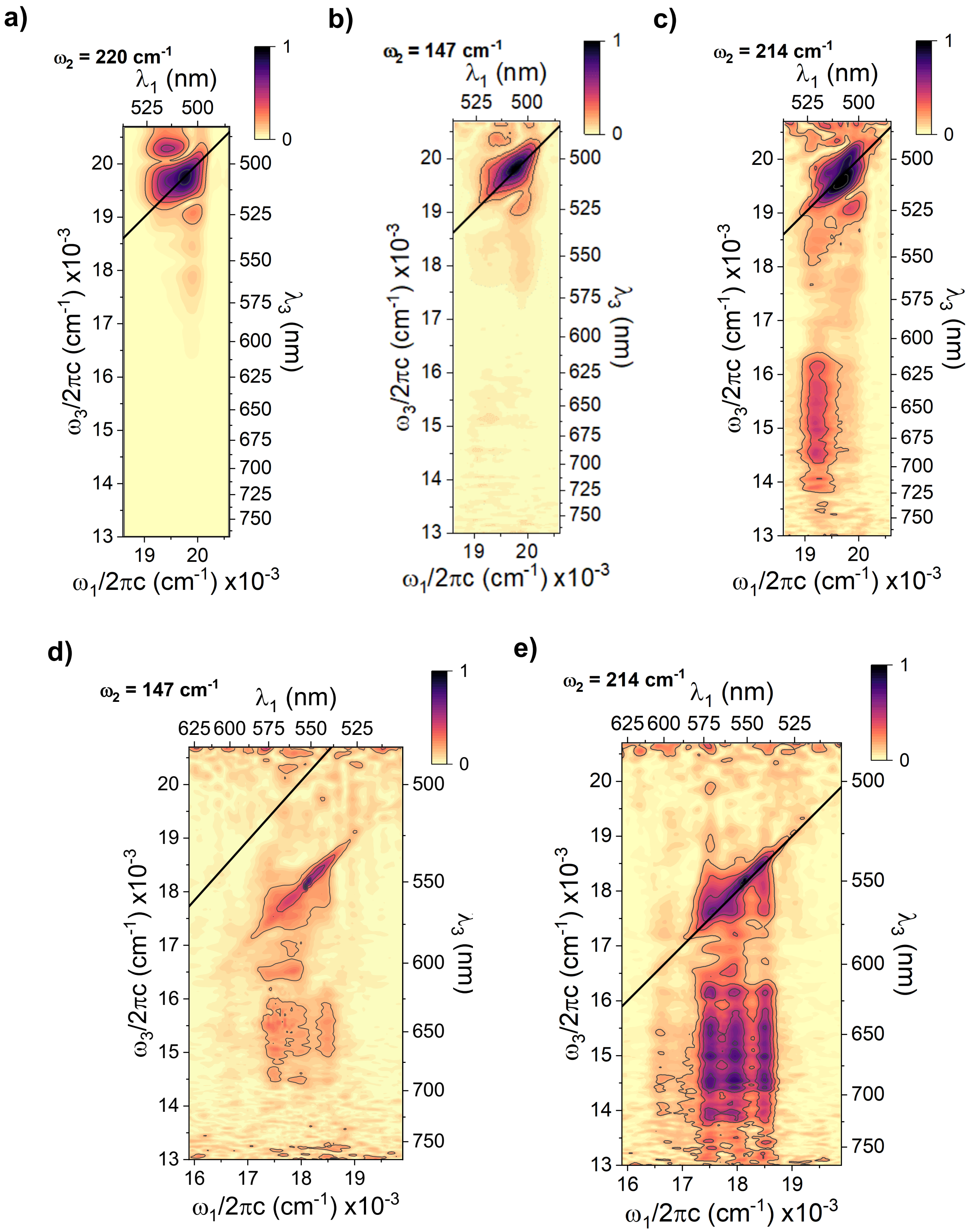

Figure 1.6 Quantum beatmaps of the (a) 220 cm^{-1} vibronic mode in **Ph-BD** when excited with the blue pump, and the 147 and 214 cm^{-1} vibronic modes of **Jul-BD** when excited with the (b,c) blue pump and (d,e) green pump, in THF.

observed in the 214 cm^{-1} beatmap. Additionally, the strength of this feature in the SE region shows a significant pump-dependence, as it grows much stronger with increasing pump wavelength in both solvents. This finding suggests the 147 cm^{-1} and 214 cm^{-1} modes engage in connecting the LE and CT states.

Finally, we analyzed the beatmaps of **Jul-BD** upon photoexcitation of the CT band using the green pump. Though the frequencies of these modes are the same as those observed upon blue pump photoexcitation, the beatmaps themselves are quite different due to the change in wave packets used to launch the coherences in the system. In these beatmaps, there is very little signal around the LE GSB, and much stronger signal around the CT GSB and SE regions, indicating that these modes are strongly involved in CT state evolution. Perhaps the most striking example of this is within the beatmap of the 174 cm^{-1} mode, which shows strong intensity in the CT SE region in THF, while there is none with blue pump excitation (Figure S1.28c). In toluene, the 147 cm^{-1} mode is strongly centered about the CT GSB, while the 214 cm^{-1} mode has greater intensity in the CT SE region, with hardly any at the CT GSB region (Figures S1.27d and S1.27e). This phenomenon becomes clearer when looking at the THF data depicted above in Figures 1.6d and 1.6e. Here it is apparent that the shapes for these two modes are quite similar, save that the feature for the 214 cm^{-1} mode extends redder than for the 147 cm^{-1} mode. This indicates that the 147 cm^{-1} mode is likely involved specifically in the CT state dynamics, which lacks that redder SE feature, while the 214 cm^{-1} seems to be involved in both CT and CT$_{\text{rlx}}$ states, as suggested by the power spectra (Figure S1.26).

Computational Analysis. DFT calculations were performed on **Jul-BD** to further investigate the mechanistic details related to the red shift that occurs in relaxation from CT to CT$_{\text{rlx}}$. Results for

DFT calculations on **Ph-BD** can be seen in the Supporting Information (Figure S1.29). Visualizations of the HOMO/LUMOs can be found in the SI as well. (Figure S1.31). Geometry optimizations on neutral **Jul-BD**, **Jul-BD** CS state, and several **Jul-BD** partial CT states, namely, 0.7 CT, 0.8 CT and 0.9 CT were performed, where the coefficients reflect the portion of a charge transferred from **Jul** to **BD**, to investigate structural changes accompanied by electron transfer. The results show gradual increase in the dihedral angle with increasing CT character from neutral **Jul** (21.3° twist) to 0.9 CT (36.6° twist) and a drastic increase in the angle upon complete CS, where the donor and acceptor units are nearly perpendicular with an 88.7° twist (Figure 1.7a and Figure S1.32).

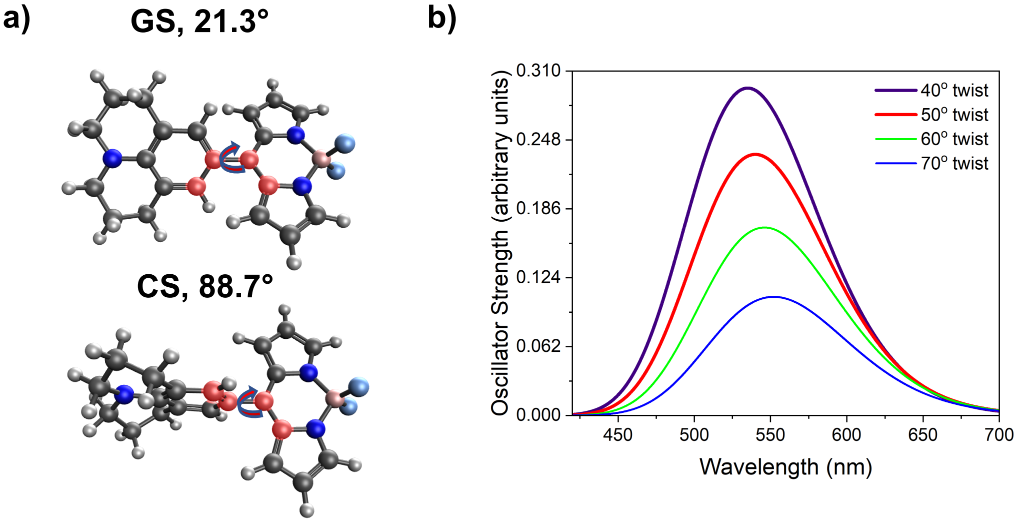

Figure 1.7 (a) Calculated optimized geometries for **Jul-BD** in the ground state (top) and CS state (bottom) (b) calculated absorption from TD-DFT of **Jul-BD** with 0.8 CT character with different fixed dihedral angles. Atoms involved with dihedral twisting are highlighted in red for both GS and CS states.

Next, a normal mode analysis was performed on the neutral, partial 0.8 CT, and CS states of **Jul-BD** as well as on **Ph-BD**, to visualize the active Raman vibrational modes identified in the 2DES data (Figure S1.30). For **Jul-BD**, torsional motion of **Jul** about the single bond joining it to

BD is observed in most electronic states for all three vibronic modes, 147, 174 cm^{-1} and 214 cm^{-1}. This is consistent with earlier studies on TICT states that have long been shown to exhibit similar emission dynamics and properties as a function of their rotation,[51, 87, 88] though we note that the fully charge-separated state of **Jul-BD** in THF is not emissive. Interestingly, the 147 cm^{-1} mode in the GS and CS state and the 174 cm^{-1} mode in the partial CT state exhibit a molecular breathing motion along the center-to-center axis that modulates the distance between **Jul** and **BD**. This sort of vibration has been previously observed in **BD** compounds and is suggested to participate in LE dynamics.[19] Indeed, the same type of molecular breathing motion is observed in **Ph-BD** for its active Raman mode at 220 cm^{-1} (Figure S1.29).

Finally, we held the degree of partial CT constant at 0.8 CT and changed the dihedral angle between the **Jul** and **BD** units. Holding that angle at 40°, 50°, 60°, and 70° to simulate greater amounts of torsional motion, we calculated the optimized geometry of the molecule and simulated the absorption spectra (Figure 1.7b). These calculations show red shifting of the CT absorption band with increasing dihedral angle, suggesting the red shifting we observe in transient experiments indeed results from conformational relaxation of the molecule upon core twisting between the **Jul** and **BD** units. This finding is consistent with previous work on TICT states that shows these types of torsional motions are associated with charge transfer in D-A systems.[51, 87, 88] This trend is also consistent with the observation of **Jul-^{3*}BD** formation in toluene, where the greater orthogonality allows for a change in spin angular momentum upon charge recombination via the spin-orbit CT intersystem crossing (SOCT-ISC) mechanism.[89] Moreover, while TICT states have been known for decades, these findings suggest that in addition to molecular twisting to increase the D-A dihedral angle playing a role in CT and CS, molecular vibrations, which result in zero net molecular motion overall, corresponding to torsional motion between the donor and acceptor are also playing a role in this system as electron density is transferred from the donor to the acceptor.

The overall system dynamics described by these findings in tandem with our experimental results are illustrated in the potential energy surface diagram as shown in Figure 1.8, with the reaction coordinate depicted as the yellow line. As the system traverses this path, core twisting to increase the D-A dihedral angle promotes electronic state evolution and the wavepacket moves down the potential surface. The Raman-active vibrational modes facilitate this overall relaxation, ultimately pushing the system to continue along the PES and reach the lower energy states.

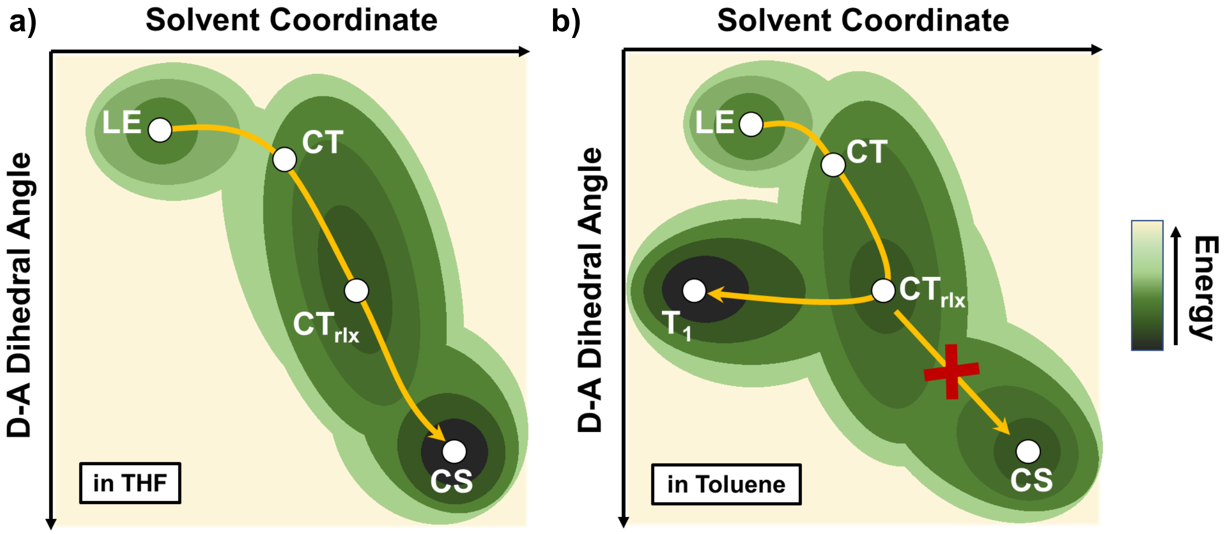

Figure 1.8 Schematic potential energy surfaces describing the dynamics of **Jul-BD** in (a) THF and (b) toluene as functions of dihedral angle between the julolidine and BODIPY cores and the solvent relaxation coordinate.

1.5 Conclusion

This study identified and characterized the time evolution of the optically bright CT state in a **Jul-BD** dyad and a **Ph-BD** control molecule. Ultrafast TA and TRF spectroscopies were used to elucidate the dynamics of both systems in THF and toluene upon photoexcitation using a range of photoexcitation pump wavelengths to access the **Ph-BD** LE and **Jul-BD** LE and CT states based on their steady-state absorption spectra. Exciting **Jul-BD** in either solvent across all pump wavelengths results in the formation of an initial bright CT state followed by a second conformationally relaxed state, CT_{rlx}. In THF, full CS was then observed while in toluene the CT_{rlx} state recombines to give **Jul-^{3*}BD**. We attribute this change to the different polarities of the solvents modulating the energy of the CS state. Only two species are observed upon photoexcitation of **Ph-BD**, an initial singlet LE state and its conformational relaxation before returning to the GS. Ultrafast 2DES was used to further characterize these dynamics at faster timescales and ascertain which vibronic interactions play role in the CT process.

Detailed analysis of the TA, TRF, and 2DES data for **Jul-BD** reveal the spectral red shift that occurs when $CT \rightarrow CT_{rlx}$. DFT calculations show that torsional motion of **Jul** and **BD** about the single bond joining them, which increases the dihedral angle between them, occurs with increasing CT character, is responsible for this red shifting. FFT power spectra and quantum beatmaps were obtained from the 2DES measurements to identify vibrational modes coupled with electronic states and DFT calculations were used to visualize their effects on a molecular level. These modes reveal the importance of both **Jul-BD** torsional motion and breathing motion between the donor and acceptor units associated with the flow of electron density from **Jul** to **BD** along with coupling between electronic states.

Understanding the fundamental characteristics of these types of molecular D-A systems gives insight into the parameters at play when considering the flow of electrons. Our approach to this question ultimately provides further insight into the nature of TICT states and how their properties can be optimized for new technologies. Moreover, these findings show how torsional and compression motions can play a role in charge separation between donors and acceptors whose π systems are at large dihedral angles within the active layer of organic photovoltaics.

1.6 Supporting Information

1.6.1 Materials, Methods, and Synthesis

Materials. All chemicals and solvents were purchased from commercial suppliers and were used without further purification.

Synthesis:

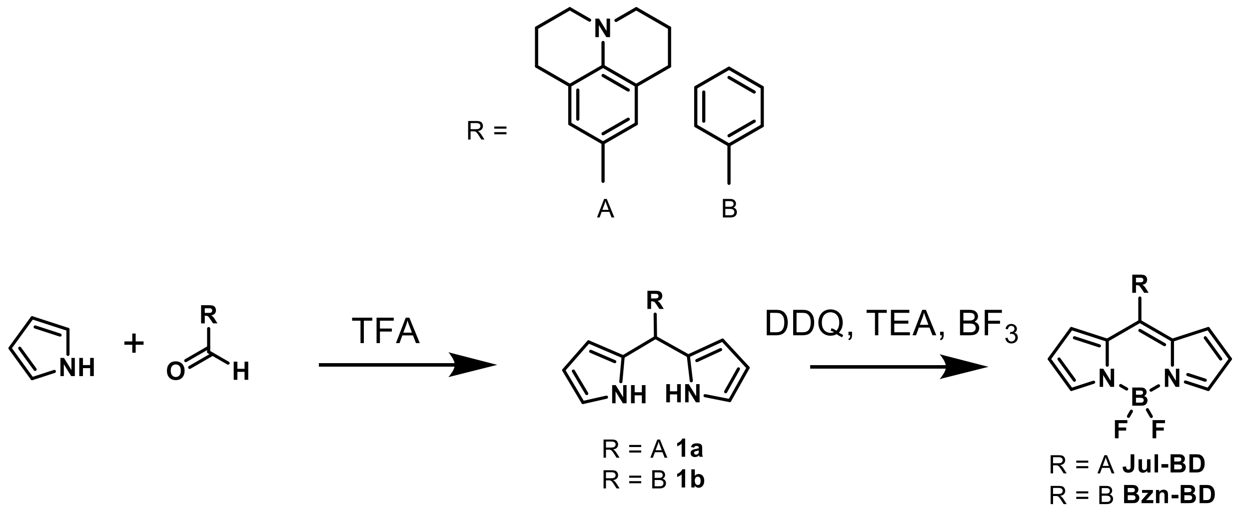

Scheme S1.2. Synthetic scheme for **Jul-BD** and **Bzn-BD**

Preparation of ***1a***

A solution of *p*-julolidinealdehyde (500 mg) in pyrrole (20 mL) was bubbled with N_2 gas for 15 minutes. Trifluoroacetic acid (0.05 mL) was added and the solution turned from yellow to red/purple. The flask was covered in aluminum foil to protect it from light and left to stir overnight at room temperature under N_2 gas. The pyrrole was removed via rotary evaporation and the reaction mixture was dissolved in DCM (45 mL) and washed with H_2O (3 x 100 mL). The product was then purified by column chromatography using silica gel. 3% triethylamine in hexanes was run through the silica before loading the material to neutralize the silica. The product was purified using DCM/hexanes (1:2) as eluent yielding **1a** as an orange solid (150 mg). ^{1}H NMR (CDCl3, 500 MHz): δ (ppm) = 7.90z (s, 2H), 6.65 (s, 4H), 6.15 (s, 2H), 5.95 (s, 2H), 5.28 (s, 1H), 3.11 (t, J = 5.5 Hz, 4H), 2.70 (t, J = 6.0 Hz, 4H), 1.96 (m, 4H). ^{13}C NMR (CDCl3, 100 MHz): δ (ppm) = 141.9, 133.5, 128.9, 126.6, 121.7, 116.6, 108.2, 106.7, 50.2, 43.1, 27.4, 22.2. MS-MALDI (m/z) calculated for $C_{21}H_{23}N_3$: 318.20, found: 318.22.

*Preparation of **1b***

The same procedure was used as for **1a**. ^{1}H NMR (CDCl3, 500 MHz): δ (ppm) = 7.92 (s, 2H), 7.26 (m, 5H), 6.70 (ddd, J = 2.5 Hz, J' = 2.5 Hz, J'' = 1.5 Hz, 2H), 6.18 (dd, J = 5.8 Hz, J′ = 2.6 Hz, 2H), 5.93 (m, 2H), 5.49 (s, 1H). ^{13}C NMR (CDCl3, 100 MHz): δ (ppm) = 149.5, 146.5, 130.7, 129.4, 123.9, 117.9, 108.7, 107.5, 43.5.

*Preparation of **Jul-BD***

To a solution of **1a** (130 mg) in DCM (15 mL) was added DDQ (220 mg), turning the solution from orange to dark blue/purple. The solution was then stirred at room temperature overnight under N_2 gas. Triethylamine (0.5 mL) and boron trifluoride diethyletherate (1 mL) were then added and the reaction was stirred overnight at room temperature under N_2 gas. The solution was then washed with H_2O (3 x 100 mL). The DCM was removed via rotary evaporation and the material was purified using column chromatography on silica gel with DCM/hexanes (2:1) as eluent to afford a deep blue solid (35 mg). ^{1}H NMR (CDCl3, 500 MHz): δ (ppm) = 7.81 (s, 2H), 7.12 (s, 2H), 7.04 (d, J = 4.0, 2H), 6.50 (dd, J' = 4.0, J'' = 1.9, 2H), 3.31 (t, J = 6.0, 4H), 2.80 (t, J = 6.0 Hz, 4H), 2.01 (m, 4H). ^{13}C NMR (CDCl3, 100 MHz): δ (ppm) = 148.6, 146.0, 140.6, 134.2, 131.1, 130.2, 121.2, 120.9, 117.1, 50.0, 27.7, 21.4. MS-MALDI (m/z) calculated for $C_{21}H_{20}N_3F_2B$: 363.22, found: 363.21.

Preparation of ***Ph-BD***

The same procedure was used as for **Jul-BD**. ^{1}H NMR (CDCl3, 500 MHz): δ (ppm) = 7.93 (s, 2H), 7.54 (m, 5H), 6.93 (d, J = 3.5 Hz, 2H), 6.53 (d, J = 3.5 Hz, 2H). ^{13}C NMR (CDCl3, 100 MHz): δ (ppm) = 147.3, 144.0, 134.7, 133.6, 131.5, 130.8, 130.4, 128.4, 118.6.

1.6.2 Steady State Optical Characterization

Gaussian Fits of UV-Vis

The LE and CT absorption bands of **Jul-BD** in THF and toluene were fit to gaussian curves to determine their relative contributions at various excitation wavelengths as shown in Figure S1.9.

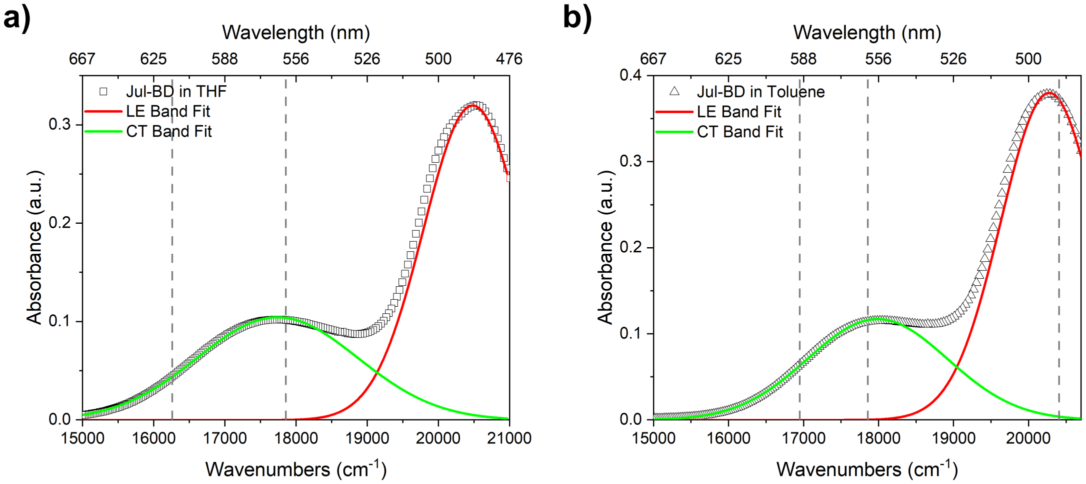

Figure S1.9. Gaussian fits of singlet and CT bands of **Jul-BD** in (a) THF and (b) toluene with dashed lines indicating the pump wavelengths used in fsTA experiments.

Normalized Absorption and Emission Crossing Points

The various normalized absorption and emission spectra of both compounds are reported here. For CT and CT$_{rlx}$ of **Jul-BD**, the spectra were normalized to the CT absorption band, while the spectra were normalized to the LE absorption band of **Ph-BD** for the LE state.

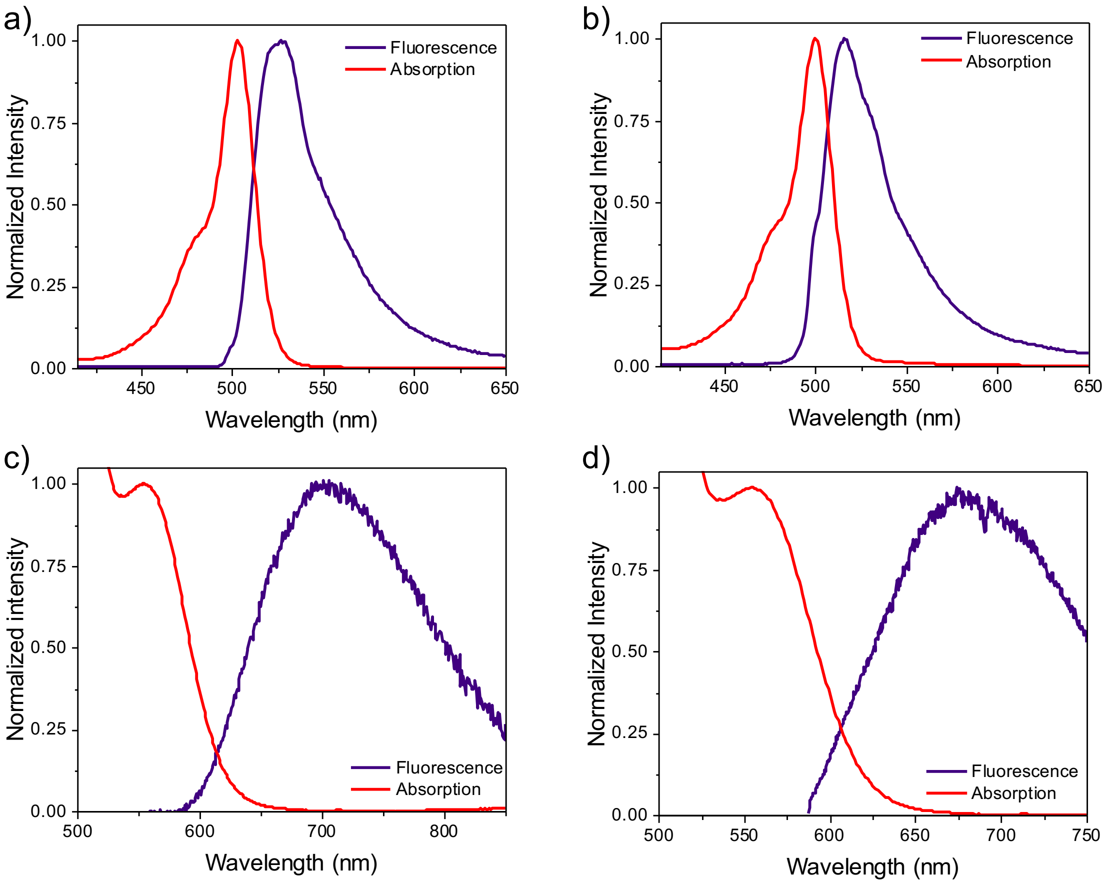

Figure S1.10. Normalized absorption and emission spectra for (a) **Ph-BD** in toluene, (b) **Ph-BD** in THF, (c) **Jul-BD** in toluene with the CT emission from TRF, and (d) **Jul-BD** in toluene with the CTrlx emission from TRF.

Molar Extinction Coefficients

Molar extinction coefficients (ε) were measured for both **Jul-BD** and **Ph-BD** in THF and toluene yielding the following results: ε(**Ph-BD**, THF) = 34,091 cm^{-1}M^{-1}, ε(**Ph-BD**, toluene) = 33,715 cm^{-1}M^{-1}, ε(**Jul-BD**, THF) = 8,330 cm^{-1}M^{-1}, and ε(**Jul-BD**, toluene) = 8,150 cm^{-1}M^{-1}.

Absorption Spectrum of Julolidine Cation

To obtain the absorption spectrum of the oxidized **Jul-BD**, so as to be able to identify the spectral features of **Jul**$^{•+}$ within the TA and 2DES experiments, tris (4-bromophenyl)ammoniumyl hexachloroantimonate was added to a solution of **Jul-BD** in toluene (Figure S1.11). The disappearance of the CT band as well as the appearance of a new absorptive feature are evidence that chemical oxidation occurred.

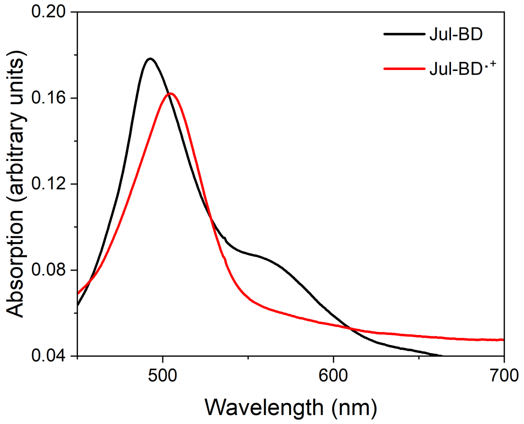

Figure S1.11 Absorption spectra of **Jul-BD** with the addition of oxidant magic blue in toluene.

1.6.3 Electrochemical Analysis

Differential Pulse Voltammetry

Electrochemical measurements were performed on a CH Instrument 750E electrochemical workstation. Measurements were made using a 1.0 mm diameter glassy carbon working electrode, a platinum wire auxiliary electrode, and a silver wire reference electrode in 0.1 M solutions of n-butylammonium hexafluorophosphate ($TBAPF_6$) in acetonitrile purged with argon. Ferrocene was used as an internal standard.

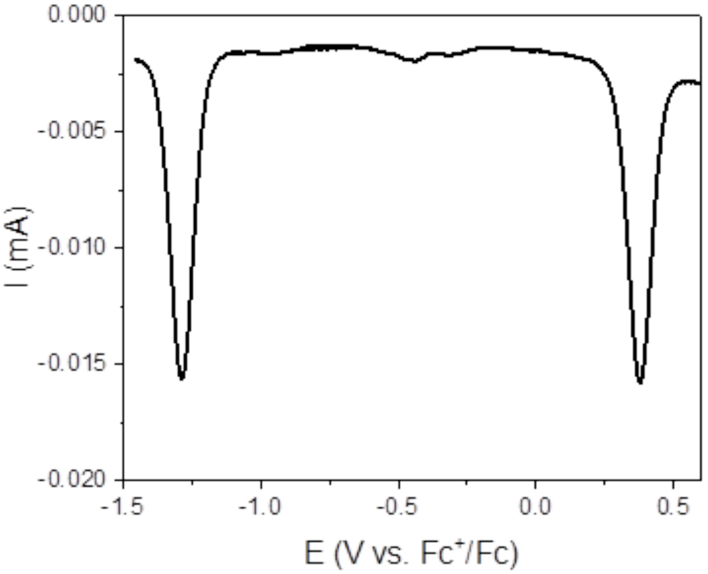

Figure S1.12 Differential pulse voltammetry (DPV) spectrum of **Jul-BD** measured in acetonitrile.

Weller Equation Analysis

The Weller equation was applied to these data to correct for the different dielectric constants between acetonitrile, the solvent electrochemical potentials were measured in, and THF and toluene, the solvents transient experiments were performed in, as follows:

$$\Delta G = E_{ox} - E_{red} - (\frac{e^2}{r_{DA}\varepsilon_s}) + (e^2(\frac{1}{2r_D} + \frac{1}{2r_A})(\frac{1}{\varepsilon_s} - \frac{1}{\varepsilon_{sp}}) \qquad \text{(Eqn. S1.1)}$$

where E_{ox} and E_{red} are the oxidation and reduction potentials of the donor and acceptor, respectively, in the solvent electrochemical measurements were taken with a static dielectric constant ε_{sp}, e is the charge of an electron, r_{DA} is the ion pair distance, r_D and r_A are the ionic radii, and ε_s is the static dielectric constant of the solvent we are comparing against.{Greenfield, 1996 #64

1.6.4 Fitting Methodology for TRF and TA Data

Data Processing for TA Data

Prior to kinetic analysis, the TA data were scatter-subtracted and chirp-corrected using Surface Xplorer 4 (Ultrafast Systems, LLC).

Kinetic Fitting Methodology

All kinetic analysis was performed using home written programs in MATLAB and was based on a global fit to selected single-wavelength kinetics. An assumption of a uniform instrument response of w = 300 fs for fsTA (full width at half maximum, FWHM) across the frequency domain and a fixed time-zero (t_0) is implicit in the global analysis. Kinetic data from the entire 320-850 nm window were fitted using the global analysis described below. The population dynamics in toluene and THF overlap with the non-resonant solvent response, which was modeled as the decay of a separate population with a fixed decay rate smaller than the instrument response. Each specified wavelength was given an initial amplitude that is representative of the spectral intensity at time t_0. The rate constants and t_0 were shared among the various kinetic data and varied globally across the kinetic data to fit to the models described below. Datasets were globally fit to a specified kinetic model and the resultant populations were used to deconvolute the dataset and reconstruct the evolution-associated spectra. Below are the first-order kinetic models of each system with rate matrix K and initial species population vector P:

1. TRF of **Ph-BD**:

$$K = (-k_{A\to GS}) \quad P = (1) \tag{Eqn. S1.2}$$

2. TRF of **Jul-BD**:

$$K = \begin{pmatrix} -k_{A\to B} & 0 \\ k_{A\to B} & -k_{B\to GS} \end{pmatrix} \quad P = \begin{pmatrix} 1 \\ 0 \end{pmatrix} \tag{Eqn. S1.3}$$

3. TA of **Jul-BD**:

$$K = \begin{pmatrix} -1/0.1 & 0 & 0 & 0 \\ 0 & -k_{A\to B} & 0 & 0 \\ 0 & k_{A\to B} & -k_{B\to C} & 0 \\ 0 & 0 & k_{B\to C} & -k_{C\to GS} \end{pmatrix} \quad P = \begin{pmatrix} 1 \\ 1 \\ 0 \\ 0 \end{pmatrix} \tag{Eqn. S1.4}$$

4. TA of **Ph-BD**:

$$K = \begin{pmatrix} -1/0.1 & 0 & 0 \\ 0 & -k_{A\to B} & 0 \\ 0 & k_{A\to B} & -k_{B\to GS} \end{pmatrix} \quad P = \begin{pmatrix} 1 \\ 1 \\ 0 \end{pmatrix} \tag{Eqn. S1.5}$$

The MATLAB program numerically solved the differential equations through matrix methods and then convoluted the solutions with a fixed Gaussian instrument response function with width w = 0.3 ps (FWHM) before utilizing a least-squares fitting using a Levenberg-

Marquardt method to find the parameters that result in matches to the kinetic data. Uncertainties in reported time constants were taken as the standard deviation of the fits from multiple replicates unless stated otherwise.

1.6.5 Time-resolved Fluorescence Spectroscopy

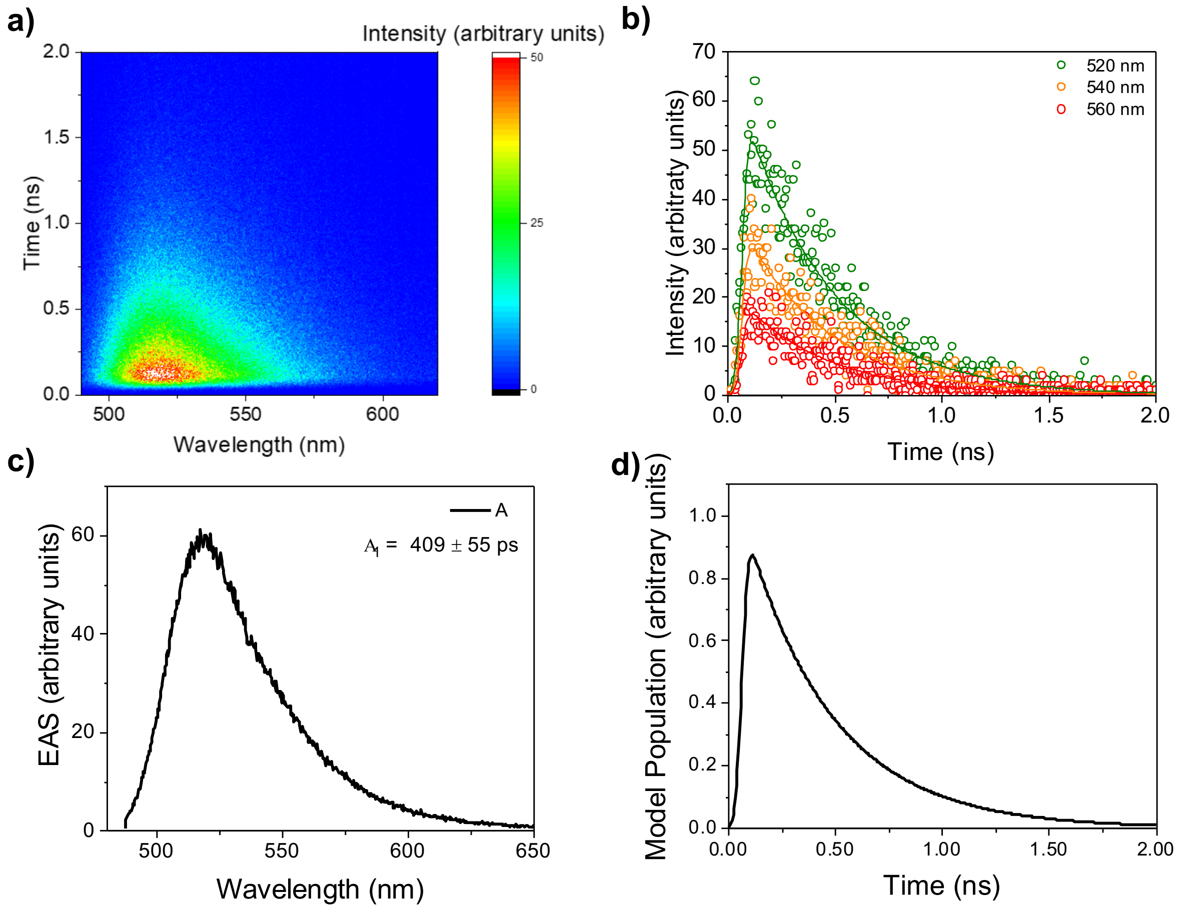

Figure S1.13 (a) TRF spectra of **Ph-BD** in toluene excited at 450 nm over a 2 ns window. (b) Selected wavelengths and kinetic fits from global analysis. (c) Evolution-associated spectra and time constant. (d) Population curves of kinetic states**.**

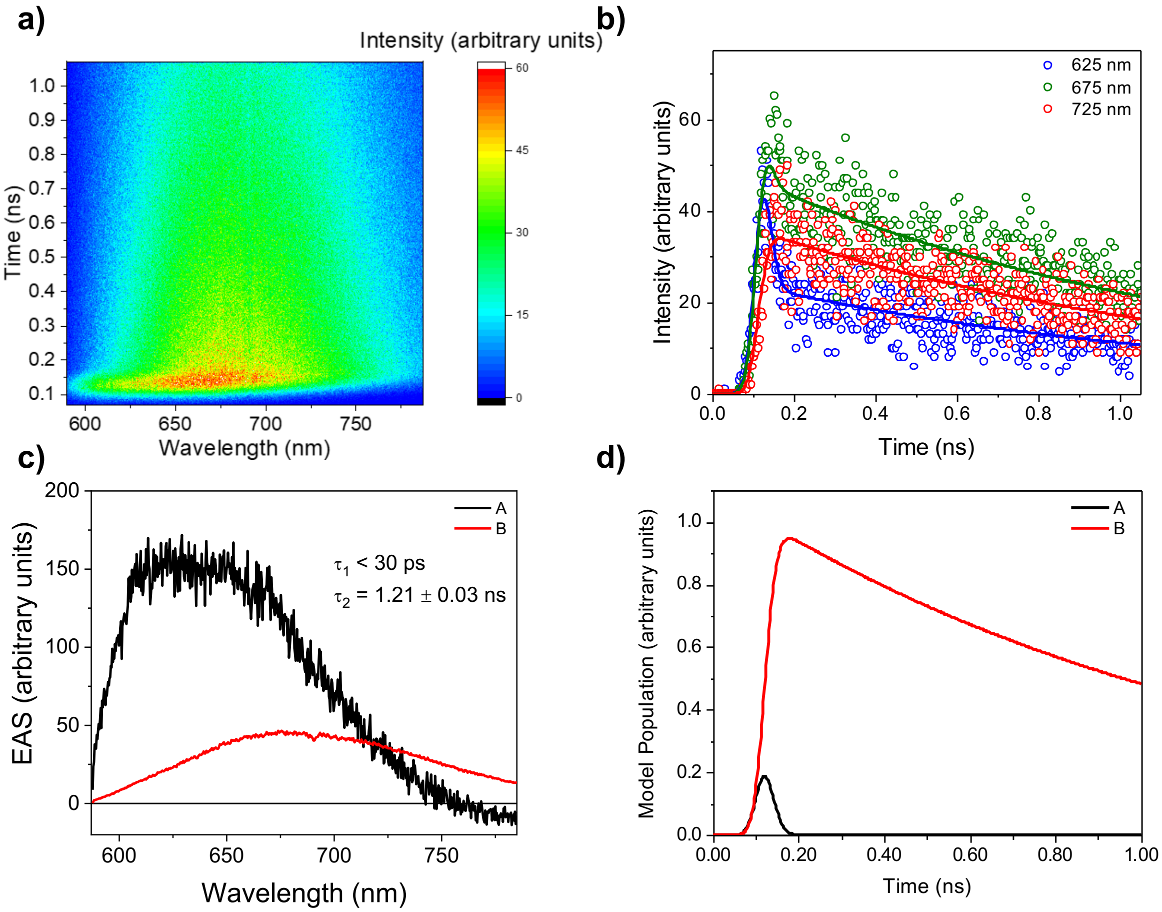

Figure S1.14 (a) TRF spectra of **Jul-BD** in toluene excited at 570 nm over a 1 ns window. (b) Selected wavelengths and kinetic fits from global analysis. (c) Evolution-associated spectra and time constant. (d) Population curves of kinetic states.

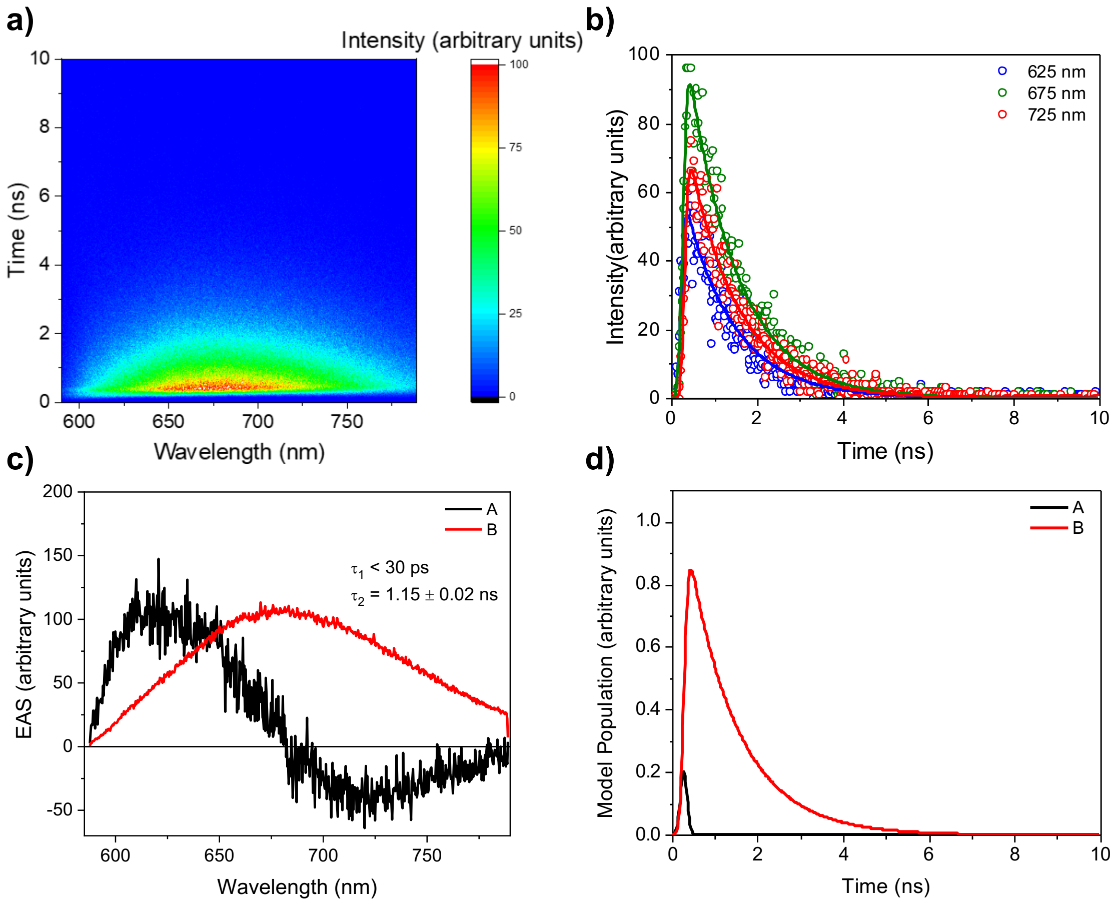

Figure S1.15 (a) TRF spectra of **Jul-BD** in toluene excited at 570 nm over a 10 ns window. (b) Selected wavelengths and kinetic fits from global analysis. (c) Evolution-associated spectra and time constant. (d) Population curves of kinetic states.

1.6.6 Transient Absorption Spectroscopy

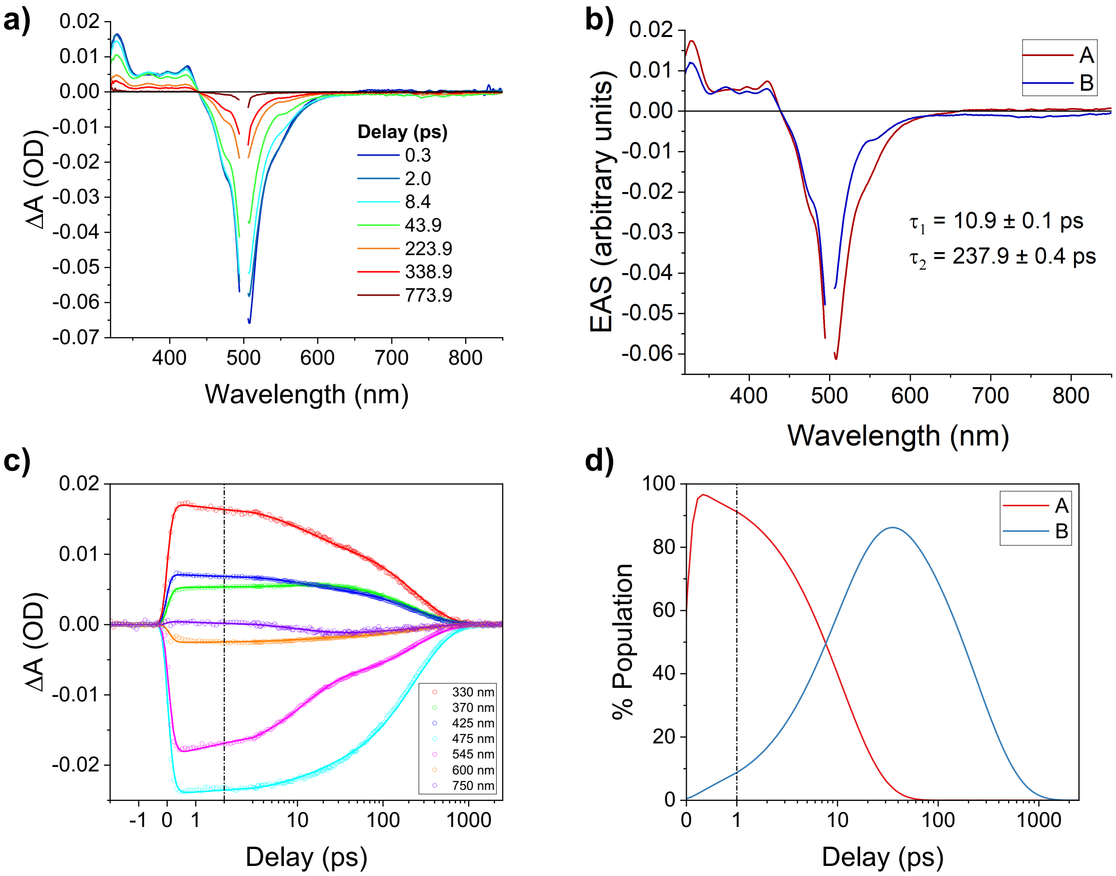

Figure S1.16 (a) TA spectra of **Ph-BD** in THF excited at 500 nm along with relevant (a) evolution-associated species spectra, (c) selected wavelength kinetic fits from global analysis, and (d) population dynamics of each species.

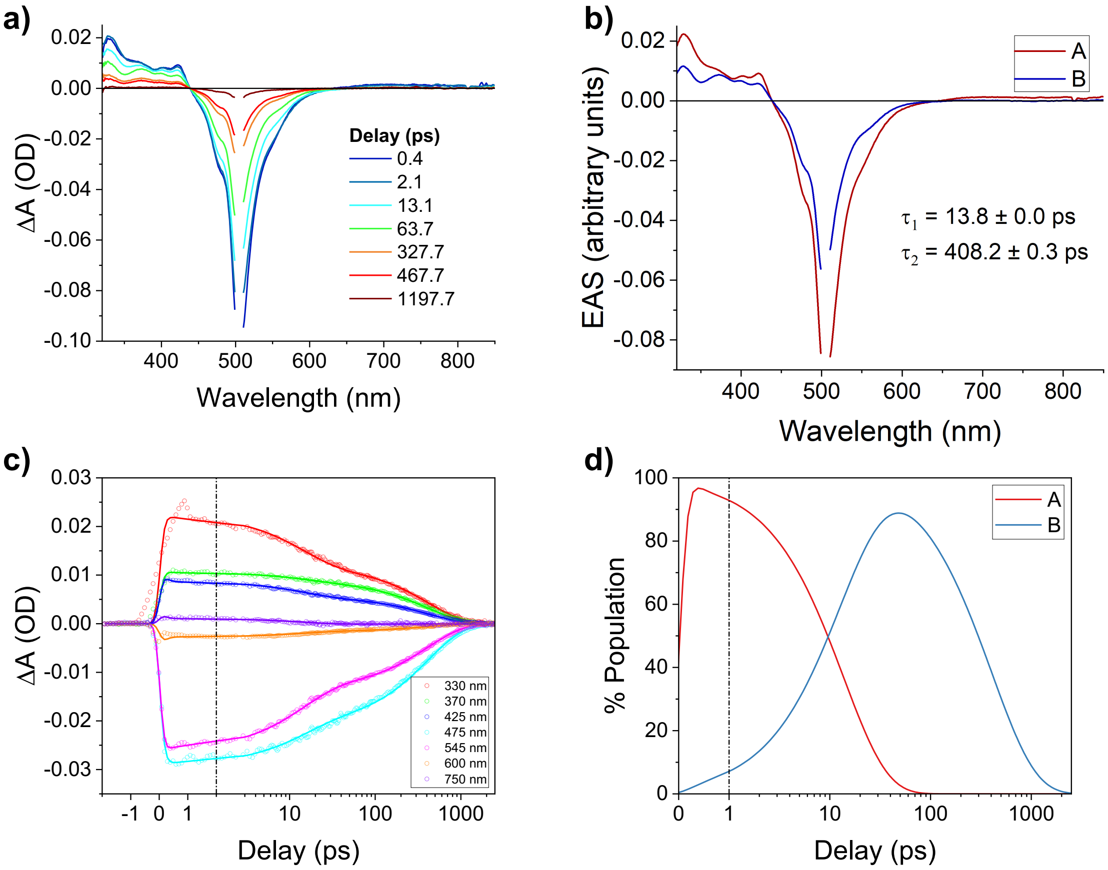

Figure S1.17 (a) TA spectra of **Ph-BD** in toluene excited at 505 nm along with relevant (a) evolution-associated species spectra, (c) selected wavelength kinetic fits from global analysis, and (d) population dynamics of each species.

The **Ph-BD** excited-state dynamics in THF and toluene following excitation of its $S_1 \leftarrow S_0$ absorption band are shown in Figures S1.16-S1.17. The first species formed exhibits a GSB signature centered at 500 nm and 505 nm in THF and toluene, respectively, along with an emissive shoulder 45 nm (1750 cm^{-1}) red of the GSB. This is consistent with the fluorescence measured in the steady state. In < 15ps, this species relaxes into a second state, with a similar shape but lower contribution from fluorescence and slightly different shape of the GSB. The system then returns back to the ground state in hundreds of picoseconds. The kinetics of both processes are faster in THF than in toluene.

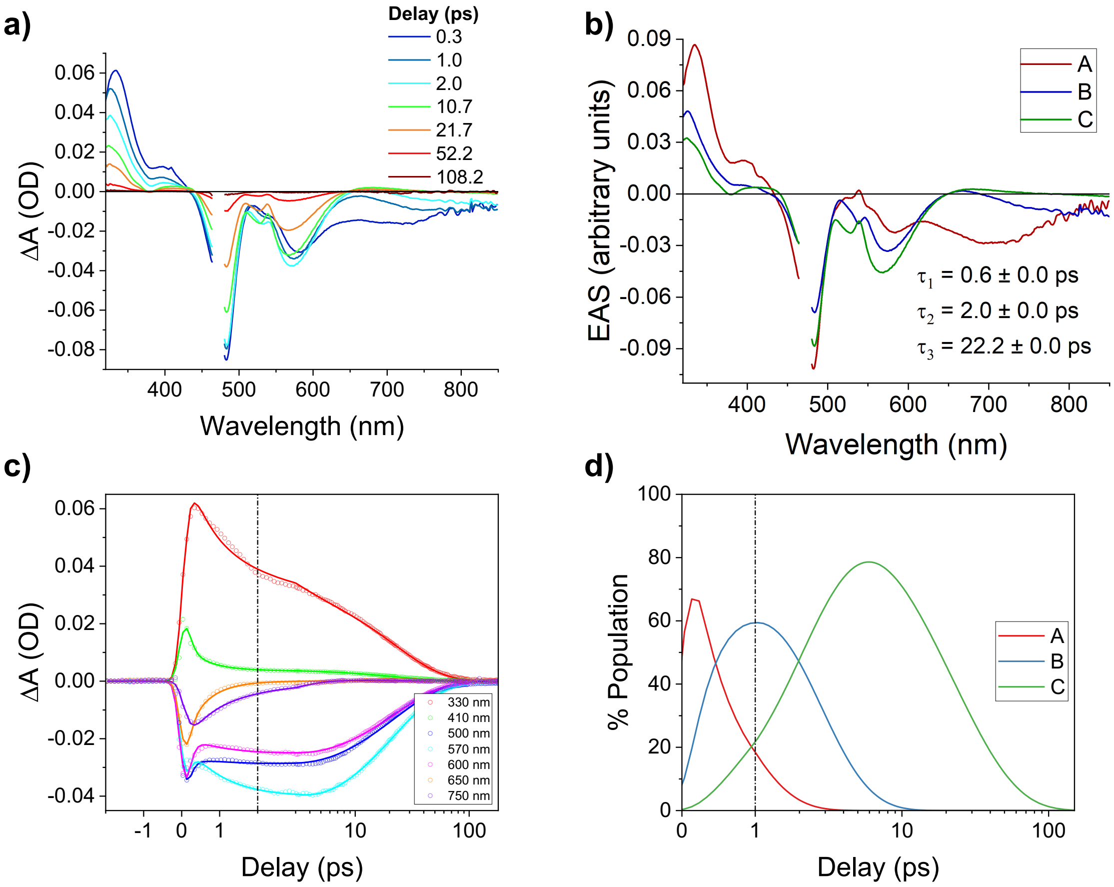

Figure S1.18 (a) TA spectra of **Jul-BD** in THF excited at 475 nm along with relevant (a) evolution-associated species spectra, (c) selected wavelength kinetic fits from global analysis, and (d) population dynamics of each species.

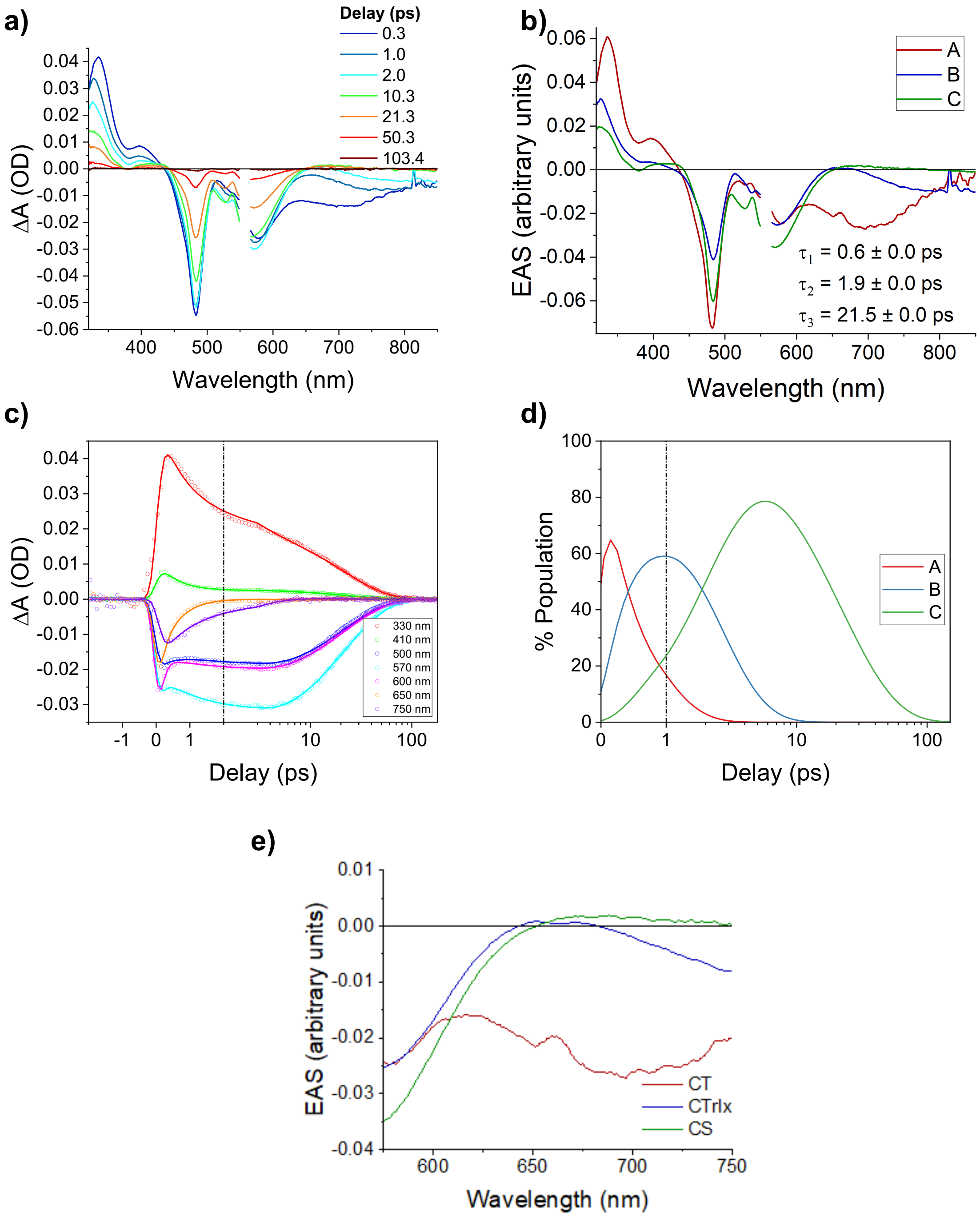

Figure S1.19 (a) TA spectra of **Jul-BD** in THF excited at 560 nm along with relevant (a) evolution-associated species spectra, (c) selected wavelength kinetic fits from global analysis, (d) population dynamics of each species, and (e) evolution-associated species spectra zoomed in at the region of the **BD**$^{\bullet-}$ ESA feature.

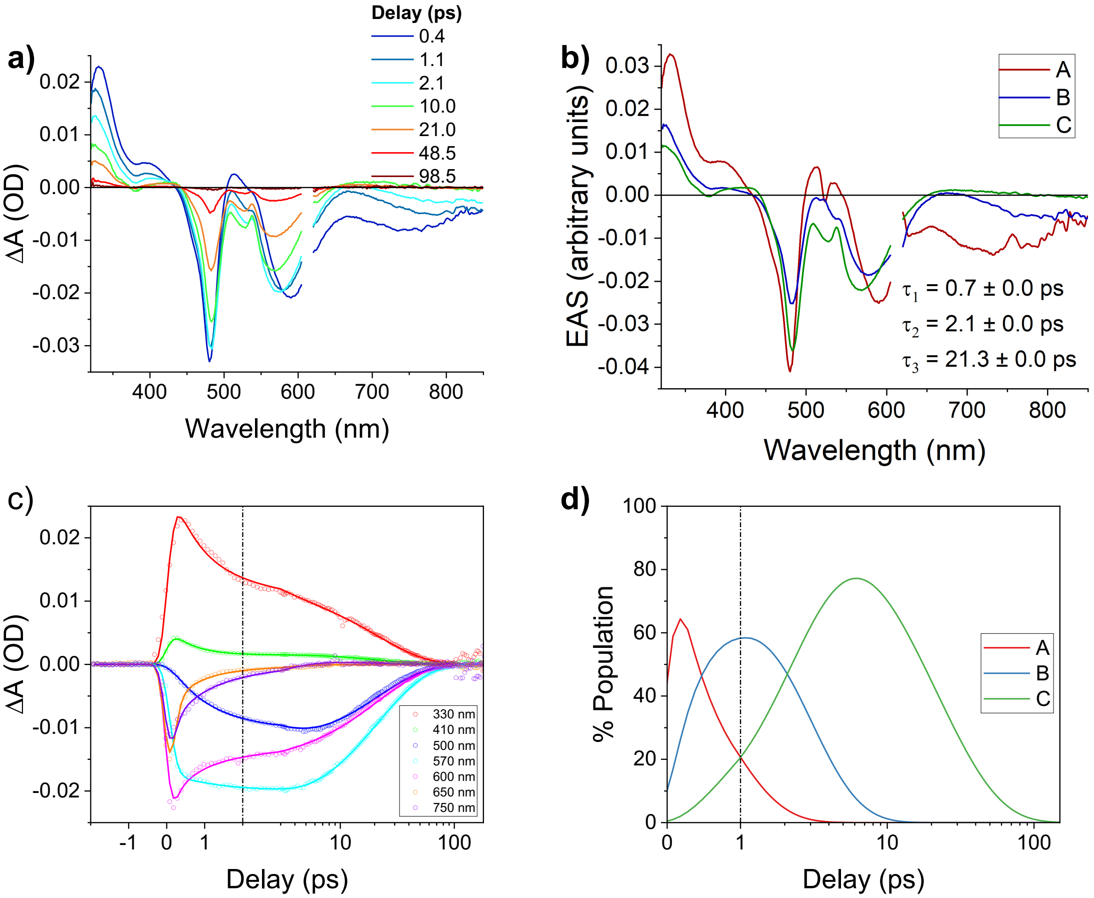

Figure S1.20 (a) TA spectra of **Jul-BD** in THF excited at 615 nm along with relevant (a) evolution-associated species spectra, (c) selected wavelength kinetic fits from global analysis, and (d) population dynamics of each species.

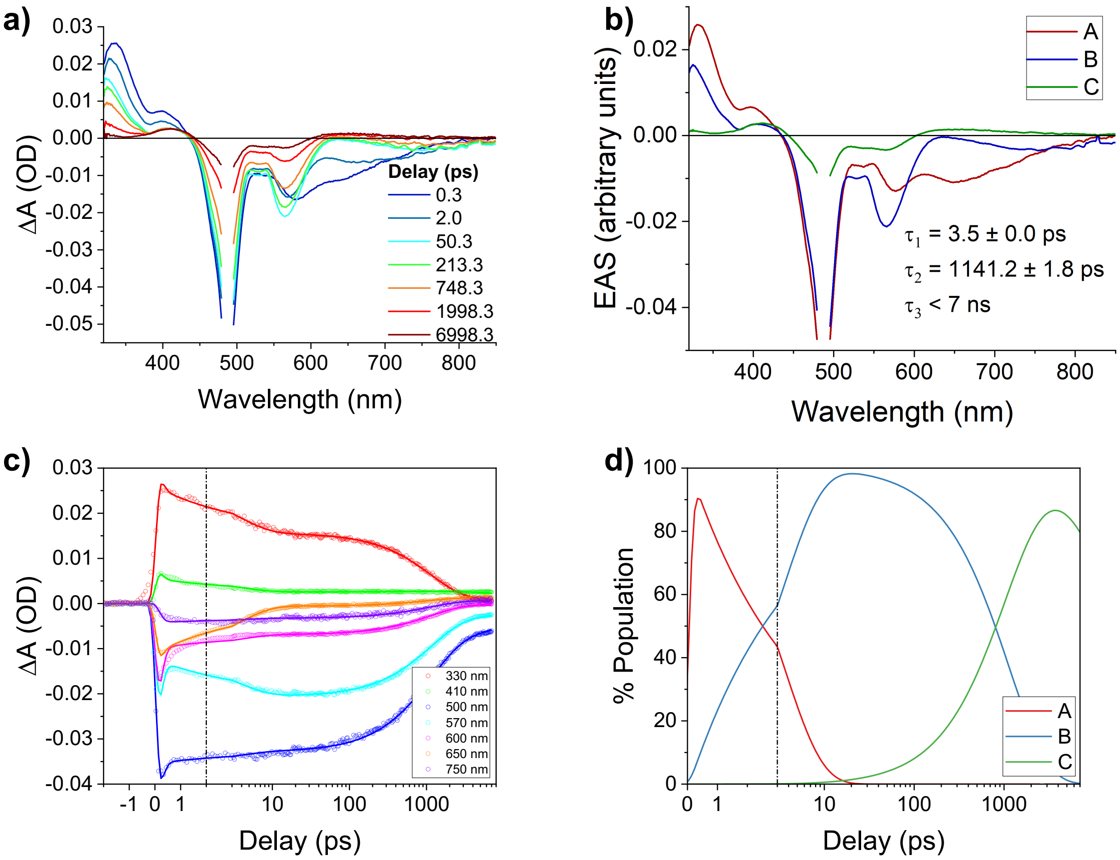

Figure S1.21 (a) TA spectra of **Jul-BD** in toluene excited at 490 nm along with relevant (a) evolution-associated species spectra, (c) selected wavelength kinetic fits from global analysis, and (d) population dynamics of each species.

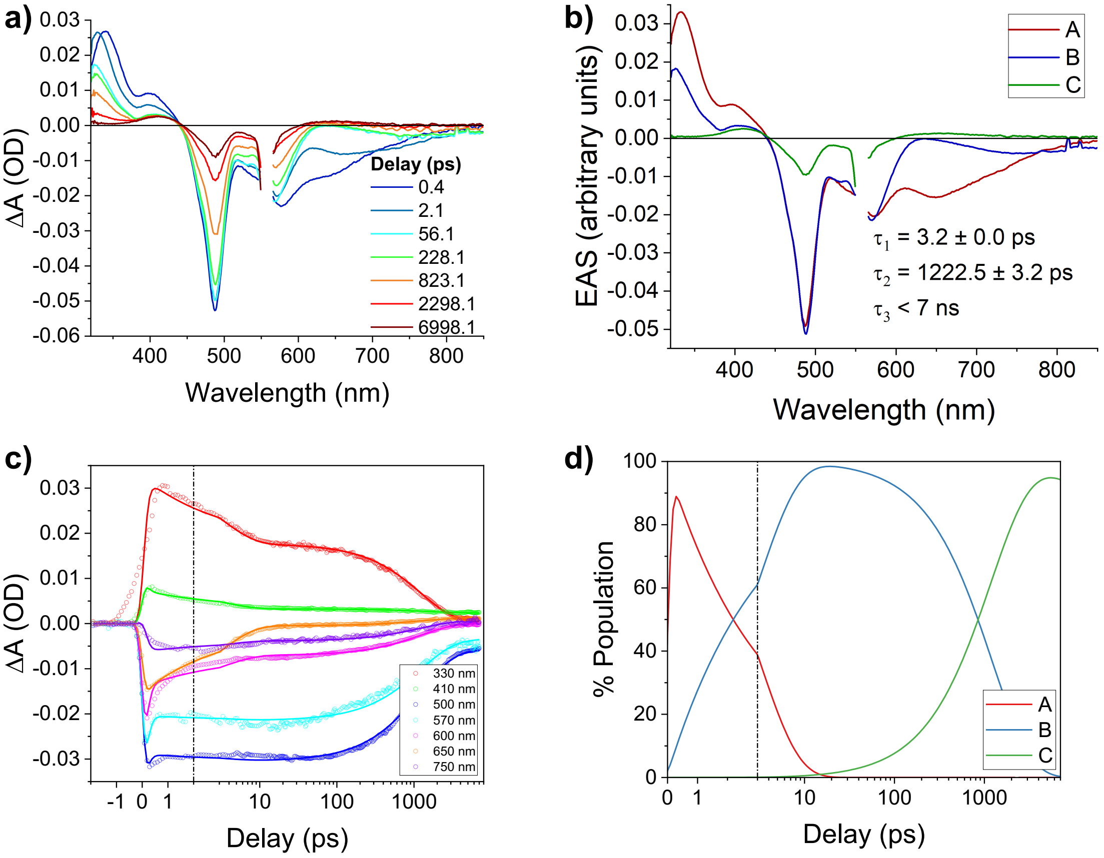

Figure S1.22 (a) TA spectra of **Jul-BD** in toluene excited at 560 nm along with relevant (a) evolution-associated species spectra, (c) selected wavelength kinetic fits from global analysis, and (d) population dynamics of each species.

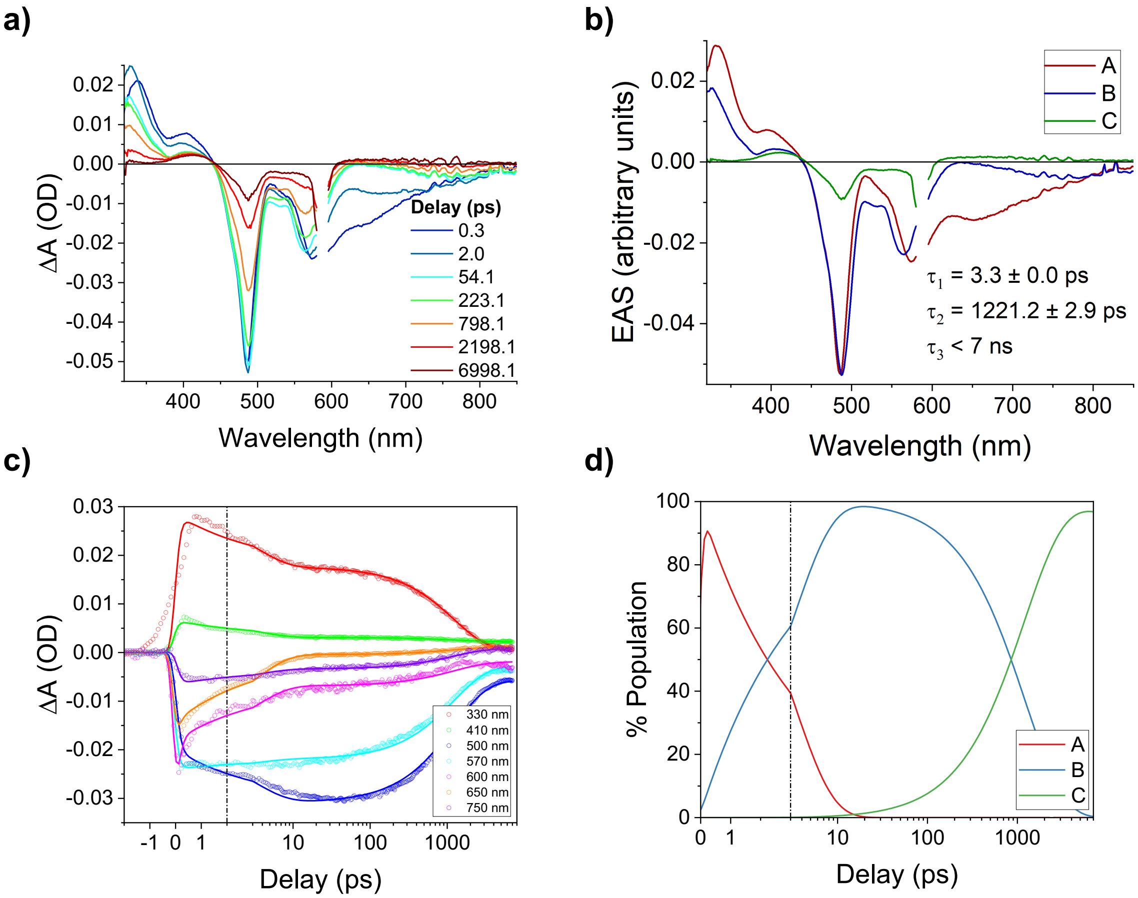

Figure S1.23 (a) TA spectra of **Jul-BD** in toluene excited at 590 nm along with relevant (a) evolution-associated species spectra, (c) selected wavelength kinetic fits from global analysis, and (d) population dynamics of each species.

1.6.7 Two-Dimensional Electronic Spectroscopy

2DES experiments were conducted using an experimental apparatus previously described.[90] The pump and probe were parallel in polarization and the pump energy at the sample was approximately 4 nJ/pulse for the blue pump and 6 nJ/pulse for the green pump. We used absorptive four-frame phase cycling to remove pump scatter background signals from the 2DES data. Data were averaged with 5000 laser cycles for each 2D spectrum.

Pulse Characterization

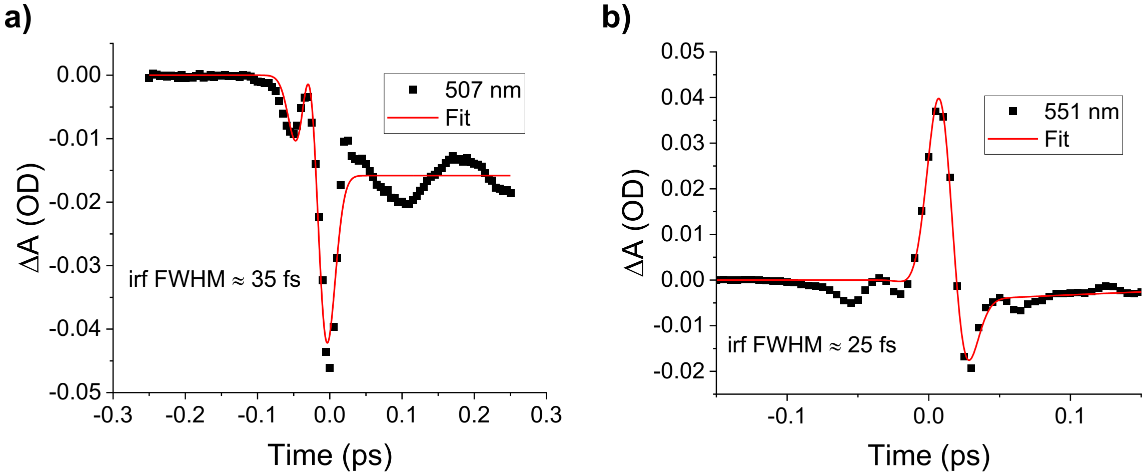

Figure S1.24 Fitted instrument response function for (a) blue and (b) green NOPA pump pulses in THF.

Additional 2DES Data in Toluene

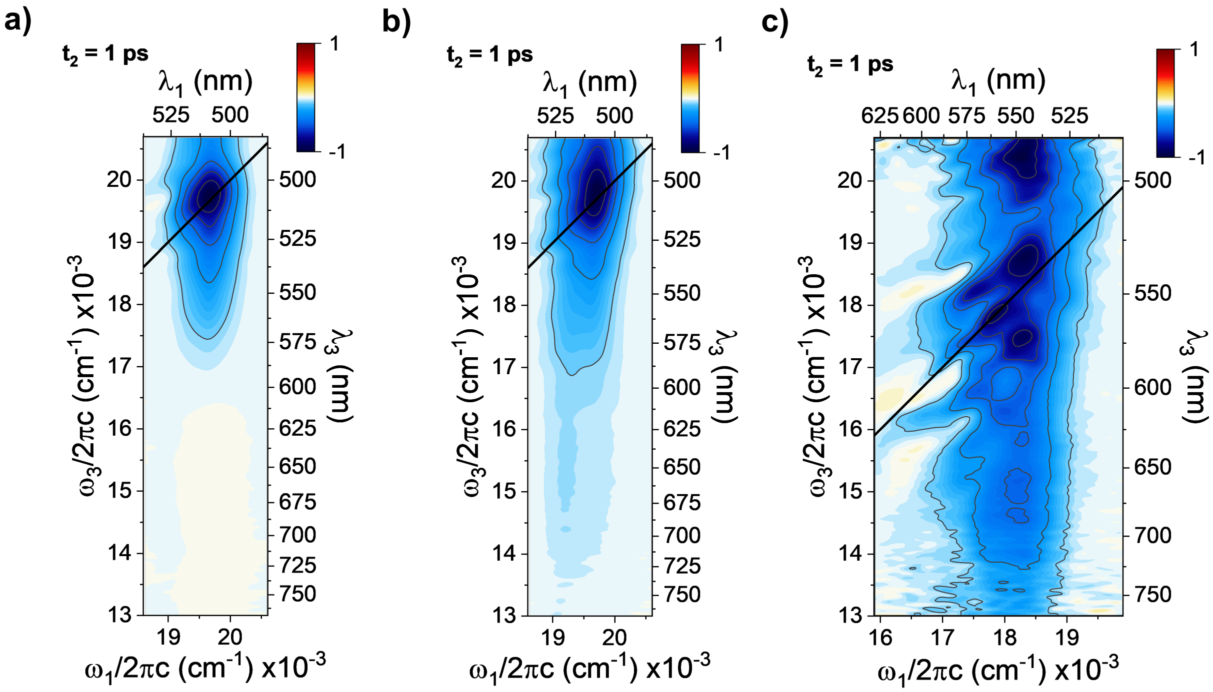

Figure S1.25 Representative 2DES spectra of (a) **Ph-BD** excited with the blue pump, and **Jul-BD** excited with the (b) blue pump and (c) green pump, all in toluene at a 1 ps waiting time.

Additional 2DES data in toluene resembles those of THF closely, save for increased scattering and noise in the toluene green pump data, leading to its more amorphous spectral features. As well, kinetics and evolution are substantially changed relative to those in THF, as discussed in the fsTA section above and the main text. All 2DES plots presented in this paper have been 11th order gaussian smoothed before being normalized to their highest absolute intensity value.

Power spectra from 2DES data

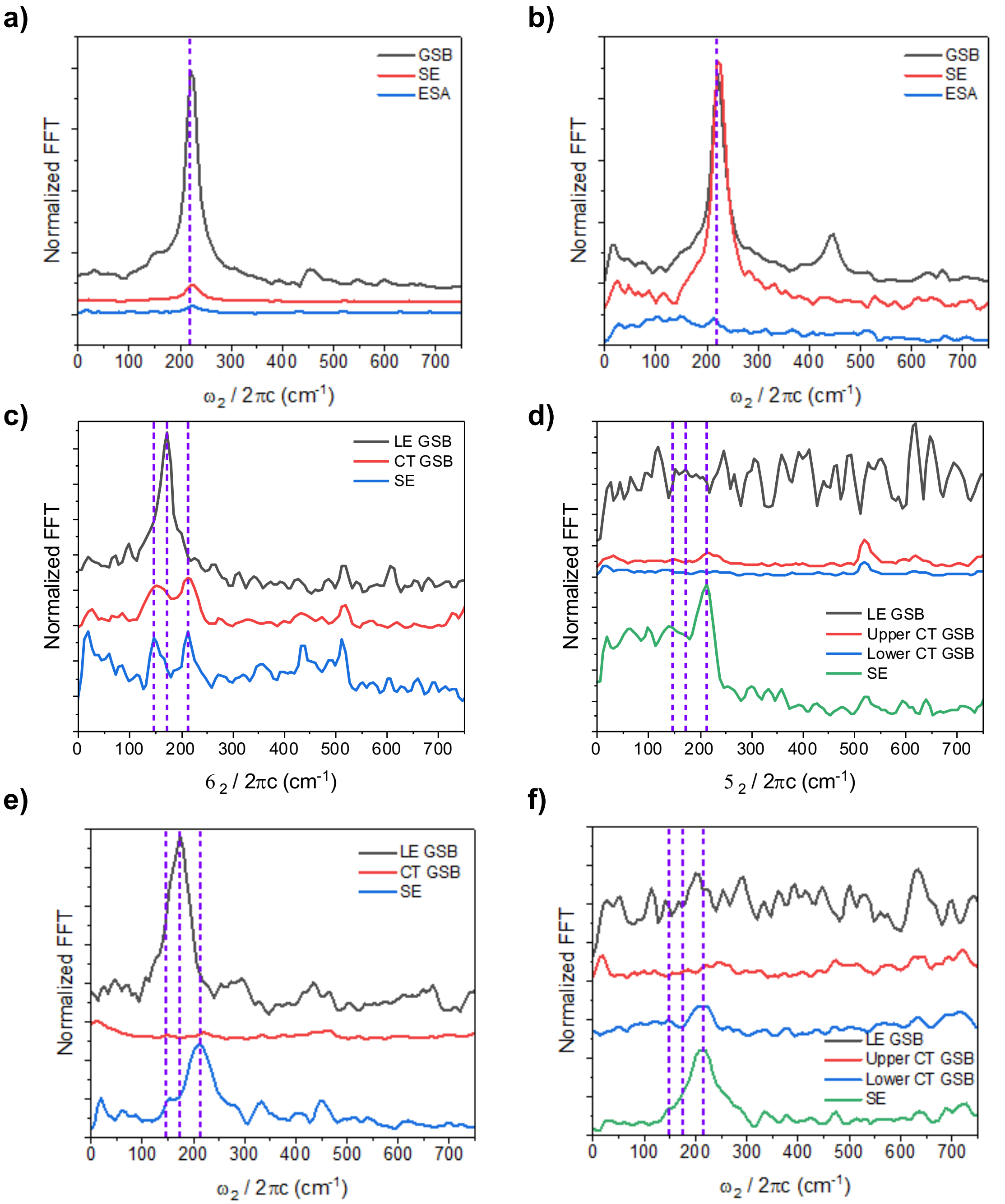

Figure S1.26 Power spectra for **Ph-BD** upon blue pump photoexcitation in (a) toluene and (b) THF. Power spectra for **Jul-BD** (c) in toluene upon blue pump photoexcitation, (d) in toluene upon green pump photoexcitation, (e) in THF upon blue pump photoexcitation, and (f) in THF upon green pump photoexcitation.

The power spectra depicted in Figure S1.26 were formed upon averaging and analyzing a 100 cm^{-1} diameter box, centered at pump and probe regions of interest. These regions of interest for **Ph-BD** were centered at $\omega_1 = 19750$ cm^{-1} and $\omega_3 = 19850$ cm^{-1} for the singlet GSB, $\omega_1 = 19750$ cm^{-1} and $\omega_3 = 17750$ cm^{-1} for the singlet SE, and $\omega_1 = 19750$ cm^{-1} and $\omega_3 = 15500$ cm^{-1} for the singlet ESA. For **Jul-BD** excited with the blue pump these regions were centered at $\omega_1 = 19750$ cm^{-1} and $\omega_3 = 19950$ cm^{-1} for the LE GSB, $\omega_1 = 19500$ cm^{-1} and $\omega_3 = 17600$ cm^{-1} for the CT GSB, and $\omega_1 = 19250$ cm^{-1} and $\omega_3 = 16000$ cm^{-1} for the CT SE. When examining the green pump excitation data for **Jul-BD** these regions were selected to be centered at $\omega_1 = 18350$ cm^{-1} and $\omega_3 = 20550$ cm^{-1} for the LE GSB, $\omega_1 = 18000$ cm^{-1} and $\omega_3 = 18750$ cm^{-1} for the upper probe energy CT GSB, $\omega_1 = 18000$ cm^{-1} and $\omega_3 = 17700$ cm^{-1} for the lower probe energy CT GSB, and $\omega_1 = 18000$ cm^{-1} and $\omega_3 = 15500$ cm^{-1} for the CT SE.

All FFT data in THF were normalized to the 914 cm^{-1} THF mode while all data in toluene were normalized to the 1005 cm^{-1} toluene mode for comparison.

Additional Quantum Beatmaps

All quantum beatmaps were 11th order gaussian smoothed before being normalized to their highest intensity values in each beatmap window.

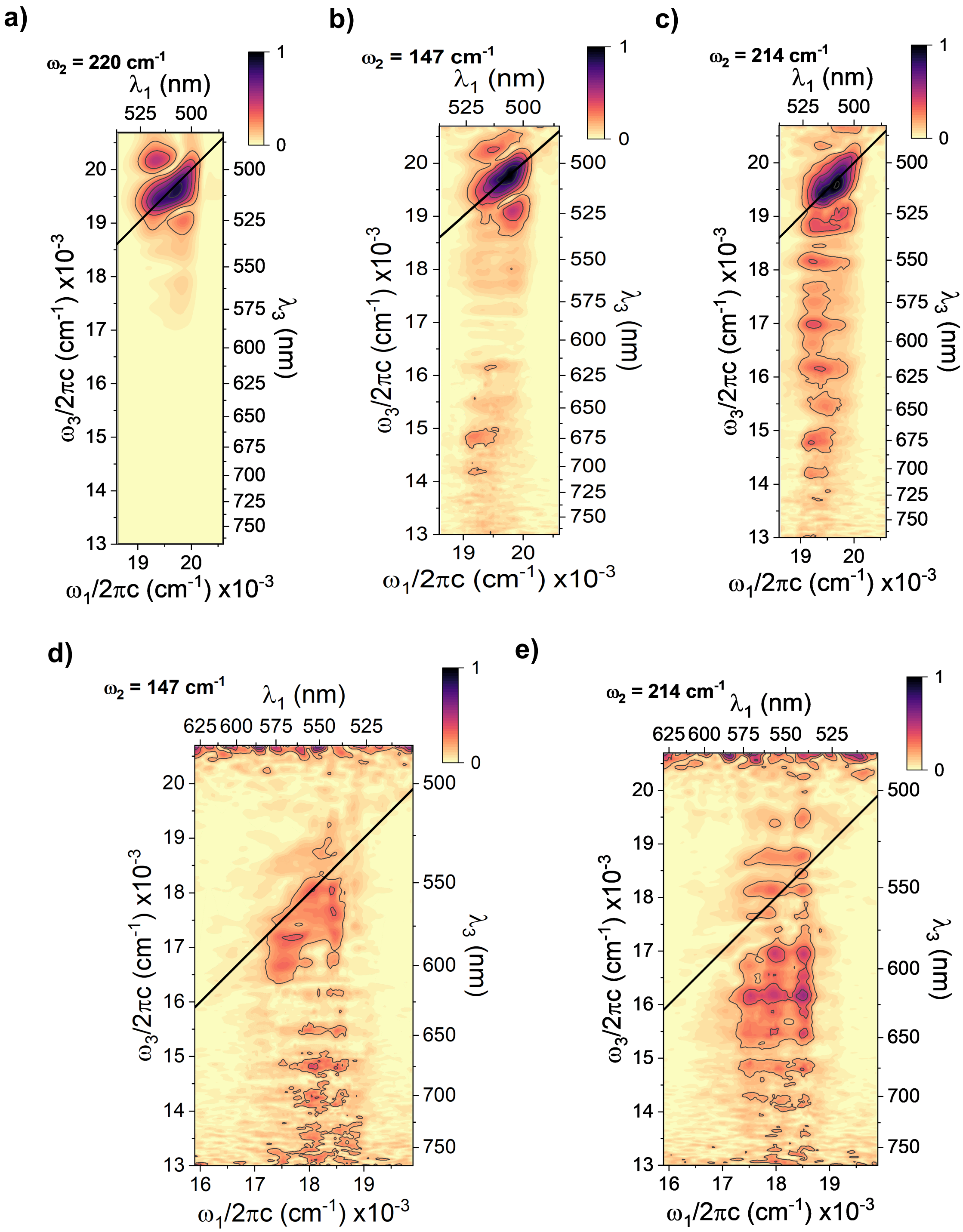

Figure S1.27 Quantum beatmaps of the (a) 220 cm^{-1} vibronic mode in **Ph-BD** when excited with the blue pump, and 147 and 214 cm^{-1} vibronic modes of **Jul-BD** when excited with the (b,c) blue pump and (d,e) green pump, in toluene.

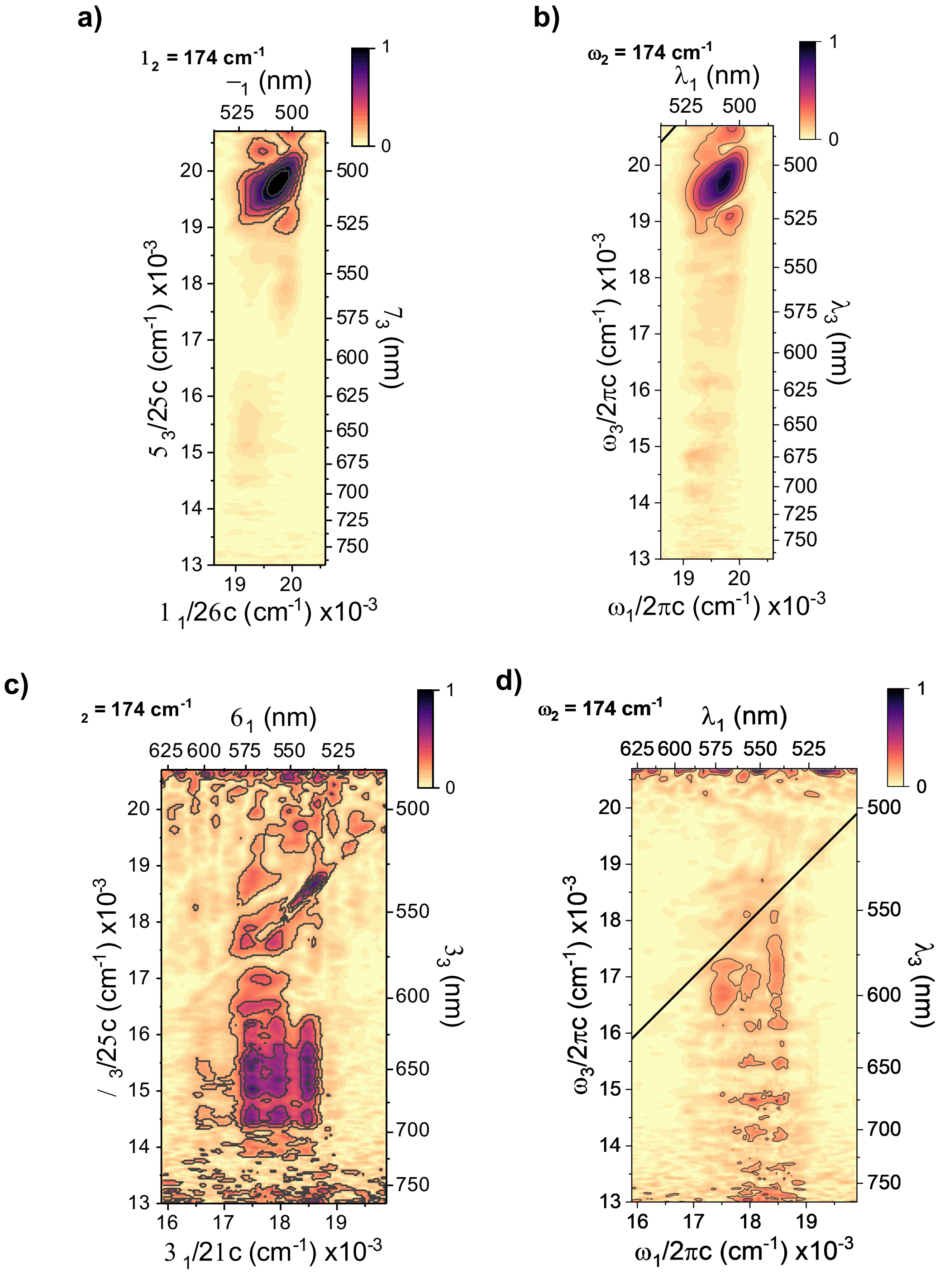

Figure S1.28 Quantum beatmaps of the 174 cm^{-1} vibronic mode in **Jul-BD** when excited with the blue pump in (a) THF and (b) toluene, and the green pump in (c) THF and (d) toluene.

1.6.8 Density Functional Theory Computational Details and Results

Calculated Raman Vibrational Modes

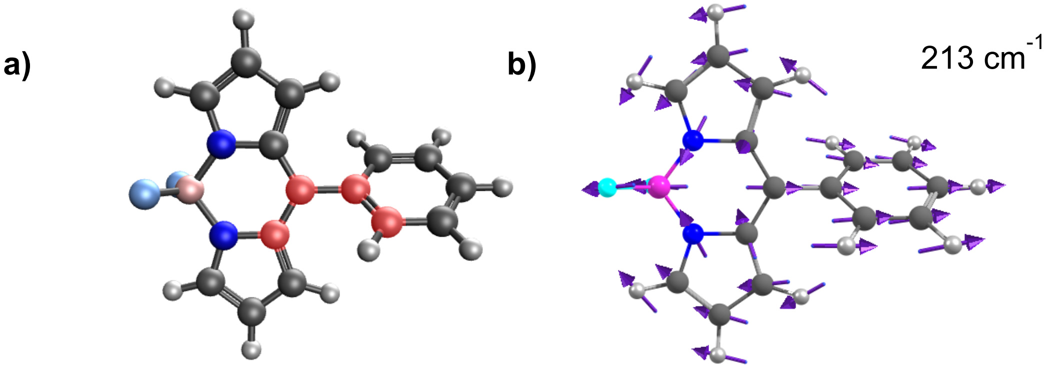

Figure S1.29. Visualizations of calculated (a) geometry and (b) frequency for active Raman

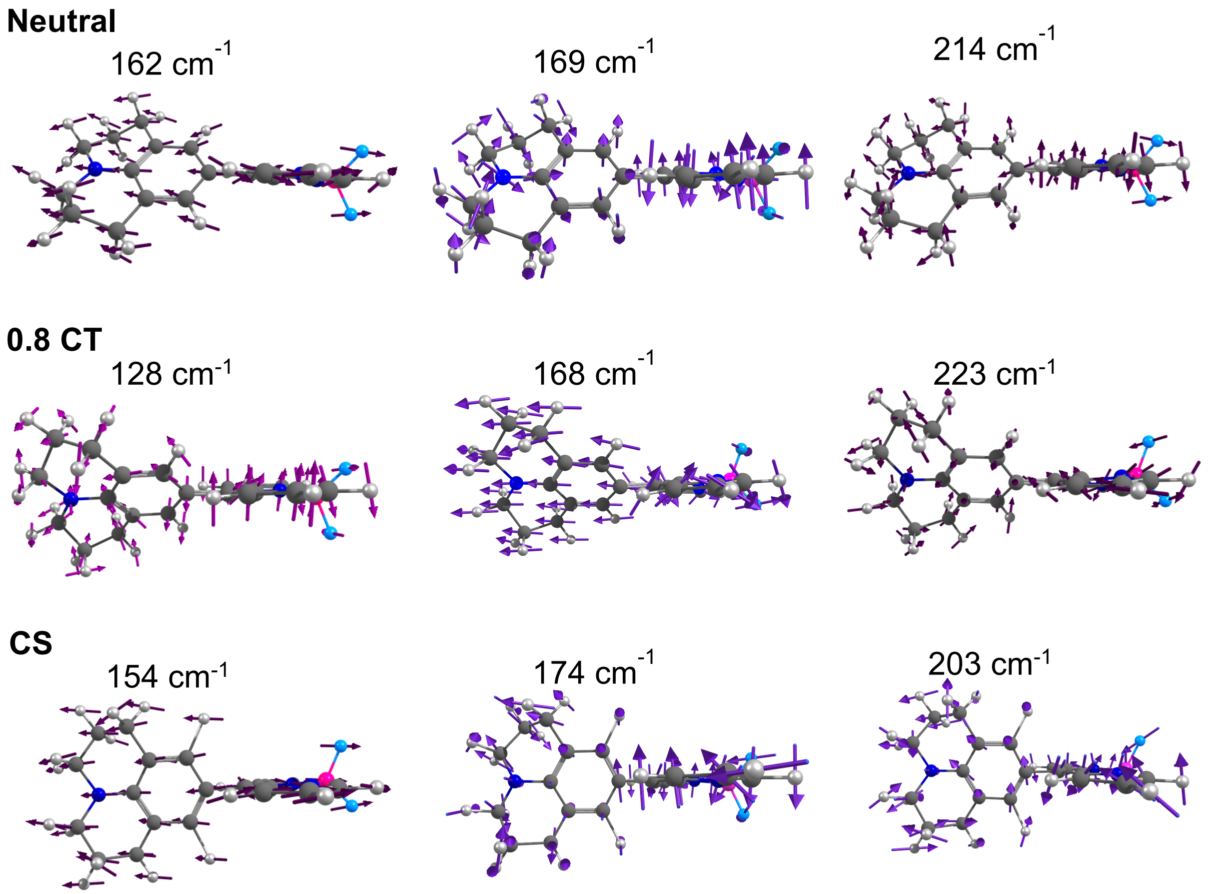

Figure S1.30 Visualizations of calculated frequencies for active Raman modes found in 2DES of **Jul-BD** with different degrees of charge transfer.

Calculated HOMO/LUMOs

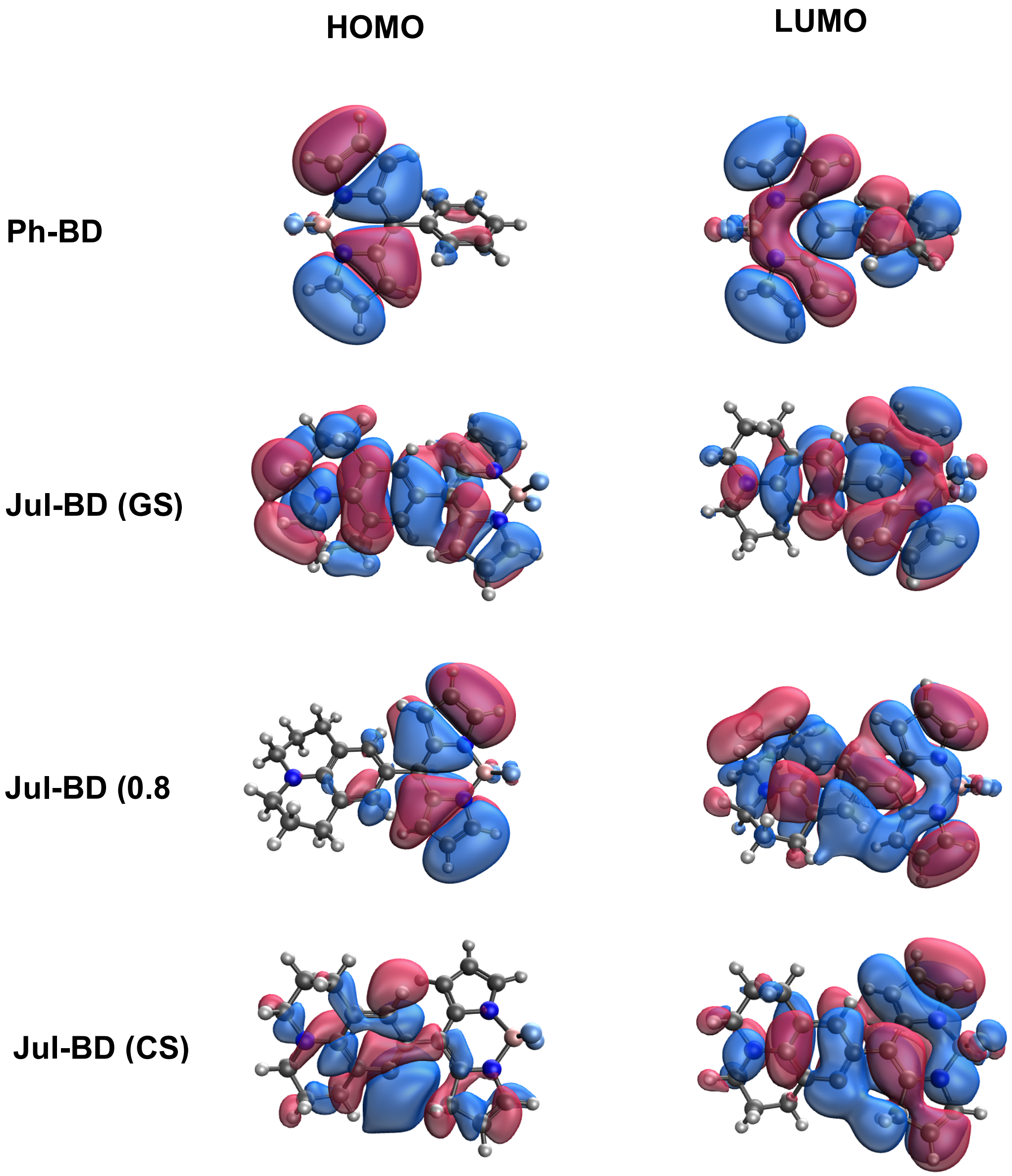

Figure S1.31 Visualizations of calculated HOMOs and LUMOs.

Calculated Optimized Geometries

As described in the main text, Density functional theory (DFT) calculations using Q-Chem 5.1 were performed on **Jul-BD** at the level of ωB97X-D/6-31G*. Constrained DFT (CDFT) calculations were utilized for calculations involving compounds with CT character and compounds with specified geometric constraints. For the CT calculations negative charge was placed on the atoms belonging to the BODIPY and positive charge was placed on the atoms belonging to the julolidine. For the geometric constraints, the same four atoms were selected, two on each side of the sigma bond connecting the julolidine to the BODIPY (Figure S1.27). Frequencies were scaled by a factor of 0.96. It should be noted that for the CS state normal mode analysis the calculation yielded one imaginary frequency. We believe this is a consequence of the constrained nature of the geometry optimization calculation where we placed a positive charge on the julolidine portion of the molecule and a negative charge on the BODIPY portion.

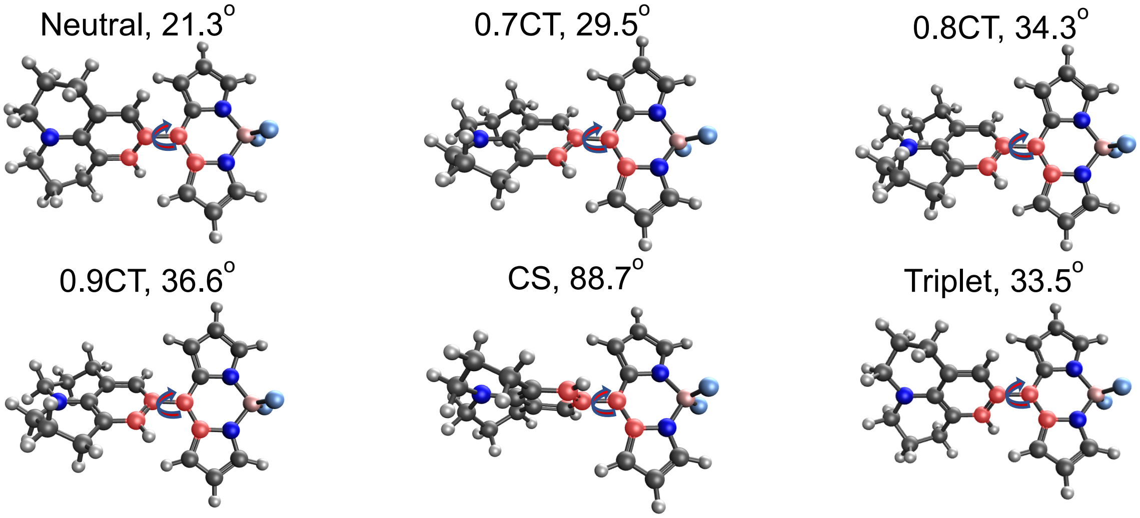

Figure S1.32 Calculated geometry optimizations of **Jul-BD** in the ground state, partial CT state, CS state, and triplet state.

Optimized Geometry Coordinates

Neutral ***Ph-BD***:

C	-0.36389	-1.20166	-0.02802
N	-1.75627	-1.17300	0.03834
B	-2.64882	0.11641	0.01524
N	-1.65446	1.29391	0.29471
C	-0.26347	1.21480	0.26304
C	0.38928	-0.01802	0.07915
C	-1.99206	2.56107	0.57256
C	-0.83633	3.35233	0.73123
C	0.25151	2.51006	0.54335
C	0.03428	-2.55493	-0.20472
C	-1.12165	-3.32424	-0.22245
C	-2.20272	-2.43191	-0.07589
F	-3.21719	0.26227	-1.23759
F	-3.60734	0.05916	1.00738
C	1.87051	-0.06590	0.02041
C	2.57199	0.74815	-0.88548
C	3.96371	0.70083	-0.94871
C	4.67760	-0.14852	-0.10130
C	3.99088	-0.95513	0.80817
C	2.59867	-0.91978	0.86649
H	-3.03314	2.84479	0.65098
H	-0.81872	4.40695	0.96921
H	1.29912	2.76413	0.62075
H	1.05281	-2.90104	-0.30715
H	-1.19622	-4.39750	-0.33113
H	-3.26461	-2.63886	-0.06066
H	2.01829	1.39864	-1.55563
H	4.48969	1.32680	-1.66427
H	5.76253	-0.18106	-0.14872
H	4.53937	-1.61145	1.47826
H	2.06895	-1.53535	1.58698

Neutral ***Jul-BD***:

C	1.96952	-1.16761	0.29592
N	3.35480	-1.20225	0.22818
B	4.29321	0.00968	-0.07215
N	3.33613	1.16264	-0.50826

C	1.94985	1.13278	-0.48350
C	1.25270	-0.01351	-0.06469
C	3.71588	2.33604	-1.02019
C	2.59287	3.11195	-1.34689
C	1.47946	2.35291	-1.01989
C	1.52786	-2.41527	0.79189
C	2.65512	-3.19644	0.99615
C	3.75919	-2.40556	0.64268
F	5.16264	-0.29662	-1.10227
F	4.97672	0.36329	1.07756
C	-0.21425	-0.00547	-0.01611
C	-0.90919	1.03770	0.60732
C	-2.29093	1.05127	0.69281
C	-3.03896	0.01078	0.09289
C	-2.35059	-1.03362	-0.56894
C	-0.96677	-1.03713	-0.58989
N	-4.41530	0.01597	0.14575
C	-5.22203	-1.10163	-0.31708
C	-5.16857	1.12265	0.71158
C	-3.01641	2.16551	1.40500
C	-3.14477	-2.13341	-1.22671
C	-4.41967	-2.39032	-0.42709
C	-4.36447	2.41428	0.73331
H	4.76590	2.56274	-1.14373
H	2.61024	4.09827	-1.78777
H	0.44051	2.61045	-1.16844
H	0.49925	-2.68254	0.98707
H	2.69407	-4.20999	1.36874
H	4.81370	-2.64149	0.68459
H	-0.34912	1.84122	1.07870
H	-0.45464	-1.84427	-1.10715
H	-5.67321	-0.85647	-1.29207
H	-6.04899	-1.23995	0.39164
H	-6.07586	1.25663	0.10857
H	-5.49687	0.86928	1.73294
H	-2.40639	3.07471	1.40218
H	-3.18149	1.89966	2.45867
H	-2.54036	-3.04348	-1.29839
H	-3.41177	-1.84856	-2.25416
H	-4.15670	-2.74640	0.57578
H	-5.03801	-3.15863	-0.90119
H	-4.20596	2.76526	-0.29310
H	-4.93443	3.18387	1.26288

*0.7 CT **Jul-BD**:*

C	1.96541	-1.16624	-0.25554
N	3.35209	-1.19210	-0.18546
B	4.28118	0.04764	0.00306
N	3.34056	1.16672	0.53275
C	1.95469	1.13504	0.53332
C	1.24477	0.00057	0.07934
C	3.73656	2.29467	1.12861
C	2.62421	3.04057	1.54158
C	1.50256	2.30844	1.18135
C	1.54393	-2.41311	-0.77563
C	2.67830	-3.18728	-0.96745
C	3.77080	-2.39123	-0.59781
F	4.82193	0.40610	-1.22007
F	5.26870	-0.22033	0.93276
H	4.79002	2.50457	1.25073
H	2.65057	3.98613	2.06369
H	0.47237	2.55268	1.39496
H	0.52697	-2.69119	-1.00803
H	2.72596	-4.19919	-1.34345
H	4.82810	-2.61546	-0.63179
C	-0.21964	0.01288	0.11312
C	-0.97732	-1.12783	0.41927
C	-2.35721	-1.14572	0.33988
C	-3.05116	0.01234	-0.08712
C	-2.30591	1.16575	-0.42851
C	-0.92630	1.13836	-0.34125
N	-4.42325	0.01530	-0.17133
C	-5.16618	1.12234	-0.75221
C	-5.23589	-1.09628	0.29507
C	-3.14390	-2.37575	0.72101
C	-3.03278	2.39366	-0.91727
C	-4.30026	1.98220	-1.66147
C	-4.49525	-1.96600	1.30022
H	-5.60080	1.74201	0.04850
H	-6.00518	0.70247	-1.32160
H	-6.14163	-0.68098	0.75501
H	-5.56285	-1.70749	-0.56165
H	-2.57632	-2.97651	1.43894
H	-3.30810	-3.00987	-0.16179
H	-2.37697	2.98747	-1.56223
H	-3.30524	3.03627	-0.06810

H	-4.03173	1.41290	-2.55897
H	-4.87406	2.85702	-1.98212
H	-4.34443	-1.40533	2.23005
H	-5.10746	-2.84159	1.53687
H	-0.47585	-2.00916	0.80687
H	-0.37256	2.01044	-0.67673

*0.8 CT **Jul-BD**:*

C	1.92921	-1.14596	-0.37739
N	3.31553	-1.19392	-0.34716
B	4.27637	-0.05429	0.10719
N	3.34924	1.17193	0.36903
C	1.96214	1.15987	0.39635
C	1.23172	0.02275	-0.00887
C	3.76596	2.34963	0.84301
C	2.66940	3.14686	1.19820
C	1.53376	2.39563	0.93421
C	1.47372	-2.34849	-0.96784
C	2.59116	-3.11785	-1.25384
C	3.70546	-2.36363	-0.86021
F	5.18255	0.22419	-0.89958
F	4.92124	-0.40498	1.28078
H	4.82344	2.55795	0.92986
H	2.71565	4.14184	1.61706
H	0.50955	2.67685	1.12983
H	0.44469	-2.59018	-1.18989
H	2.61542	-4.09531	-1.71367
H	4.75761	-2.60038	-0.93778
C	-0.23254	0.03459	0.04455
C	-0.96767	-1.09392	0.43690
C	-2.34981	-1.12244	0.41028
C	-3.06695	0.01066	-0.04376
C	-2.34338	1.14737	-0.47583
C	-0.96079	1.13269	-0.43770
N	-4.44203	0.00293	-0.07119
C	-5.21351	1.08399	-0.66205
C	-5.22946	-1.07649	0.50262
C	-3.11592	-2.33484	0.87766
C	-3.09515	2.34424	-1.00361
C	-4.39662	1.89159	-1.65991
C	-4.43508	-1.89653	1.50850
H	-5.59958	1.74642	0.12960

H	-6.08490	0.64158	-1.16122
H	-6.10623	-0.63203	0.99087
H	-5.60684	-1.73095	-0.29952
H	-2.51371	-2.91057	1.58771
H	-3.32731	-3.00153	0.02955
H	-2.47112	2.89678	-1.71360
H	-3.32761	3.03829	-0.18359
H	-4.17221	1.27260	-2.53643
H	-4.98746	2.74768	-1.99962
H	-4.23389	-1.29139	2.40016
H	-5.03237	-2.75892	1.81984
H	-0.44263	-1.95629	0.83705
H	-0.42705	1.98988	-0.83769

0.9 CT ***Jul-BD****:*

C	1.92588	-1.14194	-0.40676
N	3.31226	-1.18879	-0.38485
B	4.27303	-0.05174	0.07708
N	3.34642	1.17584	0.33746
C	1.95945	1.16268	0.36916
C	1.22981	0.02381	-0.02911
C	3.76275	2.35786	0.80050
C	2.66584	3.15677	1.15216
C	1.53040	2.40214	0.89743
C	1.46646	-2.34467	-0.99307
C	2.58263	-3.11258	-1.28807
C	3.69938	-2.35765	-0.90185
F	5.18440	0.22859	-0.92427
F	4.91094	-0.40694	1.25299
H	4.82017	2.56873	0.88197
H	2.71218	4.15546	1.56210
H	0.50560	2.68343	1.09046
H	0.43546	-2.58702	-1.20550
H	2.60462	-4.08958	-1.74897
H	4.75109	-2.59361	-0.98733
C	-0.23469	0.03352	0.02380
C	-0.96298	-1.08504	0.45374
C	-2.34556	-1.11396	0.44519
C	-3.06823	0.00865	-0.02555
C	-2.35079	1.13530	-0.49303
C	-0.96757	1.12227	-0.47065
N	-4.44392	0.00001	-0.03529

C	-5.22255	1.07111	-0.63429
C	-5.22358	-1.06573	0.57330
C	-3.10495	-2.31527	0.95033
C	-3.10886	2.32014	-1.03922
C	-4.42112	1.85394	-1.66389
C	-4.41656	-1.86329	1.58719
H	-5.59197	1.75190	0.14976
H	-6.10430	0.62189	-1.10851
H	-6.09385	-0.61028	1.06308
H	-5.61178	-1.73822	-0.20853
H	-2.49369	-2.87396	1.66624
H	-3.32606	-3.00194	0.12087
H	-2.49495	2.85318	-1.77252
H	-3.32776	3.03498	-0.23349
H	-4.21160	1.21394	-2.52891
H	-5.01625	2.70278	-2.01413
H	-4.20470	-1.23866	2.46277
H	-5.00943	-2.71891	1.92453
H	-0.43108	-1.93925	0.86281
H	-0.43784	1.97302	-0.88973

*CS **Jul-BD**:*

C	1.96094	-0.97212	0.74754
N	3.35427	-0.96710	0.68741
B	4.25299	0.07855	-0.08132
N	3.24036	0.91707	-0.95757
C	1.84999	0.88568	-0.87767
C	1.26923	-0.04850	-0.02351
C	3.56657	1.83913	-1.85423
C	2.40399	2.45541	-2.39211
C	1.31660	1.87831	-1.78907
C	1.54555	-2.03113	1.63740
C	2.69886	-2.62244	2.08448
C	3.78878	-1.93798	1.47857
F	5.13870	-0.57718	-0.89507
F	4.86359	0.90854	0.82428
H	4.60635	2.03476	-2.08394
H	2.39982	3.23746	-3.13695
H	0.28536	2.14684	-1.97927
H	0.53984	-2.32648	1.90676
H	2.78734	-3.45597	2.76568
H	4.85010	-2.11682	1.59505

H	-0.07779	1.64655	2.04124
H	-0.24716	-1.82155	-1.93693
C	-0.21426	-0.05121	0.03081
C	-0.84209	0.72514	1.00224
C	-2.27153	0.75688	1.01529
C	-2.99939	0.06720	0.03621
C	-2.32782	-0.67516	-0.94001
C	-0.90482	-0.77649	-0.94306
N	-4.41809	0.16558	-0.03262
C	-5.21085	-0.89281	-0.63521
C	-5.12458	0.85701	1.01774
C	-2.98486	1.57511	2.05046
C	-3.15186	-1.38496	-1.96884
C	-4.38273	-1.99276	-1.30150
C	-4.33948	2.05377	1.53958
H	-5.89297	-0.44913	-1.38145
H	-5.86153	-1.35737	0.12954
H	-6.09806	1.18765	0.62238
H	-5.35395	0.18005	1.86982
H	-2.33373	2.42488	2.30666
H	-3.14364	1.03582	3.00991
H	-2.51647	-2.16026	-2.41731
H	-3.48618	-0.73803	-2.80608
H	-4.04037	-2.70391	-0.54005
H	-5.02755	-2.54076	-2.00377
H	-4.19027	2.76556	0.71838
H	-4.92328	2.55610	2.32327

*CS **Jul-BD**:*

C	1.96328	-1.15527	0.35725
N	3.33229	-1.18336	0.34267
B	4.28086	0.00411	0.01987
N	3.32869	1.14094	-0.44249
C	1.95999	1.11284	-0.43845
C	1.22215	-0.01558	-0.02126
C	3.72940	2.34720	-0.93134
C	2.60412	3.13292	-1.25331
C	1.49033	2.38008	-0.95580
C	1.49996	-2.44591	0.81978
C	2.61709	-3.21338	1.06249
C	3.73839	-2.41318	0.76354
F	5.15527	-0.33574	-0.99965
F	4.97658	0.38465	1.15672

C	-0.25525	-0.00923	-0.00854
C	-0.96990	0.94867	0.71582
C	-2.35736	0.96978	0.74989
C	-3.08824	0.01039	0.01604
C	-2.38337	-0.95741	-0.73210
C	-0.99536	-0.95557	-0.72246
N	-4.47265	0.01923	0.02834
C	-5.26363	-1.02617	-0.59373
C	-5.23782	1.07122	0.67091
C	-3.10281	2.00576	1.55410
C	-3.15795	-1.97976	-1.52588
C	-4.46660	-2.30526	-0.81000
C	-4.42326	2.34253	0.86586
H	4.78188	2.57165	-1.03017
H	2.63284	4.13015	-1.66865
H	0.44948	2.63632	-1.08899
H	0.46087	-2.71042	0.95046
H	2.65052	-4.23209	1.42164
H	4.79197	-2.64301	0.83481
H	-0.42301	1.69202	1.29286
H	-0.46948	-1.70458	-1.31161
H	-5.66762	-0.67130	-1.55672
H	-6.12595	-1.23383	0.05428
H	-6.11451	1.28680	0.04518
H	-5.62050	0.72038	1.64409
H	-2.48685	2.90316	1.67488
H	-3.30949	1.62641	2.56499
H	-2.55530	-2.88338	-1.66599
H	-3.38315	-1.59163	-2.52947
H	-4.24939	-2.77015	0.15887
H	-5.07145	-3.01012	-1.38911
H	-4.22308	2.80211	-0.10921
H	-5.00823	3.05543	1.45547

Chapter 2: Hybrid Crystal Structure in D-A_4 Yields Charge Migration for Long-Lived CS State and Ultrafast Charge Separation

Jeremy M. Fisher,† Malik Williams,† Jonathan Palmer, Ryan M. Young,* and Michael R. Wasielewski*

Department of Chemistry and Institute for Sustainability and Energy at Northwestern (ISEN),
Northwestern University, Evanston, IL 60208-3113

2.1 Abstract

As the demand for efficient solar energy capturing systems increases, research into charge separation dynamics in solid-state systems is at an all-time high. Crystalline donor-acceptor systems serve as an excellent platform for studying the parameters at play in developing effective organic systems for solar energy capture. In this paper we investigate a four-pathway donor-acceptor system comprised of a single extended perylene core chromophore electron donor covalently linked to four identical naphthalene diimide (NDI) electron acceptors, (**Per-(NDI)$_4$**). A single NDI acceptor-containing analogue (**Per-NDI**) as well as the extended perylene alone (**Per-(Ph)$_4$**) were also synthesized as controls for comparison. Transient absorption experiments measured in solution reveal statistical rate enhancement of charge separation in **Per-(NDI)$_4$** compared to **Per-NDI**. In contrast, the charge recombination rate seems to be unaffected by the presence of multiple NDI units. This suggests that upon charge separation, the NDI anion is fully localized, not interacting with any neighboring NDI units in **Per-(NDI)$_4$**. A single crystal of **Per-(NDI)$_4$** was also grown and characterized using X-ray crystallography and transient absorption microscopy. The single crystal exhibits very fast charge separation kinetics (under 1 ps) in addition to a very long-lived charge separated (CS) state. We suggest here that the explanation for this long-lived CS state results from a hybrid crystal structure wherein the transferred electron hops to

neighboring NDI units along discrete NDI stacks that lie next to the donor-acceptor stacks, where the CS occurs.

2.2 Introduction

Crystalline organic materials have proven very useful in investigating the precise dynamics and parameters at play in solid-state organic systems upon photoexcitation.[11, 46, 57, 91-96] The major advantage of using crystalline materials is that their structure can be thoroughly understood. Using the structural knowledge of these systems in tandem with kinetic analysis sheds light on the structure-dynamics relationship and ultimately helps lead the way toward elucidating important guidelines in developing promising systems for efficient solar energy capture and conversion in devices.

Two important criteria in realizing efficient performance from these materials are 1) fast charge transfer (CT) and 2) effective ability to fully dissociate and migrate the formed charges.[5, 95, 97] Many studies on donor-acceptor (DA) co-crystals, wherein unattached electron donors and acceptors are mixed together to form a single crystal containing both molecules, have been conducted to elucidate the nature of CT exciton generation and evolution as well as charge migration/hopping.[96, 98-107] Two general structural patterns appear in DA co-crystal studies: mixed stacks with alternating DADA and segregated donor and acceptor stacks.[96, 105, 106] These packing structures result from nonbonding interactions such as π-π stacking, CT, and halogen- and hydrogen-bonding.[96, 101] Because the structure of co-crystals is governed by these non-covalent interactions, it is difficult to exercise control over the structural relationship between the donors and acceptors, as they are not directly connected. Growing single crystals of covalently attached

DA systems offers the advantage of a fixed donor-acceptor connectivity as well as direct control over the stoichiometric ratio of the donors to acceptors. Studying these covalently attached DA single crystals could help further bridge the gap in understanding the structure-dynamics relationship, as comparisons could be made between the DA system as it interacts in a single crystal and an ensemble of distinct single molecules dispersed in solution. Additionally, with the built-in connectivity of such covalently attached systems, it could be possible to access a variety of other types of packing structures.

In this study, we synthesized and characterized a DA system where a single extended perylene core is covalently attached to four naphthalene diimide acceptors (**Per-(NDI)$_4$**). A single NDI-containing compound, **Per-NDI**, and the extended perylene core alone, **Per-(Ph)$_4$**, were also synthesized as control compounds to better understand the dynamics in **Per-(NDI)$_4$**. Studying these three compounds in solution reveals a CT rate in **Per-(NDI)$_4$** four-fold faster than that observed for **Per-NDI**. For CR on the other hand, the solution data shows both NDI-containing compounds exhibit a very similar rate. This suggests CT occurs with statistical rate enhancement in **Per-(NDI)$_4$** from the presence of four NDI acceptors, but for CR, the presence of multiple NDI units has no effect, indicating that once CT occurs, the NDI anion is localized on a single NDI moiety without interaction from the other three NDI units connected to the same perylene core.

We additionally grew and characterized single crystals of **Per-(NDI)$_4$** and **Per-(Ph)$_4$**. The crystal structure for **Per-(NDI)$_4$** contains aspects of both structural motifs often found in DA co-crystals mentioned above: NDI stacks and ADAADA patterned NDI-Per wires. This unusual combination of both packing types yields very fast CT and long-lived CS state. Using the data collected in solution and on single crystals, we suggest the mechanisms responsible for these desirable behaviors.

2.3 Methods

2.3.1 Synthesis. Per-(Ph)4, **Per-NDI**, and **Per-(NDI)$_4$** were synthesized using Suzuki coupling reactions of Perylene-(BPin)$_4$ with NDI-Br and/or Phenyl-Br (Scheme 2.1). Further details can be found in the Supporting Information (SI)

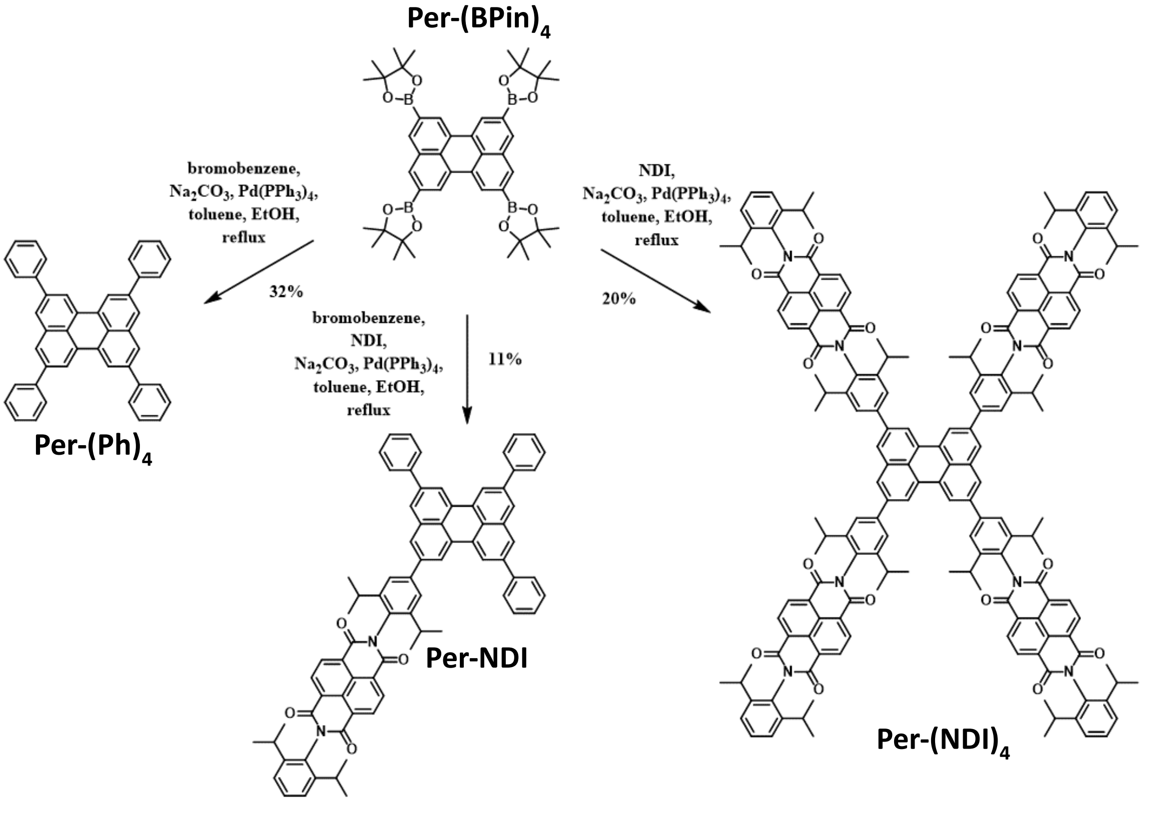

Scheme 2.1 Synthetic scheme for **Per-(Ph)4**, **Per-NDI**, and **Per-(NDI)$_4$**.

2.3.2 Steady-State Optical Spectroscopy. UV-visible-NIR steady-state absorption spectra were measured at room temperature using a Shimadzu UV-1800 spectrometer. NIR emission was measured using a HORIBA Nanolog fluorimeter.

2.3.3 Electrochemistry. Electrochemical measurements were performed on a CH Instrument 750E electrochemical workstation. Measurements were made using a 1.0 mm diameter glassy carbon working electrode, a platinum wire auxiliary electrode, and a silver wire pseudo-reference electrode in 0.1 M solutions of n-butylammonium hexafluorophosphate ($TBAPF_6$) in acetonitrile purged with argon. Ferrocene was used as an internal standard.

2.3.4 Transient Absorption Spectroscopy. Femtosecond transient absorption (TA) experiments were performed on an apparatus that has been described previously.[82] Tunable excitation pulses were generated by using a commercial colinear optical parametric amplifier (TOPAS-Prime, Light-Conversion, LLC). The polarization was spatially randomized to eliminate the effects of polarization-dependent dynamics. Spectra were collected using commercial spectrometers (customized Helios/Eos, Ultrafast Systems, LLC). The total instrument response function was ~300 fs. Transient spectra were averaged for at least 3 s per delay point. Prepared samples had an absorbance of 0.2-0.7 at the excitation wavelength and were irradiated in 2-mm pathlength quartz cuvettes with 0.4-0.8 μJ/pulse focused to ~0.2 mm diameter spot.

2.3.5 X-ray Crystallography. Intensity data of a yellow-orange irregular shaped single crystal of **Per-(NDI)$_4$** were collected at 150.00(10) K. A suitable single crystal with dimensions of 0.072×0.146×0.28 mm3 was mounted on a MiTeGen loop with paratone oil on an XtaLAB Synergy diffractometer equipped with a micro-focus rotating anode X-ray tube Rigaku Cu X-ray source and a Hybrid Pixel Array Detector (HyPix) detector. Temperature of the crystal was controlled with an Oxford Cryosystems low-temperature device. Data reduction was performed with the CrysAlisPro software using an empirical absorption correction. The structure was solved with the ShelXT structure solution program using the Intrinsic Phasing solution method and by using Olex2 as the graphical interface. The model was refined with ShelXL using least squares minimization.

2.3.6 Steady-State Absorption (SSA) Microscopy. Steady-state absorption spectra were collected on the crystals using a Xenon arc lamp (Oriel Instruments, model 66902). The beam was spatially filtered through a pinhole and polarized using a Glan–Thompson polarizer. A motorized (ELL14K, Thorlabs) achromatic half-wave plate (SAQWP05M-700, Thorlabs) was used to rotate the linear polarization. The beam was then sent into the back port of an upright microscope (Eclipse Ti–U, Nikon). In the microscope the beam was directed through an internal mirror to a 20× reflective objective lens (LMM15X, Thorlabs) to focus on the sample. The transmitted part was collected using a second objective lens and then sent to a home-built spectrometer (Richardson Gratings, 52A15BK-224C) and focused onto a fast line-scan camera (OctoPlus, Teledyne e2v), sampling at 100 000 lines/s. For absorption measurements, a reference spectrum (on bare glass) and a transmission spectrum (through a single cocrystal) were collected for each polarization in the range 0–360° in 10° steps. A dark spectrum, with no light on the sample, was subtracted from all reference and transmission spectra.

2.3.7 Femtosecond Transient Absorption Microscopy (fsTAM). The 1040 nm output from a commercial Yb:KGW, 4 W, 100 kHz repetition rate, 300 fs, amplified laser system (Spirit-One, Spectra-Physics) was divided into two beams. One beam was sent to an optical parametric amplifier (OPA) (Spirit-OPA-8, Light Conversion) to generate the pump beam wavelengths. The pump was sent to a quarter-wave plate, which converted it to a circularly polarized beam, and then into an electro-optic amplitude modulator (EO-AM-NR-C4, Thorlabs), which was phase-synchronized to the laser output and a polarizer to amplitude-modulate the beam at 50 kHz. The laser pulses passing through the EOM suffer severe time stretching of up to a few ps; thus, a lab-built two-prism compressor was used to recompress them to ~200 fs as measured using a lab-built autocorrelator. The other 1040 nm beam was sent to a double-pass linear delay line (Newport, IMS600LM), and then focused into an 8 mm thick undoped YAG crystal for white light continuum generation. The beam was then recollimated and the fundamental was removed using a 1000 nm short-pass filter. The pump and probe beams were coaxially combined using a 50:50 beamsplitter and sent into the microscope system and spectrometer described above. The polarizations of the pump and the probe beams were varied independently using two achromatic half-wave plates. The pump and probe power on the sample were each set to 2 μW using two neutral density filters. The pump and probe focused spot size (4 standard deviations of a Gaussian, or 95% of the beam intensity) on the sample were 2.9 μm, giving pump and probe fluence of 0.6 mJ/cm2 and 0.3 mJ/cm2, respectively. To further mitigate systematic baseline shifts during the measurement, the TA spectrum at each delay point was individually referenced to a fixed negative delay point (−10 ps).

2.3.8 Nanosecond Transient Absorption Microscopy (nsTAM). A nanosecond-pulsed 405 nm laser (NPL41B, Thorlabs) was used as a pump. The laser output was combined with the same white light continuum beam used in the fsTAM apparatus, and both beams were sent to the microscope through the same optical path as described above. The pump–probe delay was electronically modified using a delay generator (DG645, Stanford Research). The pump was electronically triggered at 50 kHz using lab-built electronics.

2.3.9 Density Functional Theory Computations. Density functional theory (DFT) calculations using Q-Chem 5.1 were performed on all **Per-(Ph)$_4$**, **Per-NDI**, and **Per-(NDI)$_4$** at the level of B3LYP/6-31G* to calculate optimized geometries as well as the triplet energy level for **Per-(Ph)$_4$**.

2.4 Results and Discussion

2.4.1 System Energetics

Steady-State Optical Spectroscopy. The UV-visible absorption spectra of **Per-(Ph)$_4$**, **Per-NDI**, and **Per-(NDI)$_4$** are shown in Figure 2.1. All solution-phase spectra were collected in 1,4-dioxane. **Per-(Ph)$_4$** absorbs slightly red-shifted compared to perylene at λ_{max} = 399, 422, and 450 nm due to its increased conjugation with the phenyl extensions. The NDI moieties in **Per-(NDI)$_4$** absorb at λ_{max} = 340, 359, and 378 nm. **Per-(Ph)$_4$** fluoresces at λ_{max} = 457 nm with a minor Stokes shift of 0.04 eV.

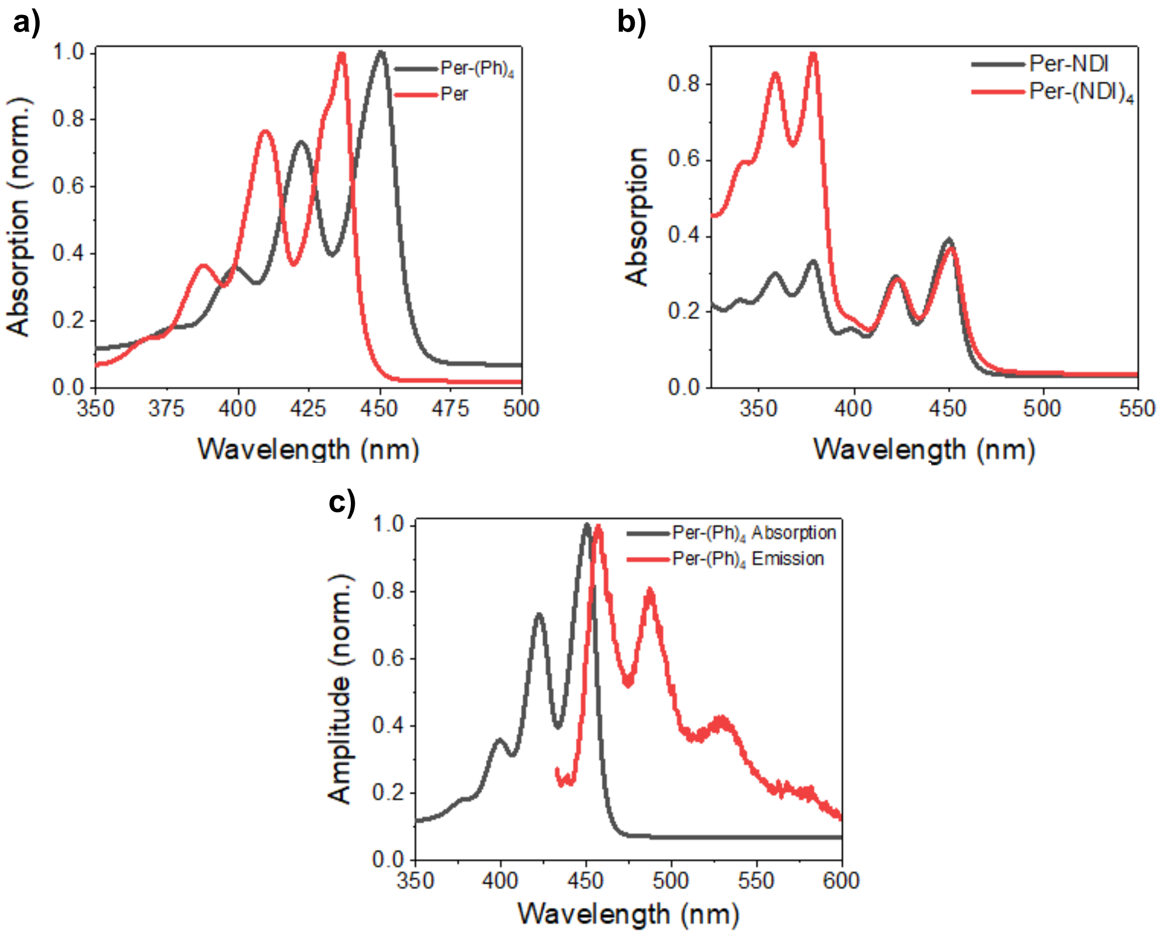

Figure 2.1 (a-b) UV-Vis absorption spectra of **Per-(Ph)$_4$, Per-(NDI)$_4$,** and **Per-(NDI)$_4$**. (c) Emission spectrum of **Per-(Ph)$_4$** normalized and overlayed with its absorption spectrum.

The absorption spectra of **Per-(Ph)$_4$**$^+$ and **Per-(NDI)$_4$**$^-$ were obtained (Figure S2.9) following oxidation of **Per-(Ph)$_4$** using single electron oxidant, tris(4-bromophenyl)ammoniumyl hexachloroantimonate ('Magic Blue'), and reduction of **Per-(NDI)$_4$** using single electron reductant, cobaltocene. **Per-(Ph)$_4$**$^+$ has an absorptive feature at 640 nm that is slightly red-shifted compared to unfunctionalized perylene cation, as well as an additional absorption feature at 1000 nm. **Per-(NDI)$_4$**$^-$ absorbs at λ_{max} = 471 and 607 nm, which is consistent with NDI$^-$ absorption in the literature.[108, 109]

Electrochemistry. Cyclic voltammograms (CV) spectra for **Per-(Ph)$_4$** and **Per-(NDI)$_4$** in 0.1 M TBAPF$_6$ DCM can be seen in Figure S2.10. The oxidation potential of **Per-(Ph)$_4$** was measured to be E_{ox} = 1.1 eV vs SCE and the reduction potential of Per-(NDI)$_4$ was measured to be E_{rred} = -0.38 eV vs SCE.

Electron-Transfer Energetics. The lowest singlet electronic excited-state energy can be calculated by taking the crossing point of the normalized absorption and emission spectra of **Per-(Ph)$_4$**, which is to act as the chromophore. This yields an S$_1$ lowest electronic excited energy of 2.74 eV.

To account for coulombic interactions in the radical pair, as well as the different dielectric constants of the solvents used for electrochemical measurements (DCM) and transient optical measurements (1,4-dioxane), the Weller equation was applied to the redox potentials measured in DCM.[85] This yields a radical pair energy of 1.8 eV in 1,4-dioxane and a ΔG_{CS} of -0.9 eV, indicating ET in these systems is thermodynamically favorable. The full energetic scheme of the compound can be seen in Figure 2.2. The T$_1$ energy was calculated by DFT as 1.7 eV. See SI for details.

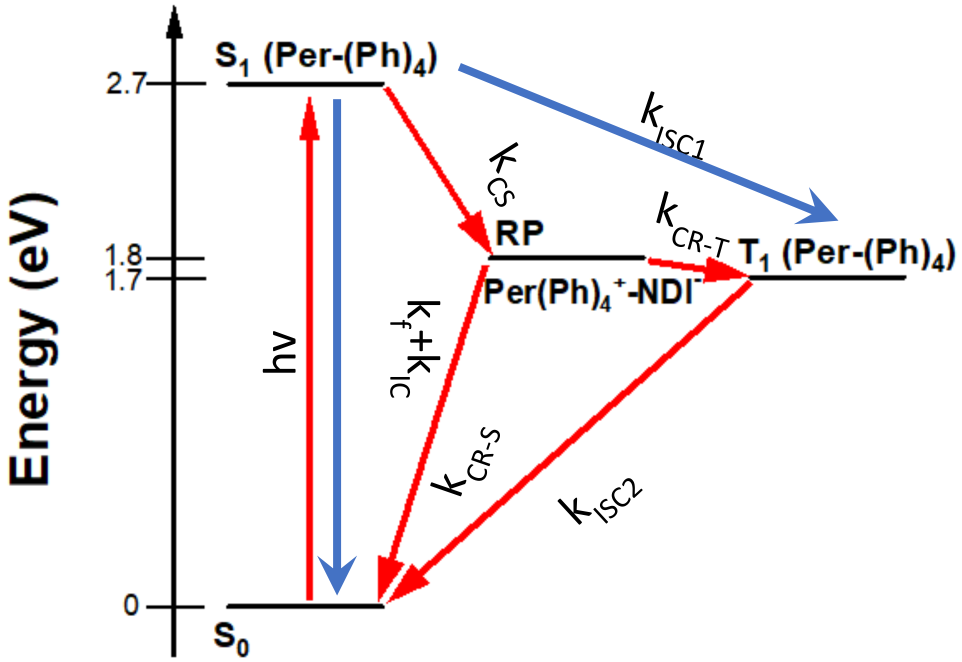

Figure 2.2 Jablonski diagram of **Per-(NDI)**$_4$.

2.4.2 Solution Dynamics

Transient Absorption Spectroscopy. **Per-(Ph)**$_4$, **Per-NDI**, and **Per-(NDI)**$_4$ were investigated using pump-probe TA spectroscopy at room temperature in 1,4-dioxane.

Per-(Ph)$_4$ was first characterized to obtain the transient features attributed to the ^{1*}**Per-(Ph)**$_4$ and ^{3*}**Per-(Ph)**$_4$ excited states. All TA spectra (Figure 2.3) show ground state bleach as negative features at 422 nm and 451 nm. The transient ^{1*}**Per-(Ph)**$_4$ species, which can be seen at early pump-probe time delays in the fsTA data (Figure 2.3a-b), shows a negative feature at 486nm as a stimulated emission as well as positive excited state absorption features at 554, 747, 813, and 1235 nm. At long pump-probe delays, the nsTA data (Figure 2.3c-d) indicate production of the

^{3*}**Per-(Ph)$_4$** excited state with a decay rate constant of $k_{CR\text{-}T}$ = (4.7 ± 0.6 ns)$^{-1}$, as seen most prominently by the broad positive feature at 510 nm. This decay constant is comprised of contributions from internal conversion ((k_{IC}) and fluorescence (k_f), as well as intersystem crossing (k_{ISC1}): $k = k_{IC} + k_f + k_{ISC1}$.

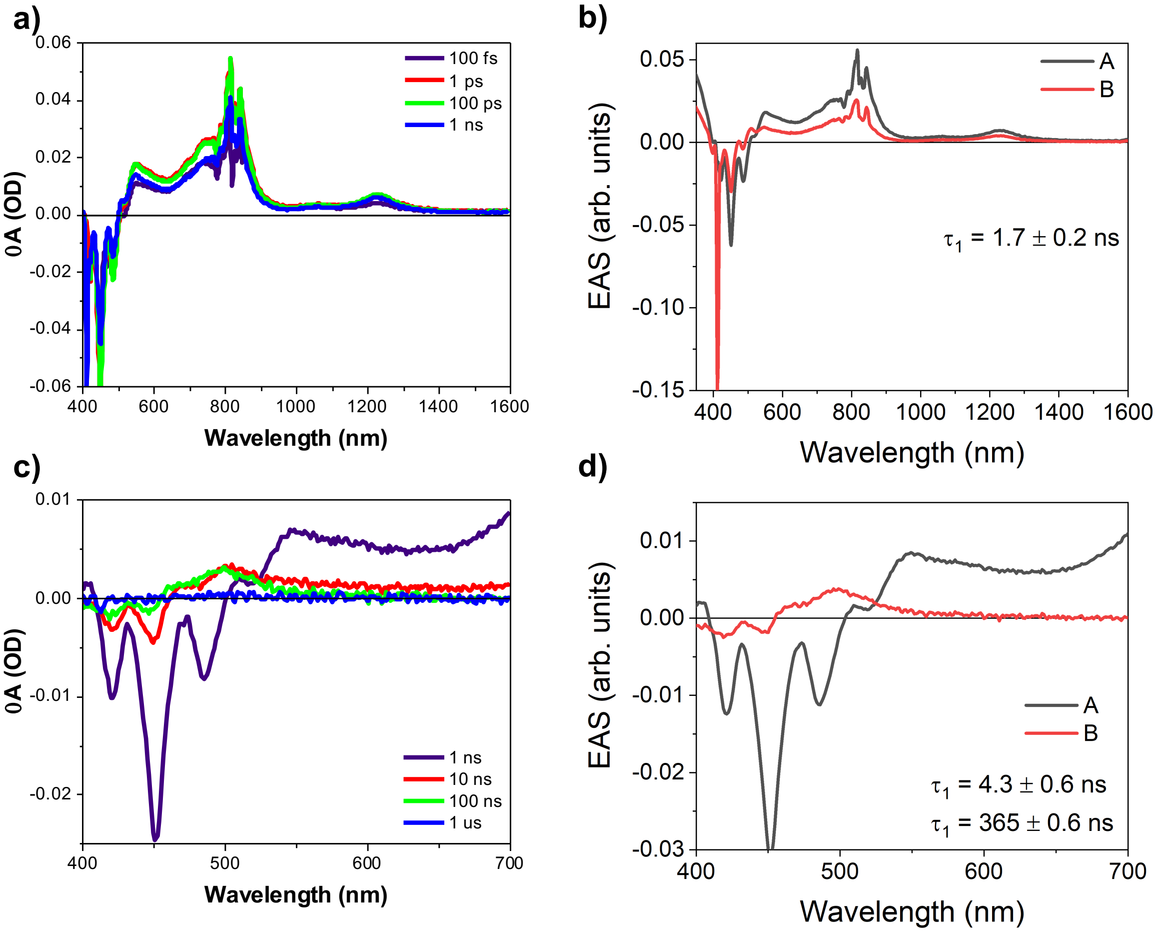

Figure 2.3 (a) fsTA data and (b) Evolution-associated spectra of **Per-(Ph)$_4$** in 1,4-dioxane with λ_{ex} = 414 nm. (c) nsTA data and(d) Evolution-associated spectra of **Per-(Ph)$_4$** in 1,4-dioxane with λ_{ex} = 414 nm.

The kinetics of **Per-NDI** and **Per-(NDI)$_4$** were analyzed next (Figures 2.4 and 2.5). Both NDI-containing compounds show population of ^{1*}**Per-(Ph)$_4$** followed by ET to form **Per-(Ph)$_4$$^+$-**

NDI$^-$ (consistent with the steady-state ionic species' absorption at 471, 607, 640, and 1000 nm see figures S2.9). The charge separation rate constants were measured to be k_{CS} = (12.4 ± 0.3 ps)$^{-1}$ and (3.3 ± 0.3 ps)$^{-1}$ for **Per-NDI** and **Per-(NDI)$_4$** respectively. The ratio of the rates in these compounds is thus $k_{4\text{NDI}/1\text{NDI}}$ = 3.8 ± 0.4. This is the result of statistical rate enhancement due to the presence of 4 NDI acceptors on **Per-(NDI)$_4$**. After CS, charge recombination partially to the lower-lying local **^{3*}Per-(Ph)$_4$** excited state is observed with rates of $k_{CR\text{-}S} + k_{CR\text{-}T}$ = (6.1 ± 0.6 ns)$^{-1}$ and (5.6 ± 0.6 ns)$^{-1}$ for **Per-NDI** and **Per-(NDI)$_4$** respectively. These data show that the CR dynamics are unchanged within error between **Per-(NDI)$_4$** and **Per-NDI**, in contrast to the CS rates, where statistical rate enhancement was observed. This can be explained by the localized nature of the NDI$^-$ radical anion resulting from CS. Though **Per-(NDI)$_4$** contains four pathways for CS, each individual CS event only occurs through one of those pathways, with one of the four available NDI moieties. This results in a **Per-(Ph)$_4$$^+$-NDI$^-$** radical pair unperturbed by the other three NDI moieties. Following triplet formation, each system then decays back to the ground state through intersystem crossing (k_{ISC2}) in hundreds of nanoseconds.

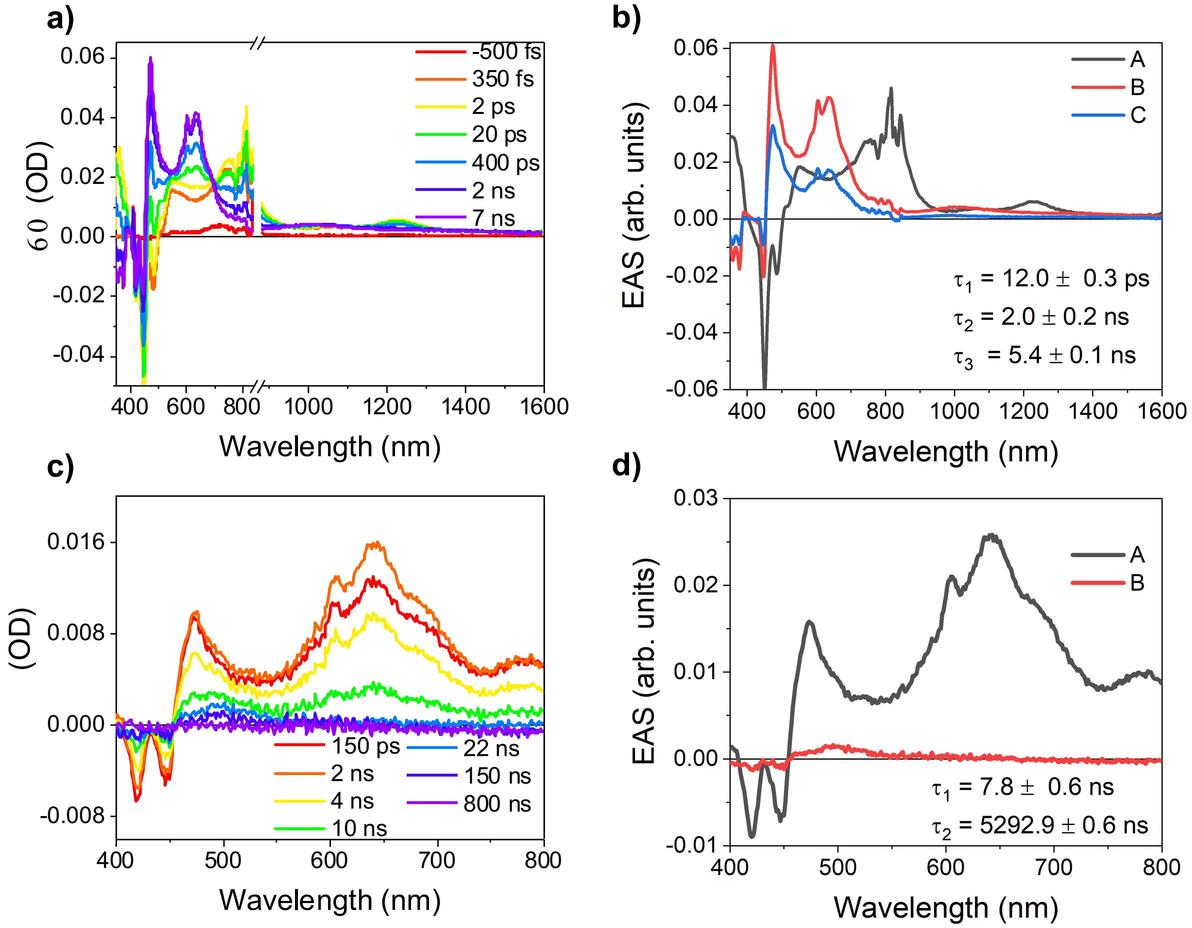

Figure 2.4. (a) fsTA data and (b) Evolution-associated spectra of **Per-NDI** in 1,4-dioxane with λ_{ex} = 414 nm. (c) nsTA data and(d) Evolution-associated spectra of **Per-NDI** in 1,4-dioxane with λ_{ex} = 414 nm.

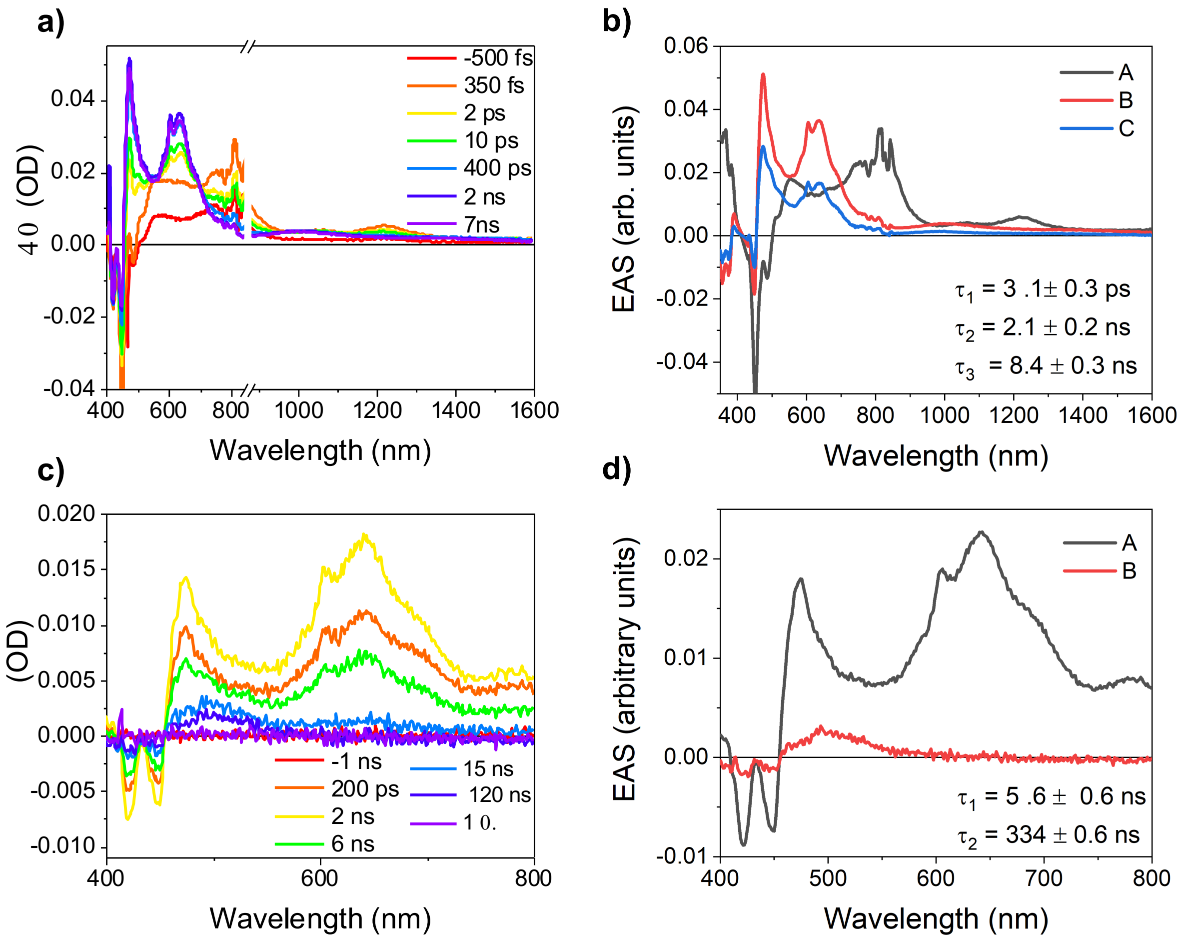

Figure 2.5 (a) fsTA data and (b) Evolution-associated spectra of **Per-(NDI)$_4$** in 1,4-dioxane with λ_{ex} = 414 nm. (c) nsTA data and(d) Evolution-associated spectra of **Per-(NDI)$_4$** in 1,4-dioxane with λ_{ex} = 414 nm.

2.4.3 Solid State Characterization and Dynamics

X-Ray Diffraction. Single crystals were grown for **Per-(Ph)$_4$** and **Per-(NDI)$_4$** via slow diffusion using chloroform/MeOH (counter-solvent) and xylenes/MeOH (counter-solvent), respectively. The **Per-(Ph)$_4$** single crystal (Figure S2.20) shows slip stacking in its packing structure along its long axis of 3.51 Å as a result of the large dihedral angle between the phenyl rings and the perylene core (measured to be between 35-40 degrees for all four units). There is no significant slip stacking along the short axis. The center-to-center distance for π-π stacking between each **Per-(Ph)$_4$** molecules is 4.93 Å.

For the **Per-(NDI)$_4$** single crystals (Figure 2.6), in each molecule, two NDI units opposite each other are angled at 64.5° relative to the plane of the perylene core while the other two are angled at 48.2 °. Any two NDI units separated by the short axis of the perylene core are 19.421 Å apart while any two separated by the long axis are 15.346 Å apart from center to center. This can be explained by the obtuse 119.60 ° angle of the NDI relative to the short axis of the perylene core fanning those constituents farther apart than the ones separated by the long axis. Each NDI is 11.320 Å away from the perylene core center-to-center. The overall packing structure of the **Per-(NDI)$_4$** single crystals can be described as consisting of two types of regions: intermolecular NDI stacks and intermolecular NDI-Per wires. For each **Per-(NDI)$_4$** molecule, the two NDI units at an angle of 48.2 ° relative to the perylene core contribute to the NDI stacks and the two NDI moieties with the more severe 64.5 ° twist relative to the core contribute to the NDI-per wires. The NDI stacks consist of co-facial NDI units from neighboring **Per-(NDI)$_4$** molecules stacked on top of each other with at a distance of 7.162 Å center-to-center. In the NDI-Per wires, each perylene core is sandwiched between two NDI moieties, each from a separate neighboring **Per-(NDI)$_4$** molecule, one above and one below, at an angle of 62.82 ° from the plane of the perylene, forming a Z-shaped type of pattern. Both NDI units sit at a distance of 5.646 Å from the perylene center-to-center. The distance from one perylene to the next is 22.272 Å center-to-center. The nearest NDI to one of the NDI in the NDI-Per wires belongs to a neighboring **Per-(NDI)$_4$** molecule and is part of the NDI stacks. This intermolecular NDI-NDI distance is 9.293 Å. Both the NDI stacks and the NDI-Per wires run along the c-axis of the crystal packing structure.

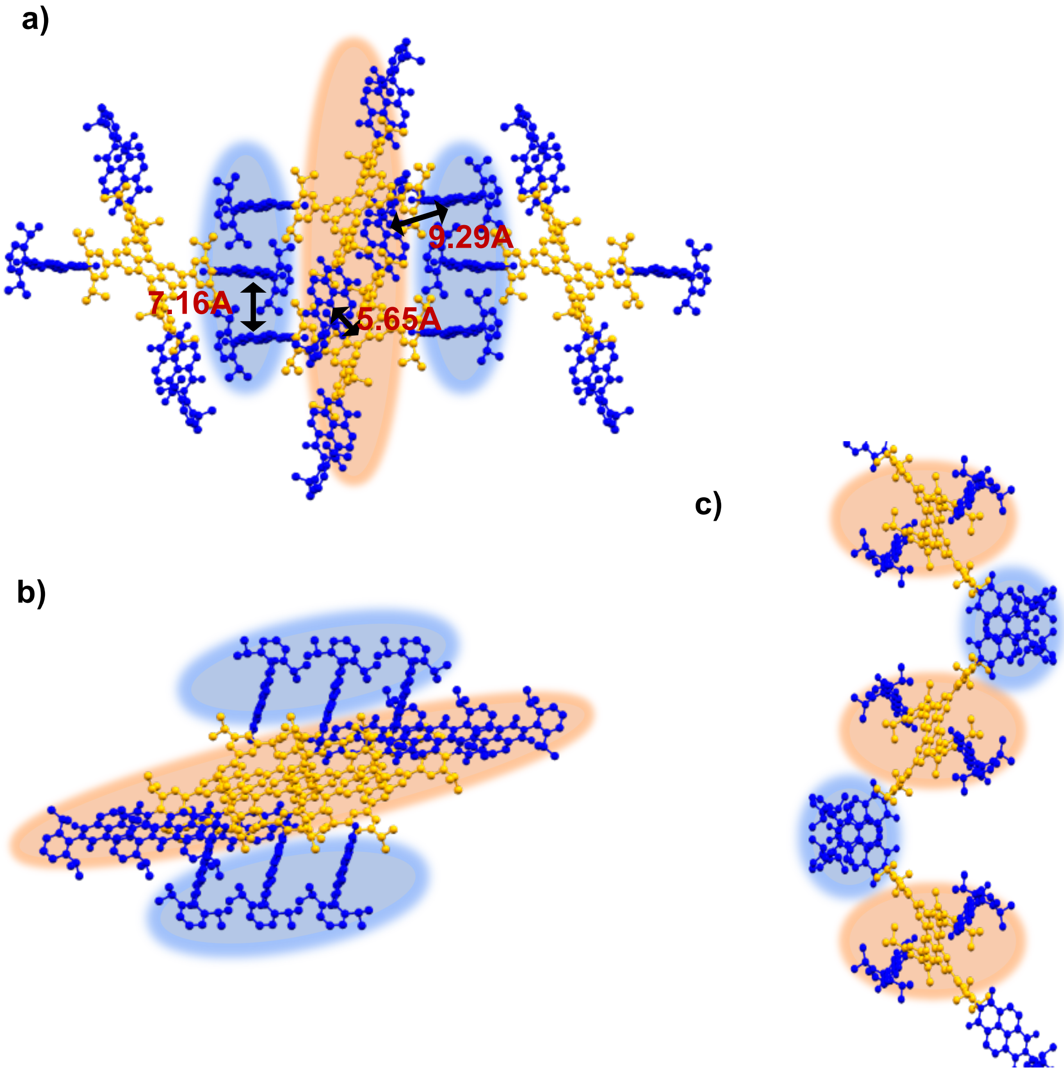

Figure 2.6 Crystal structures from XRD for **Per-(NDI)$_4$** along the a) a-axis, b) b-axis, and c) c- with the extended perylene moieties highlighted in orange the NDI moieties highlighted in blue. The NDI stacks are additionally shaded in blue and the NDI-Per wires in orange.

Steady-State Absorption (crystals). Steady-state absorption measurements for a **Per-(NDI)$_4$** single crystal can be seen in Figure 2.7. This broad absorptive feature represents the CT band of **Per-**

(NDI)$_4$ formed due to the donor-acceptor stacking discussed above. Because **Per-(Ph)$_4$** absorption occurs only at wavelengths lower than our instrument range, no signal was found for those crystals.

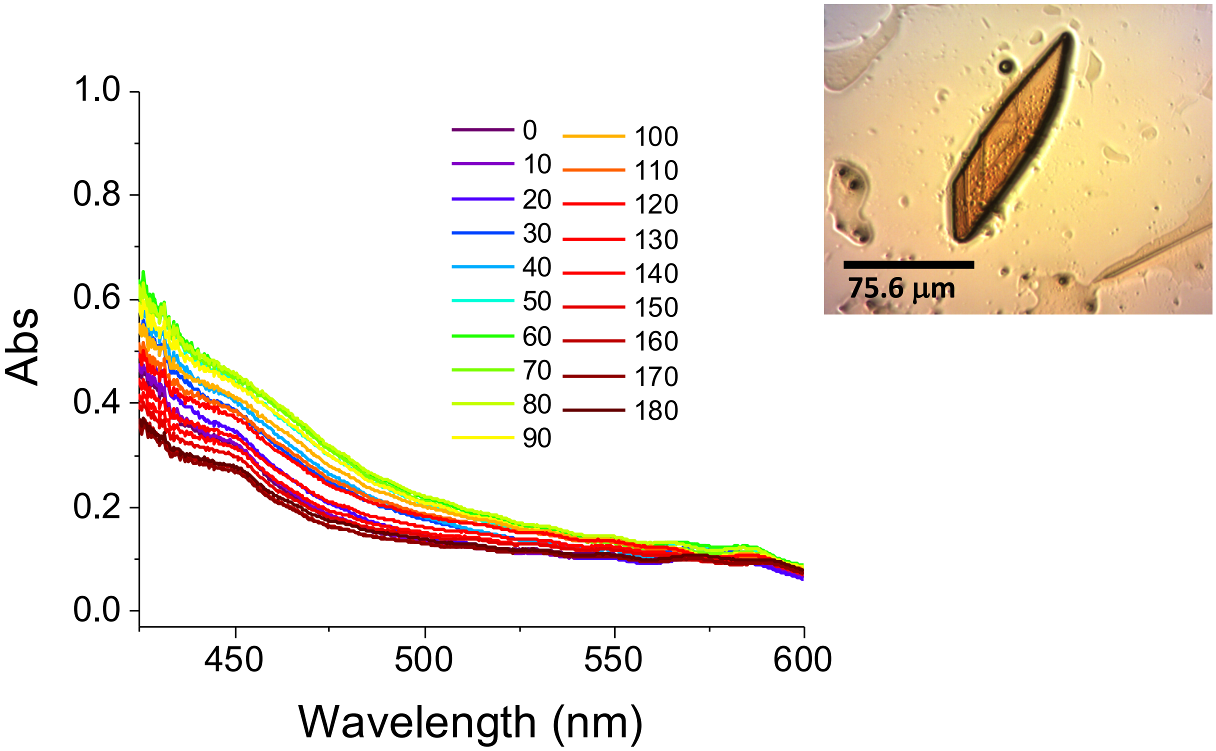

Figure 2.7 Steady-state absorption spectrum of a **Per-(NDI)$_4$** crystal at different polarizations.

Transient Absorption Microscopy Spectroscopy (crystals). Transient absorption microscopy (TAM) was employed to probe the excited-state optical dynamics in **Per-(Ph)$_4$** and **Per-(NDI)$_4$** single crystals. For **Per-(Ph)$_4$**, the fsTAM shows a single broad absorptive feature centered at 660 nm. The signal for this species is formed within the 300 fs IRF of the instrument and survives the entire fsTAM experiment, for several nanoseconds, and there is no observable signal in the nsTAM. We assign this species to be the ^{1*}**Per-(Ph)4** singlet exciton state. The ^{1*}**Per-(Ph)4** exciton likely relaxes to the ^{3*}**Per-(Ph)4** state before returning to ground state, but the TAM setup could not capture any of its features as they likely appear at bluer wavelengths than the detection window of the experimental probe used.

For **Per-(NDI)$_4$**, the TAM shows a single sharp absorptive feature at 620 nm atop a broad sloping signal, which appears within the 300 fs IRF of the fsTAM instrument and survives beyond the 15 μs lifetime of the nsTAM experiments. This feature agrees well with the absorption spectrum collected on a chemically reduced film of **NDI$^-$** (Figure S2.21d). Furthermore, a film of chemically oxidized **Per-(Ph)$_4$$^+$** revealed significant broadening of its absorptive feature in this region, potentially explaining the absence of a distinct absorptive feature for **Per-(Ph)$_4$$^+$** in the TAM spectra even though it was observed in the solution TA data (Figure S2.21c).

We turn to the crystal structure to reconcile this kinetic data with those observed in solution. When comparing the proximity of the **Per-(Ph)$_4$** center to its closest neighboring NDI, in solution all four intramolecular NDI moieties are 11.320 Å away, while in the single crystal the two closest NDI units belong to neighboring molecules and are 5.646 Å away. This is the origin of the CT band and hence the much faster charge separation rate observed in the single crystal versus in solution.

In addition to a very fast charge separation rate (<300 fs), the **Per-(NDI)$_4$** single crystals also exhibit an extremely long-lived charge separated state. Two aspects of the crystal structure likely contribute to this feat. Firstly, the two NDI moieties lying above and below each Perylene core are angled 62.82^o away from the plane of the perylene. This prevents the π-π interaction from being too strong and allows the separated charges to remain separated for a more substantial amount of time. Next, in solution, once the electron was transferred to an intramolecular NDI unit, it was observed that the electron was localized entirely on that unit, without experiencing stabilization through delocalization or hopping with neighboring NDI units. This is a result of NDI being too far apart from its closest intramolecular neighbor, which lies at a distance of 15.346 Å.

This explains why the charge recombination rates for **Per-(NDI)$_4$** and **Per-NDI** were functionally the same in solution. In the **Per-(NDI)$_4$** single crystal, however, each NDI is only 9.293 Å from its closest neighboring NDI unit, which belongs to a neighboring molecule. Additionally, this closest NDI moiety is positioned in the middle of an NDI stack, where it is sandwiched co-facially between two NDI units lying above and below it at a distance of only 7.162 Å. This could explain the very long-lived CS state, as free migration of the electron along the NDI stacks would result in significant separation of the initially formed radical pair.

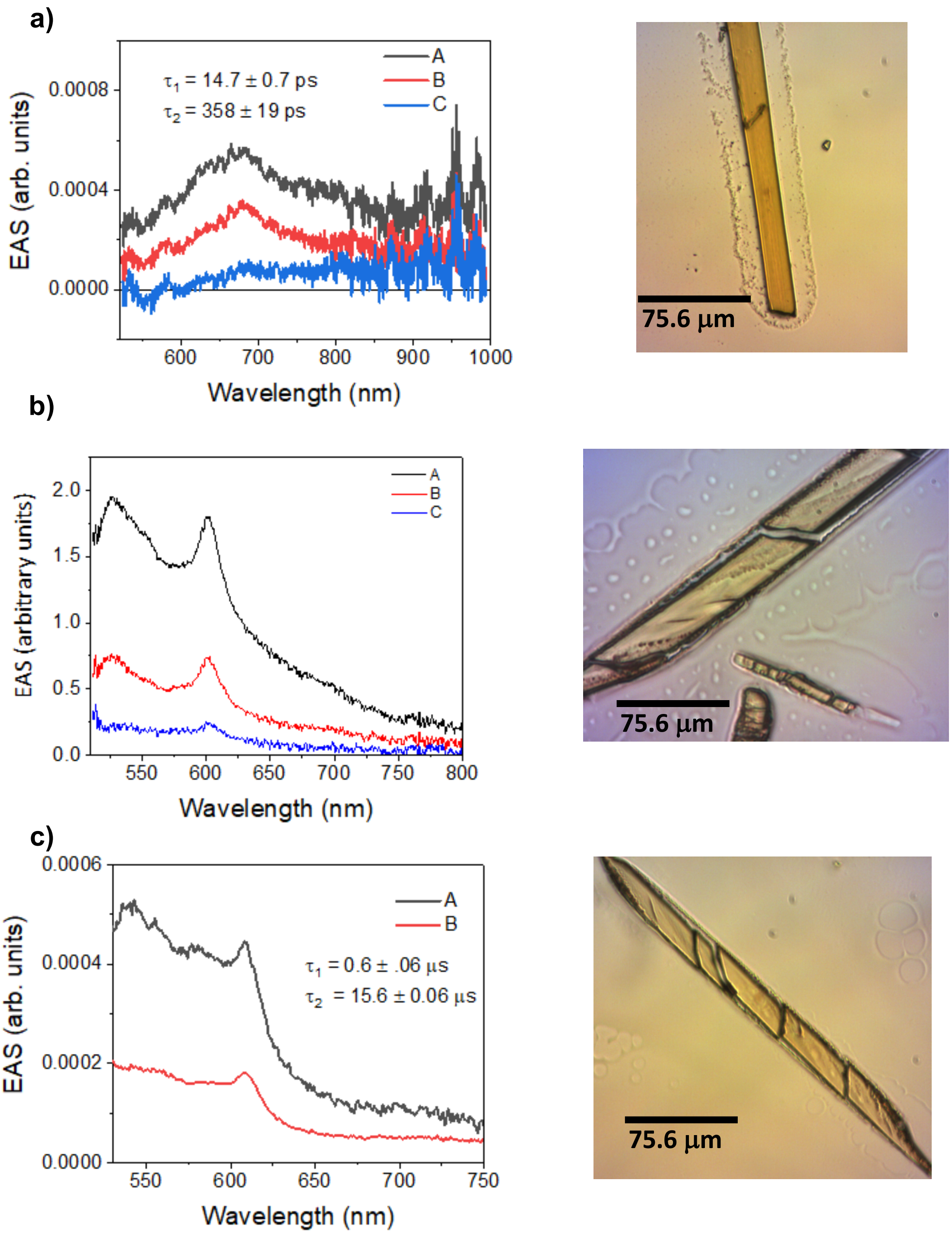

Figure 2.8 Evolution-associated spectra (ESA) extracted from (a) fsTAM data of **Per-(Ph)$_4$** (b) fsTAM data of **Per-(NDI)$_4$** crystals and (c) nsTAM data of **Per-(NDI)$_4$** single crystals with λ_{ex} = 420 nm.

2.5 Conclusion

In this paper, we report the synthesis and characterization of a four-pathway donor-acceptor system, **Per-(NDI)$_4$**, with a single extended perlyene chromophore electron donor connect to four equivalent NDI electron acceptors. Two controls, the extended perylene alone, **Per-(Ph)$_4$**, and a single acceptor analogue, **Per-NDI**, were made as well to be able to draw comparisons. In solution, transient absorption measurements reveal that the charge separation rate for **Per-(NDI)$_4$** is four fold faster than that of **Per-NDI**. This is in strak contrast with the charge recombination rates, which are very similar between the two systems. These observations can be explaied by statistical rate enhancement of the charge separation, due to the presence of four electron trasnfer pathways in **Per-(NDI)$_4$**, and lack of NDI-NDI interaction once the charge separation has occurred, resulting in unperturbed charge recombination rates from the presence of neighboring NDI units on **Per-(NDI)$_4$**. Next, a single crystal of **Per-(NDI)$_4$** was analyzed using X-ray diffraction and transient absorption microscopy spectroscopy. The measured crystal structure contains two alterating types of regions, Per-NDI ADAADA wires and NDI stacks. The transient data show very fast electron trasnfer, which can be explained by the close proximity of each perylene core to two neighboring molecules' NDI units in the Per-NDI stacks. Addtionally, the charge separated state lasts for a very long time in these crystals (~15 μs). This can be explained by the NDI stacks which lie between the Per-NDI wires. Following electron transfer from a perylene core to a neighboring NDI, the NDI$^-$ radical ion can then migrate to a neighborign NDI that resides in the NDI stacks. The anion is then free to migrate along these stacks, resulting in a long charge separated state lifetime.

2.6 Supporting Information

2.6.1 Materials, Methods, and Synthesis

Materials. All chemicals and solvents were purchased from commercial suppliers and were used without further purification.

Synthesis:

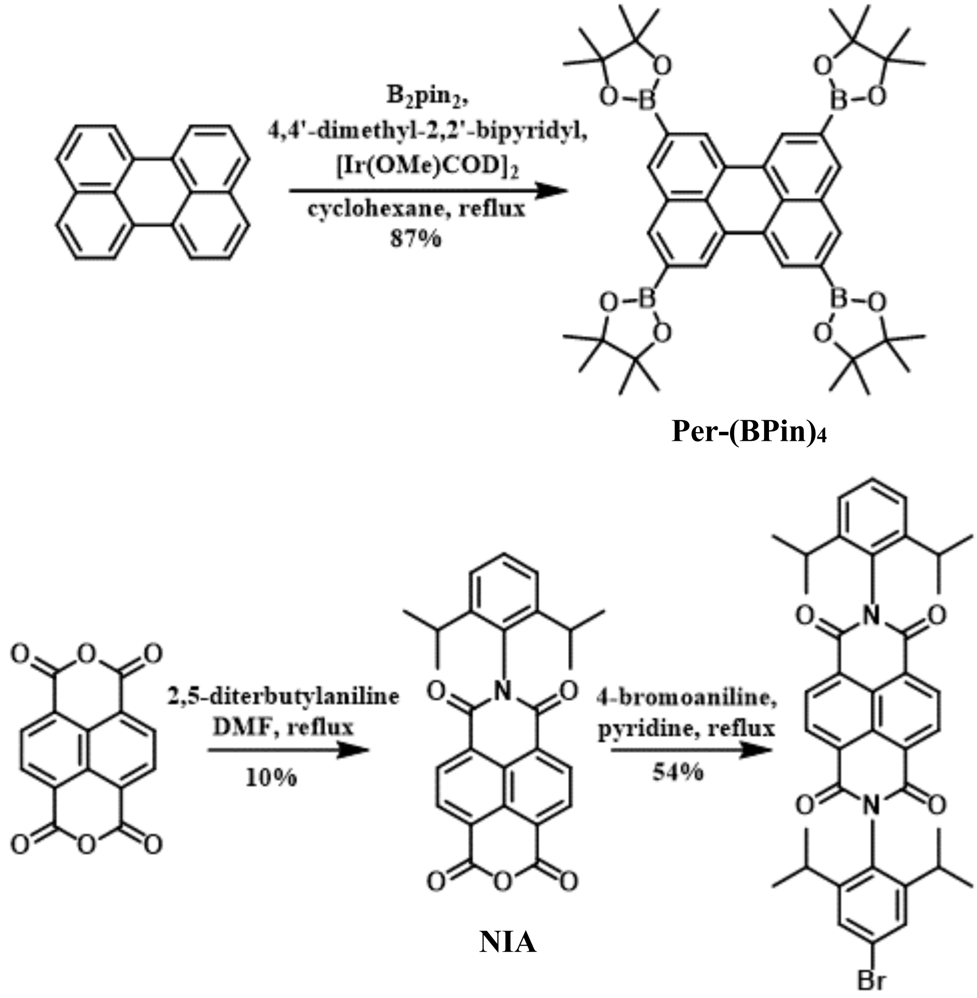

Per-(BPin)$_4$

NIA

NDI-Br

Scheme S2.2 Synthetic schemes for **Per-(BPin)$_4$**, and **NDI-Br**.

Preparation of **Per-(BPin)$_4$**

Perylene (0.5042 g, 2.0 mmol), B_2pin_2 (3.0500 g, 12 mmol), 4,4'-dimethyl-2,2'-bipyridyl (0.0802 g, 0.44 mmol), and $[Ir(OMe)COD]_2$ (0.1315 g, 0.020 mmol) were stirred under reflux in cyclohexane (20 mL) overnight. The solvent was then removed from the reaction mixture and the content was run through a silica plug in chloroform followed by chromatography on silica gel (eluent: 5% ethyl acetate in chloroform). The crude material was washed with methanol resulting in molecule **1** as a yellow powder (1.3 g, 87% yield). ^1H NMR (500 MHz, $CDCl_3$) δ 8.60 (s, 4H), 8.22 (s, 4H), 1.41 (s, 48H). ^{13}C NMR (126 MHz, $CDCl_3$) δ 141.52, 132.07 (d, J = 5.7 Hz), 130.55, 126.55, 126.25, 84.32, 24.83. MALDI (m/z) calculated = 756.4, found = 756.3.

Preparation of **NIA**

Naphthalene dianhydride (10 g, 37 mmol) was dissolved in DMF (50mL). 2,6-diisopropylaniline (3.06 g, 15 mmol) was dissolved in DMF (40mL) and added dropwise over two hours to the Naphthalene dianhydride. The reaction was stirred under reflux overnight. The product was then purified via chromatography on silica gel (eluent: DCM) (1.5190 g, 10% yield). ^1H NMR (500 MHz, $CDCl_3$) δ 8.90 – 8.83 (m, 4H), 7.50 (t, J = 7.8 Hz, 1H), 7.34 (dd, J = 7.8, 2.3 Hz, 2H), 2.66 (dhept, J = 20.5, 6.8 Hz, 2H), 1.14 (t, J = 6.3 Hz, 12H). ^{13}C NMR (126 MHz, $CDCl_3$) δ 145.47, 133.27, 131.81, 127.83, 124.34, 29.33, 23.97. MALDI (m/z) calculated = 427.1, found = 427.1.

Preparation of **NDI-Br**

NIA (0.3474 g, 0.76 mmol) and 4-bromoaniline (0.2883 g, 1.7 mmol) were stirred under reflux in pyridine (25 mL) overnight. The solvent was then removed, and the crude material was washed with methanol. The product was isolated by chromatography on silica gel (DCM) as a white solid (0.3134 g, 54% yield). ^1H NMR (500 MHz, $CDCl_3$) δ 8.87 (d, J = 0.7 Hz, 4H), 7.51 (t, J = 7.8 Hz, 1H), 7.45 (s, 2H), 7.35 (d, J = 7.8 Hz, 2H), 2.65 (dhept, J = 13.5, 6.6 Hz, 4H), 1.14 (dd, J = 6.9, 4.2 Hz, 24H). ^{13}C NMR (126 MHz, $CDCl_3$) δ 164.52, 146.12, 144.36, 133.62, 133.49, 130.97 (d, J = 5.7 Hz), 129.06 – 128.94 (m), 127.45 – 127.32 (m), 125.14, 118.63, 29.20, 28.84, 24.18, 23.43. MALDI (m/z) calculated = 664.2, found = 664.3.

Preparation of **Per-(Ph)$_4$**

Per-(BPin)$_4$ (0.5 g, 0.66 mmol), bromobenzene (1.2 g, 7.6 mmol), and $Na_2CO_{3(aq)}$ (1.5 g, 14 mmol) were dissolved in toluene (30mL) and EtOH (15mL). N_2 gas was then bubbled into the solution for 10 minutes. $Pd(PPh_3)_4$ (0.0750 g, 0.0065 mmol) was added to the reaction. The content was then stirred under reflux overnight. The reaction mixture was run through a silica plug in DCM and the product was purified by recrystallization in 1,2-dichlorobenzene as a yellow solid (0.1200 g, 32% yield). ^{1}H NMR (500 MHz, $CDCl_3$) δ 8.50 (d, J = 1.6 Hz, 4H), 7.95 (d, J = 1.4 Hz, 4H), 7.81 – 7.76 (m, 8H), 7.53 (t, J = 7.7 Hz, 8H), 7.45 – 7.41 (m, 4H). ^{13}C NMR (126 MHz, $CDCl_3$) δ 140.24, 132.02, 130.81, 129.72, 128.26, 127.71, 126.69, 122.09 (d, J = 3.8 Hz). MALDI (m/z) calculated = 556.2, found = 556.2.

Preparation of **Per-NDI**

Per-(BPin)$_4$ (0.1680 g, 0.22 mmol), bromobenzene (0.1291 g, 0.81 mmol), **NDI-Br** (0.1486 g, 0.24 mmol), and $K_2CO_{3(aq)}$ (0.3071 g, 2.2 mmol) were dissolved in toluene (9 mL) and EtOH (4.5 mL). N_2 gas was bubbled into the solution for 10 minutes and $Pd(PPh_3)_4$ (0.0200 g, 0.017 mmol) was added to the reaction. The content was stirred under reflux overnight. The product was then purified by chromatography on silica gel as a yellow powder (0.0273 g, 11% yield). ^{1}H NMR (500 MHz, $CDCl_3$) δ 8.91 (s, 2H), 8.87 (d, J = 1.1 Hz, 3H), 8.57 – 8.49 (m, 2H), 8.49 – 8.43 (m, 1H), 8.00 – 7.91 (m, 2H), 7.82 (t, J = 7.7 Hz, 5H), 7.69 (ddd, J = 16.6, 11.8, 5.4 Hz, 2H), 7.55 – 7.49 (m, 7H), 7.47 – 7.39 (m, 2H), 7.35 (t, J = 7.0 Hz, 6H), 2.69 (d, J = 6.9 Hz, 4H), 1.37 – 1.17 (m, 24H). ^{13}C NMR (126 MHz, $CDCl_3$) δ 164.62 (d, J = 5.2 Hz), 164.52, 146.12, 142.29, 140.33, 140.12, 139.72, 137.60, 134.17, 133.49, 132.05, 130.97 (d, J = 5.7 Hz), 130.83 – 130.69 (m), 130.05, 129.96, 129.88, 129.80, 129.72, 129.03 – 128.91 (m), 128.42 (d, J = 5.7 Hz), 128.33, 128.26, 127.88, 127.45 – 127.32 (m), 126.81 – 126.68 (m), 125.93, 125.65, 125.14, 122.09 (d, J = 1.9 Hz), 120.81, 29.19 (d, J = 1.4 Hz), 24.18, 23.43. MALDI (m/z) calculated =1064.5, found = 1064.5.

Preparation of **Per-(NDI)$_4$**

Per-(BPin)$_4$ (0.0613 g, 0.081 mmol), **NDI-Br** (0.2469 g, 0.40 mmol), and $Na_2CO_{3(aq)}$ (0.2000 g, 1.9 mmol) were dissolved in toluene (3.6 mL) and EtOH (1.8 mL). N_2 gas was bubbled into the solution for 10 minutes and $Pd(PPh_3)_4$ (0.0102 g, 0.0088 mmol) was added to the reaction. The content was then stirred under reflux overnight. The product was purified by chromatography on silica gel (50% hexanes in chloroform going to 5% ethyl acetate in chloroform) followed by size exclusion chromatography in DCM as a yellow powder (0.0422 g, 20% yield). ^{1}H NMR (500 MHz, $CDCl_3$) δ 8.94 – 8.87 (m, 16H), 8.71 (s, 4H), 8.16 (s, 4H), 7.85 (s, 8H), 7.51 (t, J = 7.8 Hz, 4H), 7.35 (d, J = 7.9 Hz, 8H), 2.70 (h, J = 6.8 Hz, 16H), 1.16 (d, J = 7.0 Hz, 96H). ^{13}C NMR (126 MHz, $CDCl_3$)) δ 166.58 (d, J = 3.3 Hz), 146.32, 142.49, 139.45, 135.91, 132.67, 130.78, 128.94, 127.66, 127.14, 125.07, 124.33, 124.12, 29.44, 29.33, 24.19, 23.48. MALDI (m/z) calculated =2590.2, found = 2590.2.

2.6.2 Steady State Optical Characterization (solution)

Absorption Spectra for **Per-(NDI)$_4^-$** *Anion and* **Per-(Ph)$_4^+$** *Cation*

To obtain the absorption spectrum of the reduced **Per-(NDI)$_4$**, cobaltocene was added to a solution of **Per-(NDI)$_4$** in 1,4-dioxane (Figure S2.9a). To obtain the absorption spectrum of the oxidized

Per-(Ph)₄, tris (4-bromophenyl)ammoniumyl hexachloroantimonate was added to a solution of **Per-(Ph)₄** in 1,4-dioxane (Figure S2.91b).

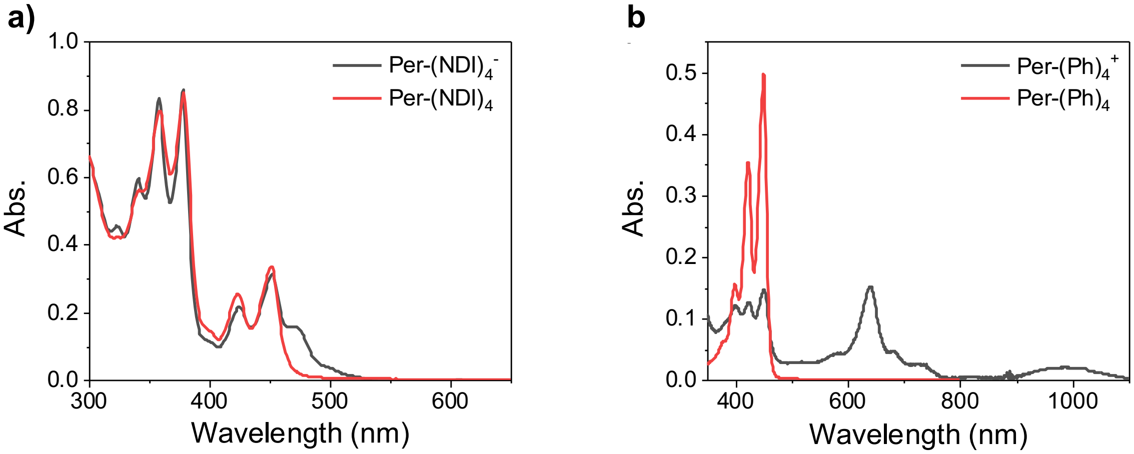

Figure S2.9 Absorption spectra for (a) **Per-(NDI)$_4^-$** and (b) **Per-(Ph)$_4^+$**.

2.6.3 Electrochemical Analysis

Cyclic Voltammetry

Electrochemical measurements were performed on a CH Instrument 750E electrochemical workstation. Measurements were made using a 1.0 mm diameter glassy carbon working electrode, a platinum wire auxiliary electrode, and a silver wire reference electrode in 0.1 M solutions of n-butylammonium hexafluorophosphate ($TBAPF_6$) in acetonitrile purged with argon. Ferrocene was used as an internal standard.

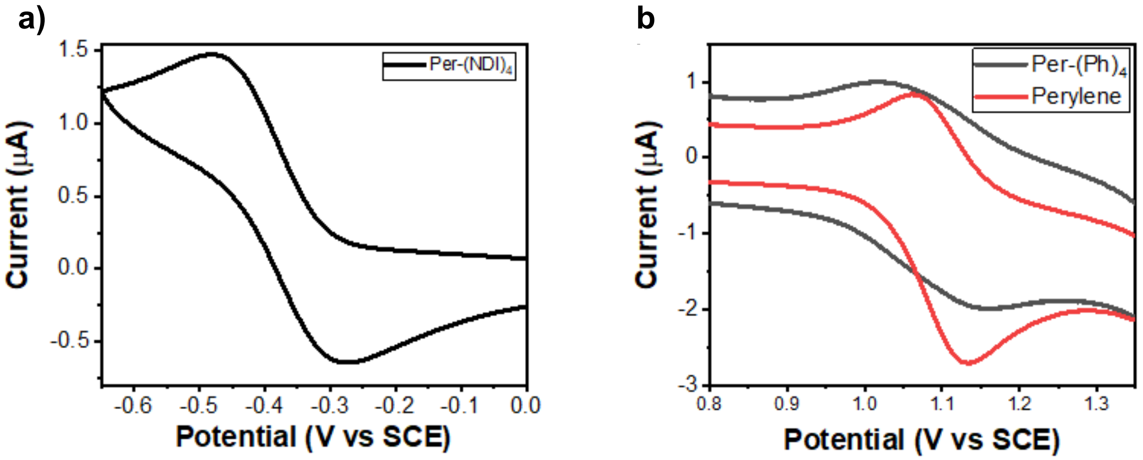

Figure S2.10 Cyclic Voltammetry (CV) spectra for (a) **Per-(NDI)$_4$** and (b) **Per-(Ph)$_4$**.

Weller Equation Analysis

The Weller equation[85] was applied to these data to correct for the different dielectric constants between acetonitrile, the solvent electrochemical potentials were measured in, and THF and toluene, the solvents transient experiments were performed in, as follows:

$$\Delta G = E_{ox} - E_{red} - \left(\frac{e^2}{r_{DA}\varepsilon_s}\right) + (e^2\left(\frac{1}{2r_D} + \frac{1}{2r_A}\right)\left(\frac{1}{\varepsilon_s} - \frac{1}{\varepsilon_{sp}}\right) \qquad \text{(Eqn. S2.1)}$$

where E_{ox} and E_{red} are the oxidation and reduction potentials of the donor and acceptor, respectively, in the solvent electrochemical measurements were taken with a static dielectric constant ε_{sp}, e is the charge of an electron, r_{DA} is the ion pair distance, r_D and r_A are the ionic radii (both calculated from the structures given by DFT calculations), and ε_s is the static dielectric constant of the solvent we are comparing against.

2.6.4 Fitting Methodology for TA and TAM Data

Data Processing for TA Data

Prior to kinetic analysis, the TA data were scatter-subtracted and chirp-corrected using Surface Xplorer 4 (Ultrafast Systems, LLC).

Kinetic Fitting Methodology

All kinetic analysis was performed using home written programs in MATLAB and was based on a global fit to selected single-wavelength kinetics. An assumption of a uniform instrument response of $w = 300$ fs for fsTA (full width at half maximum, FWHM) across the frequency domain and a fixed time-zero (t_0) is implicit in the global analysis. Kinetic data from the entire 320-850 nm window were fitted using the global analysis described below. The population dynamics in toluene and THF overlap with the non-resonant solvent response, which was modeled as the decay of a separate population with a fixed decay rate smaller than the instrument response. Each specified wavelength was given an initial amplitude that is representative of the spectral intensity at time t_0. The rate constants and t_0 were shared among the various kinetic data and varied globally across the kinetic data to fit to the models described below. Datasets were globally fit to a specified kinetic model and the resultant populations were used to deconvolute the dataset and reconstruct the evolution-associated spectra. Below are the first-order kinetic models of each system with rate matrix K and initial species population vector P:

5. fsTA of **Per-(Ph)$_4$**:

$$K = \begin{pmatrix} -k_{A\to B} & 0 \\ k_{A\to B} & -k_{B\to GS} \end{pmatrix} \quad P = \begin{pmatrix} 1 \\ 0 \end{pmatrix}$$

(Eqn. S2.2)

6. nsTA of **Per-(Ph)$_4$**:

$$K = \begin{pmatrix} -k_{A\to B} & 0 \\ k_{A\to B} & -k_{B\to GS} \end{pmatrix} \quad P = \begin{pmatrix} 1 \\ 0 \end{pmatrix}$$

(Eqn. S2.3)

7. fsTA of **Per-NDI**:

$$K = \begin{pmatrix} -1/0.1 & 0 & 0 & 0 \\ 0 & -k_{A\to B} & 0 & 0 \\ 0 & k_{A\to B} & -k_{B\to C} & 0 \\ 0 & 0 & k_{B\to C} & -k_{C\to GS} \end{pmatrix} \quad P = \begin{pmatrix} 1 \\ 1 \\ 0 \\ 0 \end{pmatrix}$$

(Eqn. S2.4)

8. nsTA of **Per-NDI**:

$$K = \begin{pmatrix} -k_{A\to B} & 0 \\ k_{A\to B} & -k_{B\to GS} \end{pmatrix} \quad P = \begin{pmatrix} 1 \\ 0 \end{pmatrix}$$

(Eqn. S2.5)

9. fsTA of **Per-(NDI)$_4$**:

$$K = \begin{pmatrix} -1/0.1 & 0 & 0 & 0 \\ 0 & -k_{A\to B} & 0 & 0 \\ 0 & k_{A\to B} & -k_{B\to C} & 0 \\ 0 & 0 & k_{B\to C} & -k_{C\to GS} \end{pmatrix} \quad P = \begin{pmatrix} 1 \\ 1 \\ 0 \\ 0 \end{pmatrix}$$

(Eqn. S2.6)

10. nsTA of **Per-(NDI)$_4$**:

$$K = \begin{pmatrix} -k_{A\to B} & 0 \\ k_{A\to B} & -k_{B\to GS} \end{pmatrix} \quad P = \begin{pmatrix} 1 \\ 0 \end{pmatrix} \qquad \text{(Eqn. S2.7)}$$

11. fsTAM of **Per-(Ph)₄**:

$$K = \begin{pmatrix} -1/0.01 & 0 & 0 & 0 \\ 0 & -k_{A\to B} & 0 & 0 \\ 0 & k_{A\to B} & -k_{B\to C} & 0 \\ 0 & 0 & k_{B\to C} & -k_{C\to GS} \end{pmatrix} \quad P = \begin{pmatrix} 1 \\ 1 \\ 0 \\ 0 \end{pmatrix} \qquad \text{(Eqn. S2.8)}$$

12. fsTAM of **Per-(NDI)₄**:

$$K = \begin{pmatrix} -1/0.01 & 0 & 0 & 0 \\ 0 & -k_{A\to B} & 0 & 0 \\ 0 & k_{A\to B} & -k_{B\to C} & 0 \\ 0 & 0 & k_{B\to C} & -k_{C\to GS} \end{pmatrix} \quad P = \begin{pmatrix} 1 \\ 1 \\ 0 \\ 0 \end{pmatrix} \qquad \text{(Eqn. S2.9)}$$

13. nsTAM of **Per-(NDI)₄**:

$$K = \begin{pmatrix} -k_{A\to B} & 0 \\ k_{A\to B} & -k_{B\to GS} \end{pmatrix} \quad P = \begin{pmatrix} 1 \\ 0 \end{pmatrix} \qquad \text{(Eqn. S2.10)}$$

The MATLAB program numerically solved the differential equations through matrix methods and then convoluted the solutions with a fixed Gaussian instrument response function with width *w* = 0.3 ps (FWHM) before utilizing a least-squares fitting using a Levenberg-Marquardt method to find the parameters that result in matches to the kinetic data. Uncertainties in reported time constants were taken as the standard deviation of the fits from multiple replicates unless stated otherwise.

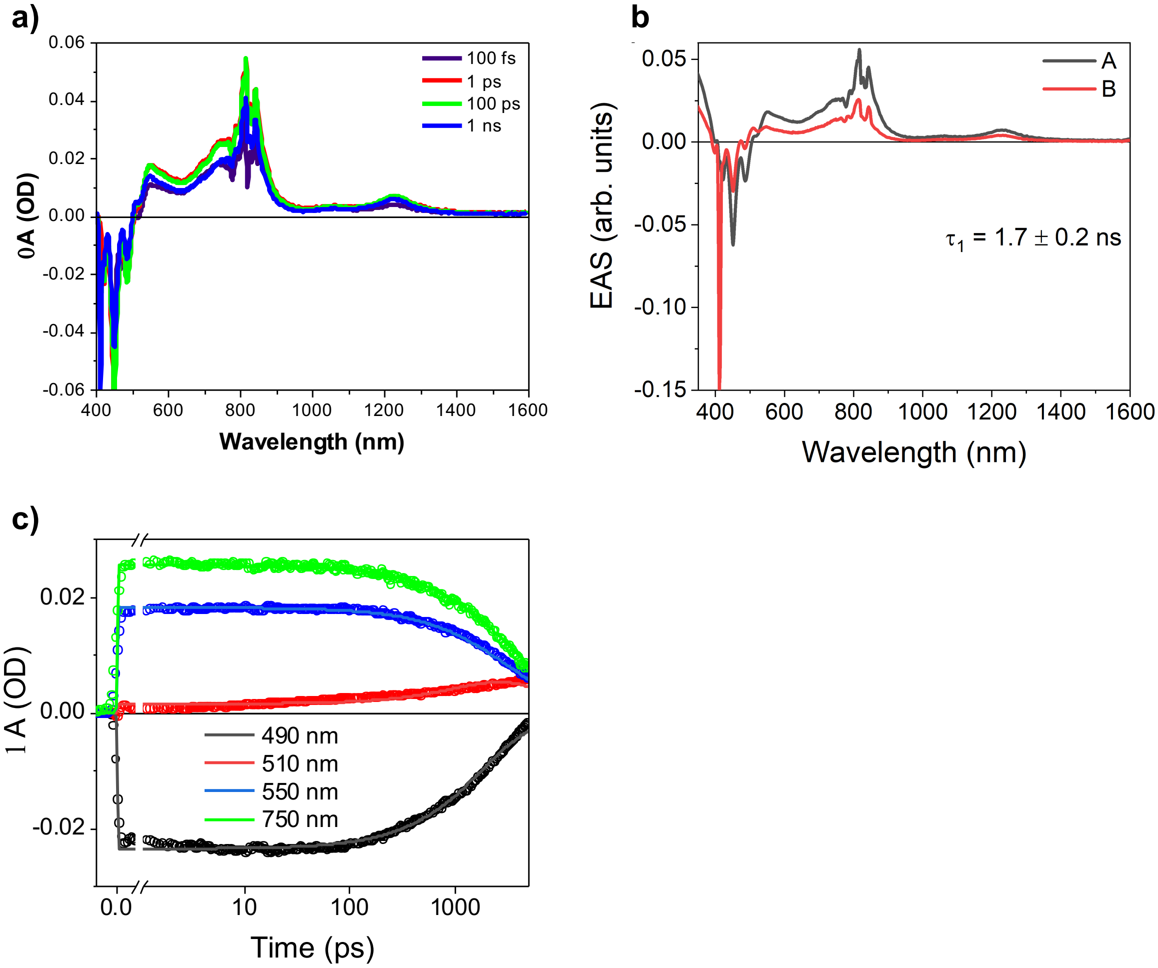

Figure S2.11 Kinetic analysis of fsTA data for **Per-(Ph)$_4$** with (a) data at selected time delays, (b) evolution associated spectra, and (c) traces of wavelength fits.

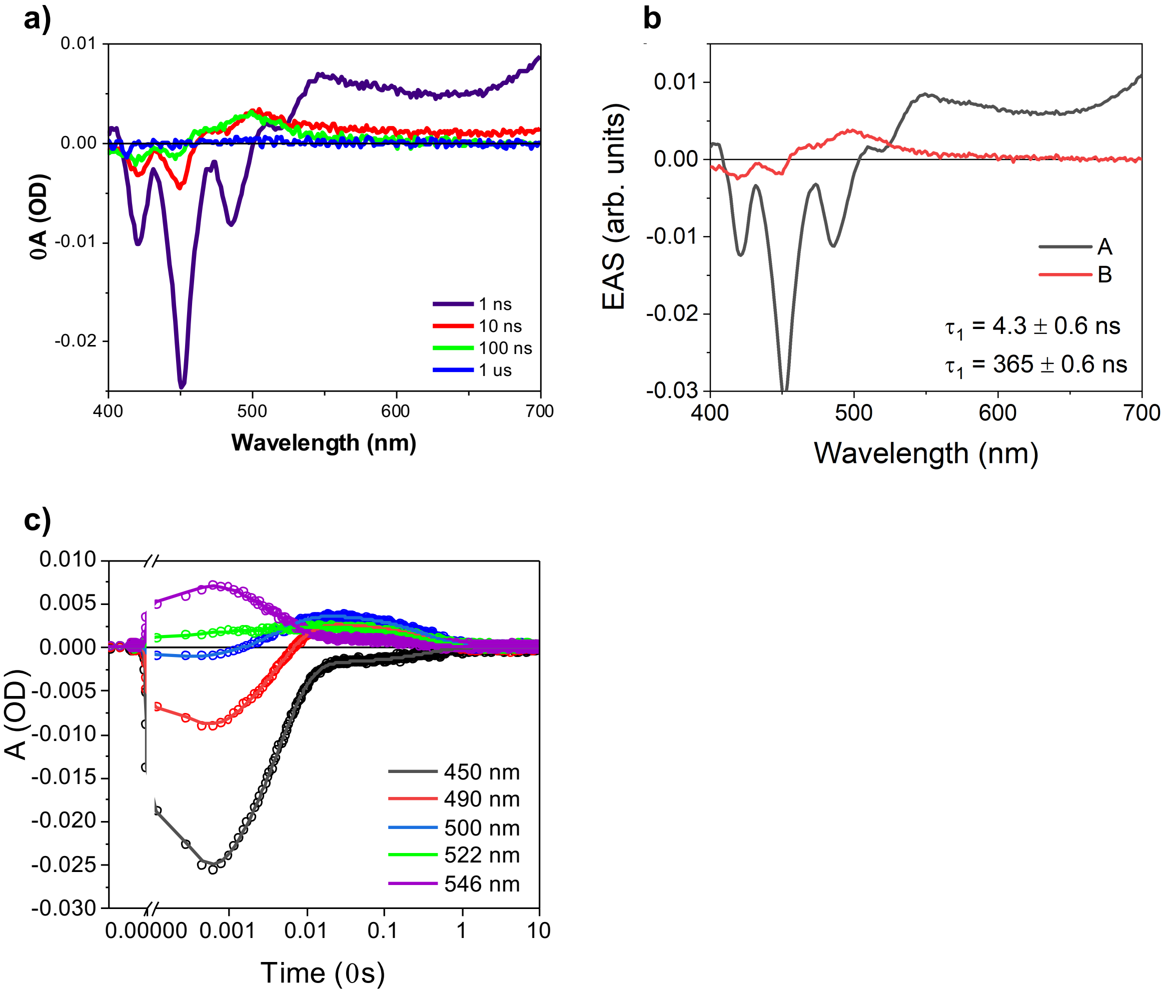

Figure S2.12 Kinetic analysis of nsTA data for **Per-(Ph)$_4$** with (a) data at selected time delays, (b) evolution associated spectra, and (c) traces of wavelength fits.

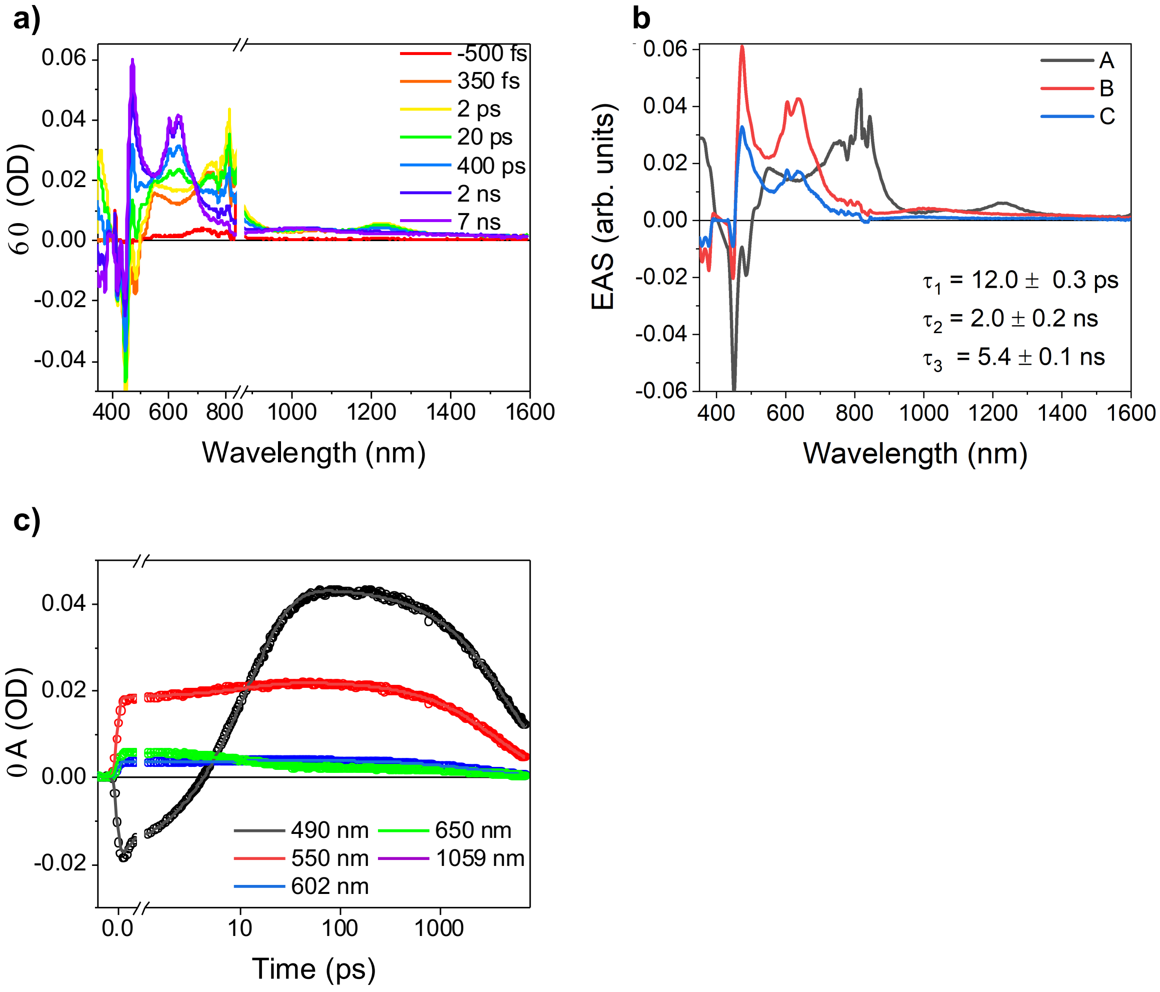

Figure S2.13 Kinetic analysis of fsTA data for **Per-NDI** with (a) data at selected time delays, (b) evolution associated spectra, and (c) traces of wavelength fits.

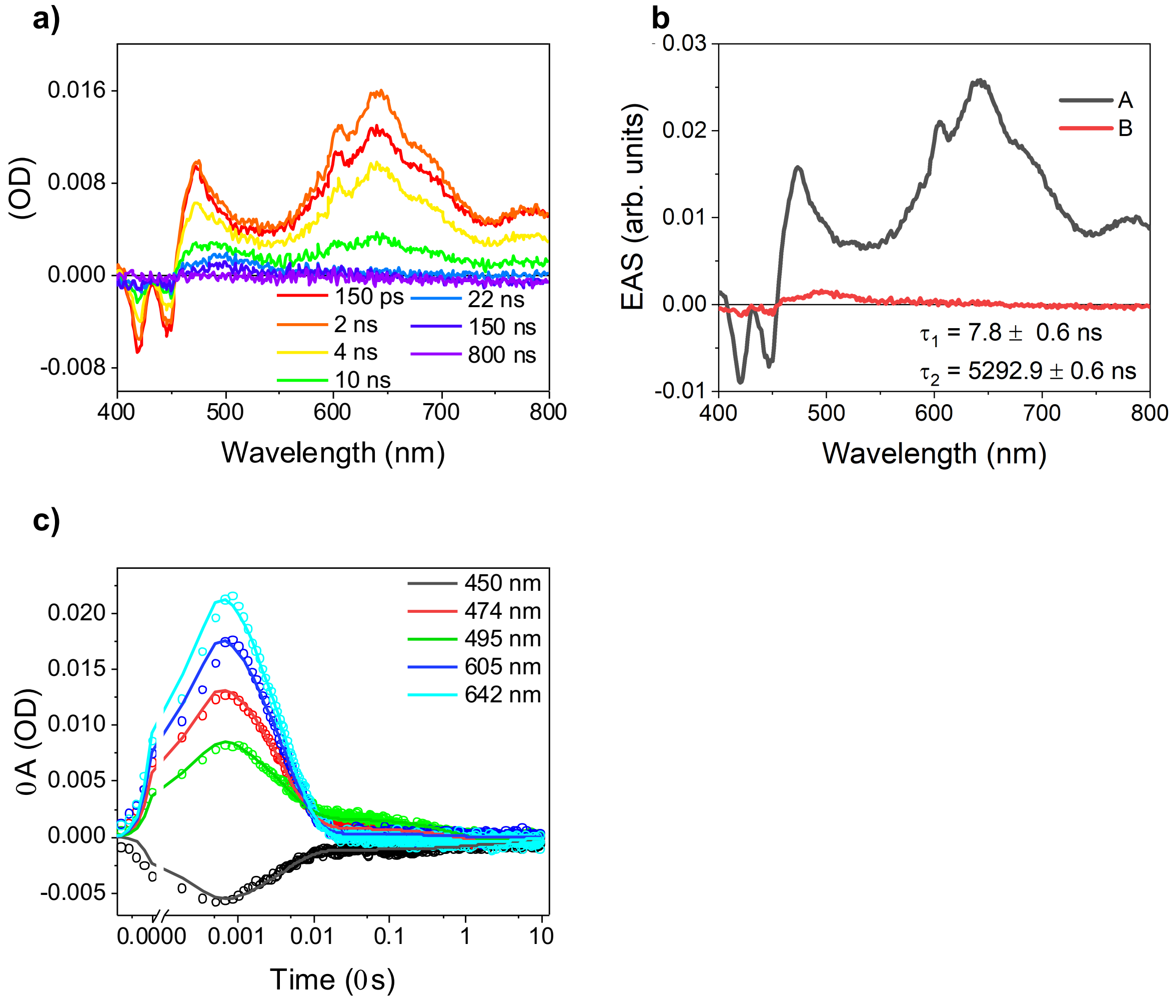

Figure S2.14. Kinetic analysis of nsTA data for **Per-NDI** with (a) data at selected time delays, (b) evolution associated spectra, and (c) traces of wavelength fits.

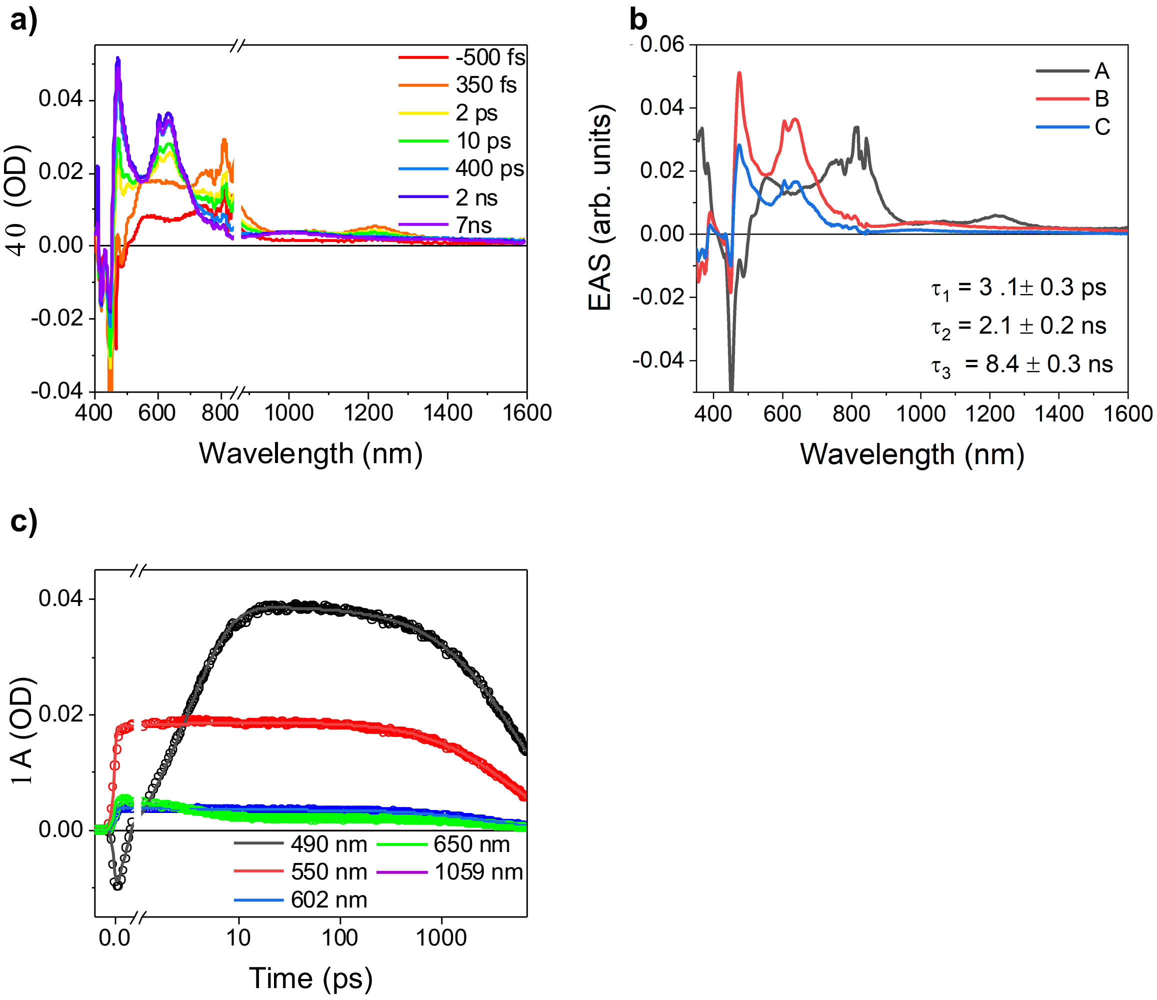

Figure S2.15 Kinetic analysis of fsTA data for **Per-(NDI)₄** with (a) data at selected time delays, (b) evolution associated spectra, and (c) traces of wavelength fits.

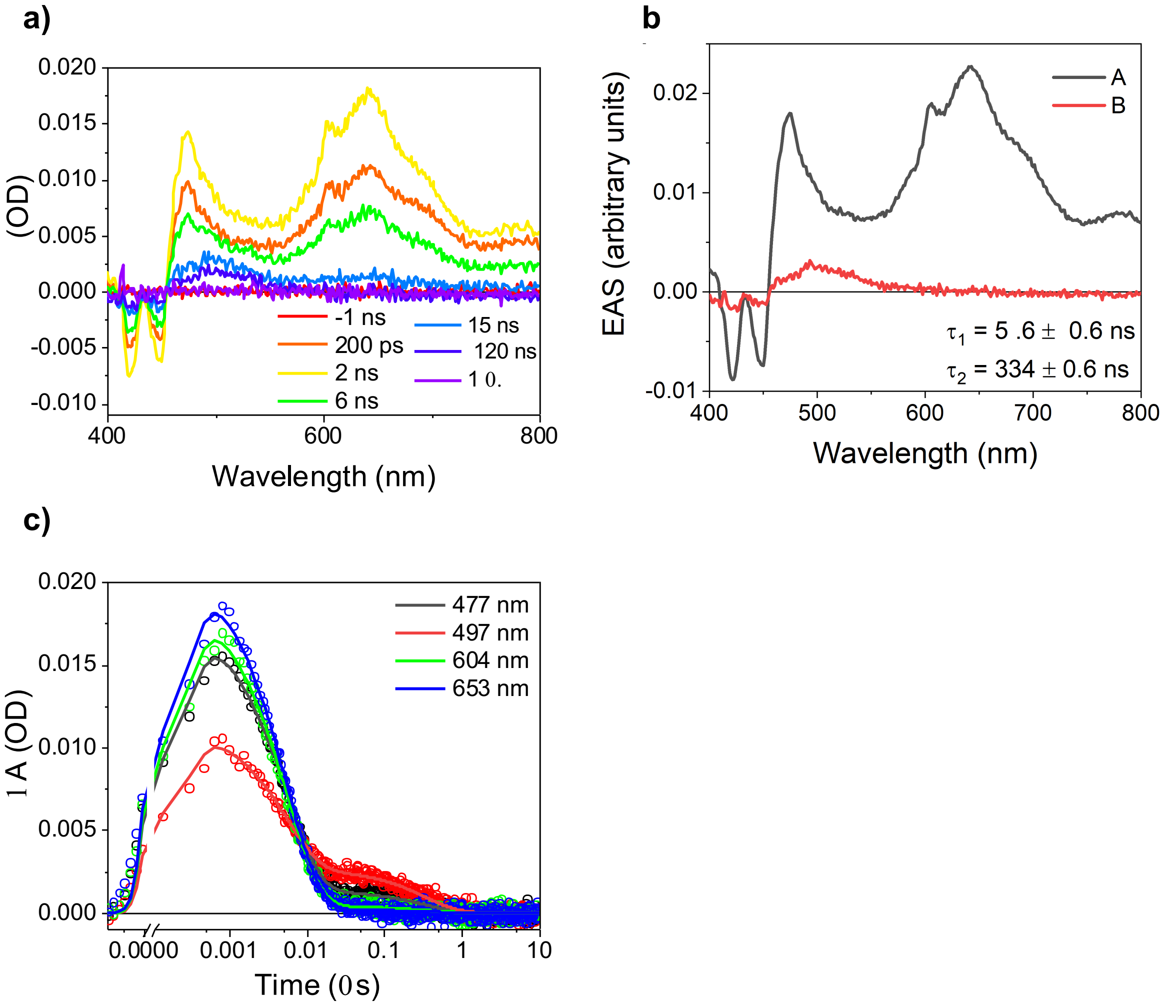

Figure S2.16 Kinetic analysis of nsTA data for **(Per-NDI)₄** with (a) data at selected time delays, (b) evolution associated spectra, and (c) traces of wavelength fits.

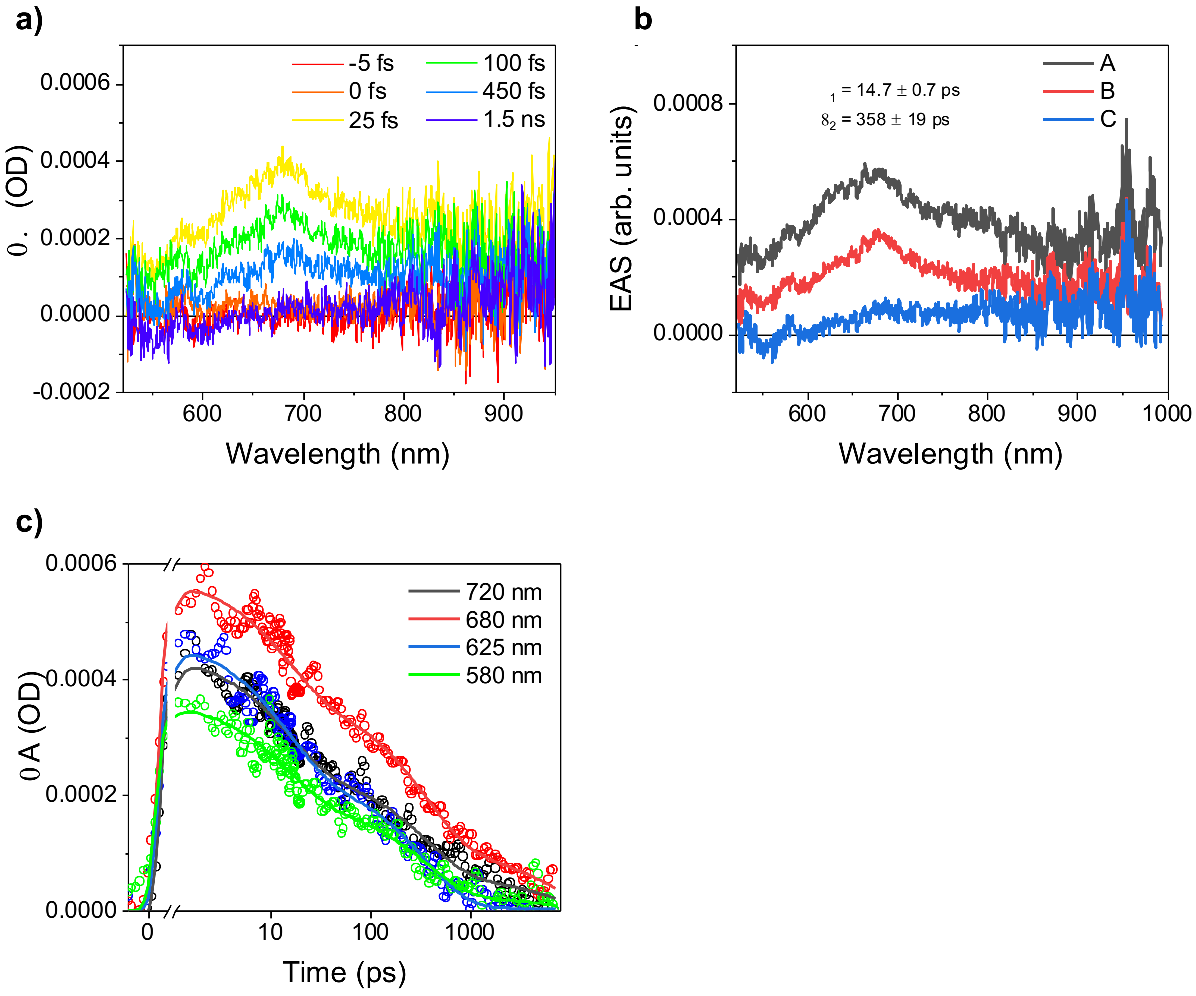

Figure S2.17 Kinetic analysis of fsTAM data for **Per-(Ph)$_4$** with (a) data at selected time delays, (b) evolution associated spectra, and (c) traces of wavelength fits.

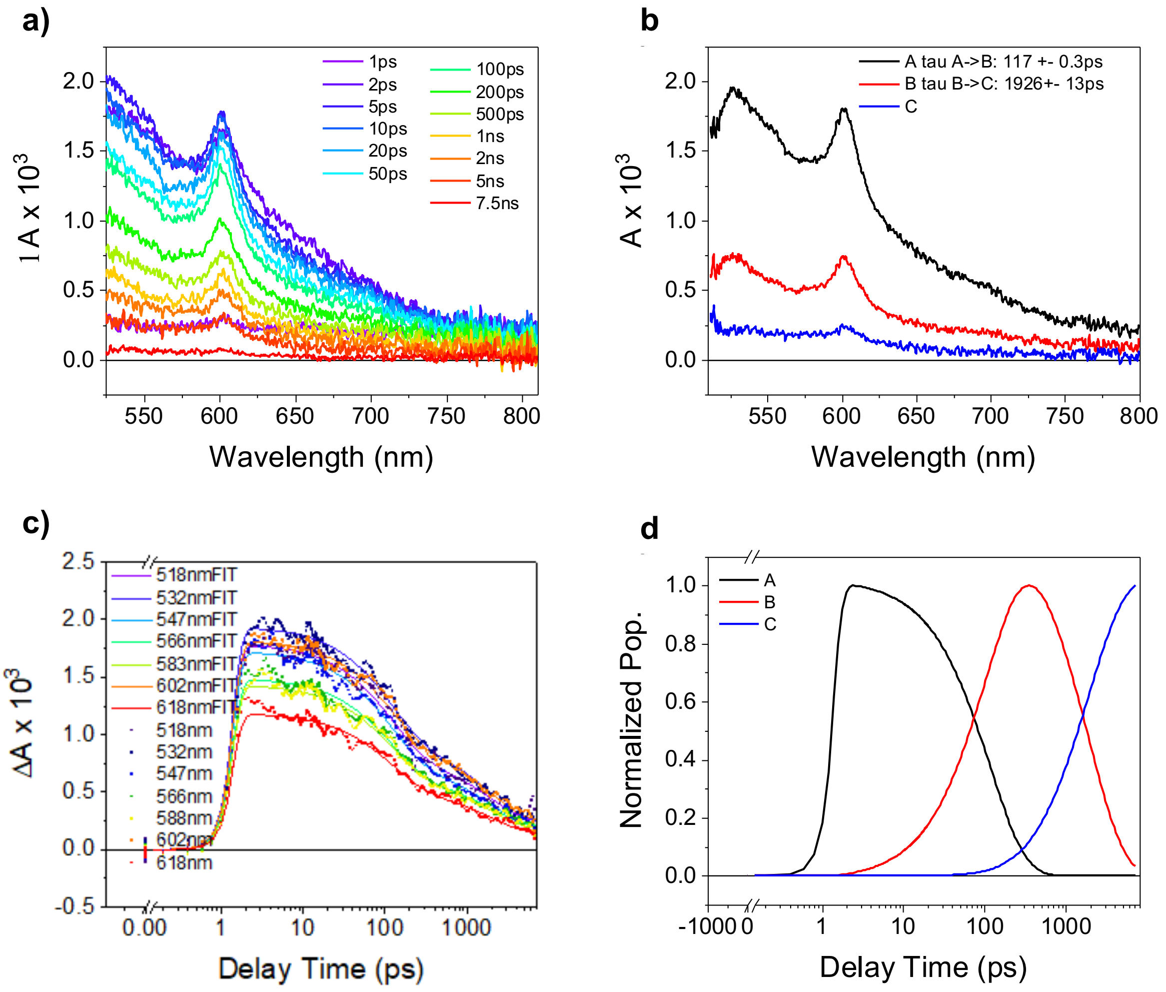

Figure S2.18. Kinetic analysis of fsTAM data for **Per-(NDI)$_4$** with (a) data at selected time delays, (b) evolution associated spectra, (c) traces of wavelength fits, and (d) population dynamics.

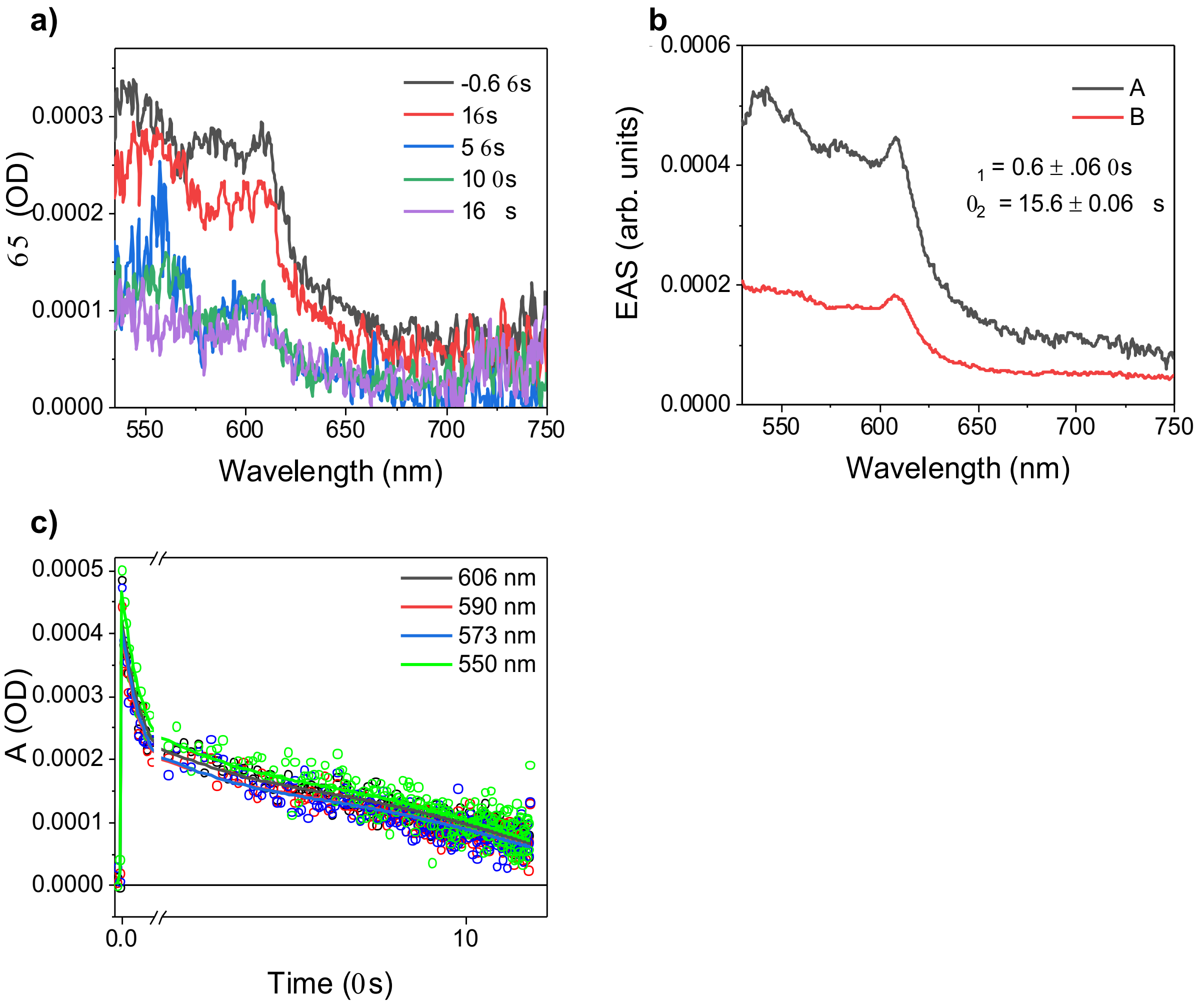

Figure S2.19 Kinetic analysis of nsTAM data for **Per-(NDI)$_4$** with (a) data at selected time delays, (b) evolution associated spectra, and (c) traces of wavelength fits.

2.6.5 Solid State Data

Crystal Structure for **Per-(Ph)$_4$**

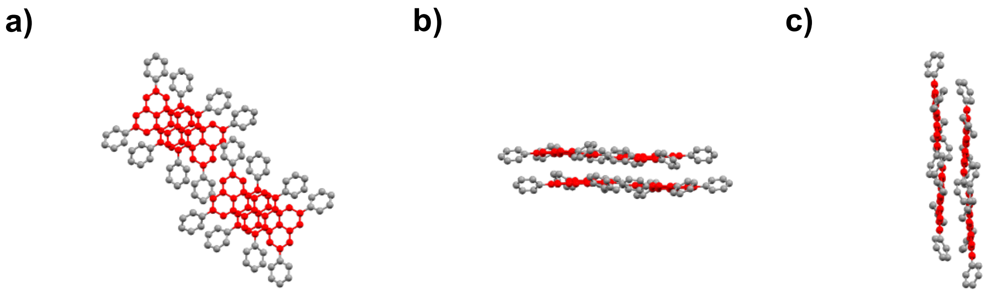

Figure S2.20 Crystal structures from XRD of **Per-(Ph)$_4$** along the a) a-axis, b) b-axis, and c) c-axis of its unit cell with the perylene core highlighted in red and the phenyl extensions highlighted in grey.

Table 1 Crystal data and structure refinement for **Per-(Ph)$_4$.**	
Identification code	Per-4Ph
Empirical formula	$C_{44}H_{28}$
Formula weight	556.66
Temperature/K	100.0
Crystal system	triclinic
Space group	P-1
a/Å	7.040(3)
b/Å	20.011(7)
c/Å	20.011(7)
α/°	94.68
β/°	90
γ/°	90
Volume/Å^3	2809.6(17)
Z	4

ρ_{calc}g/cm^3	1.316
μ/mm^{-1}	0.566
F(000)	1168.0
Crystal size/mm^3	0.165 × 0.099 × 0.057
Radiation	CuKα (λ = 1.54178)
2Θ range for data collection/°	4.43 to 119.896
Index ranges	$-7 \leq h \leq 7$, $-17 \leq k \leq 22$, $-21 \leq l \leq 15$
Reflections collected	9651
Independent reflections	6982 [R_{int} = 0.1232, R_{sigma} = 0.2951]
Data/restraints/parameters	6982/0/793
Goodness-of-fit on F^2	0.901
Final R indexes [I>=2σ (I)]	R_1 = 0.0956, wR_2 = 0.2283
Final R indexes [all data]	R_1 = 0.2984, wR_2 = 0.3422
Largest diff. peak/hole / e Å^{-3}	0.32/-0.42

Table 2 Crystal data and structure refinement for **Per-(NDI)$_4$.**	
Identification code	1034-Xyl_EtOH-1_auto
Empirical formula	C148H108N8O16
Formula weight	2254.42
Temperature/K	225.00(10)
Crystal system	monoclinic

Space group	P21/c
a/Å	18.6879(9)
b/Å	41.4176(13)
c/Å	14.0750(7)
α/°	90
β/°	111.449(6)
γ/°	90
Volume/Å3	10139.7(9)
Z	7
ρcalcg/cm3	2.584
μ/mm-1	1.355
F(000)	8260.0
Crystal size/mm3	0.28 × 0.146 × 0.072
Radiation	Cu Kα (λ = 1.54184)
2Θ range for data collection/°	7.986 to 102.926
Index ranges	-10 ≤ h ≤ 18, -41 ≤ k ≤ 39, -14 ≤ l ≤ 8
Reflections collected	21078
Independent reflections	9756 [Rint = 0.0234, Rsigma = 0.0357]
Data/restraints/parameters	9756/1043/1042
Goodness-of-fit on F2	1.223
Final R indexes [I>=2σ (I)]	R1 = 0.0896, wR2 = 0.2868
Final R indexes [all data]	R1 = 0.1122, wR2 = 0.3100

Largest diff. peak/hole / e Å-3	0.53/-0.33

Absorption Spectra for Ion Films

The film of **Per-(Ph)$_4$**$^+$ was prepared by adding ‘magic blue’ to a solution of **Per-(Ph)** in Dichloromethane (DCM) and then drop casting the solution onto a glass slide. The film of **Per-(NDI)$_4$**$^-$ was prepared by adding cobaltocene to **Per-(NDI)$_4$** in DCM in the glovebox. The solution was then drop casted onto a glass slide in the glovebox.

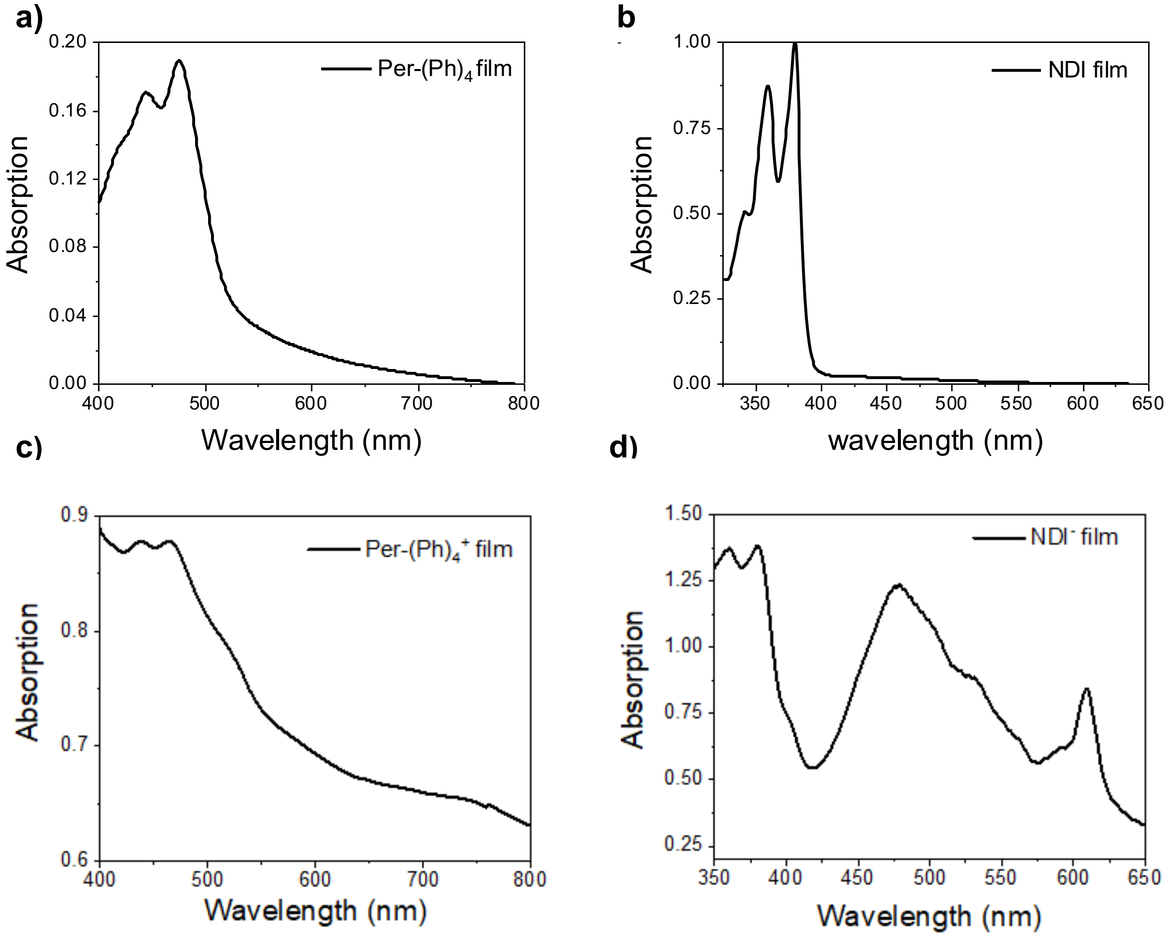

Figure S2.21. Absorption spectra of (a) neutral **Per-(Ph)$_4$** film, (b) neutral **NDI** film, (c) **Per-(Ph)$_4$**$^+$ film, and (d) **NDI**$^-$ film. Both films were prepared via drop casting onto a glass slide following chemical oxidation or reduction when applicable.

2.6.6 DFT Calculations

Optimized geometry for **Per-(Ph)$_4$**

C	1.23020	-3.56665	0.00782
C	0.00004	-2.86495	0.00001
C	0.00002	-1.43328	0.00001
C	1.25105	-0.73850	0.00697
C	2.42522	-1.48027	0.01745
C	2.44050	-2.89619	0.01914
C	-1.23011	-3.56668	-0.00781
C	-2.44043	-2.89626	-0.01913
C	-2.42518	-1.48034	-0.01744
C	-1.25103	-0.73853	-0.00695
C	-1.25105	0.73850	0.00697
C	-0.00002	1.43328	0.00001
C	1.25102	0.73853	-0.00695
C	-0.00004	2.86495	0.00001
C	1.23011	3.56668	-0.00781
C	2.44043	2.89626	-0.01913
C	2.42518	1.48034	-0.01744
C	-2.42522	1.48027	0.01745
C	-2.44050	2.89619	0.01914
C	-1.23020	3.56665	0.00782
C	3.73118	-3.63177	0.03655
C	-3.73109	-3.63186	-0.03655
C	-3.73118	3.63177	0.03655
C	3.73109	3.63186	-0.03655
C	3.90086	-4.80876	-0.71169
C	5.10853	-5.50457	-0.68851
C	6.17467	-5.03697	0.08226
C	6.02171	-3.86757	0.82920
C	4.81340	-3.17265	0.80626
C	-3.90077	-4.80885	0.71168
C	-5.10842	-5.50466	0.68849
C	-6.17457	-5.03707	-0.08228
C	-6.02162	-3.86767	-0.82922
C	-4.81331	-3.17274	-0.80626
C	-4.81340	3.17265	0.80626
C	-6.02172	3.86757	0.82920
C	-6.17467	5.03697	0.08226
C	-5.10852	5.50457	-0.68850
C	-3.90086	4.80876	-0.71168
C	4.81331	3.17274	-0.80626

C	6.02162	3.86767	-0.82922
C	6.17457	5.03707	-0.08228
C	5.10842	5.50466	0.68849
C	3.90077	4.80885	0.71168
H	1.20684	-4.65287	0.03523
H	3.38341	-0.97500	-0.00523
H	-1.20672	-4.65290	-0.03523
H	-3.38339	-0.97509	0.00525
H	1.20672	4.65290	-0.03523
H	3.38338	0.97509	0.00524
H	-3.38341	0.97500	-0.00523
H	-1.20684	4.65287	0.03523
H	3.08505	-5.16464	-1.33489
H	5.21986	-6.40857	-1.28166
H	7.11664	-5.57846	0.09979
H	6.84235	-3.49890	1.43918
H	4.69672	-2.27907	1.41342
H	-3.08495	-5.16472	1.33489
H	-5.21976	-6.40867	1.28164
H	-7.11653	-5.57857	-0.09981
H	-6.84225	-3.49901	-1.43919
H	-4.69664	-2.27915	-1.41342
H	-4.69672	2.27907	1.41341
H	-6.84235	3.49890	1.43917
H	-7.11664	5.57846	0.09978
H	-5.21986	6.40857	-1.28165
H	-3.08505	5.16464	-1.33489
H	4.69664	2.27915	-1.41342
H	6.84225	3.49901	-1.43919
H	7.11653	5.57857	-0.09981
H	5.21976	6.40867	1.28164
H	3.08495	5.16472	1.33489

Optimized geometry for **Per-NDI**

C	*4.39164*	*0.16509*	*0.17290*
C	*5.19461*	*1.40450*	*0.17793*
C	*6.61480*	*1.31098*	*0.03550*
C	*7.28165*	*0.05017*	*-0.07833*
C	*6.48564*	*-1.19178*	*0.00410*
C	*5.06262*	*-1.09787*	*0.12011*
C	*4.61949*	*2.66041*	*0.32207*
C	*5.37621*	*3.85758*	*0.30986*

C	*6.74720*	*3.76704*	*0.14481*
C	*7.39148*	*2.51325*	*0.00976*
C	*8.79443*	*2.43766*	*-0.16719*
C	*9.43795*	*1.22043*	*-0.30488*
C	*8.65912*	*0.03845*	*-0.25284*
C	*7.07001*	*-2.45149*	*-0.02515*
C	*6.31756*	*-3.64946*	*0.04199*
C	*4.94028*	*-3.55721*	*0.13823*
C	*4.28801*	*-2.30093*	*0.17771*
C	*2.87525*	*-2.22261*	*0.24879*
C	*2.22592*	*-1.00138*	*0.25428*
C	*3.00435*	*0.18079*	*0.22072*
C	*4.70352*	*5.17291*	*0.46584*
C	*0.74395*	*-0.91263*	*0.27999*
C	*7.00059*	*-4.96824*	*0.00508*
C	*11.47210*	*0.18419*	*-1.36143*
C	*11.77312*	*2.02631*	*0.16488*
C	*13.15234*	*1.95845*	*-0.02452*
C	*13.69787*	*1.00167*	*-0.88262*
C	*12.85159*	*0.11464*	*-1.55021*
C	*8.10411*	*-5.18843*	*-0.83604*
C	*8.74051*	*-6.42830*	*-0.87327*
C	*8.28782*	*-7.47518*	*-0.06832*
C	*7.19287*	*-7.27085*	*0.77332*
C	*6.55740*	*-6.03086*	*0.81034*
C	*0.06996*	*0.01550*	*-0.53026*
C	*-1.31850*	*0.09873*	*-0.52474*
C	*-2.06041*	*-0.74069*	*0.30514*
C	*-1.41322*	*-1.66584*	*1.12243*
C	*-0.02338*	*-1.75137*	*1.10402*
C	*3.45898*	*5.42405*	*-0.13569*
C	*2.83211*	*6.66131*	*0.00468*
C	*3.43594*	*7.67487*	*0.75076*
C	*4.67190*	*7.43963*	*1.35584*
C	*5.29777*	*6.20197*	*1.21549*
N	*-3.50403*	*-0.64390*	*0.30760*
C	*-4.23296*	*-1.73787*	*-0.21251*
C	*-4.07327*	*0.54994*	*0.80765*
C	*-5.55486*	*0.65951*	*0.73996*
C	*-6.32568*	*-0.40127*	*0.20734*
C	*-5.71255*	*-1.58937*	*-0.25750*
C	*-7.73946*	*-0.27018*	*0.13620*
C	*-8.35184*	*0.91930*	*0.59926*
C	*-7.57678*	*1.94216*	*1.12214*

C	*-6.17724*	*1.81218*	*1.19274*
C	*-8.51048*	*-1.33105*	*-0.39720*
C	*-7.88859*	*-2.48748*	*-0.84023*
C	*-6.48873*	*-2.61657*	*-0.77081*
C	*-9.82954*	*1.07926*	*0.52262*
N	*-10.54948*	*0.00921*	*-0.04842*
C	*-9.99061*	*-1.20699*	*-0.49041*
C	*-11.98622*	*0.17126*	*-0.18106*
C	*-12.84419*	*-0.32867*	*0.80801*
C	*-14.21494*	*-0.13671*	*0.60840*
C	*-14.70671*	*0.52414*	*-0.51653*
C	*-13.84159*	*1.02595*	*-1.49401*
C	*-12.32364*	*-1.04947*	*2.02657*
C	*-14.36039*	*1.77404*	*-2.69946*
O	*-10.39965*	*2.07896*	*0.92438*
O	*-10.69478*	*-2.10186*	*-0.92644*
O	*-3.66780*	*-2.74273*	*-0.60725*
O	*-3.37530*	*1.44056*	*1.26000*
H	*13.80307*	*2.64775*	*0.50725*
H	*13.26528*	*-0.62835*	*-2.22711*
H	*8.44769*	*-4.38813*	*-1.48577*
H	*9.58704*	*-6.57843*	*-1.53826*
H	*5.72389*	*-5.87304*	*1.48915*
H	*6.83785*	*-8.07614*	*1.41123*
H	*0.47523*	*-2.46144*	*1.75735*
H	*-1.99335*	*-2.31475*	*1.77035*
H	*-1.82637*	*0.81347*	*-1.16424*
H	*0.63837*	*0.65980*	*-1.19452*
H	*2.99101*	*4.65114*	*-0.73921*
H	*1.87320*	*6.83601*	*-0.47631*
H	*5.14656*	*8.21826*	*1.94727*
H	*6.24653*	*6.01785*	*1.71199*
H	*-8.50229*	*-3.28568*	*-1.24410*
H	*-5.99425*	*-3.51663*	*-1.12028*
H	*-8.07138*	*2.84243*	*1.47094*
H	*-5.56333*	*2.60973*	*1.59747*
H	*-14.91143*	*-0.51681*	*1.35183*
H	*-11.60288*	*-0.43664*	*2.58102*
H	*-11.82346*	*-1.98597*	*1.75196*
H	*-13.14358*	*-1.29593*	*2.70748*
H	*-15.39848*	*1.50480*	*-2.91985*
H	*-13.76010*	*1.56411*	*-3.59154*
H	*-14.33103*	*2.85961*	*-2.53647*
C	*-12.46912*	*0.83243*	*-1.30602*

H	*-11.76092*	*1.20146*	*-2.04350*
H	*-15.78047*	*0.65076*	*-0.63476*
H	*8.14853*	*-2.54534*	*-0.07216*
H	*9.18510*	*-0.90571*	*-0.33145*
H	*9.36049*	*3.36367*	*-0.22348*
H	*7.35158*	*4.66890*	*0.09465*
H	*3.55150*	*2.75037*	*0.48300*
H	*2.47418*	*1.12540*	*0.25610*
H	*2.30201*	*-3.14598*	*0.25636*
H	*4.33278*	*-4.45807*	*0.15502*
C	*10.90840*	*1.14201*	*-0.50186*
H	*11.35826*	*2.75496*	*0.85585*
H	*10.81995*	*-0.49370*	*-1.90539*
H	*8.78455*	*-8.44125*	*-0.09563*
H	*14.77327*	*0.94726*	*-1.02902*
H	*2.94660*	*8.63882*	*0.86116*

Optimized geometry for **Per-(NDI)$_4$**

C	-1.11726	-0.72417	0.03711
C	-1.29467	0.74091	-0.01924
C	-0.13882	1.58232	0.03842
C	1.18535	1.04199	0.07677
C	1.36459	-0.42257	0.00441
C	0.20715	-1.26301	0.02050
C	-2.54637	1.33292	-0.11970
C	-2.73094	2.73680	-0.13306
C	-1.61685	3.55085	-0.03150
C	-0.31354	3.00351	0.05812
C	0.82017	3.84717	0.15149
C	2.09859	3.32338	0.22568
C	2.25858	1.91690	0.18175
C	2.61813	-1.01440	-0.07111
C	2.80573	-2.41828	-0.10992
C	1.68613	-3.23018	-0.05210
C	0.38194	-2.68387	0.02120
C	-0.75384	-3.52795	0.07982
C	-2.03393	-3.00595	0.13867
C	-2.19330	-1.59905	0.10947
C	-4.09580	3.30927	-0.25273
C	-3.22353	-3.88911	0.23751
C	4.16989	-2.99355	-0.21908
C	4.47952	3.91283	-0.33211

C	3.25317	5.35030	1.16239
C	4.37077	6.16884	1.29751
C	5.54447	5.85550	0.61437
C	5.59848	4.73053	-0.20629
C	5.15618	-2.37478	-1.00410
C	6.42776	-2.92605	-1.13083
C	6.74059	-4.11847	-0.47694
C	5.77623	-4.74425	0.31546
C	4.50984	-4.18318	0.44536
C	-4.40841	-3.59095	-0.45516
C	-5.52986	-4.40814	-0.34711
C	-5.48561	-5.53926	0.46536
C	-4.31889	-5.85993	1.15712
C	-3.19920	-5.04169	1.04015
C	-5.04858	2.73201	-1.10810
C	-6.32733	3.26800	-1.22672
C	-6.67953	4.39087	-0.47963
C	-5.75120	4.97971	0.37786
C	-4.47141	4.44376	0.48498
N	6.71677	6.68982	0.76780
C	7.80189	6.14964	1.49497
C	6.68494	7.97613	0.18439
C	7.90575	8.81082	0.35033
C	9.01960	8.31166	1.06753
C	9.00133	7.01684	1.63933
C	10.17698	9.12370	1.21523
C	7.94829	10.08078	-0.20314
C	9.09520	10.88384	-0.05930
C	10.19704	10.41738	0.63995
C	11.29099	8.62328	1.93161
C	11.24968	7.35239	2.48261
C	10.10352	6.54886	2.33713
C	11.40097	11.28027	0.78027
N	12.47342	10.74806	1.52405
C	12.51220	9.45790	2.09390
C	13.64387	11.58843	1.70199
C	13.74189	12.34218	2.86850
C	14.84310	13.17159	3.09889
C	15.83522	13.22073	2.11294
C	15.73027	12.46228	0.94889
C	14.63432	11.62522	0.71229
N	8.04385	-4.71221	-0.63478
C	8.81123	-4.94301	0.52635
C	8.45561	-5.04703	-1.96208

C	9.74329	-5.67999	-2.10552
C	10.54412	-5.94564	-0.99504
C	10.11920	-5.59016	0.31798
C	10.17085	-6.03840	-3.49870
C	11.50187	-6.70430	-3.56773
C	12.26103	-6.95909	-2.47524
C	11.82049	-6.58817	-1.14416
C	10.93330	-5.85491	1.42306
C	12.16932	-6.47132	1.26812
C	12.60724	-6.84042	-0.02073
C	13.56719	-7.63535	-2.65835
N	14.29319	-7.89153	-1.47838
C	13.91884	-7.50439	-0.16395
C	15.55304	-8.57867	-1.62485
C	15.59044	-9.92861	-1.45064
C	16.72471	-7.82940	-1.94014
C	18.03292	-9.88594	-1.90423
C	16.84205	-10.72719	-1.58711
C	17.95207	-8.53497	-2.07087
C	16.66431	-11.88172	-2.62280
C	14.52567	10.81605	-0.55590
C	14.96710	13.96449	4.37883
N	-6.66099	-6.37165	0.60601
C	-6.63170	-7.65140	0.00822
C	-7.74355	-5.83852	1.34171
C	-8.93998	-6.70965	1.48719
C	-8.95937	-7.99975	0.90481
C	-7.84968	-8.49018	0.17518
C	-10.11186	-8.81773	1.05825
C	-11.21909	-8.32846	1.79274
C	-11.17650	-7.06236	2.35449
C	-10.03633	-6.25196	2.20083
C	-10.13076	-10.10905	0.47761
C	-9.03309	-10.56685	-0.23383
C	-7.89190	-9.75704	-0.38536
C	-12.43088	-9.17355	1.97058
N	-12.41099	-10.44039	1.35172
C	-11.32544	-10.98233	0.63359
C	-13.59306	-11.27059	1.49692
C	-13.70714	-12.13576	2.59425
C	-14.86800	-12.91100	2.66768
C	-15.86568	-12.82989	1.69665
C	-15.74305	-11.96262	0.60686
C	-12.63042	-12.23444	3.64626

C	-16.82880	-11.84746	-0.43735
N	-8.01288	4.94174	-0.58930
C	-9.08571	4.14529	-0.12579
C	-10.44808	4.73098	-0.24155
C	-10.62563	6.02456	-0.78745
C	-9.52062	6.78574	-1.23729
C	-8.14185	6.23455	-1.14726
C	-9.71845	8.05194	-1.76541
C	-11.01471	8.59289	-1.85589
C	-12.11196	7.86553	-1.42311
C	-11.93551	6.56891	-0.88268
C	-11.54470	4.00351	0.19332
C	-12.84161	4.54171	0.09803
C	-13.04008	5.80649	-0.43255
C	-14.41826	6.35984	-0.52327
N	-14.54440	7.64405	-1.09236
C	-13.47497	8.45478	-1.52429
C	-15.88510	8.18733	-1.21479
C	-16.42805	8.94969	-0.17164
C	-17.72830	9.43076	-0.35335
C	-18.45135	9.16608	-1.51596
C	-17.89925	8.40669	-2.55247
C	-16.59984	7.91893	-2.37791
C	-15.65445	9.23673	1.09119
C	-18.66307	8.13479	-3.82727
O	13.50206	9.06054	2.68395
O	11.47074	12.39066	0.28082
O	5.70379	8.36955	-0.42191
O	7.74614	5.03070	1.97367
O	8.40067	-4.62412	1.63794
O	7.72753	-4.80229	-2.92646
O	14.02778	-7.96646	-3.74159
O	14.67680	-7.73233	0.76565
O	-13.39672	-8.80403	2.61642
O	-11.37677	-12.10915	0.17091
O	-5.65330	-8.03768	-0.60699
O	-7.68711	-4.72331	1.82909
O	-8.89346	3.03703	0.34280
O	-7.16701	6.85786	-1.52969
O	-15.39588	5.74694	-0.12977
O	-13.67092	9.57807	-1.95594
H	4.33635	7.04434	1.93805
H	6.51275	4.49566	-0.74181
H	4.91746	-1.46688	-1.55071

H	7.16954	-2.44688	-1.75910
H	3.77996	-4.66600	1.08852
H	6.02421	-5.65866	0.84255
H	-2.30346	-5.28117	1.60542
H	-4.29216	-6.74024	1.79148
H	-6.43866	-4.16763	-0.88946
H	-4.44660	-2.71962	-1.10214
H	-4.77771	1.86762	-1.70724
H	-7.05098	2.81507	-1.89634
H	-6.03033	5.85175	0.96004
H	-3.76181	4.89473	1.17221
H	-11.38078	3.01463	0.60820
H	-13.70458	3.97856	0.43714
H	-11.17719	9.58482	-2.26408
H	-8.85534	8.61492	-2.10433
H	7.08143	10.43947	-0.74785
H	9.13656	11.87810	-0.49128
H	10.06295	5.55310	2.76563
H	12.11734	6.99284	3.02549
H	10.56870	-5.56554	2.40313
H	12.81043	-6.68112	2.11638
H	10.17183	-5.14395	-4.14752
H	9.41237	-6.67726	-3.98560
H	11.88441	-7.00325	-4.54022
H	-9.07274	-11.56016	-0.66814
H	-7.02827	-10.10893	-0.93955
H	-12.03806	-6.71264	2.91329
H	-9.99474	-5.25978	2.63743
H	-14.98961	-13.59605	3.50308
H	-16.13418	7.31739	-3.15436
H	-19.46244	9.55445	-1.61567
H	-18.18464	10.02104	0.43744
H	16.70374	13.85989	2.25637
H	16.51622	12.52161	0.19998
H	12.94542	12.27630	3.60482
H	18.84707	-7.96544	-2.30773
C	16.66614	-6.34656	-2.11489
H	16.30286	-5.85753	-1.20063
H	15.97109	-6.07700	-2.92056
H	17.64972	-5.93515	-2.35560
H	17.57263	-12.49098	-2.66917
H	16.46208	-11.47434	-3.61723
H	15.82976	-12.52822	-2.33306
H	-12.47459	-11.27409	4.15252

H	-11.67152	-12.54172	3.21169
H	-12.90168	-12.97191	4.40736
H	-17.46919	-12.73527	-0.44524
H	-16.40853	-11.72539	-1.44181
H	-17.47367	-10.97905	-0.24775
C	-14.58340	-11.18404	0.52402
H	-14.44395	-10.50097	-0.31004
H	-16.75240	-13.45304	1.78845
H	-19.74445	8.17439	-3.66040
H	-18.41984	7.14824	-4.23613
H	-18.42389	8.87598	-4.60152
H	-14.73304	9.79254	0.87932
H	-15.37391	8.31183	1.60962
H	-16.25330	9.83645	1.78293
H	13.99360	14.10553	4.85947
H	15.40004	14.95433	4.19636
H	15.61798	13.45395	5.10094
H	15.43178	10.92120	-1.16003
H	13.67716	11.14660	-1.16715
H	14.38780	9.74926	-0.34369
H	3.50640	-0.39395	-0.08419
H	3.26591	1.52659	0.26866
H	0.67110	4.92345	0.14138
H	-1.72582	4.63175	-0.05558
H	-3.43362	0.71268	-0.16844
H	-3.20210	-1.20968	0.18417
H	-0.60412	-4.60401	0.05848
H	1.79286	-4.31041	-0.09754
C	3.28709	4.20485	0.35011
H	2.35119	5.58482	1.71984
H	4.52537	3.04695	-0.98582
H	14.67317	-10.45817	-1.20954
H	17.02821	-11.23276	-0.61778
H	18.98862	-10.39302	-2.01132

Chapter 3: Co-facial Porphyrin Dimer for Coherent Multipathway Electron Trasnfer

Jeremy M. Fisher, Brian T. Phelan, Yunfan Qiu, Paige J. Brown, Ryan M. Young,* and Michael R. Wasielewski*
Department of Chemistry and Institute for Sustainability and Energy at Northwestern (ISEN),
Northwestern University, Evanston, IL 60208-3113

3.1 Abstract

In this thesis chapter I report the successful synthesis of a co-facial porphyrin dimer where the porphyrin units act as chromophores and electron donors. The porphyrins are covalently linked to a triptycene bridge, locking them into the co-facial geometry, with a benzoquinone electron acceptor on the third triptycene ring to act as an electron acceptor. This molecule is well-suited for 2DES studies, as the pump and probe parameters fit well with the instrument setup. This will allow us to directly observe the coherent porphyrin excited state upon photoexcitation followed by coherent multi-pathway electron transfer to the single benzoquinone acceptor in a frozen matrix at cryogenic temperatures. This project is still ongoing. Thus far, we have conducted steady state characterizations to build our understanding of the system energetics and elucidated room temperature kinetics of the system using fsTA and nsTA in the visible, NIR, and IR regions. Indeed, there is significant evidence of porphyrin-porphyrin interaction in the co-facial dimer, an important criterion for achieving multi-pathway coherent electron transfer. Additionally, electron transfer in this molecule occurs within 1ps, which should be fast enough for the coherent dynamics to survive until charge separated state formation.

3.2 Introduction

As the need for sustainable energy sources rises, improving photoinduced electron transfer (ET) to increase overall light-energy harvesting efficiency has received a great deal of attention.[28, [110-117] One aspect of this process currently under investigation is the role of coherence.[117-124] Indeed, there are many types of coherent interactions that have demonstrated their role in dictating electronic and energetic dynamics such as vibrational coherence,[125-128] electronic coherence,[126, 129-132] and vibronic coherence.[17, 57, 133-136] Coherent interactions impact parameters such as ET rate and efficiency. The type of coherence we explore in this study is an electronic coherence between ET pathways in a multi-pathway D-A system.

Theoretical and experimental work suggests coherence between multiple ET pathways could allow for constructive interference to enhance the rate of ET.[90, 137-142] The mechanism of this enhancement involves the multiple acceptor units acting as a single delocalized acceptor with renormalized coupling to the donor and to the bath. For a single donor interacting with two degenerate acceptors, at low temperature, assuming fast bath relaxation and weak system-bath coupling,[90, 139] the rate can be expressed as

$$k_{CS} \propto \left(V_{DA}{}^2 V_{SB}^2\right) / (\Delta G_{CS})^2 \tag{Eqn. 3.1}$$

where V_{DA} is the donor-acceptor coupling and V_{SB} is the system-bath coupling. Here, the coupling between the acceptor moieties leads to the production of bonding and anti-bonding orbitals with normalized $V_{DA}(bonding) = \sqrt{2}V_{DA}$ and V_{DA}(*anti-bonding*) = 0. V_{SB} is similarly renormalized to $\sqrt{2}V_{SB}$. Therefore, according to this model, rate enhancement due to coherent ET could be as high as $k_{CS} \propto (\sqrt{2}V_{DA})^2(\sqrt{2}V_{SB})^2 = 4V_{DA}{}^2V_{SB}{}^2 = 4 \text{ x } k_{CS}$.[139]

In order to achieve this type of acceptor delocalization, the energetic degeneracy of the multiple acceptors must survive long enough for the ET to occur to the delocalized superposition state. This can be difficult to achieve, as system-bath interactions typically dephase electronic coherences very quickly—within 100 femtoseconds[143, 144]—through lifting the degeneracy of the multiple ET pathways.

Theoretical analysis has shown that using a glassy viscous bath at cryogenic temperatures could achieve reduced bath fluctuations for prolonged electronic coherence lifetimes, as the glassy matrix not only reduces bath fluctuations, but also extends the spatial range of those fluctuations such that they can be correlated across locations.[145] This would aid in preserving pathway degeneracy in multi-pathway donor-acceptor systems. There is also experimental work supporting the validity of this concept.[90, 139] Our group has previously published work on a two-acceptor system where a single donor connected to two acceptors (D-2A) was compared to a control compound with a single acceptor (D-A) in solution at room temperature and in glassy m-THF at cryogenic temperatures.[139] The D-2A system showed statistical rate enhancement of ET as compared to D-A by a factor of ~2.5 in solution at room temperature but showed even further enhancement by a factor of ~5 in glassy m-THF at cryogenic temperatures. The suggested mechanism for this greater-than-statistical rate enhancement is that the glassy medium as well as the cryogenic temperatures preserves the pathway degeneracy for a longer time in the D-2A system, yielding coherent ET.[139]

To further investigate this type of electronic coherence rate enhancement, we designed and synthesized a multi-pathway 2DA system, where two co-facial Zn-porphyrin (Por) chromophore electron donors are connected through a triptycene bridge to a single benzoquinone (BQ) acceptor (**2DA**). The analogous monomer was also synthesized for comparison (**1DA**). Both compounds were also synthesized with protecting groups on the benzoquionone to prevent the ET pathway as control references (**1P** and **2P**). This particular system offers the advantage of being well-suited for two-dimensional electronic spectroscopy (2DES) studies, as the Q-band of the Por units falls within the bandwidth of the pump pulses achievable with this instrument. With this method, we hope to directly launch a coherent, delocalized excitation onto the co-facial Por units in the dimer and watch as the ET occurs to the BQ. Using 2DES, we can track the coherences and if the ET occurs in **2DA** before the electronic coherence is lost, we hope to see the coherence transfer along with the electron.[146]

This research project is still ongoing, as 2DES measurements are in the process of being collected and analyzed. In this chapter I report the successful synthesis of the molecules for this study (Scheme 3.1) as well as preliminary measurements, both steady-state and transient, to start putting together our understanding of the overall system energetics and dynamics.

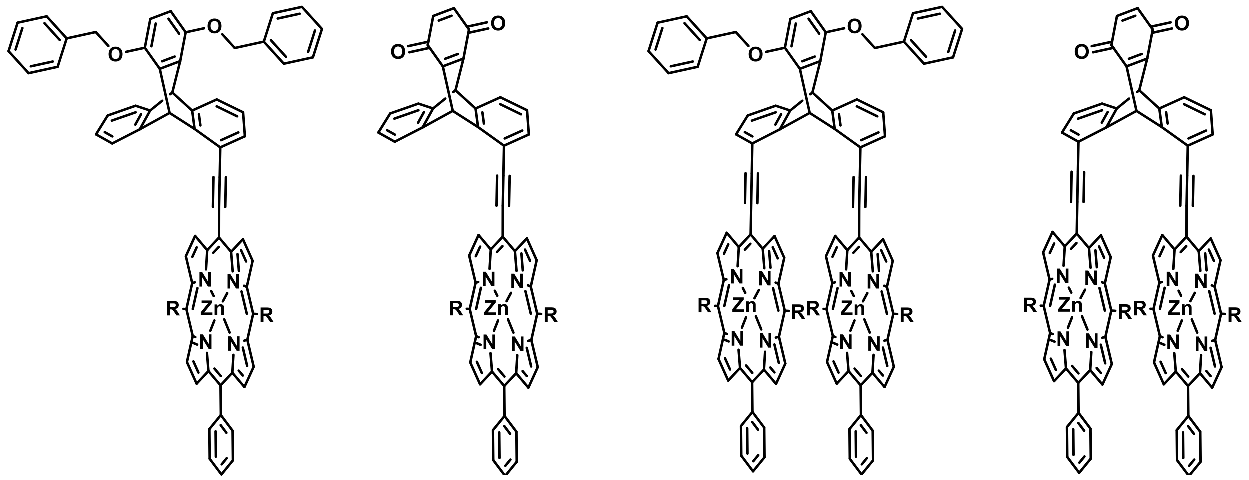

1P **1DA** **2P** **2DA**

Scheme 3.1 Molecules investigated in this study.

3.3 Methods

3.3.1 Synthesis. The Porphyrin derivatives studied in this paper were prepared as shown in the Supporting Information (SI).

3.3.2 Steady-State Optical Spectroscopy. UV-visible-NIR steady-state absorption spectra were measured at room temperature using a Shimadzu UV-1800 spectrometer. NIR emission was measured using a HORIBA Nanolog fluorimeter.

3.3.2 Electrochemistry. Electrochemical measurements were performed on a CH Instrument 750E electrochemical workstation. Measurements were made using a 1.0 mm diameter glassy carbon working electrode, a platinum wire auxiliary electrode, and a silver wire pseudo-reference electrode in 0.1 M solutions of n-butylammonium hexafluorophosphate ($TBAPF_6$) in THF purged with argon. Ferrocene was used as an internal standard.

3.3.3 Spectroelectrochemistry. Spectroelectrochemical measurements were performed using a CH Instrument 750E electrochemical workstation and a Shimadzu UV-1800 spectrometer. Bulk electrolosis and cuolometry was employed to hold a steady current at 1.5 eV for oxidation and -1 eV for reduction while UV-Vis absorption spectrum was obtained.

3.3.4 Transient Absorption Spectroscopy. Femtosecond transient absorption (TA) experiments were performed on an apparatus that has been described previously.[82] Tunable excitation pulses were generated by using a commercial colinear optical parametric amplifier (TOPAS-Prime, Light-Conversion, LLC). The polarization was spatially randomized to eliminate the effects of polarization-dependent dynamics. Spectra were collected using commercial spectrometers (customized Helios/Eos, Ultrafast Systems, LLC). The total instrument response function was ~300 fs. Transient spectra were averaged for at least 3 s per delay point. Prepared samples had an absorbance of 0.2-0.7 at the excitation wavelength and were irradiated in 2-mm pathlength quartz cuvettes with 0.4-0.8 μJ/pulse focused to ~0.2 mm diameter spot.

3.3.6 Fourier Transform Infrared Spectroscopy. FTIR data were collected at room temperature on a Bruker Tensor 37 FTIR Spectrometer equipped with a Mid IR detector and KBr beam splitter. The spectrum was collected in attenuated total reflectance mode in the range of 4000 to 400 cm^{-1}. The data were averaged over 16 scans. The OPUS software was used for the data acquisition.

3.3.6 Time-Resolved Infrared Spectroscopy. Femtosecond transient infrared absorption spectroscopy was performed using an instrument described previously.[147] Briefly, a regeneratively amplified Ti:sapphire oscillator/amplifier (Solstice, Spectra-Physics) provided the fundamental (1 kHz, 795 nm, 100 fs) that was split to pump two commercial optical parametric amplifiers (TOPAS-C, Light Conversion). One OPA was used to generate the excitation pulse and the other was used to generate the mid-infrared probe pulse. The excitation pulse was centered at 632 nm for the monomer samples and 625 nm for the dimer samples with 3 μJ/pulse at the sample for all measurements. The pump polarization was pseudo-randomized (DPU-25A, Thorlabs) to suppress polarization effects from molecular rotation and tumbling in solution. The measurement was performed using a customized time-resolved mid-infrared spectrometer (HELIOS Fire, Ultrafast Systems LLC) where the mid-infrared probe split into separate signal and reference paths, was spectrally dispersed using an iHR-320 Horiba spectrograph with either a 50 or 150 groove/mm grating and detected using a 64 element dual row MCT array detector (Femtosecond Pulse Acquisition Spectrometer, Infrared Systems Development). The samples were prepared as solutions in 1,4-dioxane or deuterated 1,4-dioxane in variable pathlength cells (Luer-DLC-M25, Harrick Scientific) using 500 μm PTFE spacers and CaF 2 windows. The samples were rastered randomly in two dimensions to minimize local heating and sample degradation. The transient spectra were frequency calibrated by matching ground-state bleach features to the features observed in the steady-state FTIR spectra.

3.3.7 Two-Dimensional Electronic Spectroscopy. 2DES experiments were conducted using an apparatus described earlier.[83] Pump pulses were generated using a noncollinear optical parametric amplifier (Spirit NOPA-3H, Spectra-Physics). Pump pulses with two distinct spectral profiles were used, one with a 480-545 nm bandwidth and one with a 500-640 nm bandwidth. Both NOPA pump beams were tuned to co-excite both the LE and CT absorption bands, but the shorter wavelength pulse is biased towards the LE absorption transition, while the longer wavelength pulse is biased towards the CT band.

3.3.8 Density Functional Theory Computations. Density functional theory (DFT) calculations using Q-Chem 5.1 were performed on 1DA and 2DA at the level of B3LYP/6-31G* for calculations on neutral ground state compounds and ωB97X-D/6-31G* for calculations on compounds with positive of negative charge. Absorption spectra and IR- and Raman- active modes were calculated using time-dependent DFT (TDDFT).

3.4 Results and Discussion

3.4.1 System Energetics

Steady-State Optical Spectroscopy. The UV-visible absorption spectra of **1P**, **2P**, **1DA**, and **2DA** in 1,4-dioxane are shown in Figure 3.1a-b. All four compounds show Soret band absorption at λ_{max} = 420 nm and 440 nm for the dimer and monomer compounds, respectively, and Q-band absorption at λ_{max} = 624 nm and 632 nm for the dimer and monomer compounds, respectively. There is no observable difference between the protected and analogous donor-acceptor systems. Between the monomer and dimer systems, however, there is blue shifting in both Soret and Q-band absorption in the dimers compared to the monomers. This is often observed in H-type aggregates with face-to-face stacking, as is the case in the dimers in this study.[148-150]

Steady-state emission spectra were measured for **1P** and **2P** in 1,4-dioxane as well (Figure 3.1c). They exhibit emission at λ_{max} = 645 nm and 655 nm, respectively. This red-shifted emission from the dimer in comparison to the monomer is again a result of the H-type aggregation of the porphyrins in **2P**.[30, 149]

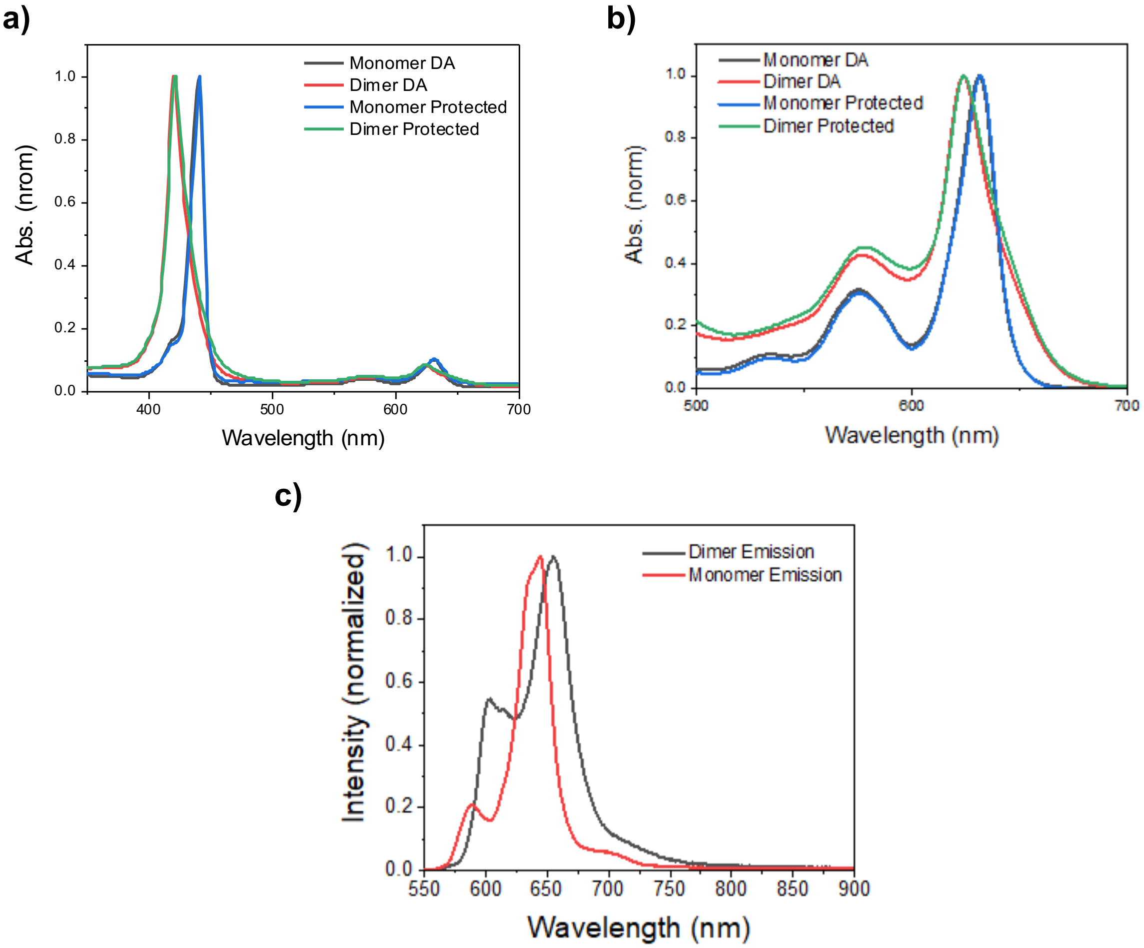

Figure 3.1 UV-Vis absorption spectra for **1P**, **2P**, **1DA**, and **2DA** normalized to a) the Soret band and b) the Q-band of the porphyrin derivative and c) emission spectra for **1P** and **2P**.

We used these steady-state optical measurements to calculate the approximate energy levels for the lowest singlet excited state for the monomer and dimer compounds from the crossing point of their normalized absorption and emission spectra. The data yield E_{LE} = 2.0 eV and 1.9 eV in 1,4-dioxane for the monomers and dimers, respectively.

Electrochemistry. Cyclic voltammetry (CV) and differential pulse voltammetry (DPV) measurements on **1DA** reveal a reduction potential of -0.61 eV vs SCE and an oxidation potential of 0.67 eV vs. SCE in THF (Figure 3.2a-b). CV and DPV measurements were also collected on **2P** and splitting of the porphyrin oxidation by 250 meV was observed as a result of the H-type aggregation of the two porphyrin moieties (Figure 3.2c-d).[139]

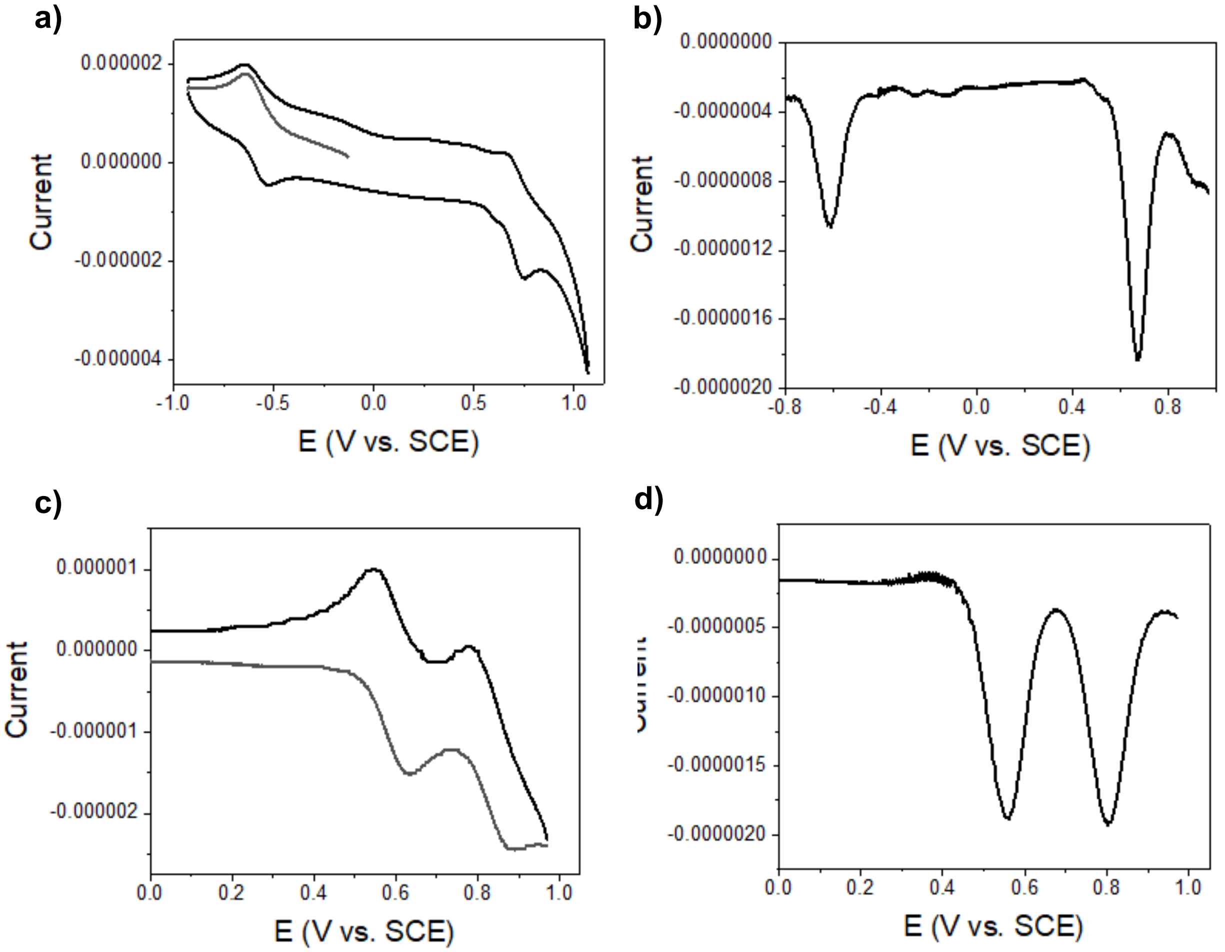

Figure 3.2 (a) CV spectrum for **1P**, (b) DPV spectrum for **1P**, (c) CV spectrum for **2P**, and (d) DPV spectrum for **2P**.

We used these redox potentials to calculate the CS state energy of the porphyrin-containing DA systems in THF using the Weller equation, which corrects for the different dielectric constants between THF, the solvent in which the electrochemical potentials were measured, and 1,4-dioxane, the solvent in which the transient optical experiments were performed (see the SI for details).[85] This gives the energy of the fully charge-separated state as 1.53 eV for both **2DA** and **1DA**.

Spectroelectrochemistry. Spectroelectrochemistry was employed to obtain the absorption features of singly oxidized and reduced **1DA**. These data enable identification of the radical pair in transient absorption measurements. The spectra indicate **1DA**$^+$ has absorptive features at 700 and 400 nm and **1DA**$^-$ has absorptive features at 590 and 1000 nm (Figure S3.9).

Fourier Transform Infrared Spectroscopy. Fourier transform infrared (FTIR) spectroscopy measurements were taken in solutions of 1,4-dioxane for all four compounds (Figure S3.10). The spectra for singly oxidized **1P** and **2P** were additionally measured following oxidation with magic blue, for identification in TRIR experiments.

3.4.2 Excited-State Dynamics

Transient Absorption Spectroscopy. Transient absorption spectroscopy measurements were performed on all four compounds.

Upon photoexcitation of the Q-band, the transient absorption spectra of **1P** and **2P** in the UV-vis and NIR regions are quite similar, with the spectra for **2P** generally slightly blue-shifted compared to those for **1P** (Figure 3.3). Both compounds show ground-state bleach (GSB) at 440 and 420 nm for the Soret band and 632 and 624 nm for the Q-band, respectively along with excited state absorption (ESA) features at 390, 460, 610, 688, 1210, 1377, and 1486 nm for **1P** and at 376, 440, 598, 682, and a broad feature centered at 1080 nm for **2P**. In both compounds, this lowest singlet excited state then relaxes down to a lower-lying triplet state with time constants of τ_{trip} = 1.3 ± 0.03 ns and τ_{trip} = 1.6 ± 0.03 ns for **1P** and **2P**, respectively. This relaxation manifests as a slight red shift in the ESA features at ~385 and ~685 nm as well as the appearance of a new ESA feature at ~530 nm in both compounds.

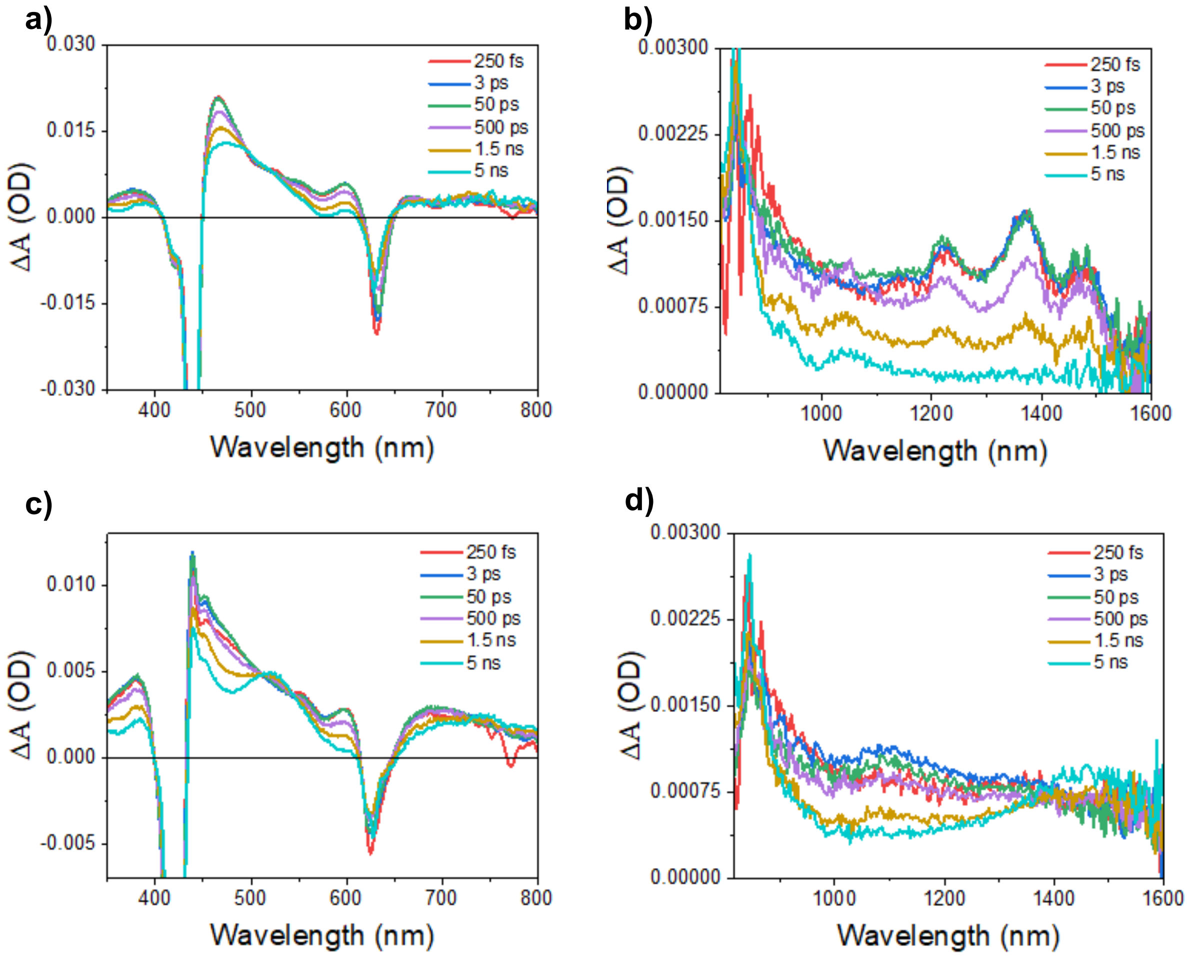

Figure 3.3 Spectra from fsTA at selected timestamps for **1P** in (a) the UV-vis region and (b) the NIR region and **2P** in (c) the UV-vis region and (d) the NIR region.

Upon photoexcitation of the Q-band, the transient absorption spectra of **1DA** and **2DA** in the UV-vis and NIR regions exhibit the same initial formation of the lowest singlet stated states, but rather than relaxing to the lower-lying triplet state, these compounds undergo CS. This is most clearly evidenced by the ESA peak in the NIR at ~1000 nm in both compounds and occurs with time constants of $\tau_{CS} = 2.2 \pm 0.3$ ps and $\tau_{CS} = 0.9 \pm 0.3$ ps for **1DA** and **2DA**, respectively (Figure

3.4). This twofold rate enhancement of CS in **2DA** suggests delocalization of the initially formed singlet excited state, such that both CS pathways become available.

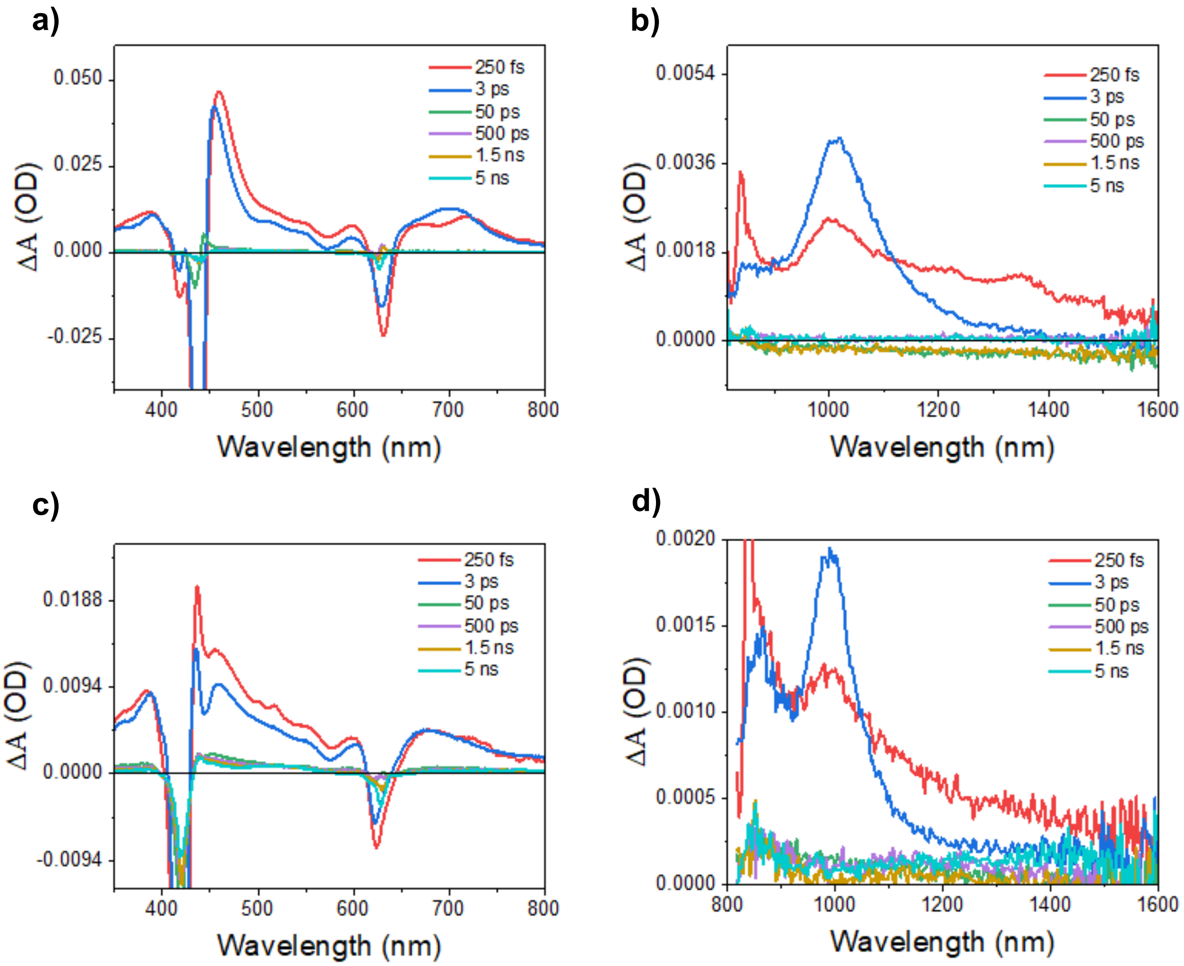

Figure 3.4 Spectra from fsTA at selected timestamps for **1DA** in (a) the UV-vis region and (b) the NIR region and **2DA** in (c) the UV-vis region and (d) the NIR region.

Time Resolved Infrared Spectroscopy. Time resolved IR spectroscopy was collected using two solvents, 1,4-dioxane for probing the aromatic region (1200-2000 cm^{-1}) (Figure 3.5) and 1,4-dioxane-d8 for probing the ethynyl region (1900-2400 cm^{-1}) (Figure 3.6). In the aromatic region **1P** and **2P** initially form their respective lowest-lying singlet excited state, exhibited by ESA features at 1355 and 1475 cm^{-1} in **1P** and at 1350, 1425, and 1475 cm^{-1} for **2P**. This singlet state then undergoes relaxation to the lower-lying porphyrin triplet state with time constants of τ_{trip} = 1.6 ± 0.005 ns and τ_{trip} = 1.8 ± 0.005 ns for **1P** and **2P**, respectively. This triplet state exhibits slight shifting of the low-energy peaks to higher energies, as well as a new ESA feature at 1555 cm^{-1} for **1P**. For **2P**, there is a similar shift in the 1350 and 1475 cm^{-1} peaks as occurs in **1P** and the new 1555 cm^{-1} ESA feature appears as well. Additionally, the 1425 cm^{-1} ESA feature present in the **2P** singlet excited state that was not present in the **1P** singlet excited state is no longer present in the **2P** triplet state. For **1DA** and **2DA**, the initially formed lowest-lying excited singlet state features are largely obscured by their more intense CS state spectra. Additionally, a large amount of the populations has already undergone CS within the 500 fs IRF of the instrument making them additionally difficult to resolve. The CS states contain several identifying features, but are most notably identified by the benzoquinone GSB at 1680 cm^{-1} and absorption of the benzoquinone anion at 1510 cm^{-1}. These CS states then return to the ground state without triplet formation with time constants of τ_{GS} = 11.0 ± 0.5 ps and τ_{GS} = 10.2 ± 0.5 ps for **1DA** and **2DA**, respectively.

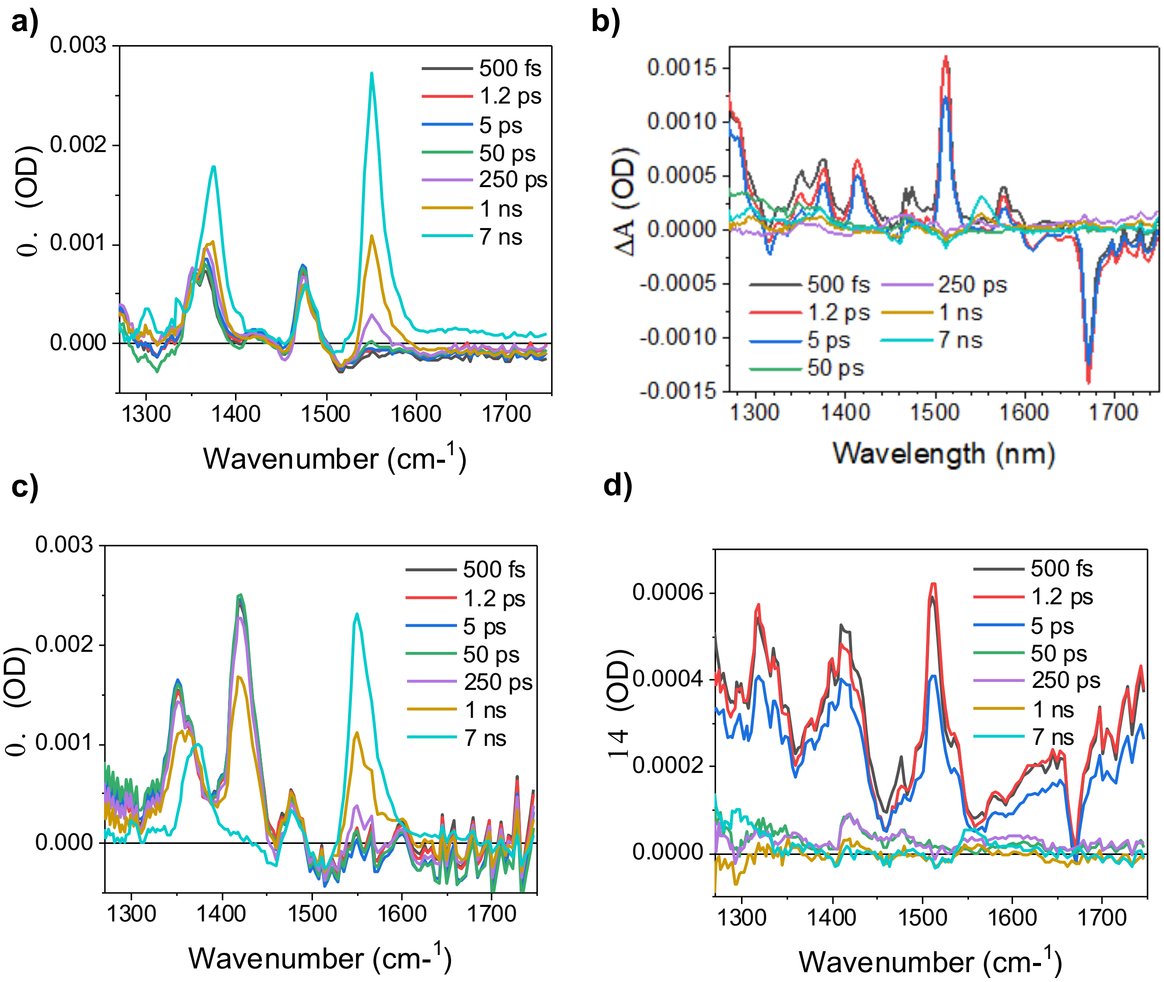

Figure 3.5 Selected spectra from fsIR collected in 1,4-dioxane-d8 for (a) **1P**, (b) **1DA**, (c) **2P**, and (d) **2DA**.

In the undeuterated 1,4-dioxane where the ethynyl region was probed, there was no signal observed for **1P**. The lowest-lying singlet excited state for **2P**, however, exhibits very broad absorption across the entire probe window before relaxing to the triplet state with a time constant of $\tau_{trip} = 1.8 \pm 0.005$ ns. For **1DA** and **2DA**, both compounds show formation of their respective CS states followed by returning to the ground state. The spectra for the respective CS states, however, are very different in this region. The **1DA** CS state has a sharp absorptive feature at 2155 cm^{-1} as well as a weaker broad feature at ~2275 cm^{-1}. For **2DA**, the CS state, like the excited singlet state, exhibits very broad baseline absorption spanning the entire probe window. On top of this wide, broad absorption there are ESA features in similar positions to those observed in the **1DA** CS state. These differences in the CS state absorption spectra indicate porphyrin-porphyrin interaction once the cation is formed.

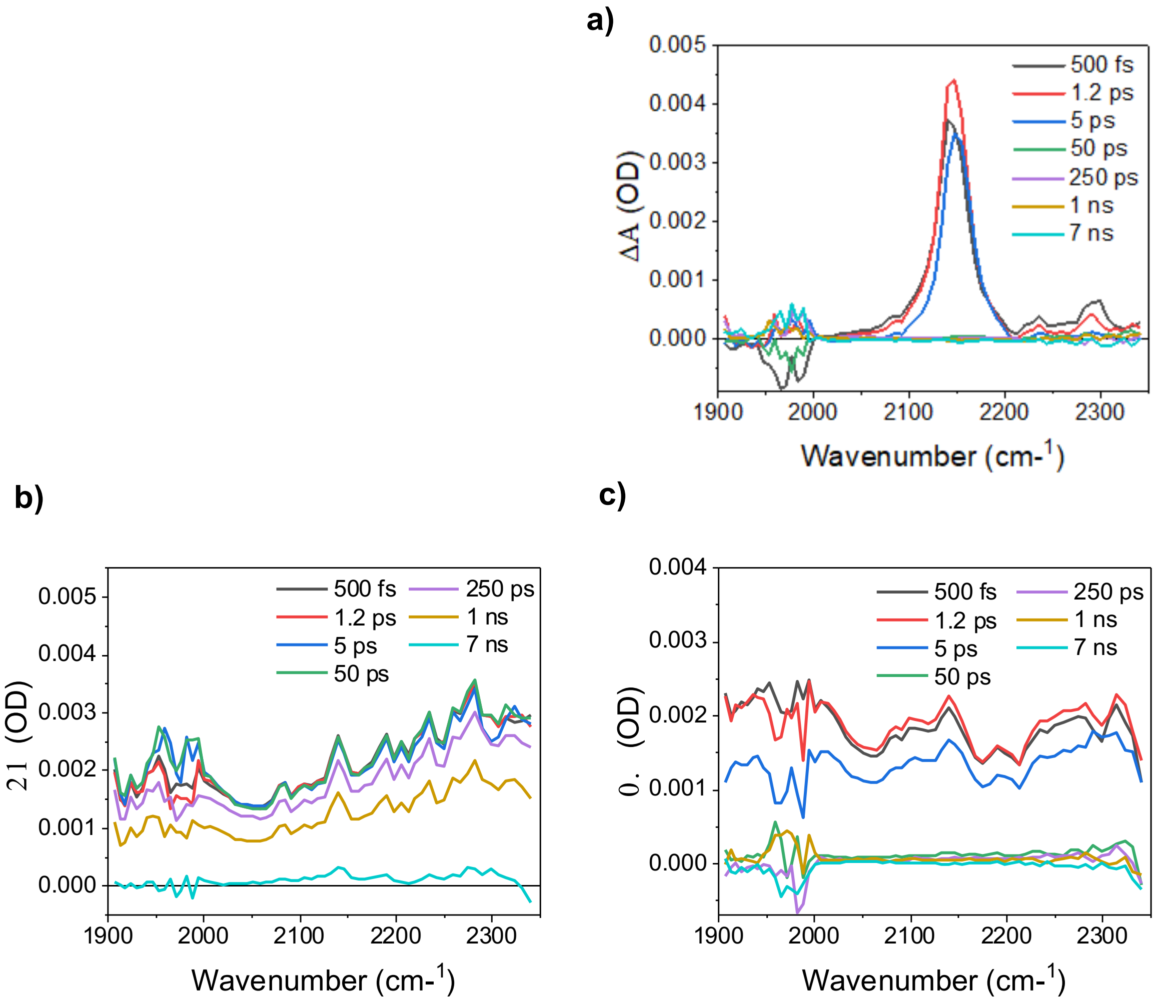

Figure 3.6 Selected spectra from fsIR collected in 1,4-dioxane for (a) **1DA**, (b) **2P**, and (d) **2DA**.

3.4.3 Calculations

Ground State Optimizations DFT calculations were conducted to visualize the geometry and electron density of **1DA** and **2DA** in its neutral ground state and singly oxidized and reduced states according to procedures described above in the methods section (Figure 3.7). In the neutral ground state **1DA** is oriented such that the porphyrin is twisted 82^o clockwise relative to the BQ acceptor. For the neutral ground state of **2DA**, both porphyrins are also rotated clockwise, but with a much smaller angle of ~40 degrees relative to the BQ, due to the steric bulk of containing two porphyrin moieties. The geometries for the singly reduced and oxidized states of **1DA** are very similar to each other, with the porphyrin twisted 23^o and 26^o counterclockwise relative to the BQ, respectively. For **2DA**, the two porphyrins are twisted by ~5^o relative to the BQ in the singly reduced state and are twisted by ~50^o counterclockwise relative to the BQ in the singly oxidized state. In both compounds, there is a clear trend of the porphyrin moieties twisting in a counterclockwise direction relative to the BQ as either a positive or negative charge is placed on the molecule, with a greater degree of twisting occurring in the singly oxidized compounds.

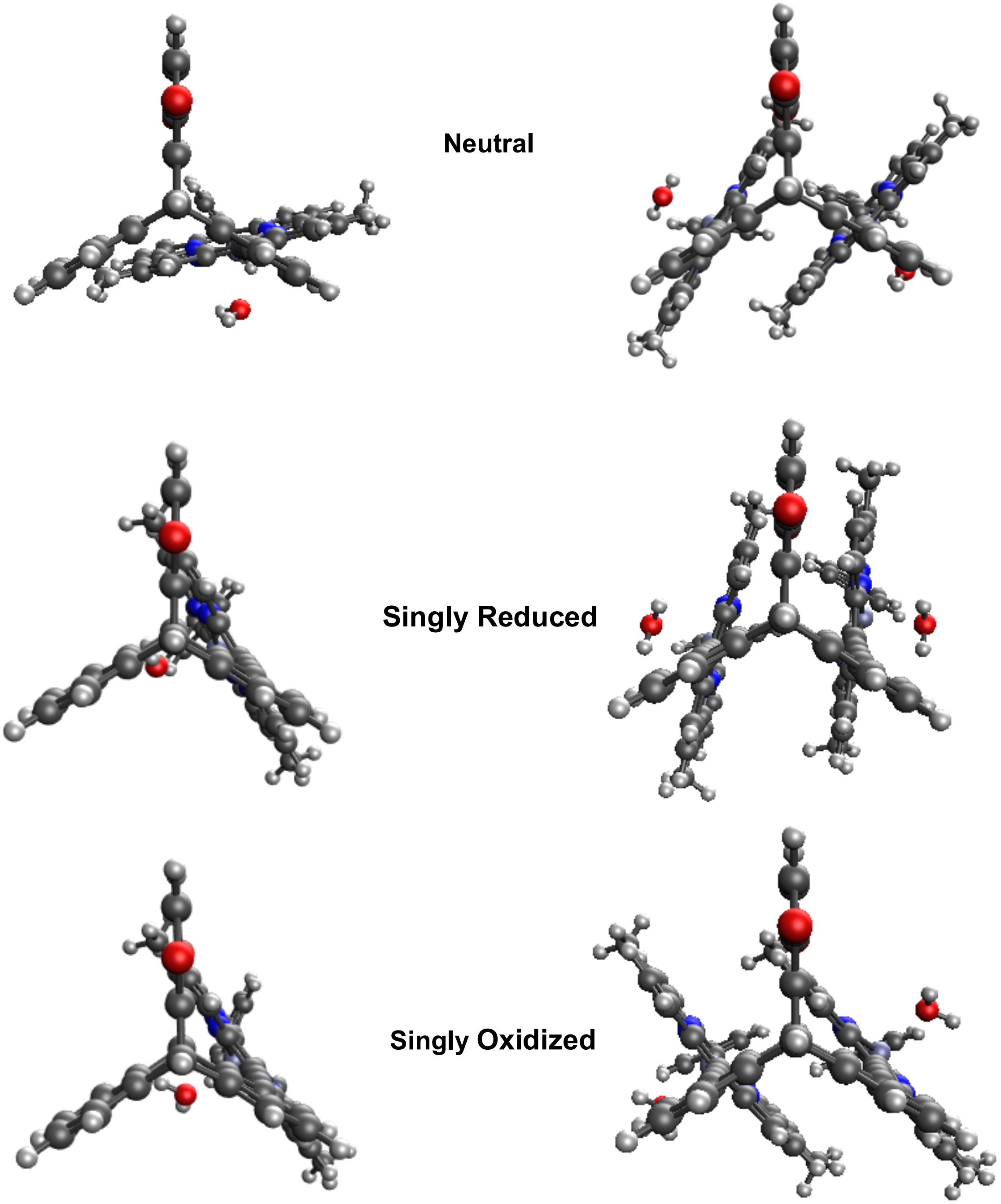

Figure 3.7 Visualizations of optimized geometries for **1DA** and **2DA** in the neutral ground state, singly oxidized state, and singly reduced state.

Next, TD-DFT calculations were run to visualize the HOMO and LUMO for each of these states (Figure 3.8). Unsurprisingly, these calculations show that in the neutral ground state, the HOMO for both compounds resides on the porphyrin units, with delocalization across both porphyrins in **2DA**, while the LUMO resides on the BQ. This result is reaffirmed in the HOMOs for the singly reduced and oxidized compounds, where the anion resides on the BQ and the cation on the porphyrins, again delocalized across both for **2DA**.

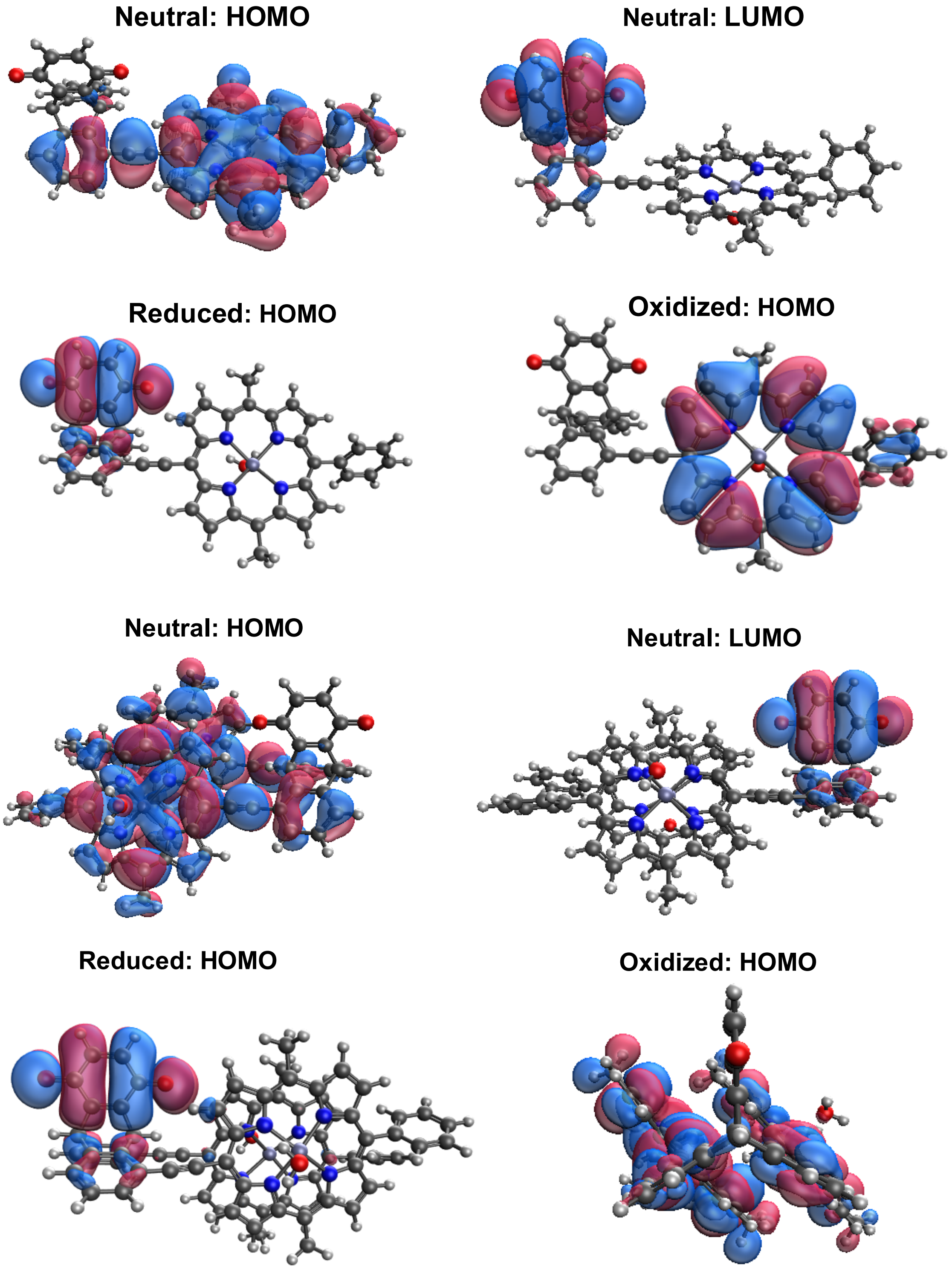

Neutral: HOMO

Neutral: LUMO

Reduced: HOMO

Oxidized: HOMO

Neutral: HOMO

Neutral: LUMO

Reduced: HOMO

Oxidized: HOMO

Figure 3.8 Visualizations of HOMO/LUMO for **1DA** and **2DA** in the neutral ground state, singly oxidized state, and singly reduced state.

3.5 Conclusion

In this chapter I have reported the successful synthesis and preliminary characterizations on a Zn-porphyrin co-facial dimer linked through a triptycene bridge to a benzoquinone electron acceptor. The monomer analogue as well as analogues for the monomer and dimer with protecting groups on the benzoquinone to turn off any ET pathway were synthesized and characterized as well. These studies reveal extensive evidence of porphyrin-porphyrin interaction manifested as shifted ground state UV-Visible absorption features, split electrochemical oxidation potential, and statistical rate enhancement of CS when comparing the dimer to the monomer. This evidence of strong inter-porphyrin interaction along with the very fast electron transfer make this system very promising for achieving coherent multi-pathway electron transfer. Next steps for this project include collecting 2DES measurements at room temperature and at cryogenic temperatures in a frozen matrix.

3.6 Supporting Information

3.6.1 Materials, Methods, and Synthesis

Materials. All chemicals and solvents were purchased from commercial suppliers and were used without further purification. ^{1}H and ^{13}C NMR spectra were recorded on a Varian 500 MHz spectrometer at room temperature. ^{1}H and ^{13}C chemical shifts are listed in parts per million (ppm) and are referenced to residual protons or carbons of the deuterated solvents. High Resolution Mass Spectra (HRMS) were obtained with an Agilent LCTOF 6200 series mass spectrometer using electrospray ionization (ESI) and APPI.

Synthesis:

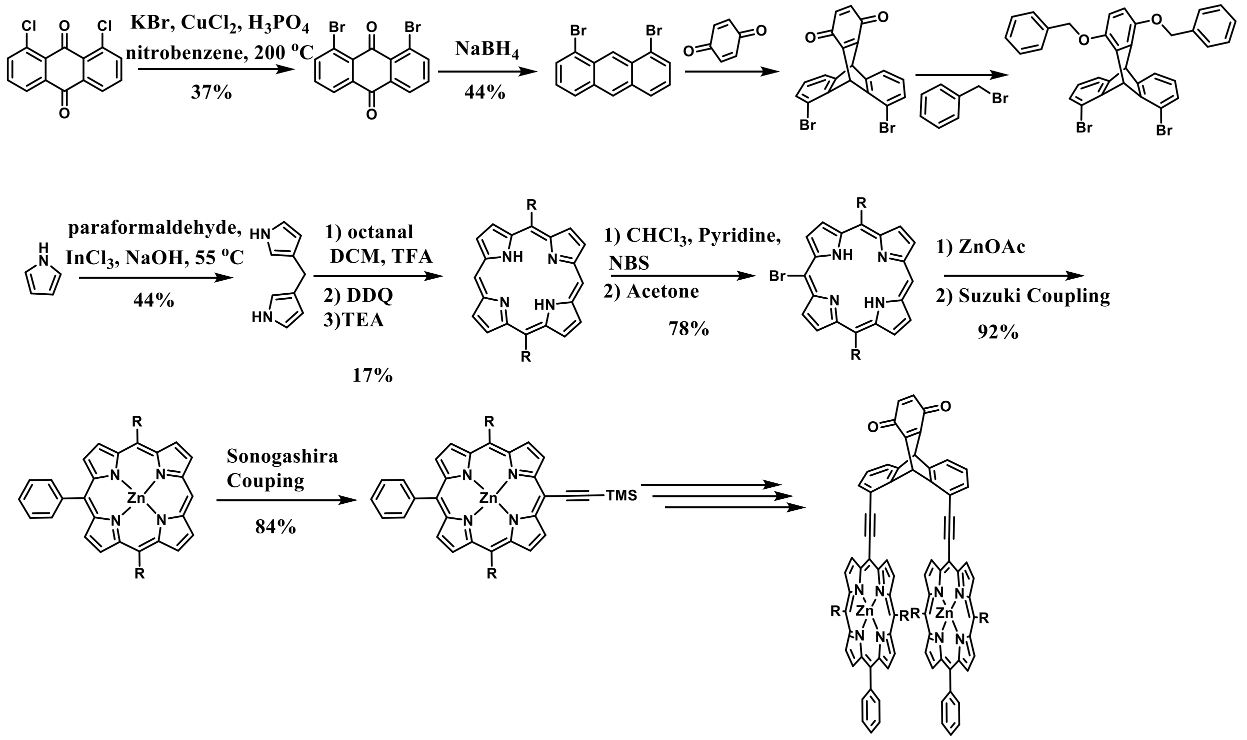

Scheme S3.1. Synthetic scheme for **Zn-Por** monomer and dimer donor-acceptor systems

1,8-dibromo-9,10-anthraquionone: 1,8-dichloro-9,10-anthraquionone (5 g), KBr (10 g), $CuBr_2$ (50 mg), 85% H_3PO_4 (10 mL), and nitrobenzene (50 mL) were added to a 250 mL round bottom flask equipped with a magnetic stir bar and condenser. The reaction mixture was stirred under reflux at 200°C for three days under nitrogen. The crude mixture was purified using silica gel chromatography (DCM/Hexanes, 1:1) yielding the desired product as bright yellow powder (2.4 g, 37% yield). ^{1}H NMR (500 MHz, CDCl3) δ 8.26 – 8.21 (m, 1H), 8.01 (dd, J = 7.9, 1.3 Hz, 1H), 7.53 (t, J = 7.8 Hz, 1H). ^{13}C NMR (126 MHz, CDCl3): δ 181.82, 181.37, 141.04, 135.01, 133.46, 133.14, 126.85, 233.03. MS-MALDI (m/z) calculated = 365.9, found = 365.9

1,8-dibromoanthracene: 1,8-dibromo-9,10-anthraquionone (300 mg), NaOH (80 mg), and 1-propanol (200 mL) were added to a 500 mL round bottom flask equipped with a magnetic stir bar.

N_2 gas was bubbled through the reagents for 15 minutes and then $NaBH_4$ (1.5 g) was added and a condenser placed on top of the flask. The reaction mixture was then stirred under reflux overnight under nitrogen at 105°C. The desired product was then isolated using silica gel chromatography (15% DCM in hexanes) yielding the desired product as a yellow powder (121 mg, 44% yield). ^1H NMR (500 MHz, CDCl3) δ 9.20 (d, J = 1.1 Hz, 1H), 8.43 (s, 1H), 7.97 (dq, J = 8.5, 0.9 Hz, 2H), 7.83 (dd, J = 7.1, 1.0 Hz, 2H), 7.33 (dd, J = 8.5, 7.1 Hz, 2H). ^{13}C NMR (126 MHz, CDCl3) δ 133.04, 131.27, 130.30, 128.47, 128.22, 126.61, 123.82. MS-MALDI (m/z) calculated = 335.9, found = 335.8.

BQ-Br$_2$: 1,8-dibromoanthracene (100 mg), 1,4-benzoquinone (200 mg), and toluene (70 mL) were added to a 250 mL round bottom flask equipped with a magnetic stir bar and condenser. The reaction mixture was stirred under reflux overnight under nitrogen at 120°C. The product was then purified using silica gel chromatography (25% DCM in hexanes) and then leftover 1,4-benzoquionone was removed via sublimation under vacuum at 100°C. This yielded the desired product as a yellow powder (114 mg, 87% yield). ^1H NMR (500 MHz, Acetone) δ 7.42 (d, J = 7.3 Hz, 2H), 7.19 (d, J = 8.1 Hz, 2H), 6.91 (t, J = 7.7 Hz, 2H), 6.63 (d, J = 2.7 Hz, 2H), 6.60 (s, 1H), 5.86 (s, 1H). ^{13}C NMR (126 MHz, CDCl3) δ 145.87, 142.66, 135.67, 135.25, 129.67, 127.32, 123.43, 120.07, 48.17, 46.54. MS-MALDI (m/z) calculated = 441.9, found = 441.9

HQ-Br$_2$: BQ-Br$_2$ (80 mg), zinc dust (250 mg), THF (10 mL), and AcOH (10 mL) were added to a 250 mL round bottom flask and were sonicated for 30 minutes. The crude reaction mixture was then added to a separation funnel and was extracted with DCM/H_2O three times. The organic layer was then dried down and subjected to silica gel chromatography (short plug, 20% hexanes in DCM) yielding the desired product as a white solid (80 mg, quantitative conversion). ^1H NMR

(500 MHz, Acetone) δ 7.98 (d, J = 1.4 Hz, 1H), 7.89 (s, 1H), 7.33 (d, J = 7.3 Hz, 2H), 7.12 (dt, J = 8.2, 1.3 Hz, 2H), 6.83 (td, J = 7.8, 1.6 Hz, 2H), 6.77 (d, J = 1.7 Hz, 1H), 6.32 (t, J = 2.0 Hz, 2H), 5.89 (d, J = 1.7 Hz, 1H). ^{13}C NMR (126 MHz, Acetone) δ 148.77, 144.91, 128.65, 127.00, 123.09, 118.74, 113.78, 113.35, 48.22, 46.16. MS-MALDI (m/z) calculated = 444.0, found = 444.2.

Bzn$_2$HQ-Br$_2$: HQ-Br$_2$ (50 mg), K_2CO_3 (67 mg), benzyl bromide (0.15 mL), and acetone (10 mL) were added to a 50 mL round bottom flask equipped with a magnetic stir bar and condenser. The reaction mixture was then stirred under reflux overnight under nitrogen at 60°C. The desired product was then purified using silica gel chromatography (20% DCM in hexanes) yielding the desired product as a white solid (65 mg, 93% yield). ^{1}H NMR (500 MHz, CDCl3) δ 7.59 (d, J = 7.6 Hz, 2H), 7.44 – 7.37 (m, 7H), 7.29 (t, J = 7.8 Hz, 3H), 7.19 (d, J = 8.1 Hz, 2H), 7.00 (s, 1H), 6.84 (t, J = 7.7 Hz, 2H), 6.56 (s, 2H), 5.91 (s, 1H), 5.10 (s, 2H), 5.02 (s, 2H). ^{13}C NMR (126 MHz, CDCl3) δ 147.97, 144.62, 128.97, 128.63, 128.46, 127.42, 127.00, 126.72, 122.87, 48.41, 46.32. MS-MALDI (m/z) calculated = 624.0, found = 623.9.

Dipyrromethane: pyrrole (150 mL) and paraformaldehyde (750 mg) were added to a 500 mL round bottom flask equipped with a magnetic stir bar and were stirred un nitrogen at 55°C for twenty minutes. $InCl_3$ (480 mg) was then added and the mixture was stirred for an additional 2.5 hours at 55°C under nitrogen. The heat was then removed, NaOH (2.5 g) was added to the reaction, and the mixture was stirred for another hour at room temperature. The pyrrole was then removed using rotary evaporation and the desired product was purified using silica gel chromatography (short plug, pure DCM). This yielded the desired product as a white solid (2.3 g, 44% yield). ^{1}H NMR (500 MHz, CDCl3) δ 7.79 (s, 2H), 6.68 – 6.59 (m, 2H), 6.14 (p, J = 2.9 Hz, 2H), 6.02 (dd, J = 4.7, 2.3 Hz, 2H), 3.98 – 3.93 (m, 2H). ^{13}C NMR (126 MHz, CDCl3) δ 128.73, 117.11, 107.62, 106.58. 53.41.

R_2-Por: Dipyrromethane (1.5 g), octanal (1.03 g), and DCM (1.2 L) were added to a 2 L round bottom flask equipped with a magnetic stir bar. The reaction mixtures was bubbled with N_2 gas. TFA (0.425 mL) was then added dropwise over the course of 20 minutes and the reaction was stirred at room temperature under nitrogen for 3.5 hours. 2,3-dichloro-5,6-dicyano-1,4-benzoquionone (3.1 g) was then added and the mixture was stirred for 1 hour. Triethylamine (12.5 mL) was then added to quench the reaction. The desired product was then purified using silica gel chromatography (DCM/Hexanes, 1:1) yielding the desired product as a purple solid (886 mg, 17% yield). ^{1}H NMR (500 MHz, CDCl3) δ 10.15 (s, 2H), 9.56 (d, J = 4.5 Hz, 4H), 9.39 (d, J = 4.5 Hz, 4H), 5.03 – 4.96 (m, 4H), 2.58 – 2.48 (m, 4H), 1.51 (p, J = 5.8 Hz, 7H), 1.33 (pd, J = 7.0, 4.4 Hz, 8H), 0.87 (td, J = 5.9, 4.8, 2.8 Hz, 7H), -2.94 (s, 2H). ^{13}C NMR (126 MHz, CDCl3) δ 147.49, 144.20, 131.88, 127.83, 118.86, 104.26, 38.69, 34.68, 31.95, 30.58, 29.42, 22.72, 14.11 (d, J = 5.9 Hz). MS-MALDI (m/z) calculated = 506.3, found = 506.3.

R_2-Por-Br: R_2-Por (250 mg), pyridine (0.11 mL) and chloroform (100 mL) were added to a 500 mL round bottom flask equipped with a magnetic stir bar and nitrogen gas was bubbled through for 10 minutes. N-bromosuccinimide (130 mg) was separately dissolved in chloroform (50 mL) and was added slowly to the reaction mixture using a slow addition funnel over the course of 1 hour. After 7 minutes of stirring, acetone (15 mL) was added to quench the reaction. The mixture was then washed with DCM/H_2O, dried with sodium sulfate, and the desired product was purified using silica gel chromatography (30 % DCM in hexanes). This yielded the desired product as a purple solid (225 mg, 78% yield). ^{1}H NMR (500 MHz, CDCl3) δ 10.01 (s, 1H), 9.78 (d, J = 4.8

Hz, 2H), 9.48 (dd, J = 4.8, 1.5 Hz, 4H), 9.29 (d, J = 4.6 Hz, 2H), 4.95 – 4.86 (m, 4H), 2.49 (p, J = 7.5 Hz, 6H), 1.77 (p, J = 7.7 Hz, 6H), 1.52 – 1.49 (m, 6H), 1.33 (dt, J = 7.2, 3.6 Hz, 8H), -2.87 (s, 2H). ^{13}C NMR (126 MHz, Acetone) δ 164.49, 159.56, 158.43, 139.97, 139.47, 138.24, 136.53, 123.46, 119.71, 114.46, 110.73, 105.45, 101.21, 31.77 (d, J = 3.6 Hz), 29.33 (d, J = 2.4 Hz), 28.71, 28.64, 27.60 (d, J = 6.2 Hz), 22.74 (d, J = 2.9 Hz), 14.10 (d, J = 2.1 Hz). MS-MALDI (m/z) calculated = 584.3, found = 582.2.

R_2-R'-Por: R_2-Por-Br (225 mg), phenylboronic acid (400 mg), THF (100 mL),and Na_2CO_3 (300 mg) were added to a two-neck 250 mL round bottom flask equipped with a magnetic stir bar and condenser. The mixture was then subjected to three cycles of freeze-pump-thaw. $Ph(PPh_3)_4$ (20 mg) was then added and the mixture was stirred under reflux overnight under nitrogen at 70ºC. The crude reaction mixture was then subjected to silica gel chromatography (30% DCM in hexanes) yielding the desired product as a purple/blue solid (210 mg, 93% yield). ^{1}H NMR (500 MHz, CDCl3) δ 10.15 (s, 2H), 9.56 (d, J = 4.5 Hz, 4H), 9.39 (d, J = 4.5 Hz, 4H), 5.03 – 4.96 (m, 4H), 2.58 – 2.48 (m, 4H), 1.85 – 1.74 (m, 4H), 1.51 (p, J = 5.8 Hz, 6H), 1.37 – 1.31 (m, 8H), 0.87 (td, J = 5.9, 4.8, 2.8 Hz, 4H) -2.98 (s, 2H). ^{13}C NMR (126 MHz, CDCl3) δ 143.09, 135.79, 134.39, 131.79 (d, J = 32.9 Hz), 128.27, 127.60, 127.18, 126.42, 125.54, 119.35, 103.81, 38.71, 34.99, 34.25, 31.93, 31.61, 30.55, 30.34, 29.41, 22.70 (d, J = 5.5 Hz), 21.20, 14.13 (d, J = 1.6 Hz). MS-MALDI (m/z) calculated = 582.4, found = 582.2

R_2-R'-Por-Br: R_2-R'-Por (200 mg), N-bromosuccinimide (60 mg), and DCM (40 mL) were added to a 250 mL round bottom flask equipped with a magnetic stir bar. The reaction mixture was then stirred for 3 hours at room temperature under nitrogen. The reaction mixture was then subjected to silica gel chromatography (30% DCM in hexanes) yielding the desired product as a purple/blue solid (210 mg, 92% yield). ^{1}H NMR (500 MHz, CDCl3) δ 9.73 – 9.68 (m, 2H), 9.45 (dd, J = 5.0, 2.6 Hz, 2H), 9.34 (d, J = 4.8 Hz, 2H), 8.79 (d, J = 4.7 Hz, 2H), 8.13 (dd, J = 6.7, 1.8 Hz, 2H), 7.77 – 7.70 (m, 3H), 4.93 – 4.85 (m, 4H), 2.47 (p, J = 8.0 Hz, 5H), 1.78 – 1.67 (m, 7H), 1.49 (tdd, J = 7.3, 4.1, 2.6 Hz, 7H), 1.16 – 0.98 (m, 7H), -2.70 (s, 2H). ^{13}C NMR (126 MHz, CDCl3) δ 206.11, 146.11, 133.26, 127.79, 127.23 (d, J = 38.1 Hz), 125.69, 125.50, 124.95, 52.43, 40.94, 30.91, 30.79, 29.62, 28.68, 28.35, 21.71, 21.61, 13.14. MS-MALDI (m/z) calculated = 660.3, found = 660.3.

R_2-R'-ZnPor-Br: R_2-R'-Por-Br (200 mg), zinc acetate dihydrate (1 g), chloroform (25 mL), and MeOH (7 mL) were added to a 100 mL round bottom flask and stirred overnight at room temperature under nitrogen. The mixture was then subjected to silica gel chromatography (short plug, 50% DCM in hexanes) yielding the desired product as a purple/blue solid (218 mg, quantitative conversion). ^{1}H NMR (500 MHz, CDCl3) δ 9.57 (dd, J = 4.6, 1.1 Hz, 2H), 9.37 (d, J = 4.7 Hz, 2H), 9.32 (dd, J = 4.8, 1.2 Hz, 2H), 8.86 (d, J = 4.6 Hz, 2H), 8.19 – 8.13 (m, 2H), 7.77 – 7.72 (m, 3H), 4.77 – 4.71 (m, 4H), 2.48 – 2.39 (m, 2H), 1.77 (p, J = 7.7 Hz, 5H), 1.39 – 1.29 (m, 10H), 0.96 – 0.83 (m, 9H). ^{13}C NMR (126 MHz, CDCl3) δ 150.35, 134.30, 132.85, 132.52, 129.62, 128.94, 126.54, 121.35, 39.00, 35.57, 31.95, 30.65, 29.39, 14.15. MS-MALDI (m/z) calculated = 722.2, found = 722.2.

R_2-R'-ZnPor-ethyne-TMS: Trimethylsilylacetylene (400 mg, 0.56 mL) and THF (10 mL) were added to a two-neck round bottom flask equipped with a magnetic stir bar and condenser and the mixture was subjected to three cycles of freeze-pump-thaw. The mixture was then cooled at -78°C and n-buLi (2.5 M in hexanes) (212 mg, 1.56 mL) was added dropwise. The reaction mixture was then returned back to room temperature. In a separate flask, $ZnCl_2$ (0.5M in THF) was subjected to three cycles of freeze-pump-thaw, after which the $ZnCl_2$ was added to the trimethylsilylacetylene-containing flask via syringe. In a separate flask R_2-R'-ZnPor-Br (200 mg) and $Ph(PPh_3)_4$ (20 mg) were subjected to three cycles of vacuum/N_2 gas purging. THF was then added to the porphyrin, catalyst mixture in order to add it to the trimethylsilylacetylene-containing flask via syringe. The reaction was then stirred at 50°C overnight under nitrogen. The reaction mixture was then rinsed with DCM/H_2O and the organic layer was concentrated and subjected to silica gel chromatography (30% DCM in hexanes) yielding the desired product as a blue solid (172 mg, 84% yield). ^{1}H NMR (500 MHz, CDCl3) δ 9.74 (d, J = 4.6 Hz, 2H), 9.52 (d, J = 4.6 Hz, 2H), 9.42 (d, J = 4.7 Hz, 2H), 8.86 (d, J = 4.6 Hz, 2H), 8.17 – 8.10 (m, 2H), 7.80 – 7.68 (m, 4H), 4.94 – 4.87 (m, 4H), 2.49 (q, J = 7.8 Hz, 4H), 1.83 – 1.72 (m, 5H), 1.38 – 1.27 (m, 11H), 1.26 – 1.15 (m, 3H), 0.52 (dt, J = 6.6, 4.3 Hz, 1H), 0.49 – 0.41 (m, 2H). ^{13}C NMR (126 MHz, CDCl3) δ 207.00, 174.79, 134.29, 132.52, 129.77, 128.96, 126.50, 67.79, 53.43, 34.68, 31.60, 30.93, 29.07, 22.69 (d, J = 8.4 Hz), 20.37, 14.12, 11.43. MS-MALDI (m/z) calculated = 740.3, found = 740.3.

R_2-R'-ZnPor-ethyne-H: R_2-R'-ZnPor-ethyne-TMS (200 mg), K_2CO_3, THF (20 mL), and EtOH (20 mL) were added to a 100 mL round bottom flask equipped with a magnetic stir bar and the reaction mixture was covered with foil and stirred overnight at room temperature under air. The mixture was then subjected to silica gel chromatography (5% THF in hexanes), careful to limit exposure to light, yielding the desired product as a blue solid (180 mg, quantitative conversion). The product was brought to the next step without NMR characterization to limit exposure to air and/or light. MS-MALDI (m/z) calculated = 668.3, found = 668.4

Protected ZnPor Dimer: R_2-R'-ZnPor-ethyne-H (150 mg), Bzn_2HQ-Br_2 (30 mg), triethylamine (1.5 mL) and THF (20 mL) were added to a two-neck round bottom flask equipped with a magnetic stir bar and condenser. The mixture was then subjected to three cycles of freeze-pump-thaw. When the mixture returned to room temperature $Pd(PPh_3)_4$ (15 mg) was added under positive nitrogen pressure. The reaction was then stirred under reflux overnight under nitrogen at 70°C. The crude reaction mixture was then subjected to silica gel chromatography (3.5% EtOAc in hexanes and 25% DCM in hexanes) yielding the desired product as a green solid (48 mg, 12% yield). ^{1}H NMR (500 MHz, Acetone) δ 9.66 (d, J = 4.4 Hz, 4H), 8.25 (d, J = 4.4 Hz, 4H), 8.10 – 7.96 (m, 6H), 7.79 – 7.64 (m, 10H), 7.62 (d, J = 7.6 Hz, 3H), 7.54 (d, J = 7.4 Hz, 2H), 7.44 (d, J = 8.6 Hz, 1H), 7.41 – 7.30 (m, 5H), 7.27 (dd, J = 8.4, 6.2 Hz, 3H), 7.19 – 7.09 (m, 2H), 6.72 – 6.56 (m, 2H), 6.34 (s, 1H), 5.40 (s, 2H), 5.22 (t, J = 4.9 Hz, 3H), 5.14 (s, 2H), 4.98 (s, 1H) 4.89 (t, J = 8.2 Hz, 8H), 2.41 (q, J = 8.0 Hz, 12H), 1.70 (p, J = 7.7 Hz, 8H), 1.43 – 1.34 (m, 12H), 1.23 (m, J = 7.4, 4.1 Hz, 20H). ^{13}C NMR (126 MHz, Acetone) δ 148.31, 147.51, 138.92, 138.77, 138.17, 137.98 – 137.86 (m), 137.80, 137.45, 136.78 (d, J = 4.5 Hz), 136.53 (d, J = 6.0 Hz), 136.20, 134.91, 133.81, 132.31, 131.48 (d, J = 1.9 Hz), 129.86, 128.71, 128.57, 128.39, 127.94, 127.78 (d, J = 3.6 Hz), 127.16, 126.20, 125.45, 120.31, 119.69 (d, J = 2.4 Hz), 118.66, 117.50, 114.26 (d, J = 4.3 Hz), 114.12, 112.93, 111.87, 111.29, 111.22, 110.71, 33.02, 31.75, 30.29, 29.15, 28.99, 26.97, 26.68, 22.65, 14.10. MS-MALDI (m/z) for $C_{118}H_{110}N_8O_2Zn_2$: calculated = 1798.73346, found = 1798.72669.

$(Zn\text{-}Por)_2$-BQ: Protected ZnPor Dimer (20 mg) and DCM (10 mL) were added to a 50 mL round bottom flask equipped with a magnetic stir bar and N_2 gas was bubbled through it while the reaction mixtures was cooled with an ice bath for 20 minutes. BBr_3 (0.32 mL, 20 eq.) was then added and the mixture was stirred under nitrogen for two hours. Next, MeOH (3 mL) was added. The crude reaction mixture was then rinsed three times with DCM/H_2O and the organic layer was dried down. The dried down organic layer (green solid), p-chloranil (50 mg) and DCM (10 mL) were then added to a 50 mL round bottom flask equipped with a magnetic stir bar and the reaction mixture was stirred overnight at room temperature. The crude reaction mixture was then subjected to silica gel chromatography (20% DCM in hexanes) yielding the desired product as a green solid (11 mg, 41% yield). ^{1}H NMR (500 MHz, Acetone) δ 9.53 (d, J = 4.4 Hz, 4H), 8.28 (d, J = 4.8 Hz, 4H), 8.14 (s, 4H), 8.06 (d, J = 6.8 Hz, 2H), 7.81 – 7.67 (m, 10H), 7.57 (d, J = 46.5 Hz, 1H), 7.36 – 7.24 (m, 2H), 6.93 – 6.77 (m, 2H), 6.19 (d, J = 2.3 Hz, 1H), 4.92 (t, J = 8.2 Hz, 8H), 2.42 (q, J = 8.0 Hz, 12H), 1.69 (p, J = 7.7 Hz, 8H), 1.47 – 1.36 (m, 12H), 1.22 (dt, J = 7.4, 4.1 Hz, 20H). ^{13}C NMR (126 MHz, Acetone) δ 185.01, 184.42, 143.84, 141.88, 138.92, 138.70, 138.43, 138.05, 137.92, 137.60, 136.53 (d, J = 6.0 Hz), 136.20, 134.91, 133.81, 133.00, 132.32, 131.47, 130.31, 129.43, 128.38, 127.92, 127.80, 127.16, 122.70, 119.65, 118.66, 118.27, 114.12, 111.87, 111.29, 111.22, 93.42, 86.63, 41.32, 39.63, 33.02, 31.77, 29.15, 28.94, 26.98, 26.68, 22.66, 14.08 HRMS (m/z) for $C_{104}H_{96}N_8O_2Zn_2$: calculated = 1616.62391, found 1616.62427.

1-bromo-9,10-anthraquionone: $CuBr_2$ (2.5 g), tert-butyl nitrite (1.38 g), and acetonitrile (40 mL) were added to a 250 mL round bottom flask equipped with a magnetic stir bar and the reaction mixture was heated to 65°C. 1-amino-9,10-anthraquinone (2.2 g) was then added over the course of 1 hour and then the reaction was heated to 90°C and stirred under nitrogen for 3 hours. The reaction mixture was then cooled to room temperature and added to a beaker with 1M HCl (100 mL). The precipitate was then collected via vacuum filtration and the solid was subjected to silica gel chromatography (pure DCM) yielding the desired product as a yellow solid (1.9 g, 68% yield). This material was brought straight to the next step without characterization.

1-bromoanthracene: 1-bromo-9,10-anthraquionone (1.9 g) and isopropanol (30 mL) were added to a 100 mL round bottom flask and were cooled with an ice bath. Next, $NaBH_4$ (0.8 g) was added and the mixture was stirred for 3 hours. H_2O (10 mL) was then added and the mixture was stirred an additional 3 hours. The organic material was then extracted using toluene. After removing the toluene, acetic acid (90 mL) and $SnCl_2$ (4.2 g) and the organic material were added to a 250 mL round bottom flask equipped with a magnetic stir bar and the mixture was stirred at 100°C for 2 hours. The mixture was then cooled to room temperature and washed with DCM/H_2O three times. The organic layer was then collected and subjected to silica gel chromatography (5% EtOAc in hexanes) yielding the desired product (1.2 g, 71% yield). ^{1}H NMR (500 MHz, Acetone) δ 8.72 (s, 1H), 8.50 (s, 1H), 8.12 – 8.06 (m, 1H), 8.01 (d, J = 8.4 Hz, 2H), 7.75 (d, J = 7.1 Hz, 1H), 7.52 – 7.40 (m, 2H), 7.28 (dd, J = 8.5, 7.1 Hz, 1H). ^{13}C NMR (126 MHz, Acetone) δ 132.37, 132.18, 131.94, 130.13, 128.60, 128.24, 128.11, 127.25, 127.03, 126.61, 125.83, 125.48, 121.49. MS-MALDI (m/z) calculated = 256.0, found = 255.9.

BQ-Br: 1-bromoanthracene (100 mg), 1,4-benzoquinone (300 mg), and toluene (100 mL) were added to a 250 mL round bottom flask equipped with a magnetic stir bar and condenser and the mixture was stirred under reflux overnight under nitrogen at 120°C. The product was then purified using silica gel chromatography (25% DCM in hexanes) and then leftover 1,4-benzoquionone was removed via sublimation under vacuum at 100°C. This yielded the desired product as a yellow powder (110 mg, 71% yield). ^{1}H NMR (500 MHz, Acetone) δ 7.43 – 7.38 (m, 3H), 7.15 (d, J = 8.1 Hz, 1H), 6.98 – 6.93 (m, 2H), 6.87 (t, J = 7.7 Hz, 1H), 6.60 (s, 2H), 6.09 (s, 1H), 5.79 (s, 1H). ^{13}C NMR (126 MHz, Acetone) δ 183.06, 182.95, 151.73, 150.86, 146.88, 143.92, 143.45, 142.81, 135.54 (d, J = 3.8 Hz), 129.03, 127.41, 125.87, 125.77, 124.59 (d, J = 4.3 Hz), 123.69, 118.81, 47.59, 46.76. MS-MALDI (m/z) calculated = 362.0, found = 362.2.

HQ-Br: BQ-Br (60 mg), zinc dust (200 mg), THF (5 mL), and AcOH (5 mL) were added to a 50 mL round bottom flask and were sonicated for 30 minutes. The crude reaction mixture was then added to a separation funnel and was extracted with DCM/H_2O three times. The organic layer was then dried down and subjected to silica gel chromatography (short plug, 20% hexanes in DCM) yielding the desired product as a white solid (60 mg, quantitative conversion). ^1H NMR (500 MHz, Acetone) δ 8.72 (s, 1H), 8.51 (s, 1H), 8.13 – 8.07 (m, 1H), 8.03 – 7.97 (m, 2H), 7.88 (s, 1H), 7.76 (dd, J = 7.1, 1.0 Hz, 1H), 7.50 – 7.43 (m, 2H), 7.28 (dd, J = 8.5, 7.1 Hz, 1H), 5.49 (s, 1H), 2.67 (s, 1H), 2.64 (t, J = 1.1 Hz, 1H). ^{13}C NMR (126 MHz, Acetone) δ 147.60, 146.55, 140.78, 139.28, 132.72, 130.07, 129.75, 128.80, 126.56, 125.52, 125.43, 123.02, 117.07 (d, J = 2.6 Hz), 47.15, 46.68. MS-MALDI (m/z) calculated = 364.0, found = 364.0.

Bzn$_2$HQ-Br: HQ-Br (60 mg), K_2CO_3 (67 mg), benzyl bromide (0.15 mL), and acetone (10 mL) were added to a 50 mL round bottom flask equipped with a magnetic stir bar and condenser. The reaction mixture was then stirred under reflux overnight under nitrogen at 60°C. The desired product was then purified using silica gel chromatography (20% DCM in hexanes) yielding the desired product as a white solid (82 mg, 91% yield). ^1H NMR (500 MHz, Acetone) δ 7.51 – 7.46 (m, 2H), 7.43 – 7.39 (m, 2H), 7.34 – 7.20 (m, 8H), 7.11 (dd, J = 8.1, 1.0 Hz, 1H), 6.91 – 6.89 (m, 2H), 6.82 (dd, J = 8.1, 7.3 Hz, 1H), 6.61 (s, 2H), 6.35 (s, 1H), 5.96 (s, 1H), 5.49 (s, 1H), 5.02 – 4.99 (m, 4H). ^{13}C NMR (126 MHz, Acetone) δ 148.13, 144.28, 141.29, 139.68, 139.51, 137.00, 136.93, 132.72, 131.78 (d, J = 1.4 Hz), 128.80, 128.59 (d, J = 6.7 Hz), 128.51, 127.70, 126.56, 126.31, 125.52, 125.43, 123.02, 113.45 (d, J = 1.7 Hz), 71.85 (d, J = 2.6 Hz), 47.10, 46.82. MS-MALDI (m/z) calculated = 544.1, found = 544.0.

Protected Zn-Por Monomer: R_2-R'-ZnPor-ethyne-H (30 mg), Bzn_2HQ-Br (30 mg), triethylamine (0.3 mL) and THF (10 mL) were added to a two-neck round bottom flask equipped with a magnetic stir bar and condenser. The mixture was then subjected to three cycles of freeze-pump-thaw. When the mixture returned to room temperature $Pd(PPh_3)_4$ (7 mg) was added under positive nitrogen pressure. The reaction was then stirred under reflux overnight under nitrogen at 70°C. The crude reaction mixture was then subjected to silica gel chromatography (5% EtOAc in hexanes and 40% DCM in hexanes) yielding the desired product as a green/blue solid (42 mg, 84% yield). ^1H NMR (500 MHz, Acetone) δ 10.01 (d, J = 4.2 Hz, 2H), 9.55 (d, J = 4.5 Hz, 2H), 9.43 (d, J = 4.4 Hz, 2H), 8.69 – 8.65 (m, 2H), 8.05 (d, J = 6.8 Hz, 2H), 7.79 – 7.69 (m, 4H), 7.55 – 7.46 (m, 4H), 7.32 (dd, J = 16.6, 9.1 Hz, 3H), 7.29 – 7.22 (m, 3H), 7.17 (t, J = 7.6 Hz, 1H), 7.02 (dt, J = 22.1, 7.4 Hz, 2H), 6.65 (s, 2H), 6.25 (t, J = 7.5 Hz, 2H), 6.21 – 6.11 (m, 2H), 5.18 (s, 2H), 5.07 (s, 2H), 4.91 (t, J = 8.2 Hz, 4H), 2.41 (q, J = 8.0 Hz, 6H), 1.73 (p, J = 7.7 Hz, 4H), 1.46 – 1.38 (m, 6H), 1.23 (dt, J = 7.4, 4.1 Hz, 10H). ^{13}C NMR (126 MHz, Acetone) δ 151.56, 150.75, 149.98, 148.92, 134.11, 132.01, 130.82, 130.03, 128.64, 128.52, 128.26, 127.81, 127.75, 127.52, 127.44, 126.77, 126.67, 126.44, 125.43 (d, J = 11.6 Hz), 121.74, 70.99, 70.57, 47.83, 39.23, 35.24, 31.85, 30.33, 29.69, 22.49, 13.48. HRMS (m/z) for $C_{76}H_{68}N_4O_2Zn$: calculated = 1132.46337, found = 1132.46179.

Zn-Por-BQ: Protected Zn-Por monomer (20 mg) and DCM (10 mL) were added to a 50 mL round bottom flask equipped with a magnetic stir bar and N_2 gas was bubbled through it while the reaction mixtures was cooled with an ice bath for 20 minutes. BBr_3 (0.12 mL,) was then added and the mixture was stirred under nitrogen for two hours. Next, MeOH (0.7 mL) was added. The crude reaction mixture was then rinsed three times with DCM/H_2O and the organic layer was dried down.

The dried down organic layer (green/blue solid), p-chloranil (20 mg) and DCM (10 mL) were then added to a 50 mL round bottom flask equipped with a magnetic stir bar and the reaction mixture was stirred overnight at room temperature. The crude reaction mixture was then subjected to silica gel chromatography (20% DCM in hexanes) yielding the desired product as a green/blue solid (11 mg, 66% yield). ^{1}H NMR (500 MHz, Acetone) δ 10.04 – 9.99 (m, 2H), 9.70 (d, J = 4.6 Hz, 2H), 9.45 (d, J = 4.7 Hz, 2H), 8.68 (t, J = 3.0 Hz, 2H), 8.05 (d, J = 6.8 Hz, 2H), 7.79 – 7.57 (m, 3H), 7.54 (d, J = 6.9 Hz, 1H), 7.22 (t, J = 7.4 Hz, 1H), 7.07 – 6.94 (m, 3H), 6.82 – 6.68 (m, 2H), 5.97 (s, 1H), 4.91 (t, J = 8.2 Hz, 4H), 2.41 (q, J = 8.0 Hz, 6H), 1.73 (p, J = 7.7 Hz, 4H), 1.46 – 1.38 (m, 6H), 1.23 (dt, J = 7.4, 4.1 Hz, 10H). ^{13}C NMR (126 MHz, Acetone) δ 184.68, 184.49, 143.86, 142.56, 141.47, 140.94, 139.96, 137.79, 137.40, 134.06, 131.61, 129.89, 129.53, 128.22, 127.73, 126.45, 126.03, 125.49, 124.37, 123.05, 119.66, 93.36, 86.20, 47.51, 46.29, 31.63, 31.07, 29.58, 29.12, 27.35, 27.13, 22.69, 14.09. HRMS (m/z) $C_{62}H_{56}N_4O_2Zn$: calculated = 952.36947, found = 952.37011.

3.6.2 Steady State Analysis

Weller Equation Analysis

The Weller equation[85] was applied to the electrochemistry data to correct for the different dielectric constants between THF, the solvent electrochemical potentials were measured in, and 1,4-dioxane, the solvent transient experiments were performed in, as follows:

$$\Delta G = E_{ox} - E_{red} - \left(\frac{e^2}{r_{DA}\varepsilon_s}\right) + \left(e^2\left(\frac{1}{2r_D} + \frac{1}{2r_A}\right)\left(\frac{1}{\varepsilon_s} - \frac{1}{\varepsilon_{sp}}\right)\right) \qquad \text{(Eqn. S3.2)}$$

where E_{ox} and E_{red} are the oxidation and reduction potentials of the donor and acceptor, respectively, in the solvent electrochemical measurements were taken with a static dielectric constant ε_{sp}, e is the charge of an electron, r_{DA} is the ion pair distance, r_D and r_A are the ionic radii (both calculated from the structures given by DFT calculations), and ε_s is the static dielectric constant of the solvent we are comparing against.

Spectroelectrochemistry.

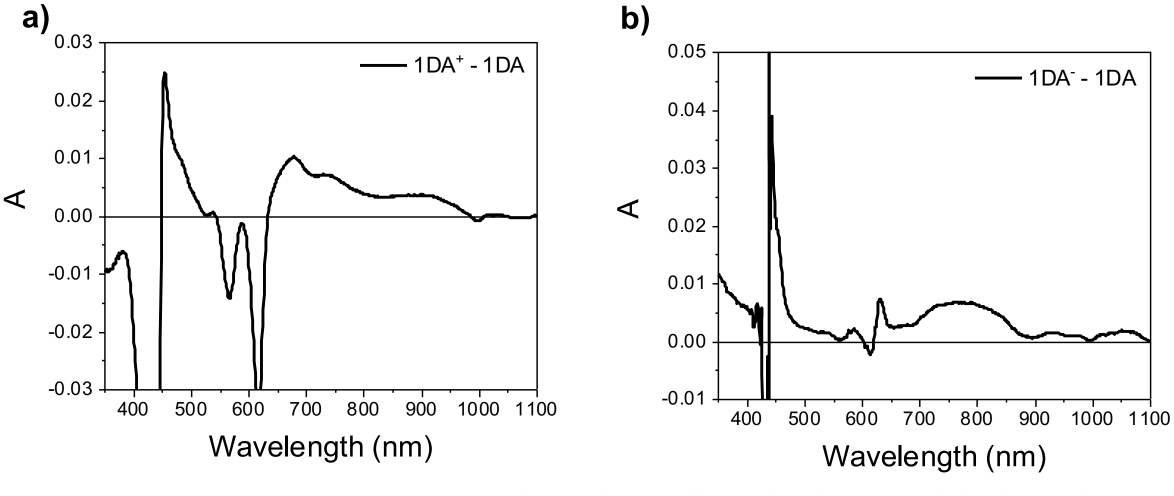

Figure S3.9 The absorption spectra of (a) electrochemically oxidized **1DA** and (b) electrochemically reduced **1DA** after subtracting the ground state**1DA** absorption, all collected in DCM. This represents the features expected in transient experiments upon charge separation to form the radical pair.

Fourier Transform Infrared Spectroscopy

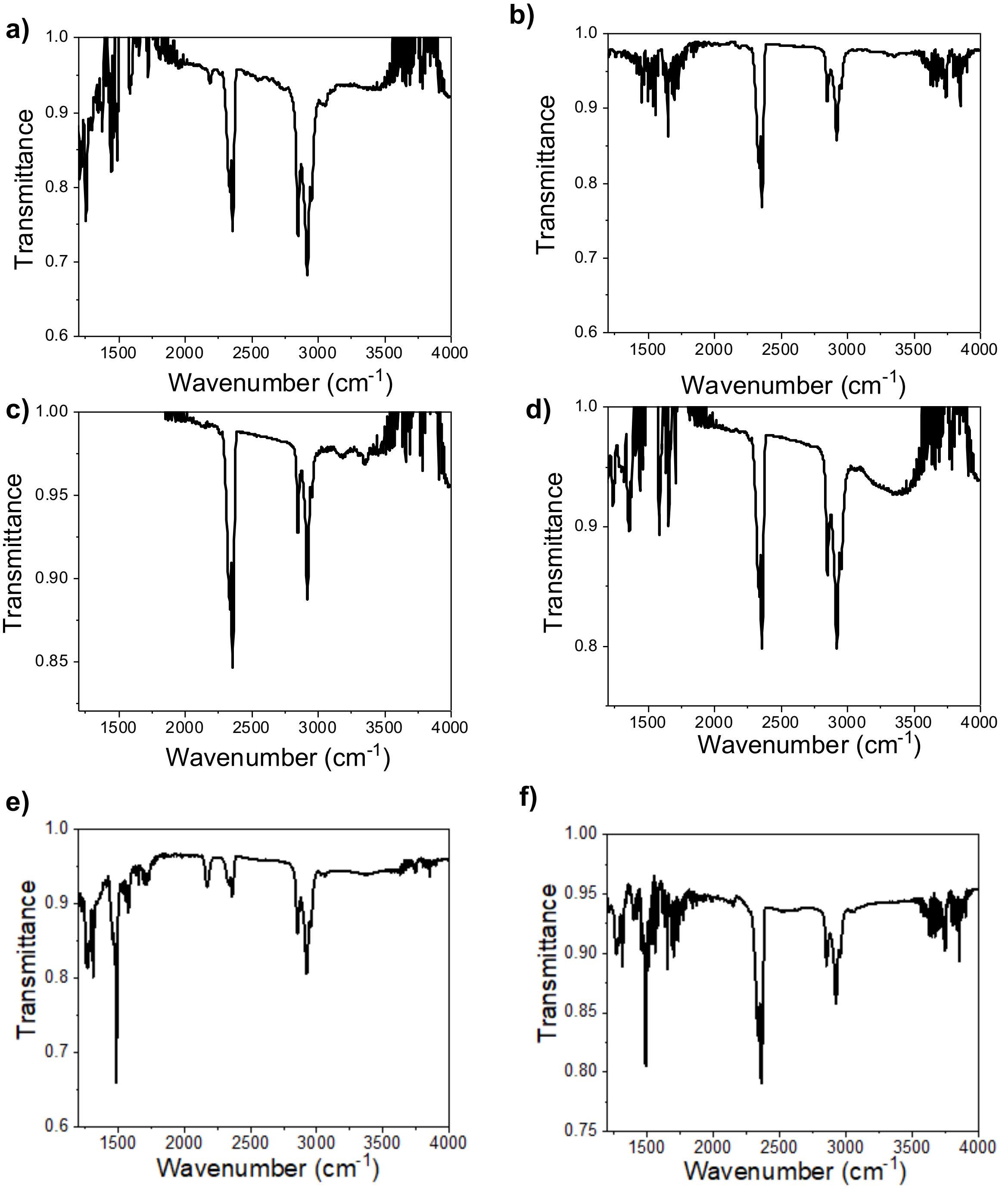

Figure S3.10 FTIR spectra taken in 1,4-dioxane for (a) **1P**, (b) **1DA** (c) **2P** (d) **2DA**, (e) chemically singly oxidized **1P** and (f) chemically singly oxidized **2P**.

3.6.3 Excited State Analysis

Kinetic Fitting Methodology

All kinetic analysis was performed using home written programs in MATLAB and was based on a global fit to selected single-wavelength kinetics. An assumption of a uniform instrument response of $w = 300$ fs for fsTA (full width at half maximum, FWHM) across the frequency domain and a fixed time-zero (t_0) is implicit in the global analysis. Kinetic data from the entire 320-850 nm window were fitted using the global analysis described below. The population dynamics in toluene and THF overlap with the non-resonant solvent response, which was modeled as the decay of a separate population with a fixed decay rate smaller than the instrument response. Each specified wavelength was given an initial amplitude that is representative of the spectral intensity at time t_0. The rate constants and t_0 were shared among the various kinetic data and varied globally across the kinetic data to fit to the models described below. Datasets were globally fit to a specified kinetic model and the resultant populations were used to deconvolute the dataset and reconstruct the evolution-associated spectra. Below are the first-order kinetic models of each system with rate matrix K and initial species population vector P:

14. fsTA of **1P** (VIS):

$$K = \begin{pmatrix} -1/0.1 & 0 & 0 \\ 0 & -k_{A\to B} & 0 \\ 0 & k_{A\to B} & -k_{B\to GS} \end{pmatrix} \quad P = \begin{pmatrix} 1 \\ 1 \\ 0 \end{pmatrix} \qquad \text{(Eqn. S3.3)}$$

15. fsTA of **2P**(VIS):

$$K = \begin{pmatrix} -1/0.1 & 0 & 0 \\ 0 & -k_{A\to B} & 0 \\ 0 & k_{A\to B} & -k_{B\to GS} \end{pmatrix} \quad P = \begin{pmatrix} 1 \\ 1 \\ 0 \end{pmatrix} \qquad \text{(Eqn. S3.4)}$$

16. fsTA of **1P** (NIR):

$$K = \begin{pmatrix} -1/0.1 & 0 & 0 \\ 0 & -k_{A\to B} & 0 \\ 0 & k_{A\to B} & -k_{B\to GS} \end{pmatrix} \quad P = \begin{pmatrix} 1 \\ 1 \\ 0 \end{pmatrix} \qquad \text{(Eqn. S3.5)}$$

17. fsTA of **2P** (NIR):

$$K = \begin{pmatrix} -1/0.1 & 0 & 0 \\ 0 & -k_{A\to B} & 0 \\ 0 & k_{A\to B} & -k_{B\to GS} \end{pmatrix} \quad P = \begin{pmatrix} 1 \\ 1 \\ 0 \end{pmatrix} \qquad \text{(Eqn. S3.6)}$$

18. fsTA of **1DA** (NIR):

$$K = \begin{pmatrix} -1/0.1 & 0 & 0 \\ 0 & -k_{A\to B} & 0 \\ 0 & k_{A\to B} & -k_{B\to GS} \end{pmatrix} \quad P = \begin{pmatrix} 1 \\ 1 \\ 0 \end{pmatrix} \qquad \text{(Eqn. S3.7)}$$

19. nsTA of **2DA** (NIR):

$$K = \begin{pmatrix} -1/0.1 & 0 & 0 & 0 \\ 0 & -k_{A\to B} & 0 & 0 \\ 0 & k_{A\to B} & -k_{B\to C} & 0 \\ 0 & 0 & k_{B\to C} & -k_{C\to GS} \end{pmatrix} \quad P = \begin{pmatrix} 1 \\ 1 \\ 0 \\ 0 \end{pmatrix} \qquad \text{(Eqn. S3.8)}$$

20. fsTAM of **1DA** (VIS):

$$K = \begin{pmatrix} -1/0.1 & 0 & 0 \\ 0 & -k_{A\to B} & 0 \\ 0 & k_{A\to B} & -k_{B\to GS} \end{pmatrix} \quad P = \begin{pmatrix} 1 \\ 1 \\ 0 \end{pmatrix} \qquad \text{(Eqn. S3.9)}$$

21. fsTAM of **2DA** (VIS):

$$K = \begin{pmatrix} -1/0.1 & 0 & 0 \\ 0 & -k_{A\rightarrow B} & 0 \\ 0 & k_{A\rightarrow B} & -k_{B\rightarrow GS} \end{pmatrix} \quad P = \begin{pmatrix} 1 \\ 1 \\ 0 \end{pmatrix} \qquad \text{(Eqn. S3.10)}$$

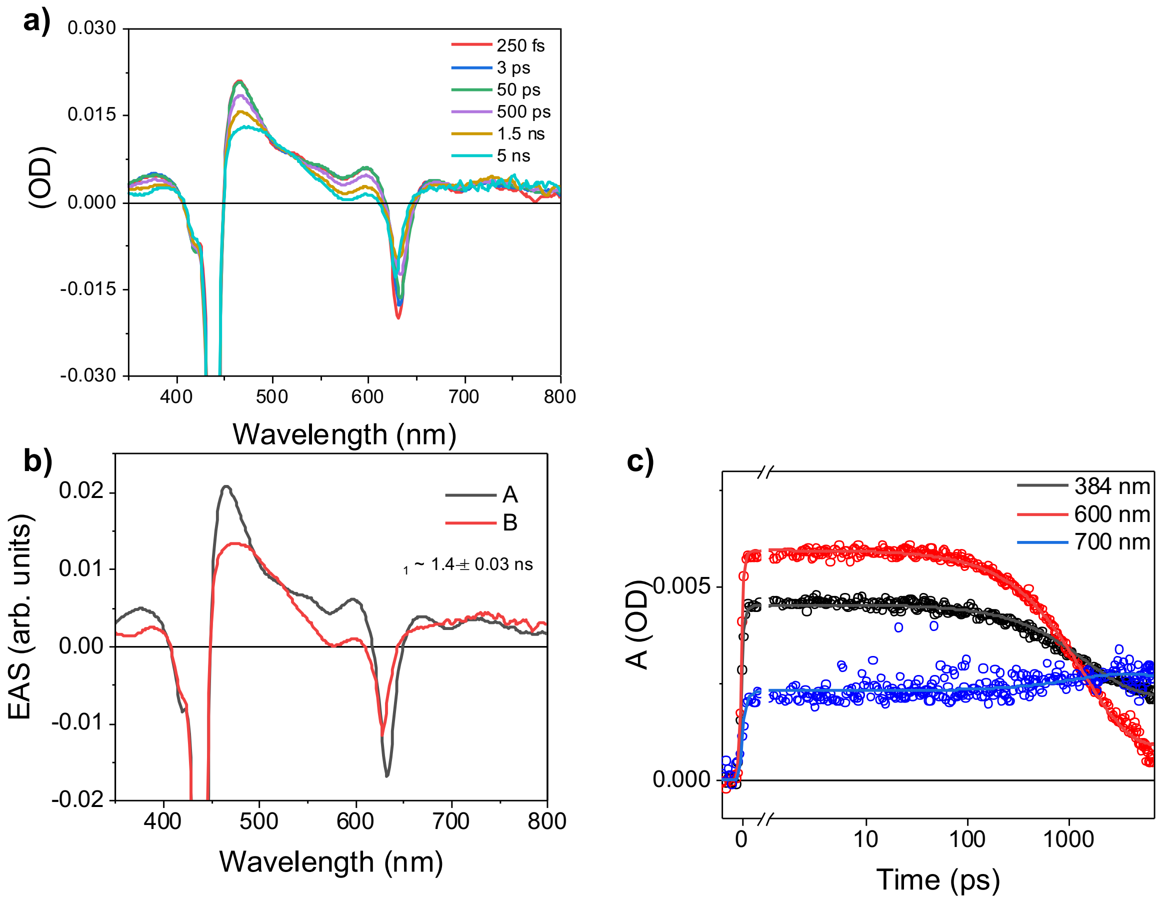

Figure S3.111 (a) TA spectra of **1P**, (b) evolution-associated species spectra, and (c) selected wavelength kinetic fits from global analysis.

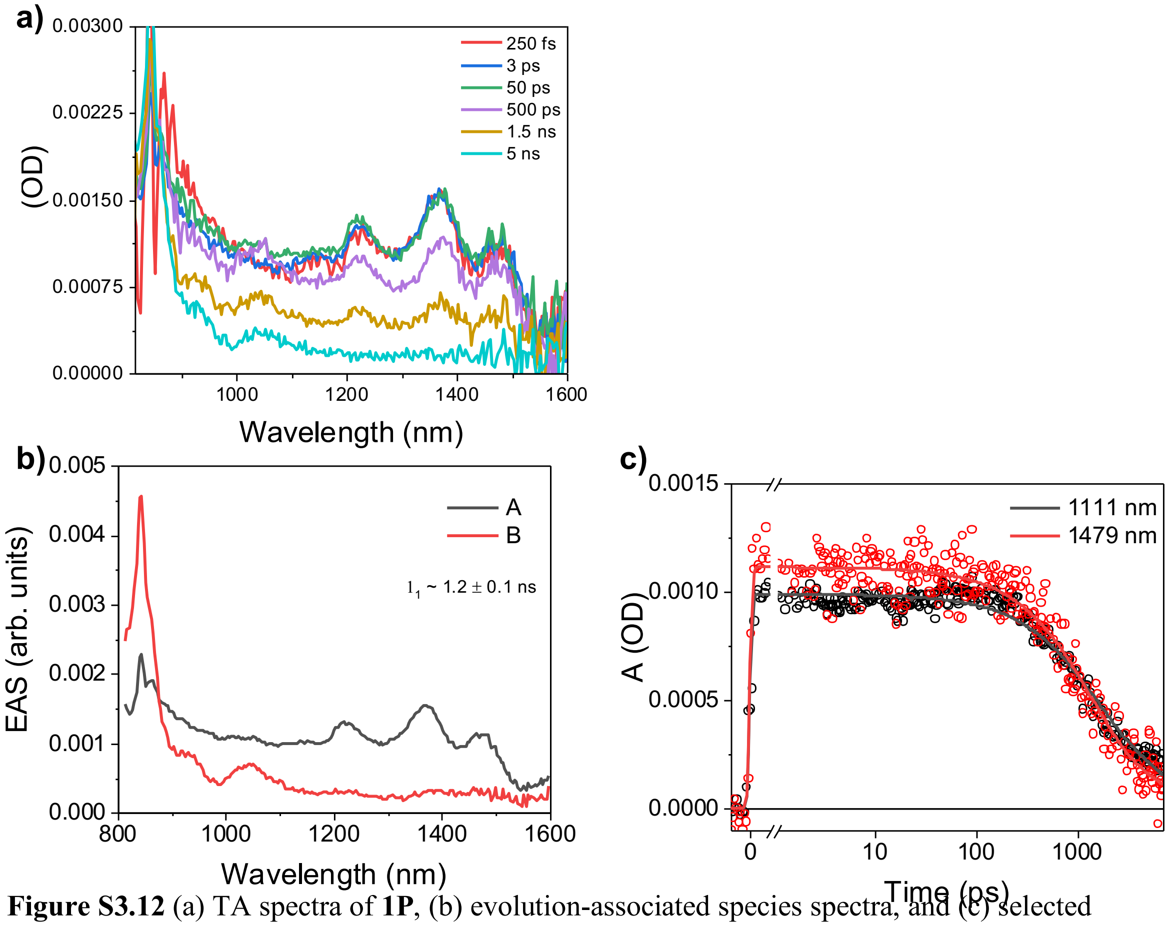

Figure S3.12 (a) TA spectra of **1P**, (b) evolution-associated species spectra, and (c) selected wavelength kinetic fits from global analysis.

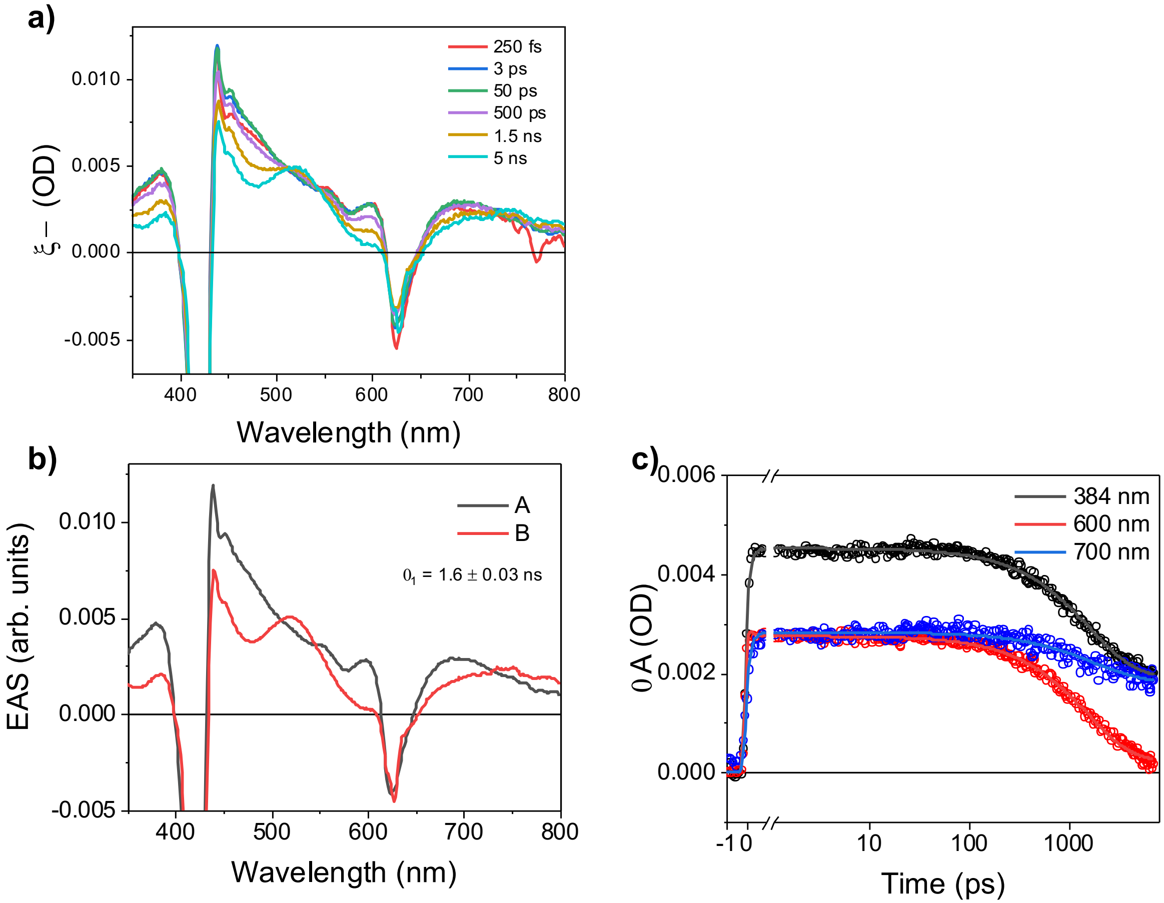

Figure S3.13 (a) TA spectra of **2P**, (b) evolution-associated species spectra, and (c) selected wavelength kinetic fits from global analysis.

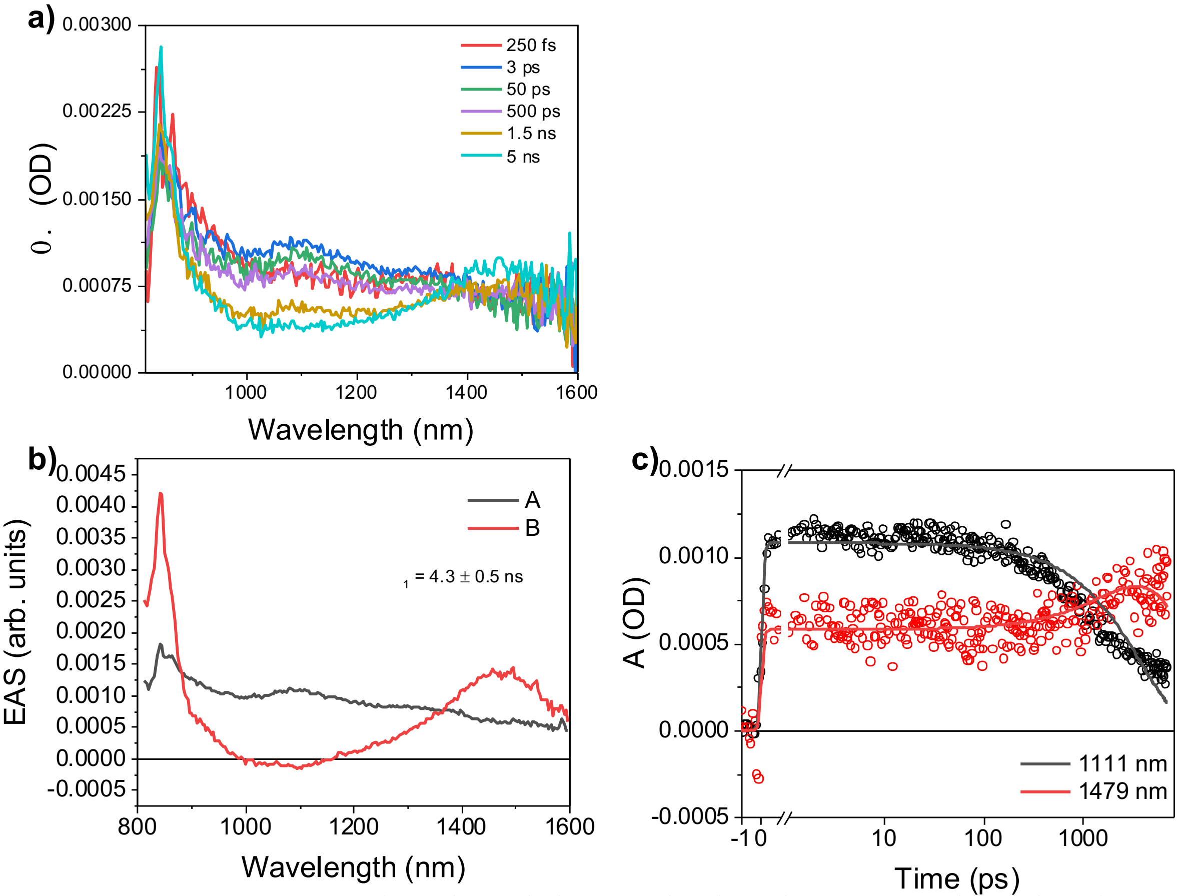

Figure S3.14 (a) TA spectra of **2P**, (b) evolution-associated species spectra, and (c) selected wavelength kinetic fits from global analysis.

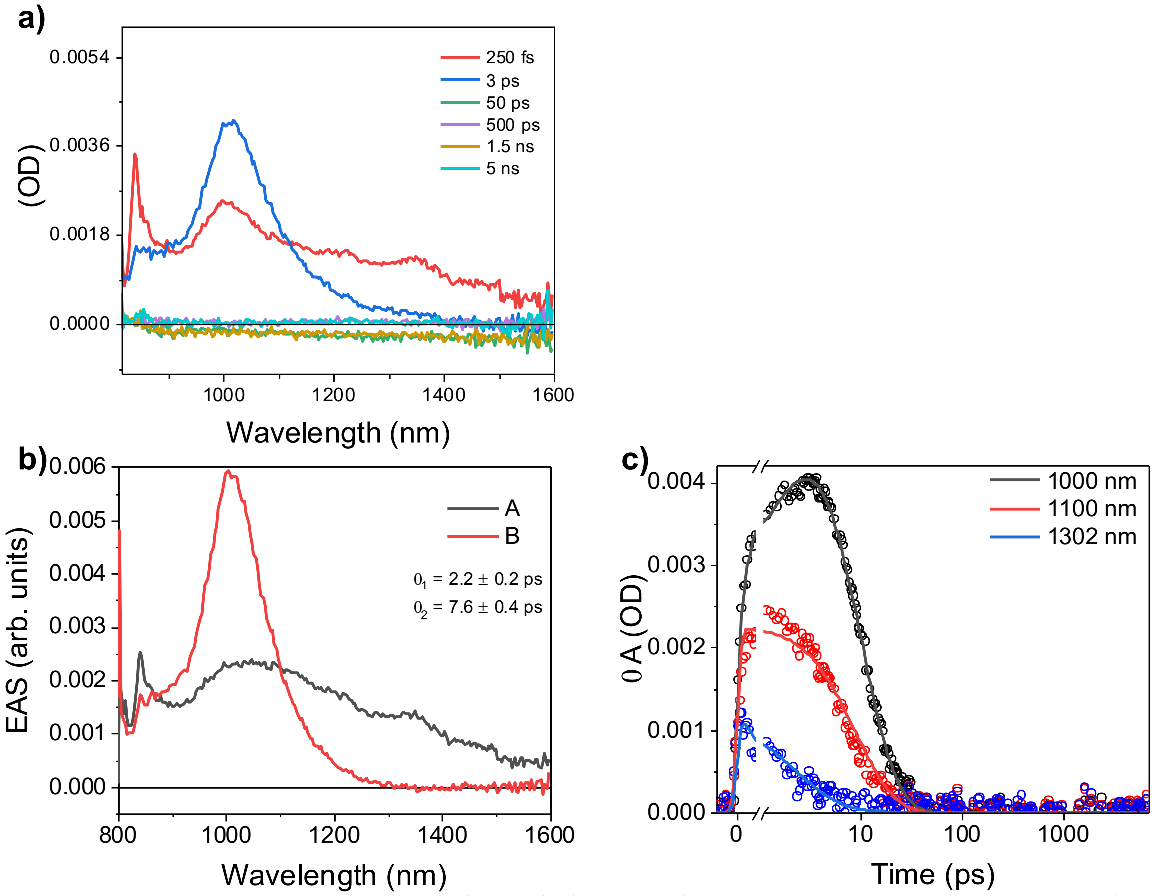

Figure S3.15 (a) TA spectra of **1DA**, (b) evolution-associated species spectra, and (c) selected wavelength kinetic fits from global analysis.

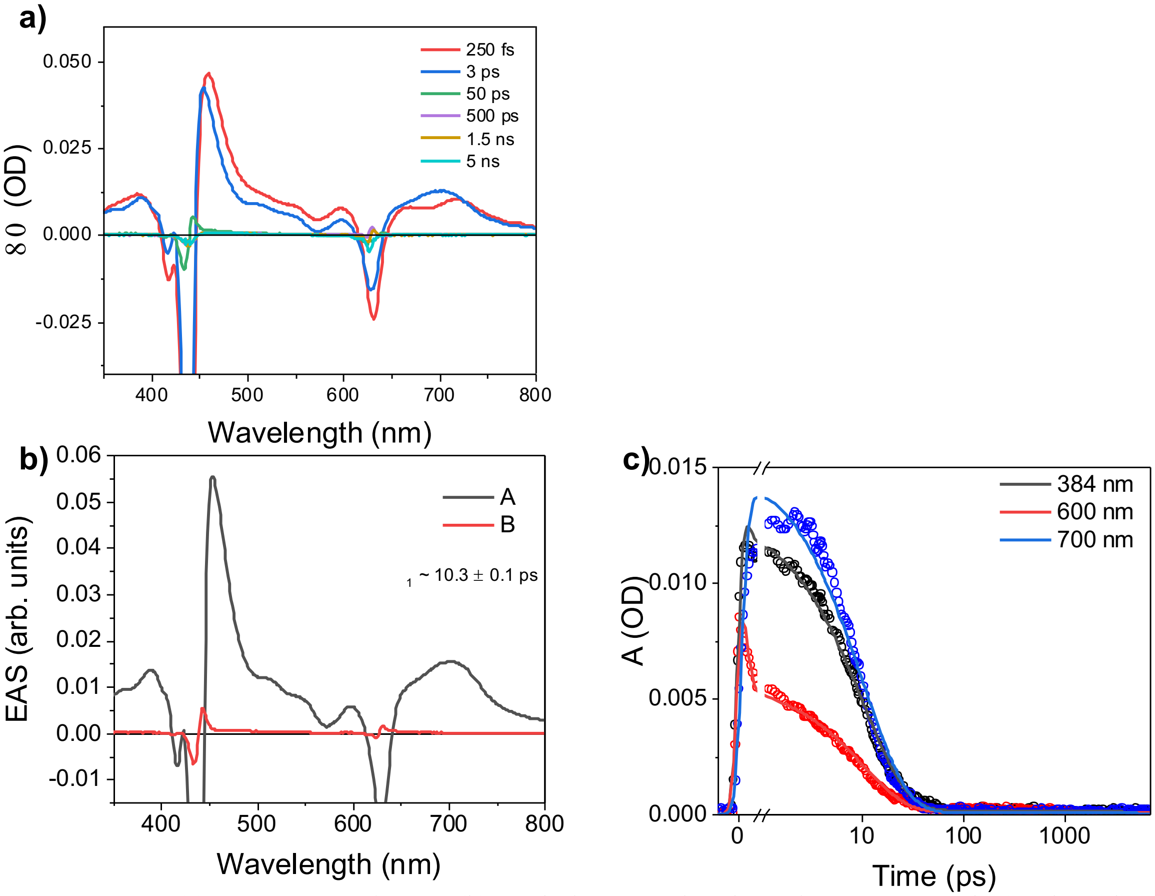

Figure S3.16 (a) TA spectra of **1DA**, (b) evolution-associated species spectra, and (c) selected wavelength kinetic fits from global analysis.

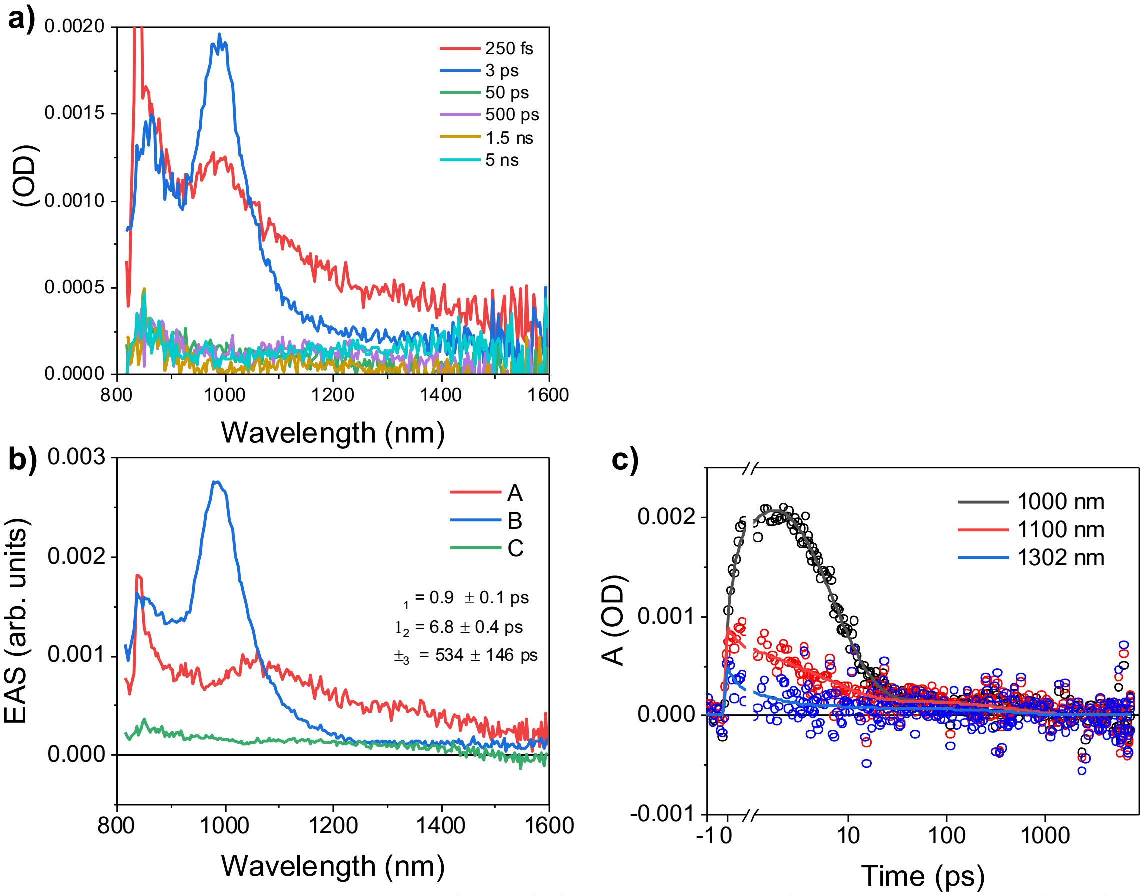

Figure S3.17 (a) TA spectra of **2DA**, (b) evolution-associated species spectra, and (c) selected wavelength kinetic fits from global analysis.

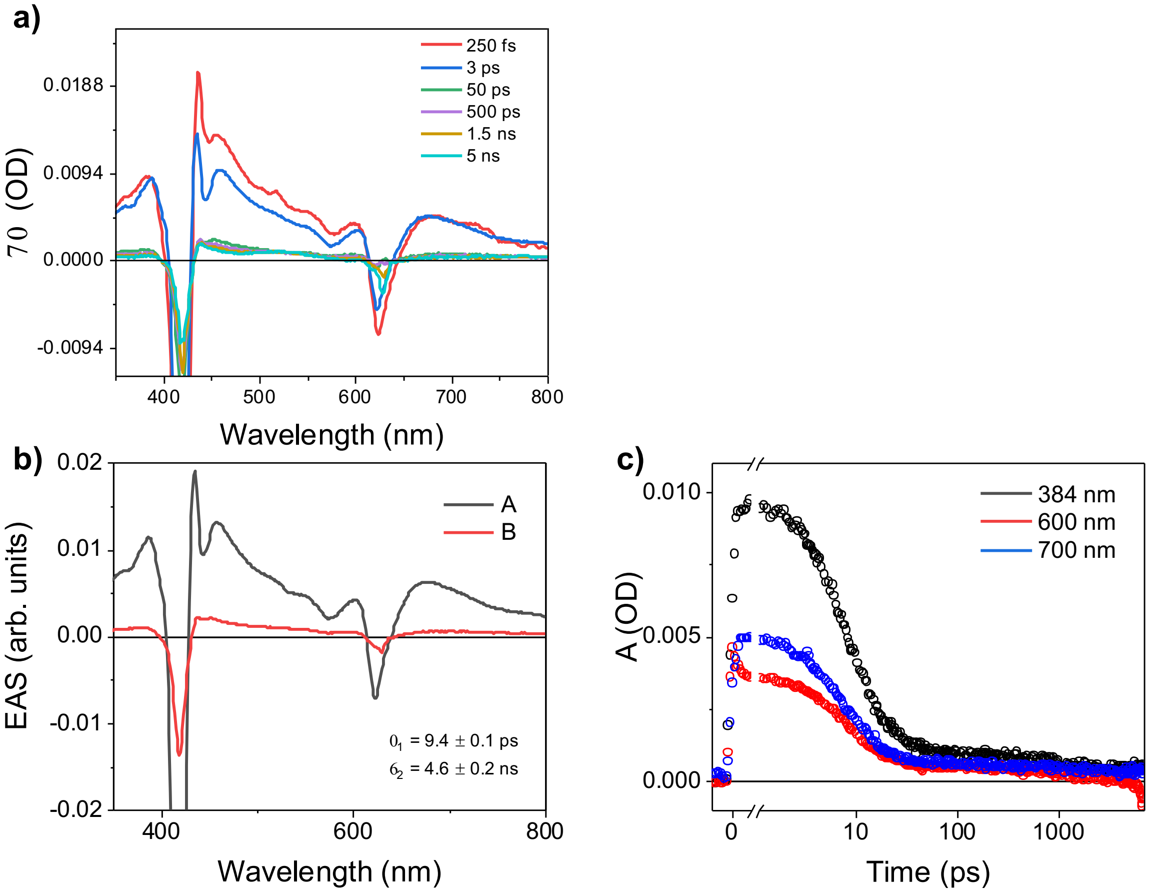

Figure S3.18 (a) TA spectra of **2DA**, (b) evolution-associated species spectra, and (c) selected wavelength kinetic fits from global analysis.

3.6.4 Density Functional Theory Computational Details and Results

Optimized Geometry Coordinates

Neutral ***1DA****:*

C	-6.84205	0.40711	1.07316
C	-7.70542	-0.26983	0.00070
C	-7.20633	-1.71922	-0.07541
C	-5.83139	-1.80837	-0.34770
C	-5.16270	-0.43570	-0.49794
C	-5.46957	0.30688	0.80749
C	-7.28696	0.37330	-1.31498
C	-8.22643	1.03811	-2.24208
C	-7.63338	1.60846	-3.48503
C	-6.31949	1.51650	-3.74770
C	-5.37531	0.83733	-2.81399

C	-5.96461	0.28687	-1.57406
C	-5.21296	-3.04739	-0.45106
C	-5.97901	-4.20872	-0.27742
C	-7.34331	-4.12043	-0.00514
C	-7.96628	-2.86846	0.09717
C	-7.30518	1.06445	2.20541
C	-6.37440	1.62885	3.08933
C	-5.01131	1.52383	2.84356
C	-4.52772	0.85237	1.69493
O	-9.42813	1.12243	-2.01190
O	-4.18214	0.74200	-3.07575
C	5.37709	-1.17008	-0.66815
C	5.86655	-2.43415	-1.16461
C	4.82240	-3.30851	-1.12034
C	3.68467	-2.58807	-0.59830
N	4.05125	-1.29073	-0.31940
C	2.39411	-3.14237	-0.44467
C	1.26201	-2.41926	-0.03660
C	-0.08910	-2.94042	0.00726
C	-0.89985	-1.92451	0.40896
C	-0.05415	-0.77592	0.62133
N	1.24855	-1.09097	0.35194
C	-0.52737	0.48639	1.05408
C	0.27778	1.62929	1.27229
C	-0.23683	2.90490	1.70754
C	0.82839	3.74336	1.80727
C	2.00434	2.99138	1.41733
N	1.63053	1.70008	1.09828
C	3.30250	3.51315	1.32305
C	4.41148	2.80576	0.80896
C	5.70562	3.40062	0.56362
C	6.49440	2.43339	0.02053
C	5.69578	1.23105	-0.04960
N	4.43041	1.48846	0.42333
C	6.15633	-0.00161	-0.54986
C	2.22847	-4.60571	-0.81702
C	3.54466	4.95422	1.73747
C	7.58375	-0.07407	-1.00099
C	8.63470	0.00616	-0.07402
C	9.96396	-0.05764	-0.49362
C	10.26572	-0.20141	-1.84904
C	9.22967	-0.28162	-2.78136
C	7.90059	-0.21903	-2.36090
C	-1.92786	0.61902	1.27778

C	-3.12660	0.73204	1.46317
Zn	2.89965	0.14548	0.66368
H	-8.77735	-0.18199	0.18216
H	-4.09934	-0.48332	-0.73079
H	-8.33190	2.09792	-4.15810
H	-5.87311	1.92471	-4.65026
H	-5.50402	-5.18269	-0.35923
H	-7.93011	-5.02551	0.12617
H	-9.03096	-2.79847	0.30592
H	-8.37127	1.14248	2.40173
H	-6.72089	2.14959	3.97771
H	-4.29398	1.95261	3.53640
H	6.87436	-2.62790	-1.50178
H	4.83214	-4.34314	-1.43299
H	-0.39672	-3.94174	-0.25732
H	-1.97049	-1.94149	0.55638
H	-1.27862	3.12004	1.89799
H	0.80030	4.78521	2.09137
H	5.97577	4.43076	0.74750
H	7.51756	2.52671	-0.31323
H	2.19491	-4.74317	-1.90578
H	3.06028	-5.20695	-0.43934
H	1.31543	-5.03371	-0.40341
H	2.74852	5.33660	2.37586
H	4.47656	5.04716	2.30226
H	3.62118	5.61947	0.86734
H	8.40256	0.11578	0.98188
H	10.76361	0.00176	0.24025
H	11.30080	-0.24970	-2.17670
H	9.45481	-0.38844	-3.83936
H	7.09597	-0.27379	-3.08897
H	-4.15012	-3.11565	-0.67006
O	3.35202	-0.85874	2.60713
H	2.53604	-1.35796	2.77850
H	3.98559	-1.52043	2.28123

*Neutral **2DA**:*

C	8.27482	-0.96546	0.83174
C	8.89168	0.10830	-0.07224
C	8.20666	1.42074	0.32990
C	6.81156	1.36122	0.21288
C	6.30796	-0.00530	-0.26946
C	6.87927	-1.02749	0.72128
C	8.38869	-0.20168	-1.47591

C	9.27578	-0.42116	-2.63686
C	8.60320	-0.71086	-3.93522
C	7.26530	-0.76037	-4.04186
C	6.37333	-0.52326	-2.87070
C	7.04311	-0.25840	-1.57985
C	6.01915	2.47940	0.51940
C	6.67722	3.64821	0.97631
C	8.05932	3.68971	1.10396
C	8.84114	2.57321	0.77394
C	8.96479	-1.81193	1.68932
C	8.24051	-2.74143	2.44849
C	6.85751	-2.81870	2.33952
C	6.14456	-1.96181	1.46786
O	10.49818	-0.37148	-2.54994
O	5.15311	-0.54270	-2.99228
C	-4.24607	-2.08510	1.04566
C	-5.12524	-1.13820	1.68908
C	-4.33639	-0.28408	2.40063
C	-2.96870	-0.70216	2.19999
N	-2.94220	-1.81265	1.38760
C	-1.84624	-0.02798	2.73259
C	-0.51302	-0.38473	2.47822
C	0.64910	0.37334	2.89816
C	1.74653	-0.28474	2.43777
C	1.26873	-1.45298	1.73962
N	-0.09754	-1.50015	1.77150
C	2.11164	-2.40397	1.11886
C	1.67337	-3.52472	0.37535
C	2.56273	-4.46282	-0.26656
C	1.77893	-5.38484	-0.88554
C	0.40043	-5.01315	-0.63578
N	0.37292	-3.87087	0.14018
C	-0.72051	-5.68126	-1.14931
C	-2.05292	-5.23973	-0.99415
C	-3.18929	-5.84163	-1.65333
C	-4.28763	-5.11866	-1.29982
C	-3.83547	-4.08120	-0.40198
N	-2.47202	-4.16787	-0.24504
C	-4.67613	-3.12618	0.19920
C	-2.12609	1.19921	3.58278
C	-0.50379	-6.93472	-1.97994
C	-6.14098	-3.20001	-0.10710
C	-6.93407	-4.25116	0.37733
C	-8.29850	-4.30802	0.08795

C	-8.89275	-3.31464	-0.69248
C	-8.11354	-2.26486	-1.18296
C	-6.74978	-2.20774	-0.89234
C	3.52101	-2.21618	1.24436
C	4.72643	-2.07818	1.34722
C	-4.19585	2.05912	-1.37640
C	-4.83659	1.21653	-2.35916
C	-3.84943	0.51178	-2.98082
C	-2.59674	0.92496	-2.39386
N	-2.83171	1.87582	-1.42955
C	-1.33727	0.40338	-2.77159
C	-0.11640	0.78063	-2.19549
C	1.18068	0.22546	-2.53312
C	2.10202	0.84480	-1.75099
C	1.37870	1.78163	-0.92331
N	0.04447	1.73345	-1.20659
C	1.98507	2.61005	0.05060
C	1.30264	3.51773	0.89834
C	1.95208	4.31009	1.91428
C	0.98112	5.04328	2.52150
C	-0.27475	4.70186	1.88542
N	-0.04084	3.75981	0.90019
C	-1.52685	5.22196	2.24399
C	-2.75494	4.80769	1.68078
C	-4.05137	5.23453	2.15015
C	-4.98515	4.58733	1.39666
C	-4.26737	3.77029	0.44805
N	-2.91114	3.91533	0.64433
C	-4.87887	2.93201	-0.50623
C	-1.34710	-0.65463	-3.86115
C	-1.59627	6.26158	3.34989
C	-6.37562	2.94796	-0.57914
C	-7.06638	4.08534	-1.02586
C	-8.46045	4.09523	-1.09331
C	-9.18959	2.96711	-0.71326
C	-8.51496	1.82994	-0.26448
C	-7.12115	1.82067	-0.19820
C	3.39640	2.52159	0.20839
C	4.60444	2.47256	0.36169
Zn	-1.37691	2.99931	-0.45555
Zn	-1.29483	-3.00831	0.97141
O	-1.62259	4.61325	-2.00383
H	-2.19591	4.13361	-2.62549
H	-2.22955	5.17580	-1.49279

O	-1.43893	-3.92660	3.02094
H	-0.74085	-3.40381	3.45123
H	-2.27003	-3.51761	3.31628
H	9.98036	0.14982	-0.02220
H	5.22549	-0.06301	-0.36714
H	9.26423	-0.87484	-4.78167
H	6.75981	-0.96538	-4.98150
H	6.07866	4.52194	1.21456
H	8.53878	4.60029	1.45247
H	9.92377	2.61012	0.86110
H	10.04739	-1.75684	1.76831
H	8.76392	-3.41162	3.12483
H	6.30070	-3.54478	2.92352
H	-6.20312	-1.13315	1.61435
H	-4.66286	0.56098	2.98934
H	0.64188	1.31012	3.43601
H	2.78470	-0.00070	2.53494
H	3.64177	-4.40631	-0.24727
H	2.11713	-6.22216	-1.47891
H	-3.15873	-6.68798	-2.32482
H	-5.30771	-5.26704	-1.62318
H	-2.43374	2.05086	2.96394
H	-2.92924	1.00636	4.30058
H	-1.25320	1.50540	4.15829
H	0.46566	-7.39168	-1.78153
H	-1.26189	-7.69020	-1.75673
H	-0.55757	-6.72479	-3.05673
H	-6.47532	-5.02341	0.98901
H	-8.89741	-5.12783	0.47620
H	-9.95495	-3.35938	-0.91837
H	-8.56494	-1.48962	-1.79708
H	-6.14146	-1.39623	-1.28227
H	-5.89850	1.17550	-2.55321
H	-3.97156	-0.22200	-3.76462
H	1.38209	-0.54761	-3.25968
H	3.16949	0.67869	-1.74047
H	3.01036	4.29191	2.13132
H	1.11606	5.73423	3.34101
H	-4.23821	5.91526	2.96891
H	-6.06025	4.64621	1.48578
H	-1.88027	-0.30109	-4.75057
H	-0.34374	-0.93159	-4.17948
H	-1.84849	-1.56907	-3.52172
H	-1.88016	5.81423	4.31198

H	-0.64332	6.77121	3.49260
H	-2.33632	7.03228	3.11857
H	-6.50344	4.96468	-1.32767
H	-8.97587	4.98439	-1.44724
H	-10.27511	2.97474	-0.76553
H	-9.07145	0.94665	0.03847
H	-6.59866	0.93863	0.15998

Singly Reduced ***1DA****:*

C	6.77610	-1.12695	0.36560
C	7.54388	0.18553	0.46639
C	6.97135	0.88402	1.69319
C	5.58362	1.06880	1.61172
C	4.98888	0.52986	0.31699
C	5.38987	-0.93717	0.28159
C	7.11093	1.01623	-0.73422
C	8.04688	1.55654	-1.69303
C	7.41091	2.30778	-2.76301
C	6.05806	2.48050	-2.85041
C	5.12373	1.93039	-1.88527
C	5.75773	1.19420	-0.81911
C	4.89792	1.68684	2.64335
C	5.60278	2.13063	3.76679
C	6.97865	1.94960	3.84713
C	7.66939	1.32072	2.80607
C	7.31237	-2.40222	0.34839
C	6.45966	-3.50753	0.24450
C	5.08871	-3.33046	0.15824
C	4.53482	-2.03533	0.17521
O	9.28881	1.38945	-1.60723
O	3.87491	2.08104	-1.97631
C	-5.18755	1.31293	-0.86481
C	-5.54592	2.58194	-1.43973
C	-4.38833	3.17061	-1.84056
C	-3.31621	2.27024	-1.50430
N	-3.82657	1.15254	-0.90620
C	-1.95349	2.53257	-1.76988
C	-0.90662	1.66708	-1.46048
C	0.49550	1.90300	-1.74623
C	1.18821	0.83839	-1.28736
C	0.21689	-0.06084	-0.71081
N	-1.04114	0.44858	-0.82485
C	0.54796	-1.29016	-0.11079

C	-0.37504	-2.21609	0.41100
C	0.00753	-3.49077	0.96427
C	-1.13464	-4.10923	1.34185
C	-2.23118	-3.21455	1.02873
N	-1.72490	-2.06838	0.45837
C	-3.58098	-3.47485	1.25686
C	-4.63011	-2.59057	0.92773
C	-6.02477	-2.89222	1.12210
C	-6.73056	-1.81885	0.68138
C	-5.76927	-0.85256	0.21973
N	-4.50271	-1.34941	0.37586
C	-6.10015	0.38902	-0.33868
C	-1.65003	3.84958	-2.45480
C	-3.99268	-4.78810	1.89010
C	-7.54870	0.75236	-0.38769
C	-8.24943	1.04243	0.78659
C	-9.59899	1.37918	0.74408
C	-10.26819	1.43131	-0.47570
C	-9.57994	1.14342	-1.65136
C	-8.23063	0.80613	-1.60675
C	1.93538	-1.61225	-0.01716
C	3.12249	-1.83869	0.07501
Zn	-2.75388	-0.37281	0.00997
H	8.62755	0.05882	0.49466
H	3.91382	0.68980	0.23850
H	8.07684	2.73246	-3.51151
H	5.61962	3.04364	-3.67186
H	5.07217	2.62055	4.57911
H	7.52126	2.29938	4.72163
H	8.74596	1.18044	2.86412
H	8.38876	-2.54037	0.40882
H	6.87582	-4.51097	0.22562
H	4.42598	-4.18602	0.06872
H	-6.54976	2.97360	-1.52446
H	-4.28297	4.13224	-2.32296
H	0.94117	2.75549	-2.23635
H	2.26222	0.71498	-1.35536
H	1.02476	-3.84851	1.03781
H	-1.21000	-5.08944	1.78951
H	-6.42494	-3.81021	1.52916
H	-7.80428	-1.69750	0.65541
H	-2.13020	3.89780	-3.43861
H	-2.02185	4.69590	-1.86665
H	-0.58342	4.00381	-2.60443

H	-3.14014	-5.41058	2.15595
H	-4.56771	-4.61841	2.80690
H	-4.62306	-5.37363	1.21124
H	-7.72399	1.00241	1.73635
H	-10.12757	1.60454	1.66600
H	-11.32164	1.69441	-0.51009
H	-10.09562	1.17649	-2.60683
H	-7.69092	0.57865	-2.52140
H	3.82243	1.82881	2.57261
O	-2.42401	1.05805	1.71207
H	-1.49647	1.25716	1.51491
H	-2.91827	1.77872	1.29412

Singly Oxidized ***1DA****:*

C	6.78520	-1.14814	0.30951
C	7.61785	0.13298	0.32365
C	7.11218	0.92083	1.53301
C	5.73568	1.16112	1.48656
C	5.07227	0.58585	0.23485
C	5.41167	-0.89987	0.25546
C	7.16646	0.92278	-0.88995
C	8.08866	1.41353	-1.93997
C	7.46502	2.18133	-3.05613
C	6.14731	2.40539	-3.10679
C	5.22449	1.89700	-2.05518
C	5.84592	1.15461	-0.94013
C	5.10395	1.84674	2.50892
C	5.86524	2.29895	3.59043
C	7.23434	2.06203	3.63576
C	7.86883	1.36709	2.60200
C	7.26701	-2.44436	0.36368
C	6.36406	-3.51416	0.36751
C	5.00075	-3.28250	0.31448
C	4.50511	-1.96349	0.25136
O	9.28547	1.20351	-1.89853
O	4.01996	2.08341	-2.12318
C	-5.21757	1.34533	-0.78545
C	-5.59173	2.64707	-1.25081
C	-4.43657	3.28364	-1.59175
C	-3.36807	2.37074	-1.31899
N	-3.85287	1.20275	-0.82488
C	-1.99146	2.66590	-1.56672
C	-0.93192	1.81335	-1.27475
C	0.45656	2.05629	-1.59185

C	1.15707	0.98242	-1.15822
C	0.19935	0.08791	-0.56834
N	-1.05074	0.58685	-0.64558
C	0.54777	-1.16847	0.00660
C	-0.37062	-2.13794	0.50117
C	0.03548	-3.40327	1.04930
C	-1.10097	-4.04239	1.41350
C	-2.20174	-3.16587	1.08489
N	-1.71154	-2.00496	0.51851
C	-3.54893	-3.45570	1.27772
C	-4.62735	-2.59949	0.89832
C	-6.00203	-2.99498	0.92724
C	-6.72379	-1.93662	0.46266
C	-5.78289	-0.89829	0.17005
N	-4.50731	-1.32877	0.43441
C	-6.12714	0.36177	-0.35499
C	-1.71519	4.00374	-2.20562
C	-3.94393	-4.77854	1.88529
C	-7.57755	0.66734	-0.48120
C	-8.39089	0.71523	0.65620
C	-9.74746	0.99570	0.53781
C	-10.30756	1.21518	-0.71796
C	-9.50556	1.16195	-1.85514
C	-8.14575	0.89626	-1.73917
C	1.91727	-1.47295	0.08945
C	3.10805	-1.71588	0.17167
Zn	-2.76731	-0.25822	0.16146
H	8.69389	-0.04382	0.33007
H	4.00347	0.79056	0.18016
H	8.14750	2.53934	-3.82053
H	5.68144	2.95636	-3.91775
H	5.38293	2.83786	4.39987
H	7.81692	2.41791	4.47949
H	8.93841	1.18142	2.63770
H	8.33617	-2.63013	0.40547
H	6.73629	-4.53225	0.40963
H	4.30202	-4.11240	0.30974
H	-6.59744	3.03630	-1.30621
H	-4.34334	4.28271	-1.99141
H	0.87331	2.91287	-2.09910
H	2.21965	0.81918	-1.26092
H	1.05525	-3.74864	1.13623
H	-1.16713	-5.02518	1.85504
H	-6.38584	-3.95761	1.23142

H	-7.79163	-1.88184	0.31187
H	-2.22282	4.07465	-3.17292
H	-2.09540	4.81372	-1.57481
H	-0.65619	4.18661	-2.36936
H	-3.10445	-5.30440	2.33393
H	-4.69545	-4.63241	2.66545
H	-4.38098	-5.43270	1.12219
H	-7.95424	0.54146	1.63543
H	-10.36673	1.03963	1.42797
H	-11.36818	1.42551	-0.81145
H	-9.94006	1.32259	-2.83664
H	-7.52168	0.84879	-2.62655
H	4.03394	2.03135	2.46953
O	-2.70986	0.65483	2.09245
H	-2.40362	1.57097	2.11757
H	-3.55580	0.63102	2.55903

Singly Reduced ***2DA:***

C	-8.11234	0.82151	1.53290
C	-8.82755	0.38246	0.25198
C	-8.29673	-1.02337	-0.03169
C	-6.89643	-1.05603	-0.14753
C	-6.24809	0.31328	0.03290
C	-6.71300	0.79506	1.40364
C	-8.28594	1.27639	-0.86596
C	-9.12974	2.09276	-1.71383
C	-8.38796	2.87082	-2.69789
C	-7.02110	2.83516	-2.80721
C	-6.18015	2.01423	-1.95185
C	-6.91832	1.23868	-0.98201
C	-6.23239	-2.26823	-0.39384
C	-7.00463	-3.44766	-0.52439
C	-8.38803	-3.40291	-0.41112
C	-9.04362	-2.18721	-0.16183
C	-8.70029	1.22248	2.72570
C	-7.88476	1.60961	3.80078
C	-6.50118	1.60592	3.67588
C	-5.89022	1.20409	2.46457
O	-10.38753	2.12645	-1.60815
O	-4.91280	1.98889	-2.04327
C	4.47879	1.67925	1.60166
C	5.43417	0.83589	2.28232
C	4.72416	0.02686	3.11687
C	3.32900	0.36229	2.95277

N	3.20868	1.36577	2.01991
C	2.27262	-0.27166	3.64121
C	0.91011	-0.00970	3.42431
C	-0.18826	-0.69753	4.07032
C	-1.34164	-0.17959	3.56696
C	-0.96175	0.82383	2.60496
N	0.40276	0.92260	2.53871
C	-1.89067	1.54318	1.81472
C	-1.55379	2.43444	0.76695
C	-2.51389	3.01430	-0.14228
C	-1.81193	3.82790	-0.97462
C	-0.41702	3.74516	-0.59300
N	-0.28754	2.87316	0.47384
C	0.64035	4.42709	-1.21348
C	2.00767	4.21098	-0.93339
C	3.08983	4.88994	-1.60805
C	4.25357	4.39299	-1.10268
C	3.89275	3.40055	-0.11703
N	2.52430	3.31655	-0.02744
C	4.81514	2.64137	0.62815
C	2.64985	-1.34982	4.64310
C	0.31977	5.44519	-2.29473
C	6.27086	2.85271	0.34780
C	7.11628	3.41638	1.31651
C	8.47502	3.60432	1.05991
C	9.01530	3.23049	-0.17215
C	8.18595	2.66832	-1.14498
C	6.82663	2.48079	-0.88724
C	-3.27798	1.35252	2.08229
C	-4.47325	1.26451	2.29859
C	4.01952	-1.52873	-1.97768
C	4.65729	-0.55358	-2.83229
C	3.66975	0.24158	-3.33087
C	2.41915	-0.24487	-2.79662
N	2.66037	-1.32771	-1.98563
C	1.16377	0.34325	-3.06553
C	-0.05833	-0.10976	-2.54416
C	-1.34152	0.53930	-2.71843
C	-2.27249	-0.20586	-2.06568
C	-1.56499	-1.32423	-1.48681
N	-0.22625	-1.25081	-1.77897
C	-2.17995	-2.34769	-0.72536
C	-1.49751	-3.39543	-0.05623
C	-2.15050	-4.35905	0.79217

C	-1.17628	-5.16917	1.29098
C	0.08468	-4.70573	0.75344
N	-0.14689	-3.62450	-0.07707
C	1.34491	-5.24348	1.06472
C	2.57301	-4.72194	0.60754
C	3.87004	-5.20430	1.02190
C	4.80476	-4.44433	0.38574
C	4.08830	-3.49540	-0.43384
N	2.73617	-3.67482	-0.26991
C	4.70176	-2.52284	-1.24919
C	1.16823	1.57126	-3.95944
C	1.40272	-6.43376	2.00767
C	6.19677	-2.53702	-1.33376
C	6.87449	-3.61317	-1.92915
C	8.26738	-3.62332	-2.01417
C	9.00959	-2.55510	-1.50644
C	8.34868	-1.47911	-0.91028
C	6.95595	-1.47172	-0.82307
C	-3.59807	-2.31878	-0.60555
C	-4.81229	-2.31348	-0.51020
Zn	1.26569	-2.60693	-1.22079
Zn	1.48878	2.29369	1.41196
H	-9.91577	0.43783	0.31541
H	-5.16547	0.29704	-0.07387
H	-8.98470	3.49919	-3.35719
H	-6.50393	3.43488	-3.55464
H	-6.49681	-4.38762	-0.72123
H	-8.96658	-4.31735	-0.51905
H	-10.12706	-2.15406	-0.07438
H	-9.78336	1.24391	2.82204
H	-8.33907	1.92672	4.73650
H	-5.87161	1.92478	4.50170
H	6.50360	0.84865	2.12941
H	5.12200	-0.74481	3.76018
H	-0.10586	-1.49788	4.79162
H	-2.36040	-0.46160	3.79267
H	-3.56514	2.76971	-0.20861
H	-2.22472	4.38105	-1.80573
H	2.98311	5.64601	-2.37365
H	5.26198	4.67169	-1.37265
H	3.53855	-1.06913	5.21469
H	1.85299	-1.52906	5.36538
H	2.86683	-2.30410	4.14457
H	-0.74326	5.67942	-2.33437

H	0.84932	6.38718	-2.11552
H	0.61955	5.08974	-3.28909
H	6.69653	3.71028	2.27454
H	9.11088	4.04663	1.82303
H	10.07383	3.37624	-0.37281
H	8.59692	2.36917	-2.10612
H	6.18397	2.03069	-1.63904
H	5.71787	-0.49075	-3.02778
H	3.78777	1.08445	-3.99678
H	-1.53409	1.46944	-3.23151
H	-3.32580	0.02442	-1.96558
H	-3.21291	-4.38624	0.98835
H	-1.31537	-5.98580	1.98516
H	4.05706	-6.00075	1.72840
H	5.87937	-4.50691	0.47860
H	1.71222	1.37850	-4.89096
H	0.16112	1.87883	-4.23638
H	1.65280	2.42182	-3.46456
H	1.57930	-6.12425	3.04726
H	0.47560	-7.00812	1.99027
H	2.20549	-7.12251	1.73214
H	6.29727	-4.44045	-2.33264
H	8.77209	-4.46435	-2.48382
H	10.09475	-2.56148	-1.57480
H	8.91359	-0.64068	-0.51070
H	6.44517	-0.63956	-0.34789
O	0.55012	-3.84323	-2.98901
H	-0.05108	-3.13204	-3.27501
H	-0.01391	-4.42421	-2.44978
O	0.95148	3.87023	2.96167
H	0.55003	3.24926	3.59371
H	0.20205	4.16737	2.41405

Singly oxidized ***2DA***:

C	8.25061	-1.10473	0.48807
C	8.88049	0.27873	0.27917
C	8.16387	1.20525	1.27093
C	6.77368	1.20509	1.09993
C	6.30654	0.28652	-0.03434
C	6.86160	-1.09868	0.30750
C	8.42223	0.73138	-1.10196
C	9.34350	1.14006	-2.18604
C	8.70732	1.55431	-3.46920
C	7.37352	1.54987	-3.63266

C	6.45081	1.12857	-2.54251
C	7.08305	0.73394	-1.26647
C	5.95411	2.00544	1.91084
C	6.57280	2.79951	2.90440
C	7.95261	2.78557	3.06960
C	8.76260	1.98657	2.25018
C	8.92053	-2.27422	0.82432
C	8.18740	-3.46113	0.97943
C	6.81294	-3.47165	0.79032
C	6.11978	-2.28521	0.44096
O	10.55974	1.14027	-2.04342
O	5.23415	1.10984	-2.70589
C	-4.08406	-3.83323	-0.46838
C	-4.80466	-4.90696	0.16793
C	-3.87454	-5.70559	0.76475
C	-2.58561	-5.11547	0.50653
N	-2.73583	-3.97520	-0.24386
C	-1.36365	-5.63201	1.00481
C	-0.11621	-5.00229	0.86776
C	1.12305	-5.46985	1.44802
C	2.08772	-4.57256	1.10596
C	1.44454	-3.55891	0.31098
N	0.11481	-3.82149	0.18204
C	2.12764	-2.43927	-0.24646
C	1.52389	-1.39241	-0.99401
C	2.24334	-0.26149	-1.52174
C	1.32048	0.53636	-2.12324
C	0.03379	-0.10929	-1.97525
N	0.19426	-1.29853	-1.28800
C	-1.18862	0.39966	-2.44575
C	-2.44753	-0.23186	-2.26793
C	-3.69126	0.29869	-2.77295
C	-4.66780	-0.58759	-2.43232
C	-4.02503	-1.65393	-1.70234
N	-2.67375	-1.41554	-1.61897
C	-4.69753	-2.77112	-1.17013
C	-1.44376	-6.93764	1.77181
C	-1.20003	1.71691	-3.19492
C	-6.18227	-2.83238	-1.33954
C	-6.76814	-3.81231	-2.15611
C	-8.15304	-3.86638	-2.31517
C	-8.97198	-2.95097	-1.65122
C	-8.39914	-1.97823	-0.82931
C	-7.01378	-1.91571	-0.67703

C	3.51911	-2.36018	-0.01085
C	4.71957	-2.31553	0.20911
C	-4.10568	3.73288	0.08674
C	-4.62572	4.82791	-0.69529
C	-3.55083	5.52487	-1.15935
C	-2.36988	4.86138	-0.66010
N	-2.73112	3.77125	0.08969
C	-1.04635	5.29626	-0.92461
C	0.11007	4.66627	-0.43933
C	1.47064	5.09358	-0.69066
C	2.29105	4.22711	-0.03668
C	1.43985	3.25872	0.60733
N	0.12749	3.53559	0.35984
C	1.92460	2.15298	1.35667
C	1.12849	1.10964	1.88655
C	1.66538	-0.05964	2.53625
C	0.60525	-0.85459	2.84568
C	-0.58880	-0.16421	2.40574
N	-0.23608	1.03756	1.82602
C	-1.90425	-0.63869	2.57047
C	-3.06533	0.07495	2.18983
C	-4.41513	-0.36482	2.45819
C	-5.25092	0.59353	1.96790
C	-4.41615	1.61004	1.37452
N	-3.09307	1.28225	1.53841
C	-4.90396	2.74954	0.70224
C	-0.91092	6.53680	-1.78641
C	-2.11387	-1.97921	3.24913
C	-6.38994	2.91019	0.60116
C	-7.05809	3.88526	1.35616
C	-8.44284	4.03105	1.25903
C	-9.17727	3.21237	0.39915
C	-8.51992	2.24396	-0.36222
C	-7.13673	2.09090	-0.25889
C	3.33189	2.07731	1.55936
C	4.53774	2.04053	1.73088
Zn	-1.50774	2.56086	1.22053
Zn	-1.23855	-2.77238	-1.02211
H	9.96636	0.28555	0.37940
H	5.22856	0.30261	-0.17957
H	9.39143	1.85554	-4.25741
H	6.89855	1.84604	-4.56368
H	5.95063	3.42391	3.53762
H	8.40718	3.40365	3.83818

H	9.84175	1.98411	2.37651
H	9.99807	-2.27202	0.96360
H	8.70123	-4.38128	1.24104
H	6.25168	-4.39468	0.89555
H	-5.87794	-5.02502	0.17511
H	-4.06319	-6.59617	1.34642
H	1.25554	-6.35327	2.05521
H	3.13501	-4.58675	1.37030
H	3.30889	-0.09577	-1.46417
H	1.52115	1.47895	-2.60906
H	-3.81308	1.22114	-3.32160
H	-5.72068	-0.53297	-2.66627
H	-1.88508	-6.78756	2.76548
H	-2.07034	-7.66265	1.24486
H	-0.46705	-7.39811	1.90996
H	-0.19915	2.08514	-3.40853
H	-1.72262	1.61496	-4.15152
H	-1.72111	2.48889	-2.61615
H	-6.13224	-4.52391	-2.67526
H	-8.59154	-4.62343	-2.95926
H	-10.05059	-2.99725	-1.77206
H	-9.02980	-1.26867	-0.30048
H	-6.56748	-1.16928	-0.02637
H	-5.67175	5.02674	-0.87708
H	-3.56831	6.40602	-1.78450
H	1.77978	5.93929	-1.28706
H	3.37095	4.22625	-0.00221
H	2.71527	-0.24964	2.70764
H	0.64733	-1.81789	3.33149
H	-4.70019	-1.27224	2.97077
H	-6.33000	0.61490	2.01103
H	-1.39464	7.39847	-1.31194
H	0.12588	6.80822	-1.97411
H	-1.39319	6.39261	-2.75975
H	-2.92504	-2.53610	2.77567
H	-1.22601	-2.60764	3.19616
H	-2.37290	-1.85212	4.30863
H	-6.48946	4.52426	2.02631
H	-8.94679	4.78596	1.85619
H	-10.25428	3.33077	0.32055
H	-9.08127	1.60976	-1.04339
H	-6.62403	1.34385	-0.85836
O	-1.42560	3.69744	3.10037
H	-0.84281	4.46480	2.97826

H	-1.01891	3.16702	3.80507
O	-0.88415	-3.84092	-2.89764
H	-0.02092	-3.64623	-3.29743
H	-0.93426	-4.80708	-2.81826

References

1. Zhang, S.; Ye, L.; Hou, J., Breaking the 10% Efficiency Barrier in Organic Photovoltaics: Morphology and Device Optimization of Well-Known PBDTTT Polymers. *Advanced Energy Materials* **2016,** *6* (11), 1502529.

2. Wang, J.; Zheng, Z.; Zu, Y.; Wang, Y.; Liu, X.; Zhang, S.; Zhang, M.; Hou, J., A Tandem Organic Photovoltaic Cell with 19.6% Efficiency Enabled by Light Distribution Control. *Adv Mater* **2021,** *33* (39), e2102787.

3. Moliton, A.; Nunzi, J.-M., How to model the behaviour of organic photovoltaic cells. *Polymer International* **2006,** *55* (6), 583-600.

4. Bakulin, A. A.; Rao, A.; Pavelyev, V. G.; van Loosdrecht, P. H.; Pshenichnikov, M. S.; Niedzialek, D.; Cornil, J.; Beljonne, D.; Friend, R. H., The role of driving energy and delocalized States for charge separation in organic semiconductors. *Science* **2012,** *335* (6074), 1340-4.

5. Brédas, J.-L.; Norton, J. E.; Cornil, J.; Coropceanu, V., Molecular Understanding of Organic Solar Cells: The Challenges. *Accounts of Chemical Research* **2009,** *42* (11), 1691-1699.

6. Clarke, T. M.; Durrant, J. R., Charge Photogeneration in Organic Solar Cells. *Chemical Reviews* **2010,** *110* (11), 6736-6767.

7. Deibel, C.; Strobel, T.; Dyakonov, V., Role of the Charge Transfer State in Organic Donor–Acceptor Solar Cells. *Advanced Materials* **2010,** *22* (37), 4097-4111.

8. Gélinas, S.; Paré-Labrosse, O.; Brosseau, C.-N.; Albert-Seifried, S.; McNeill, C. R.; Kirov, K. R.; Howard, I. A.; Leonelli, R.; Friend, R. H.; Silva, C., The Binding Energy of Charge-Transfer Excitons Localized at Polymeric Semiconductor Heterojunctions. *The Journal of Physical Chemistry C* **2011,** *115* (14), 7114-7119.

9. Shoaee, S.; Clarke, T. M.; Huang, C.; Barlow, S.; Marder, S. R.; Heeney, M.; McCulloch, I.; Durrant, J. R., Acceptor Energy Level Control of Charge Photogeneration in Organic Donor/Acceptor Blends. *Journal of the American Chemical Society* **2010,** *132* (37), 12919-12926.

10. Wienk, M. M.; Kroon, J. M.; Verhees, W. J. H.; Knol, J.; Hummelen, J. C.; van Hal, P. A.; Janssen, R. A. J., Efficient Methano[70]fullerene/MDMO-PPV Bulk Heterojunction Photovoltaic Cells. *Angewandte Chemie International Edition* **2003,** *42* (29), 3371-3375.

11. Barnsley, J. E.; Lomax, B. A.; McLay, J. R. W.; Larsen, C. B.; Lucas, N. T.; Gordon, K. C., Flicking the Switch on Donor–Acceptor Interactions in Hexaazatrinaphthalene Dyes: A Spectroscopic and Computational Study. *ChemPhotoChem* **2017,** *1* (10), 432-441.

12. Barnsley, J. E.; Shillito, G. E.; Larsen, C. B.; van der Salm, H.; Wang, L. E.; Lucas, N. T.; Gordon, K. C., Benzo[c][1,2,5]thiadiazole Donor-Acceptor Dyes: A Synthetic, Spectroscopic, and Computational Study. *J Phys Chem A* **2016,** *120* (11), 1853-66.

13. Bures, F.; Schweizer, W. B.; May, J. C.; Boudon, C.; Gisselbrecht, J. P.; Gross, M.; Biaggio, I.; Diederich, F., Property tuning in charge-transfer chromophores by systematic modulation of the spacer between donor and acceptor. *Chemistry* **2007,** *13* (19), 5378-87.
14. Burghardt, I.; Hynes, J. T., Excited-state charge transfer at a conical intersection: effects of an environment. *J Phys Chem A* **2006,** *110* (40), 11411-23.
15. Casanova, D., The Role of the π Linker in Donor–π–Acceptor Organic Dyes for High-Performance Sensitized Solar Cells. *ChemPhysChem* **2011,** *12* (16), 2979-2988.
16. Cho, Y.-J.; Lee, A.-R.; Kim, S.-Y.; Cho, M.; Han, W.-S.; Son, H.-J.; Cho, D. W.; Kang, S. O., The influence of π-conjugation on competitive pathways: charge transfer or electron transfer in new D–π–A and D–π–Si–π–A dyads. *Physical Chemistry Chemical Physics* **2016,** *18* (33), 22921-22928.
17. Gaynor, J. D.; Sandwisch, J.; Khalil, M., Vibronic coherence evolution in multidimensional ultrafast photochemical processes. *Nature Communications* **2019,** *10* (1), 5621.
18. Imahori, H.; Tamaki, K.; Araki, Y.; Sekiguchi, Y.; Ito, O.; Sakata, Y.; Fukuzumi, S., Stepwise Charge Separation and Charge Recombination in Ferrocene-meso,meso-Linked Porphyrin Dimer−Fullerene Triad. *Journal of the American Chemical Society* **2002,** *124* (18), 5165-5174.
19. Kim, S.-Y.; Cho, Y.-J.; Lee, A.-R.; Son, H.-j.; Han, W.-S.; Cho, D. W.; Kang, S. O., Influence of π-conjugation structural changes on intramolecular charge transfer and photoinduced electron transfer in donor–π–acceptor dyads. *Physical Chemistry Chemical Physics* **2017,** *19* (1), 426-435.
20. Krzeszewski, M.; Espinoza, E. M.; Červinka, C.; Derr, J. B.; Clark, J. A.; Borchardt, D.; Beran, G. J. O.; Gryko, D. T.; Vullev, V. I., Dipole Effects on Electron Transfer are Enormous. *Angewandte Chemie International Edition* **2018,** *57* (38), 12365-12369.
21. Macpherson, A. N.; Liddell, P. A.; Lin, S.; Noss, L.; Seely, G. R.; DeGraziano, J. M.; Moore, A. L.; Moore, T. A.; Gust, D., Ultrafast Photoinduced Electron Transfer in Rigid Porphyrin-Quinone Dyads. *Journal of the American Chemical Society* **1995,** *117* (27), 7202-7212.
22. McCreery, R. L., Effects of electronic coupling and electrostatic potential on charge transport in carbon-based molecular electronic junctions. *Beilstein J Nanotechnol* **2016,** *7*, 32-46.
23. Meier, H., Conjugated Oligomers with Terminal Donor–Acceptor Substitution. *Angewandte Chemie International Edition* **2005,** *44* (17), 2482-2506.
24. Purc, A.; Espinoza, E. M.; Nazir, R.; Romero, J. J.; Skonieczny, K.; Jeżewski, A.; Larsen, J. M.; Gryko, D. T.; Vullev, V. I., Gating That Suppresses Charge Recombination–The Role of Mono-N-Arylated Diketopyrrolopyrrole. *Journal of the American Chemical Society* **2016,** *138* (39), 12826-12832.
25. Ricks, A. B.; Solomon, G. C.; Colvin, M. T.; Scott, A. M.; Chen, K.; Ratner, M. A.; Wasielewski, M. R., Controlling Electron Transfer in Donor−Bridge−Acceptor Molecules Using Cross-Conjugated Bridges. *Journal of the American Chemical Society* **2010,** *132* (43), 15427-15434.
26. Roland, T.; Heyer, E.; Liu, L.; Ruff, A.; Ludwigs, S.; Ziessel, R.; Haacke, S., A Detailed Analysis of Multiple Photoreactions in a Light-Harvesting Molecular Triad with Overlapping Spectra by Ultrafast Spectroscopy. *The Journal of Physical Chemistry C* **2014,** *118* (42), 24290-24301.

27. Sung, J.; Nowak-Król, A.; Schlosser, F.; Fimmel, B.; Kim, W.; Kim, D.; Würthner, F., Direct Observation of Excimer-Mediated Intramolecular Electron Transfer in a Cofacially-Stacked Perylene Bisimide Pair. *Journal of the American Chemical Society* **2016,** *138* (29), 9029-9032.
28. Wasielewski, M. R., Photoinduced electron transfer in supramolecular systems for artificial photosynthesis. *Chemical reviews* **1992,** *92* (3), 435-461.
29. Wasielewski, M. R.; Niemczyk, M. P.; Svec, W. A.; Pewitt, E. B., Dependence of rate constants for photoinduced charge separation and dark charge recombination on the free energy of reaction in restricted-distance porphyrin-quinone molecules. *Journal of the American Chemical Society* **1985,** *107* (4), 1080-1082.
30. Rösch, U.; Yao, S.; Wortmann, R.; Würthner, F., Fluorescent H-Aggregates of Merocyanine Dyes. *Angewandte Chemie International Edition* **2006,** *45* (42), 7026-7030.
31. Aumiler, D.; Wang, S.; Chen, X.; Xia, A., Excited State Localization and Delocalization of Internal Charge Transfer in Branched Push−Pull Chromophores Studied by Single-Molecule Spectroscopy. *Journal of the American Chemical Society* **2009,** *131* (16), 5742-5743.
32. Berlin, Y. A.; Grozema, F. C.; Siebbeles, L. D. A.; Ratner, M. A., Charge Transfer in Donor-Bridge-Acceptor Systems: Static Disorder, Dynamic Fluctuations, and Complex Kinetics. *The Journal of Physical Chemistry C* **2008,** *112* (29), 10988-11000.
33. Kim, T.; Kim, W.; Vakuliuk, O.; Gryko, D. T.; Kim, D., Two-Step Charge Separation Passing Through the Partial Charge-Transfer State in a Molecular Dyad. *Journal of the American Chemical Society* **2020,** *142* (3), 1564-1573.
34. Myers, A. B., Resonance Raman Intensities and Charge-Transfer Reorganization Energies. *Chemical Reviews* **1996,** *96* (3), 911-926.
35. Rafiq, S.; Scholes, G. D., From Fundamental Theories to Quantum Coherences in Electron Transfer. *Journal of the American Chemical Society* **2019,** *141* (2), 708-722.
36. Spencer, J.; Scalfi, L.; Carof, A.; Blumberger, J., Confronting surface hopping molecular dynamics with Marcus theory for a molecular donor–acceptor system. *Faraday Discussions* **2016,** *195* (0), 215-236.
37. Han, J.; Cao, B.; Li, Y.; Zhou, Q.; Sun, C.; Li, B.; Yin, H.; Shi, Y., The role played by solvent polarity in regulating the competitive mechanism between ESIPT and TICT of coumarin (E-8-((4-dimethylamino-phenylimino)-methyl)-7-hydroxy-4-methyl-2H-chromen-2-one). *Spectrochimica Acta Part A: Molecular and Biomolecular Spectroscopy* **2020,** *231*, 118086.
38. Sasaki, S.; Drummen, G. P. C.; Konishi, G.-i., Recent advances in twisted intramolecular charge transfer (TICT) fluorescence and related phenomena in materials chemistry. *Journal of Materials Chemistry C* **2016,** *4* (14), 2731-2743.
39. Monti, F.; Venturini, A.; Nenov, A.; Tancini, F.; Finke, A. D.; Diederich, F.; Armaroli, N., Anilino-Substituted Multicyanobuta-1,3-diene Electron Acceptors: TICT Molecules with Accessible Conical Intersections. *The Journal of Physical Chemistry A* **2015,** *119* (43), 10677-10683.
40. Kasha, M., Energy Transfer, Charge Transfer, and Proton Transfer in Molecular Composite Systems. In *Physical and Chemical Mechanisms in Molecular Radiation Biology*, Glass, W. A.; Varma, M. N., Eds. Springer US: Boston, MA, 1991; pp 231-255.
41. Hoshino, M.; Uekusa, H.; Tomita, A.; Koshihara, S.-y.; Sato, T.; Nozawa, S.; Adachi, S.-i.; Ohkubo, K.; Kotani, H.; Fukuzumi, S., Determination of the Structural Features of a Long-

Lived Electron-Transfer State of 9-Mesityl-10-methylacridinium Ion. *Journal of the American Chemical Society* **2012,** *134* (10), 4569-4572.

42. Grabowski, Z. R.; Rotkiewicz, K.; Rettig, W., Structural Changes Accompanying Intramolecular Electron Transfer: Focus on Twisted Intramolecular Charge-Transfer States and Structures. *Chemical Reviews* **2003,** *103* (10), 3899-4032.

43. Ghosh, R.; Manna, B., Comparative photophysics and ultrafast dynamics of dimethylaminochalcone and a structurally rigid derivative: experimental identification of TICT coordinate. *Physical Chemistry Chemical Physics* **2017,** *19* (34), 23078-23084.

44. El-Zohry, A. M.; Orabi, E. A.; Karlsson, M.; Zietz, B., Twisted Intramolecular Charge Transfer (TICT) Controlled by Dimerization: An Overlooked Piece of the TICT Puzzle. *The Journal of Physical Chemistry A* **2021,** *125* (14), 2885-2894.

45. Chen, C.; Huang, R.; Batsanov, A. S.; Pander, P.; Hsu, Y.-T.; Chi, Z.; Dias, F. B.; Bryce, M. R., Intramolecular Charge Transfer Controls Switching Between Room Temperature Phosphorescence and Thermally Activated Delayed Fluorescence. *Angewandte Chemie International Edition* **2018,** *57* (50), 16407-16411.

46. Carlotti, B.; Consiglio, G.; Elisei, F.; Fortuna, C. G.; Mazzucato, U.; Spalletti, A., Intramolecular Charge Transfer of Push–Pull Pyridinium Salts in the Singlet Manifold. *The Journal of Physical Chemistry A* **2014,** *118* (20), 3580-3592.

47. Yang, J.-S.; Lin, C.-J., Fate of photoexcited trans-aminostilbenes. *Journal of Photochemistry and Photobiology A: Chemistry* **2015,** *312*, 107-120.

48. Sunahara, H.; Urano, Y.; Kojima, H.; Nagano, T., Design and Synthesis of a Library of BODIPY-Based Environmental Polarity Sensors Utilizing Photoinduced Electron-Transfer-Controlled Fluorescence ON/OFF Switching. *Journal of the American Chemical Society* **2007,** *129* (17), 5597-5604.

49. Sengupta, S.; Pandey, U. K., Dual emissive bodipy–benzodithiophene–bodipy TICT triad with a remarkable Stokes shift of 194 nm. *Organic & Biomolecular Chemistry* **2018,** *16* (12), 2033-2038.

50. Rettig, W.; Majenz, W.; Lapouyade, R.; Vogel, M., Adiabatic photochemistry with luminescent products. *Journal of Photochemistry and Photobiology A: Chemistry* **1992,** *65* (1), 95-110.

51. Rettig, W., Intramolecular rotational relaxation of compounds which form "twisted intramolecular charge transfer" (TICT) excited states. *The Journal of Physical Chemistry* **1982,** *86* (11), 1970-1976.

52. Li, W.; Liu, D.; Shen, F.; Ma, D.; Wang, Z.; Feng, T.; Xu, Y.; Yang, B.; Ma, Y., A Twisting Donor-Acceptor Molecule with an Intercrossed Excited State for Highly Efficient, Deep-Blue Electroluminescence. *Advanced Functional Materials* **2012,** *22* (13), 2797-2803.

53. Kundu, A.; Karthikeyan, S.; Sagara, Y.; Moon, D.; Anthony, S. P., Temperature-Controlled Locally Excited and Twisted Intramolecular Charge-Transfer State-Dependent Fluorescence Switching in Triphenylamine–Benzothiazole Derivatives. *ACS Omega* **2019,** *4* (3), 5147-5154.

54. August, J.; Palmer, T. F.; Simons, J. P.; Jouvet, C.; Rettig, W., Intramolecular charge transfer in jet-cooled aromatic amines. *Chemical Physics Letters* **1988,** *145* (4), 273-279.

55. Tanaka, H.; Shizu, K.; Nakanotani, H.; Adachi, C., Twisted Intramolecular Charge Transfer State for Long-Wavelength Thermally Activated Delayed Fluorescence. *Chemistry of Materials* **2013,** *25* (18), 3766-3771.
56. Amdursky, N.; Erez, Y.; Huppert, D., Molecular rotors: what lies behind the high sensitivity of the thioflavin-T fluorescent marker. *Acc Chem Res* **2012,** *45* (9), 1548-57.
57. Borrelli, R.; Capobianco, A.; Landi, A.; Peluso, A., Vibronic couplings and coherent electron transfer in bridged systems. *Physical Chemistry Chemical Physics* **2015,** *17* (46), 30937-30945.
58. Verma, S.; Ghosh, H. N., Tuning Interfacial Charge Separation by Molecular Twist: A New Insight into Coumarin-Sensitized TiO2 Films. *The Journal of Physical Chemistry C* **2014,** *118* (20), 10661-10669.
59. El-Zohry, A. M.; Karlsson, M., Gigantic Relevance of Twisted Intramolecular Charge Transfer for Organic Dyes Used in Solar Cells. *The Journal of Physical Chemistry C* **2018,** *122* (42), 23998-24003.
60. El-Zohry, A. M.; Cong, J.; Karlsson, M.; Kloo, L.; Zietz, B., Ferrocene as a rapid charge regenerator in dye-sensitized solar cells. *Dyes and Pigments* **2016,** *132*, 360-368.
61. Debnath, T.; Maity, P.; Lobo, H.; Singh, B.; Shankarling, G. S.; Ghosh, H. N., Extensive Reduction in Back Electron Transfer in Twisted Intramolecular Charge-Transfer (TICT) Coumarin-Dye-Sensitized TiO2 Nanoparticles/Film: A Femtosecond Transient Absorption Study. *Chemistry – A European Journal* **2014,** *20* (12), 3510-3519.
62. Sasaki, S.; Igawa, K.; Konishi, G.-i., The effect of regioisomerism on the solid-state fluorescence of bis(piperidyl)anthracenes: structurally simple but bright AIE luminogens. *Journal of Materials Chemistry C* **2015,** *3* (23), 5940-5950.
63. Zhou, D.; Wang, Y.; Jia, J.; Yu, W.; Qu, B.; Li, X.; Sun, X., H-Bonding and charging mediated aggregation and emission for fluorescence turn-on detection of hydrazine hydrate. *Chemical Communications* **2015,** *51* (53), 10656-10659.
64. Oka, Y.; Nakamura, S.; Morozumi, T.; Nakamura, H., TritonX-100 selective chemosensor based on beta-cyclodextrin modified by anthracene derivative. *Talanta* **2010,** *82* (4), 1622-6.
65. Morozumi, T.; Anada, T.; Nakamura, H., New Fluorescent "Off−On" Behavior of 9-Anthryl Aromatic Amides through Controlling the Twisted Intramolecular Charge Transfer Relaxation Process by Complexation with Metal Ions. *The Journal of Physical Chemistry B* **2001,** *105* (15), 2923-2931.
66. Kim, J.; Morozumi, T.; Hiraga, H.; Nakamura, H., Substituted position effect on twisted intramolecular charge transfer of 1- and 2-anthracene aromatic carboxamides as chemosensors based on linear polyether. *Anal Sci* **2009,** *25* (11), 1319-25.
67. Hirayama, T.; Okuda, K.; Nagasawa, H., A highly selective turn-on fluorescent probe for iron(ii) to visualize labile iron in living cells. *Chemical Science* **2013,** *4* (3), 1250-1256.
68. Fan, Y.; Wang, F.; Hou, F.; Wei, L.; Zhu, G.; Zhao, D.; Hu, Q.; Lei, T.; Yang, L.; Wang, P.; Ge, G., A novel TICT-based near-infrared fluorescent probe for light-up sensing and imaging of human serum albumin in real samples. *Chinese Chemical Letters* **2023,** *34* (2), 107557.
69. Chen, B.; Sun, X.; Li, X.; Ågren, H.; Xie, Y., TICT based fluorescence "turn-on" hydrazine probes. *Sensors and Actuators B: Chemical* **2014,** *199*, 93-100.

70. Chen, B.; Ding, Y.; Li, X.; Zhu, W.; Hill, J. P.; Ariga, K.; Xie, Y., Steric hindrance-enforced distortion as a general strategy for the design of fluorescence "turn-on" cyanide probes. *Chemical Communications* **2013,** *49* (86), 10136-10138.

71. Sutharsan, J.; Dakanali, M.; Capule, C. C.; Haidekker, M. A.; Yang, J.; Theodorakis, E. A., Rational design of amyloid binding agents based on the molecular rotor motif. *ChemMedChem* **2010,** *5* (1), 56-60.

72. Haidekker, M. A.; Theodorakis, E. A., Environment-sensitive behavior of fluorescent molecular rotors. *J Biol Eng* **2010,** *4*, 11.

73. Budzák, Š.; Jacquemin, D., Excited state intramolecular proton transfer in julolidine derivatives: an ab initio study. *Physical Chemistry Chemical Physics* **2018,** *20* (38), 25031-25038.

74. Dance, Z. E. X.; Mickley, S. M.; Wilson, T. M.; Ricks, A. B.; Scott, A. M.; Ratner, M. A.; Wasielewski, M. R., Intersystem crossing mediated by photoinduced intramolecular charge transfer: Julolidine - Anthracene molecules with perpendicular π systems. *Journal of Physical Chemistry A* **2008,** *112* (18), 4194-4201.

75. Kamkaew, A.; Lim, S. H.; Lee, H. B.; Kiew, L. V.; Chung, L. Y.; Burgess, K., BODIPY dyes in photodynamic therapy. *Chemical Society Reviews* **2013,** *42* (1), 77-88.

76. Ulrich, G.; Ziessel, R.; Harriman, A., The Chemistry of Fluorescent Bodipy Dyes: Versatility Unsurpassed. *Angewandte Chemie International Edition* **2008,** *47* (7), 1184-1201.

77. Benniston, A. C.; Clift, S.; Harriman, A., Intramolecular charge-transfer interactions in a julolidine–Bodipy molecular assembly as revealed via 13C NMR chemical shifts. *Journal of Molecular Structure* **2011,** *985* (2), 346-354.

78. Kim, T.; Lin, C.; Schultz, J. D.; Young, R. M.; Wasielewski, M. R., π-Stacking-Dependent Vibronic Couplings Drive Excited-State Dynamics in Perylenediimide Assemblies. *Journal of the American Chemical Society* **2022,** *144* (25), 11386-11396.

79. Miyata, K.; Kurashige, Y.; Watanabe, K.; Sugimoto, T.; Takahashi, S.; Tanaka, S.; Takeya, J.; Yanai, T.; Matsumoto, Y., Coherent singlet fission activated by symmetry breaking. *Nature Chemistry* **2017,** *9* (10), 983-989.

80. Musser, A. J.; Liebel, M.; Schnedermann, C.; Wende, T.; Kehoe, T. B.; Rao, A.; Kukura, P., Evidence for conical intersection dynamics mediating ultrafast singlet exciton fission. *Nature Physics* **2015,** *11* (4), 352-357.

81. Novoderezhkin, V. I.; Romero, E.; van Grondelle, R., How exciton-vibrational coherences control charge separation in the photosystem II reaction center. *Physical Chemistry Chemical Physics* **2015,** *17* (46), 30828-30841.

82. Schultz, J. D.; Shin, J. Y.; Chen, M.; O'Connor, J. P.; Young, R. M.; Ratner, M. A.; Wasielewski, M. R., Influence of Vibronic Coupling on Ultrafast Singlet Fission in a Linear Terrylenediimide Dimer. *Journal of the American Chemical Society* **2021,** *143* (4), 2049-2058.

83. Schultz, J. D.; Coleman, A. F.; Mandal, A.; Shin, J. Y.; Ratner, M. A.; Young, R. M.; Wasielewski, M. R., Steric Interactions Impact Vibronic and Vibrational Coherences in Perylenediimide Cyclophanes. *The Journal of Physical Chemistry Letters* **2019,** *10* (23), 7498-7504.

84. Lifschitz, A. M.; Young, R. M.; Mendez-Arroyo, J.; Roznyatovskiy, V. V.; McGuirk, C. M.; Wasielewski, M. R.; Mirkin, C. A., Chemically regulating Rh(i)-Bodipy photoredox switches. *Chemical Communications* **2014,** *50* (52), 6850-6852.

85. Weller, A., Photoinduced Electron Transfer in Solution: Exciplex and Radical Ion Pair Formation Free Enthalpies and their Solvent Dependence. *Zeitschrift für Physikalische Chemie* **1982,** *133* (1), 93-98.

86. Zhao, J.; Xu, K.; Yang, W.; Wang, Z.; Zhong, F., The triplet excited state of Bodipy: formation, modulation and application. *Chemical Society Reviews* **2015,** *44* (24), 8904-8939.

87. Rettig, W., Charge Separation in Excited States of Decoupled Systems—TICT Compounds and Implications Regarding the Development of New Laser Dyes and the Primary Process of Vision and Photosynthesis. *Angewandte Chemie International Edition in English* **1986,** *25* (11), 971-988.

88. Song, H.; Zhao, H.; Guo, Y.; Philip, A. M.; Guo, Q.; Hariharan, M.; Xia, A., Distinct Excited-State Dynamics of Near-Orthogonal Perylenimide Dimer: Conformational Planarization versus Symmetry Breaking Charge Transfer. *The Journal of Physical Chemistry C* **2020,** *124* (1), 237-245.

89. Dong, Y.; Sukhanov, A. A.; Zhao, J.; Elmali, A.; Li, X.; Dick, B.; Karatay, A.; Voronkova, V. K., Spin–Orbit Charge-Transfer Intersystem Crossing (SOCT-ISC) in Bodipy-Phenoxazine Dyads: Effect of Chromophore Orientation and Conformation Restriction on the Photophysical Properties. *The Journal of Physical Chemistry C* **2019,** *123* (37), 22793-22811.

90. Phelan, B. T.; Schultz, J. D.; Zhang, J.; Huang, G.-J.; Young, Ryan M.; Wasielewski, M. R., Quantum coherence in ultrafast photo-driven charge separation. *Faraday Discussions* **2019,** *216* (0), 319-338.

91. Fitzner, R.; Mena-Osteritz, E.; Mishra, A.; Schulz, G.; Reinold, E.; Weil, M.; Körner, C.; Ziehlke, H.; Elschner, C.; Leo, K.; Riede, M.; Pfeiffer, M.; Uhrich, C.; Bäuerle, P., Correlation of π-Conjugated Oligomer Structure with Film Morphology and Organic Solar Cell Performance. *Journal of the American Chemical Society* **2012,** *134* (27), 11064-11067.

92. Geng, H.; Zheng, X.; Shuai, Z.; Zhu, L.; Yi, Y., Understanding the Charge Transport and Polarities in Organic Donor–Acceptor Mixed-Stack Crystals: Molecular Insights from the Super-Exchange Couplings. *Advanced Materials* **2015,** *27* (8), 1443-1449.

93. Lunt, R. R.; Benziger, J. B.; Forrest, S. R., Relationship between Crystalline Order and Exciton Diffusion Length in Molecular Organic Semiconductors. *Advanced Materials* **2010,** *22* (11), 1233-1236.

94. Natarajan, S.; Umamaheswaran, M.; Kalyana Sundar, J.; Suresh, J.; Martin Britto Dhas, S. A., Structural, spectroscopic and nonlinear optical studies on a new efficient organic donor–acceptor crystal for second harmonic generation: l-Threoninium picrate. *Spectrochimica Acta Part A: Molecular and Biomolecular Spectroscopy* **2010,** *77* (1), 160-163.

95. Wan, X.; Li, C.; Zhang, M.; Chen, Y., Acceptor–donor–acceptor type molecules for high performance organic photovoltaics – chemistry and mechanism. *Chemical Society Reviews* **2020,** *49* (9), 2828-2842.

96. Zhang, J.; Xu, W.; Sheng, P.; Zhao, G.; Zhu, D., Organic Donor–Acceptor Complexes as Novel Organic Semiconductors. *Accounts of Chemical Research* **2017,** *50* (7), 1654-1662.

97. Thompson, B. C.; Fréchet, J. M. J., Polymer–Fullerene Composite Solar Cells. *Angewandte Chemie International Edition* **2008,** *47* (1), 58-77.

98. Garain, S.; Ansari, S. N.; Kongasseri, A. A.; Chandra Garain, B.; Pati, S. K.; George, S. J., Room temperature charge-transfer phosphorescence from organic donor–acceptor Co-crystals. *Chemical Science* **2022,** *13* (34), 10011-10019.

99. Haarer, D.; Karl, N., Charge-transfer-absorption, CT-emission- and ESR-spectroscopy with zone-refined crystals of anthracene-pyromellitic dianhydride. *Chemical Physics Letters* **1973,** *21* (1), 49-53.

100. Park, S. K.; Varghese, S.; Kim, J. H.; Yoon, S.-J.; Kwon, O. K.; An, B.-K.; Gierschner, J.; Park, S. Y., Tailor-Made Highly Luminescent and Ambipolar Transporting Organic Mixed Stacked Charge-Transfer Crystals: An Isometric Donor–Acceptor Approach. *Journal of the American Chemical Society* **2013,** *135* (12), 4757-4764.

101. Schlesinger, I.; Powers-Riggs, N. E.; Logsdon, J. L.; Qi, Y.; Miller, S. A.; Tempelaar, R.; Young, R. M.; Wasielewski, M. R., Charge-transfer biexciton annihilation in a donor–acceptor co-crystal yields high-energy long-lived charge carriers. *Chemical Science* **2020,** *11* (35), 9532-9541.

102. Li, H.; Fan, C.; Fu, W.; Xin, H. L.; Chen, H., Solution-Grown Organic Single-Crystalline Donor–Acceptor Heterojunctions for Photovoltaics. *Angewandte Chemie International Edition* **2015,** *54* (3), 956-960.

103. Wang, C.; Wang, J.; Wu, N.; Xu, M.; Yang, X.; Lu, Y.; Zang, L., Donor–acceptor single cocrystal of coronene and perylene diimide: molecular self-assembly and charge-transfer photoluminescence. *RSC Advances* **2017,** *7* (4), 2382-2387.

104. Wykes, M.; Park, S. K.; Bhattacharyya, S.; Varghese, S.; Kwon, J. E.; Whang, D. R.; Cho, I.; Wannemacher, R.; Lüer, L.; Park, S. Y.; Gierschner, J., Excited State Features and Dynamics in a Distyrylbenzene-Based Mixed Stack Donor–Acceptor Cocrystal with Luminescent Charge Transfer Characteristics. *The Journal of Physical Chemistry Letters* **2015,** *6* (18), 3682-3687.

105. Zhang, J.; Jin, J.; Xu, H.; Zhang, Q.; Huang, W., Recent progress on organic donor–acceptor complexes as active elements in organic field-effect transistors. *Journal of Materials Chemistry C* **2018,** *6* (14), 3485-3498.

106. Zhu, L.; Yi, Y.; Li, Y.; Kim, E.-G.; Coropceanu, V.; Brédas, J.-L., Prediction of Remarkable Ambipolar Charge-Transport Characteristics in Organic Mixed-Stack Charge-Transfer Crystals. *Journal of the American Chemical Society* **2012,** *134* (4), 2340-2347.

107. Zhu, W.; Zhu, L.; Zou, Y.; Wu, Y.; Zhen, Y.; Dong, H.; Fu, H.; Wei, Z.; Shi, Q.; Hu, W., Deepening Insights of Charge Transfer and Photophysics in a Novel Donor–Acceptor Cocrystal for Waveguide Couplers and Photonic Logic Computation. *Advanced Materials* **2016,** *28* (35), 7563-7563.

108. Gosztola, D.; Niemczyk, M. P.; Svec, W.; Lukas, A. S.; Wasielewski, M. R., Excited Doublet States of Electrochemically Generated Aromatic Imide and Diimide Radical Anions. *The Journal of Physical Chemistry A* **2000,** *104* (28), 6545-6551.

109. Veldkamp, B. S.; Han, W.-S.; Dyar, S. M.; Eaton, S. W.; Ratner, M. A.; Wasielewski, M. R., Photoinitiated multi-step charge separation and ultrafast charge transfer induced dissociation in a pyridyl-linked photosensitizer–cobaloxime assembly. *Energy & Environmental Science* **2013,** *6* (6), 1917-1928.

110. Ballabio, M.; Cánovas, E., Electron Transfer at Quantum Dot–Metal Oxide Interfaces for Solar Energy Conversion. *ACS Nanoscience Au* **2022,** *2* (5), 367-395.

111. Bandi, V.; D'Souza, F. P.; Gobeze, H. B.; D'Souza, F., Competitive electron transfer in a novel, broad-band capturing, subphthalocyanine–AzaBODIPY–C60 supramolecular triad. *Chemical Communications* **2016,** *52* (3), 579-581.

112. El-Khouly, M. E.; El-Mohsnawy, E.; Fukuzumi, S., Solar energy conversion: From natural to artificial photosynthesis. *Journal of Photochemistry and Photobiology C: Photochemistry Reviews* **2017,** *31*, 36-83.

113. El-Khouly, M. E.; Wijesinghe, C. A.; Nesterov, V. N.; Zandler, M. E.; Fukuzumi, S.; D'Souza, F., Ultrafast Photoinduced Energy and Electron Transfer in Multi-Modular Donor–Acceptor Conjugates. *Chemistry – A European Journal* **2012,** *18* (43), 13844-13853.

114. Makita, H.; Hastings, G., Inverted-region electron transfer as a mechanism for enhancing photosynthetic solar energy conversion efficiency. *Proceedings of the National Academy of Sciences* **2017,** *114* (35), 9267-9272.

115. Ponseca, C. S., Jr.; Chábera, P.; Uhlig, J.; Persson, P.; Sundström, V., Ultrafast Electron Dynamics in Solar Energy Conversion. *Chem Rev* **2017,** *117* (16), 10940-11024.

116. Ponseca, C. S., Jr.; Chábera, P.; Uhlig, J.; Persson, P.; Sundström, V., Ultrafast Electron Dynamics in Solar Energy Conversion. *Chemical Reviews* **2017,** *117* (16), 10940-11024.

117. Rwenyagila, E. R., A Review of Organic Photovoltaic Energy Source and Its Technological Designs. *International Journal of Photoenergy* **2017,** *2017*, 1656512.

118. Cheng, Y. C.; Fleming, G. R., Dynamics of light harvesting in photosynthesis. *Annu Rev Phys Chem* **2009,** *60*, 241-62.

119. Engel, G. S.; Calhoun, T. R.; Read, E. L.; Ahn, T.-K.; Mančal, T.; Cheng, Y.-C.; Blankenship, R. E.; Fleming, G. R., Evidence for wavelike energy transfer through quantum coherence in photosynthetic systems. *Nature* **2007,** *446* (7137), 782-786.

120. Falke, S. M.; Rozzi, C. A.; Brida, D.; Maiuri, M.; Amato, M.; Sommer, E.; De Sio, A.; Rubio, A.; Cerullo, G.; Molinari, E.; Lienau, C., Coherent ultrafast charge transfer in an organic photovoltaic blend. *Science* **2014,** *344* (6187), 1001-5.

121. Fassioli, F.; Dinshaw, R.; Arpin, P. C.; Scholes, G. D., Photosynthetic light harvesting: excitons and coherence. *J R Soc Interface* **2014,** *11* (92), 20130901.

122. Fuller, F. D.; Pan, J.; Gelzinis, A.; Butkus, V.; Senlik, S. S.; Wilcox, D. E.; Yocum, C. F.; Valkunas, L.; Abramavicius, D.; Ogilvie, J. P., Vibronic coherence in oxygenic photosynthesis. *Nat Chem* **2014,** *6* (8), 706-11.

123. Olaya-Castro, A.; Nazir, A.; Fleming, G. R., Quantum-coherent energy transfer: implications for biology and new energy technologies. *Philos Trans A Math Phys Eng Sci* **2012,** *370* (1972), 3613-7.

124. Savikhin, S.; Buck, D. R.; Struve, W. S., Oscillating anisotropies in a bacteriochlorophyll protein: Evidence for quantum beating between exciton levels. *Chemical Physics* **1997,** *223* (2), 303-312.

125. Kambhampati, P.; Son, D. H.; Kee, T. W.; Barbara, P. F., Solvent Effects on Vibrational Coherence and Ultrafast Reaction Dynamics in the Multicolor Pump−Probe Spectroscopy of Intervalence Electron Transfer. *The Journal of Physical Chemistry A* **2000,** *104* (46), 10637-10644.

126. Pisliakov, A. V.; Gelin, M. F.; Domcke, W., Detection of Electronic and Vibrational Coherence Effects in Electron-Transfer Systems by Femtosecond Time-Resolved Fluorescence Spectroscopy: Theoretical Aspects. *The Journal of Physical Chemistry A* **2003,** *107* (15), 2657-2666.

127. Song, Y.; Clafton, S. N.; Pensack, R. D.; Kee, T. W.; Scholes, G. D., Vibrational coherence probes the mechanism of ultrafast electron transfer in polymer–fullerene blends. *Nature Communications* **2014,** *5* (1), 4933.

128. Wynne, K.; Reid, G. D.; Hochstrasser, R. M., Vibrational coherence in electron transfer: The tetracyanoethylene–pyrene complex. *The Journal of Chemical Physics* **1996,** *105* (6), 2287-2297.

129. Abramavicius, V.; Pranculis, V.; Melianas, A.; Inganäs, O.; Gulbinas, V.; Abramavicius, D., Role of coherence and delocalization in photo-induced electron transfer at organic interfaces. *Scientific Reports* **2016,** *6* (1), 32914.

130. Kovalenko, S. A.; Dobryakov, A. L.; Farztdinov, V., Detecting Electronic Coherence in Excited-State Electron Transfer in Fluorinated Benzenes. *Physical Review Letters* **2006,** *96* (6), 068301.

131. Lucke, A.; Mak, C. H.; Egger, R.; Ankerhold, J.; Stockburger, J.; Grabert, H., Is the direct observation of electronic coherence in electron transfer reactions possible? *The Journal of Chemical Physics* **1997,** *107* (20), 8397-8408.

132. Mendive-Tapia, D.; Mangaud, E.; Firmino, T.; de la Lande, A.; Desouter-Lecomte, M.; Meyer, H.-D.; Gatti, F., Multidimensional Quantum Mechanical Modeling of Electron Transfer and Electronic Coherence in Plant Cryptochromes: The Role of Initial Bath Conditions. *The Journal of Physical Chemistry B* **2018,** *122* (1), 126-136.

133. Abraham, B.; Rego, L. G. C.; Gundlach, L., Electronic–Vibrational Coupling and Electron Transfer. *The Journal of Physical Chemistry C* **2019,** *123* (39), 23760-23772.

134. Fuller, F. D.; Pan, J.; Gelzinis, A.; Butkus, V.; Senlik, S. S.; Wilcox, D. E.; Yocum, C. F.; Valkunas, L.; Abramavicius, D.; Ogilvie, J. P., Vibronic coherence in oxygenic photosynthesis. *Nature Chemistry* **2014,** *6* (8), 706-711.

135. Ma, F.; Romero, E.; Jones, M. R.; Novoderezhkin, V. I.; van Grondelle, R., Vibronic Coherence in the Charge Separation Process of the Rhodobacter sphaeroides Reaction Center. *The Journal of Physical Chemistry Letters* **2018,** *9* (8), 1827-1832.

136. Torres, A.; Oliboni, R. S.; Rego, L. G. C., Vibronic and Coherent Effects on Interfacial Electron Transfer Dynamics. *The Journal of Physical Chemistry Letters* **2015,** *6* (24), 4927-4935.

137. Goldsmith, R. H.; Wasielewski, M. R.; Ratner, M. A., Scaling laws for charge transfer in multiply bridged donor/acceptor molecules in a dissipative environment. *J Am Chem Soc* **2007,** *129* (43), 13066-71.

138. Leggett, A. J.; Chakravarty, S.; Dorsey, A. T.; Fisher, M. P. A.; Garg, A.; Zwerger, W., Dynamics of the dissipative two-state system. *Reviews of Modern Physics* **1987,** *59* (1), 1-85.

139. Phelan, B. T.; Zhang, J.; Huang, G. J.; Wu, Y. L.; Zarea, M.; Young, R. M.; Wasielewski, M. R., Quantum Coherence Enhances Electron Transfer Rates to Two Equivalent Electron Acceptors. *J Am Chem Soc* **2019,** *141* (31), 12236-12239.

140. Powell, D. D.; Wasielewski, M. R.; Ratner, M. A., Redfield Treatment of Multipathway Electron Transfer in Artificial Photosynthetic Systems. *J Phys Chem B* **2017,** *121* (29), 7190-7203.

141. Skourtis, S. S.; David H. Waldeck, a.; Beratan, D. N., Inelastic Electron Tunneling Erases Coupling-Pathway Interferences. *Journal of Physical Chemistry B* **2004,** *108*, 15511-15518.

142. Vazquez, H.; Skouta, R.; Schneebeli, S.; Kamenetska, M.; Breslow, R.; Venkataraman, L.; Hybertsen, M. S., Probing the conductance superposition law in single-molecule circuits with parallel paths. *Nat Nanotechnol* **2012,** *7* (10), 663-7.

143. Duan, H.-G.; Prokhorenko, V. I.; Cogdell, R. J.; Ashraf, K.; Stevens, A. L.; Thorwart, M.; Miller, R. J. D., Nature does not rely on long-lived electronic quantum coherence for photosynthetic energy transfer. *Proceedings of the National Academy of Sciences* **2017,** *114* (32), 8493-8498.
144. Thyrhaug, E.; Tempelaar, R.; Alcocer, M. J. P.; Žídek, K.; Bína, D.; Knoester, J.; Jansen, T. L. C.; Zigmantas, D., Identification and characterization of diverse coherences in the Fenna-Matthews-Olson complex. *Nat Chem* **2018,** *10* (7), 780-786.
145. Zarea, M.; Ratner, M. A.; Wasielewski, M. R., Electron transfer in a two-level system within a Cole-Davidson vitreous bath. *J Chem Phys* **2014,** *140* (2), 024110.
146. Policht, V. R.; Niedringhaus, A.; Willow, R.; Laible, P. D.; Bocian, D. F.; Kirmaier, C.; Holten, D.; Mančal, T.; Ogilvie, J. P., Hidden vibronic and excitonic structure and vibronic coherence transfer in the bacterial reaction center. *Science Advances* **2022,** *8* (1), eabk0953.
147. Mauck, C. M.; Young, R. M.; Wasielewski, M. R., Characterization of Excimer Relaxation via Femtosecond Shortwave- and Mid-Infrared Spectroscopy. *The Journal of Physical Chemistry A* **2017,** *121* (4), 784-792.
148. Kistler, K. A.; Pochas, C. M.; Yamagata, H.; Matsika, S.; Spano, F. C., Absorption, Circular Dichroism, and Photoluminescence in Perylene Diimide Bichromophores: Polarization-Dependent H- and J-Aggregate Behavior. *The Journal of Physical Chemistry B* **2012,** *116* (1), 77-86.
149. Maiti, N. C.; Mazumdar, S.; Periasamy, N., J- and H-Aggregates of Porphyrin−Surfactant Complexes: Time-Resolved Fluorescence and Other Spectroscopic Studies. *The Journal of Physical Chemistry B* **1998,** *102* (9), 1528-1538.
150. Nüesch, F.; Grätzel, M., H-aggregation and correlated absorption and emission of a merocyanine dye in solution, at the surface and in the solid state. A link between crystal structure and photophysical properties. *Chemical Physics* **1995,** *193* (1), 1-17.